

Kern- und Teilchenphysik

Conventional Charmonia and Search for Tetraquark, Hybrid and Baryonium States at BESIII

Inaugural-Dissertation
zur Erlangung des Doktorgrades
der Naturwissenschaften im Fachbereich Physik
der Mathematisch-Naturwissenschaftlichen Fakultät
der Universität Münster

vorgelegt von
FREDERIK WEIDNER
aus MÜNSTER

Münster 2025



0009-0004-9159-9051

Dekan:	Prof. Dr. Rudolf Bratschitsch
Erster Gutachter:	Prof. Dr. Alfons Khoukaz
Zweiter Gutachter:	Prof. Dr. Anton Andronic

Tag der mündlichen Prüfung:

Tag der Promotion:

Abstract

Using the world's largest $\psi(2S)$ data sample with $(2712.4 \pm 14.3) \times 10^6$ $\psi(2S)$ events and six data samples in the energy range between (4599.53 ± 0.74) MeV and (4698.82 ± 0.37) MeV with a total integrated luminosity of (4392.4 ± 24.1) pb $^{-1}$, the reactions $\psi(2S) \rightarrow \gamma\eta'\pi^+\pi^-$ and $e^+e^- \rightarrow \eta_c K^* K$ were analyzed.

In the first analysis the η' meson was reconstructed in the two decay modes $\eta' \rightarrow \eta\pi^+\pi^-$ with $\eta \rightarrow \gamma\gamma$ and $\eta' \rightarrow \gamma\pi^+\pi^-$. In both channels significant enhancements were found at the invariant masses of the $X(1835)$, η_c and $\chi_{c1,2}$. Using one-dimensional fits to the $\eta'\pi^+\pi^-$ spectrum, the corresponding branching ratios were determined to be $\text{Br}(\eta_c \rightarrow \eta'\pi^+\pi^-) = (1.67 \pm 0.14) \times 10^{-2}$, $\text{Br}(\chi_{c1} \rightarrow \eta'\pi^+\pi^-) = (1.64 \pm 0.12) \times 10^{-3}$ and $\text{Br}(\chi_{c2} \rightarrow \eta'\pi^+\pi^-) = (2.95 \pm 0.29) \times 10^{-4}$. They are compatible with existing values and are up to a factor of six more precise. For the $X(1835)$, the product branching ratio was determined to be $\text{Br}(\psi(2S) \rightarrow \gamma X(1835)) \cdot \text{Br}(X(1835) \rightarrow \eta'\pi^+\pi^-) = (2.89 \pm 0.64) \times 10^{-5}$. This is the first observation of this state in $\psi(2S)$ decays, and its production ratio between J/ψ and $\psi(2S)$ decays was found to be consistent with that of the $X(p\bar{p})$. For the χ_{c0} no significant signal was observed consistent with CP conservation and the upper limit was measured as $\text{Br}(\chi_{c0} \rightarrow \eta'\pi^+\pi^-) < 1.46 \times 10^{-5}$ at a confidence level of 90%, an improvement of more than one order of magnitude. For the χ_{c2} decay, a partial wave analysis was performed and the data was described successfully. No significant signal was found for the $\pi_1(1600)$ and an upper limit on the product branching ratio was determined of $\text{Br}(\chi_{c2} \rightarrow \pi_1(1600)^\pm\pi^\mp) \cdot \text{Br}(\pi_1(1600)^\pm \rightarrow \eta'\pi^\pm) < 3.26 \times 10^{-5}$.

In the $e^+e^- \rightarrow \eta_c K^* K$ analysis, the η_c was reconstructed in 13 decay channels representing $(37.2 \pm 2.7)\%$ of its total width. The K^* was reconstructed in its dominant decay $K^* \rightarrow K\pi$, considering the charged and uncharged K^* . The appearing π^0 and η resonances were reconstructed in their decay into two photons, and the K_S^0 was reconstructed in its decay into $\pi^+\pi^-$. A combined fit to all final states resulted in no significant signal for the η_c meson. Upper limits for the Born cross section were calculated with the best one determined at $\sqrt{s} = (4681.92 \pm 0.30)$ MeV with $\sigma_{\text{Born}}(e^+e^- \rightarrow \eta_c K^* K) < 11.5$ pb at a confidence level of 90%. No significant signal for a contribution from the Z_{cs} was found and the upper limit on the ratio of the decay widths for $Z_{cs}^\pm \rightarrow \eta_c K^{*\pm}$ and $Z_{cs}^\pm \rightarrow (D_s^\pm \bar{D}^{*0} + D_s^{*\pm} \bar{D}^0)$ was calculated to be 3.3 at a confidence level of 90%.

Zusammenfassung

Unter Verwendung des größten $\psi(2S)$ Datensatz, bestehend aus $(2712.4 \pm 14.3) \times 10^6$ Ereignissen, sowie sechs Datensätzen mit Schwerpunktsenergien zwischen (4599.53 ± 0.74) MeV und (4698.82 ± 0.37) MeV mit einer integrierten Luminosität von (4392.4 ± 24.1) pb $^{-1}$, wurden die Reaktionen $\psi(2S) \rightarrow \gamma\eta'\pi^+\pi^-$ und $e^+e^- \rightarrow \eta_c K^* K$ analysiert.

In der ersten der beiden Analysen wurde das η' Meson in den beiden Zerfällen $\eta' \rightarrow \eta\pi^+\pi^-$ mit $\eta \rightarrow \gamma\gamma$ und $\eta' \rightarrow \gamma\pi^+\pi^-$ rekonstruiert. In beiden Kanälen wurden signifikante Signale im Bereich der Massen der $X(1835)$, η_c und der $\chi_{c1,2}$ Mesonen gefunden. Mit eindimensionalen Fits an das Spektrum des $\eta'\pi^+\pi^-$ Systems wurden die Zerfallsverhältnisse bestimmt: $\text{Br}(\eta_c \rightarrow \eta'\pi^+\pi^-) = (1.67 \pm 0.14) \times 10^{-2}$, $\text{Br}(\chi_{c1} \rightarrow \eta'\pi^+\pi^-) = (1.64 \pm 0.12) \times 10^{-3}$ und $\text{Br}(\chi_{c2} \rightarrow \eta'\pi^+\pi^-) = (2.95 \pm 0.29) \times 10^{-4}$. Diese Werte sind mit Literaturwerten kompatibel und um einen Faktor von bis zu sechs genauer. Für das $X(1835)$ Meson ergibt sich ein Wert von $\text{Br}(\psi(2S) \rightarrow \gamma X(1835)) \cdot \text{Br}(X(1835) \rightarrow \eta'\pi^+\pi^-) = (2.89 \pm 0.64) \times 10^{-5}$. Hierbei handelt es sich um die erste Beobachtung dieses Teilchens in Zerfällen des $\psi(2S)$ -Mesons und das ermittelte Verhältnis der Produktionsstärken in J/ψ und $\psi(2S)$ Zerfällen stimmt mit dem Wert für das $X(p\bar{p})$ überein. Für das χ_{c0} Meson wurde kein signifikantes Signal beobachtet, was mit der Erhaltung der CP -Quantenzahlen begründet werden kann. Hierfür wurde eine obere Grenze von $\text{Br}(\chi_{c0} \rightarrow \eta'\pi^+\pi^-) < 1.46 \times 10^{-5}$ bestimmt, was einer Verbesserung um mehr als eine Größenordnung entspricht. Für das χ_{c2} Meson wurde eine Partialwellenanalyse durchgeführt und die Daten damit erfolgreich beschrieben. Dabei wurde kein signifikantes Signal für das $\pi_1(1600)$ gefunden und für das Produkt der Zerfallsverhältnisse ergab sich $\text{Br}(\chi_{c2} \rightarrow \pi_1(1600)^\pm\pi^\mp) \cdot \text{Br}(\pi_1(1600)^\pm \rightarrow \eta'\pi^\pm) < 3.26 \times 10^{-5}$. In der $e^+e^- \rightarrow \eta_c K^* K$ Analyse wurde das η_c meson in 13 verschiedenen Zerfallskanälen rekonstruiert, was (37.2 ± 2.7) % seiner gesamten Zerfälle entspricht. Das K^* Meson wurde in seinem dominanten Zerfall $K^* \rightarrow K\pi$ nachgewiesen, wobei sowohl das geladene als auch das ungeladene K^* berücksichtigt wurden. Auftretende π^0 und η Mesonen wurden in ihren Zerfällen in zwei Photonen nachgewiesen und das K_S^0 wurde rekonstruiert im Zerfall nach $\pi^+\pi^-$. Ein kombinierter Fit an alle η_c -Zerfälle ergab kein signifikantes Signal und es wurden obere Grenzen für den Born-Wirkungsquerschnitt bestimmt. Die beste Grenze von $\sigma_{\text{Born}}(e^+e^- \rightarrow \eta_c K^* K) < 11.5$ pb ergab sich für $\sqrt{s} = (4681.92 \pm 0.30)$ MeV. Es wurde außerdem kein signifikanter Beitrag des Z_{cs} gefunden und es wurde eine obere Grenze für das Verhältnis der Zerfallsbreiten für $Z_{cs}^\pm \rightarrow \eta_c K^{*\pm}$ und $Z_{cs}^\pm \rightarrow (D_s^\pm \bar{D}^{*0} + D_s^{*\pm} \bar{D}^0)$ bestimmt, wobei sich eine Grenze von 3.3 ergab.

Contents

1. Introduction	1
2. Theory	5
2.1. The Standard Model of Particle Physics	5
2.2. Quantum Chromodynamics	6
2.2.1. The Quark Model	9
2.2.2. Baryons	10
2.2.3. Mesons	11
2.2.4. The Charmonium System	16
2.2.5. Exotic Hadrons	18
2.3. Nonrelativistic QCD	23
2.3.1. NRQCD Lagrangian	23
2.3.2. Fock State Expansion	25
2.3.3. NRQCD Factorization for P-Wave Charmonia	26
3. Experimental Setup	31
3.1. BEPCII	31
3.2. BESIII	32
3.2.1. Multilayer Drift Chamber	33
3.2.2. Time-of-Flight System	35
3.2.3. Electromagnetic Calorimeter	37
3.2.4. Muon Counter	38
3.3. Data Samples	39
3.4. BESIII Offline Software System	40
3.5. Monte Carlo Simulations	40
4. General Event Selection	45
4.1. Charged Particle Selection	45
4.1.1. Tracking	45
4.1.2. Particle Identification	47
4.2. Photon Selection	49
4.3. Vertex and Kinematic Fit	50

5. Analysis of the Decay $\psi(2S) \rightarrow \gamma\eta'\pi^+\pi^-$	55
5.1. Background Analysis	57
5.2. Background Reduction	61
5.2.1. Multidimensional Cut Optimization	64
5.2.2. Sideband Subtraction	70
5.3. Determination of $\chi_{cJ} \rightarrow \eta'\pi^+\pi^-$ Branching Ratios	75
5.4. Determination of the $\eta_c \rightarrow \eta'\pi^+\pi^-$ Branching Ratio	81
5.5. Search for the $X(1835)$	85
5.6. Systematic Uncertainties	87
5.6.1. Assignment of the η' Candidate	90
5.6.2. Kinematic Fit χ^2 Cut	91
5.6.3. Minimum Photon Energy	91
5.6.4. J/ψ Veto in the $\pi^+\pi^-$ Recoil System	92
5.6.5. J/ψ Veto in the 4π System and ρ^0 Cut	93
5.6.6. Sideband Subtraction	94
5.6.7. Continuum Background	94
5.6.8. Fitting Models	95
5.6.9. PWA	96
5.7. Search for the $\pi_1(1600)$	96
5.7.1. PWA Amplitude	96
5.7.2. Likelihood Construction	99
5.7.3. PWA Results	100
5.8. Results	106
6. Analysis of the Reaction $e^+e^- \rightarrow \eta_c K^* K$	111
6.1. Background Reduction	115
6.2. Combined Fit to the η_c	121
6.2.1. Signal Shape and Efficiency	123
6.2.2. Input-Output Check	124
6.2.3. Results	127
6.3. Calculation of the Cross Section	128
6.4. Search for Contributions of the Z_{cs}	132
7. Conclusions and Outlook	135
A. Analysis of the Decay $\psi(2S) \rightarrow \gamma\eta'\pi^+\pi^-$	139
A.1. Integration of the Three-Body Phase Space	139
A.2. Blatt-Weisskopf Barrier Factors	140
A.3. Systematic Uncertainties	140
A.3.1. Kinematic Fit χ^2 Cut	141

A.3.2. Minimum Photon Energy	142
A.3.3. J/ψ Veto in the $\pi^+\pi^-$ Recoil System	143
A.3.4. J/ψ Veto in the 4π System and ρ^0 Cut	144
A.3.5. Sideband Subtraction	145
B. Analysis of the Reaction $e^+e^- \rightarrow \eta_c K^* K$	147
B.1. Combined Fit to the η_c	148
B.2. Likelihood Profiles	159
C. Machine Learning for Event Selection	161
Bibliography	165
List of Figures	185
List of Tables	189

1. Introduction

*Stands at the sea, wonders at wondering:
I, a universe of atoms, an atom in the universe.*

Richard Feynman [1]

When Richard Feynman wrote his famous poem in 1955 [1], he was thinking about the fact that, compared to the largest and smallest objects in the universe, we as humans live at length scales that are right in the middle of the cosmic length scales: from the size of our solar system of 10^{15} m [2, 3] to the size of a proton of 10^{-15} m [4]. While the largest objects in our universe are described by astrophysics, the smallest objects are described by particle physics. In both fields, there are important open questions that science seeks to answer. One such question, relevant to both of these fields, is: What is the matter that surrounds us made of? While astrophysics tries to answer this question through indirect observations of the consequences of different matter on the largest scales, particle physics uses direct observations by trying to create different kinds of matter in the laboratory. This thesis uses the direct approach by studying the properties of certain kinds of particles.

Most of today's knowledge of particle physics is condensed in the Standard Model (SM) of particle physics [5, 6], which describes three of the four known interactions. Together with general relativity [7], it describes almost all known phenomena. However, indirect observations have shown that there must be physics beyond the SM, since, for example, the gravitational curves of galaxies [8] or the observation of neutrino oscillations [9–13] cannot be explained within the SM. To explain these phenomena, additional models have been proposed, often including additional symmetries and particles [14, 15], which should be measurable in an experiment. However, to date there is no direct measurement of physics beyond the SM.

One of the key factors in the search for new physics is a perfect understanding of the Standard Model itself, since we want to measure tiny differences from the predictions of the SM. However, there are still many of open questions within the SM itself, perhaps the most prominent ones concerning the strong interaction, which is describes by Quantum Chromodynamics. As the name suggests, this interaction is strong in the sense, that its coupling strength is about two orders of magnitude larger than for all other interactions [5].

Even more striking is the observation that the coupling strength strongly depends on the energy of a reaction and it seems to diverge towards low energies [16,17]. This observation poses a challenge for the theoretical calculation of physical observables in this energy range. In most cases, theoretical calculations involve an expansion of the observables in terms of the coupling constant of the theory, which works well for the electromagnetic and weak interaction. However, as the strong coupling diverges towards low energies, the higher terms in the expansion do not become smaller and the calculation does not converge. This is the reason why additional models are needed to calculate low energy phenomena in the strong interaction.

One such model is the Quark Model [18,19], which describes the binding of quarks and gluons into observable hadrons. The Quark Model was developed to describe an increasing number of observed particles and is based on the observation that quarks, which we know to be the fundamental particles forming the ordinary matter, can only occur in bound systems. This phenomenon, called confinement, cannot be rigorously explained mathematically from the Lagrangian of the strong interaction [17]. However, it has major implications for the possibility of observing quarks in bound systems, called hadrons. In the Quark Model, hadrons are composed of valence quarks, which determine their properties. Each quark carries a property called color charge, and the valence quarks must be combined so that their total color charge is white. This can most easily be achieved by combining three quarks with the colors red, green, and blue or by combining a quark and an antiquark with a color and its anticolor. The resulting particles are called baryons and mesons, respectively, and make up most of our surrounding matter. However, only considering color neutrality opens up the possibility for additional combinations of quarks to form hadrons, such as tetraquarks or hexaquarks [18]. In addition, the gluon, which is the mediating particle of the strong interaction, itself carries color charge and can occur as a valence particle inside a hadron. This way, additional combinations are possible, such as a glueball, which is a hadron composed only of gluons, or hybrids, which are hadrons made up of valence quarks and gluons.

The search for these exotic hadrons is a large area within hadron spectroscopy and is the main motivation for this thesis. Over the last twenty years, an increasing number of particles have been reported that are candidates for exotic hadrons [6,20]. Due to the aforementioned problems of theoretical physics to describe these low energy phenomena, and due to the experimental challenges to measure them, the classification as exotic is in most cases still an open question. To improve our understanding of these particles, it is necessary to determine their properties with improved precision, which will help us answer to the question: what are these observed particles made of? Solving this question could provide clues towards one of the most important open questions in QCD: why and how are quarks confined into hadrons.

The main tools for this task are particle accelerators and the corresponding detectors that

are built to detect the produced particles. One such accelerator is the Beijing Electron Positron Collider II (BEPCII), including the Beijing Spectrometer III (BESIII) [21] particle detector. BEPCII operates in the energy range from 2 GeV to 5 GeV [22], providing access to many of these exotic candidates. On the one hand, directly in the charmonium region between $3 \text{ GeV}/c^2$ and $4.5 \text{ GeV}/c^2$ and, on the other hand, in the decay of these charmonia, which gives access to the light hadrons in the mass region up to $2.5 \text{ GeV}/c^2$. These two different regions will be explored in this thesis.

The first part of this thesis focuses on the reaction $\psi(2S) \rightarrow \gamma\eta'\pi^+\pi^-$. On the one hand side, this reaction allows the production of known conventional mesons, known as charmonia, which are the η_c and the $\chi_{c1,2}$. While these mesons are fairly well understood, their decays are only poorly known [6], and their decays into $\eta'\pi^+\pi^-$ will be studied in this thesis. On the other hand, the reaction $\psi(2S) \rightarrow \gamma\eta'\pi^+\pi^-$ gives access to two exotic candidates, which are the $\pi_1(1600)$ [23] and the $X(1835)$ [24, 25]. While the latter can be seen as a peak in the invariant mass of the $\eta'\pi^+\pi^-$ system, the former requires a more complicated tool, known as a partial wave analysis [26]. By measuring their branching ratios and comparing them to theoretical predictions, the question of their inner structure is clarified.

The second part of this thesis concerns the analysis of the reaction $e^+e^- \rightarrow \eta_c K^* K$, which involves the search for the exotic candidate Z_{cs} [27] in the subsystem $\eta_c K^*$. This analysis involves the investigation of a large number of different η_c decays in order to improve the statistical significance of the studies performed. By determining the branching ratio of the Z_{cs} in this decay mode, the inner structure of the Z_{cs} can be analyzed, giving hints towards the question: is the Z_{cs} meson a molecule of two mesons or a compact tetraquark state? This analysis was done together with Sascha Lennartz in his Master's thesis [28] under my supervision.

This thesis is structured in such a way that the first chapter, after this introduction, presents the theoretical concepts that are necessary to understand the analyses that have been performed, as well as the current state of research. The next chapter deals with the experimental setup, which was used to collect the experimental data, as well as some of the software needed for the analyses. After that, the first general event selection criteria are described, which important for the two following analyses. The general event selection is followed by the first analysis chapter on the reaction $\psi(2S) \rightarrow \gamma\eta'\pi^+\pi^-$ describing first the more specialized event selection criteria to reduce background. Second, the determination of the physically relevant observables is presented, including a thorough analysis of the systematic uncertainties. Then, the second analysis on $e^+e^- \rightarrow \eta_c K^* K$ is explained, again consisting of some specialized event selection criteria followed by the extraction of cross sections for the reactions of interest. The last chapter contains a summary of the obtained results in the context of the current state of research as well as an outlook on possible follow-up studies.

2. Theory

In the first part of this thesis, the theoretical concepts that are necessary to understand the motivation of the conducted analyses, as well as the analysis methods, are presented. First, the Standard Model (SM) of particle physics is introduced, which is the cornerstone of all research in the field of particle physics. Then, Quantum Chromodynamics (QCD), which is a part of the SM, is discussed in more detail, which is necessary to understand the binding of quarks and gluons to hadrons in the so-called quark model. Special emphasis is placed on the charmonium system and exotic hadrons, as the investigation of these states is the main focus of the conducted analyses.

2.1. The Standard Model of Particle Physics

As a Quantum Field Theory (QFT), the Standard Model of particle physics describes three of the four known interactions of our universe and all the elementary particles that have been found [6, 29]. It includes the weak, electromagnetic and strong interactions, each with a corresponding gauge theory. Gravity, the fourth known interaction, is not incorporated because it can be neglected for basically all particle physics phenomena. Moreover, there is still no mathematical theory yet that rigorously describes gravity in conjunction with the other three forces [30]. One goal of (theoretical) particle physics is to find a Theory of Everything that includes all of the four forces. A possible example of such a theory could be supersymmetric string theory or, more generally, M-theory [14, 15]. The particles included in the SM, shown in Figure 2.1, can be divided into the fermionic part, which includes the quarks and leptons, each with a spin of $1/2$, and the bosonic part, which consists of the gauge bosons with spin 1 and the scalar Higgs boson. The quarks and leptons are organized into three generations of increasing mass. For the quarks, these are consisting of the up (u), down (d), charm (c), strange (s), top (t) and bottom (b) quarks:

$$\begin{pmatrix} u \\ d \end{pmatrix} \quad \begin{pmatrix} c \\ s \end{pmatrix} \quad \begin{pmatrix} t \\ b \end{pmatrix}. \quad (2.1)$$

Each of the up-type quarks u , c , t has an electric charge of $+2/3$, while the down-type quarks d , s , b have a charge of $-1/3$.

The lepton generations include the electron e , the muon μ and the tau τ with an electric charge of -1 and the electrically neutral neutrinos ν_e , ν_μ and ν_τ :

$$\begin{pmatrix} e \\ \nu_e \end{pmatrix} \quad \begin{pmatrix} \mu \\ \nu_\mu \end{pmatrix} \quad \begin{pmatrix} \tau \\ \nu_\tau \end{pmatrix}, \quad (2.2)$$

For each of these particles there exists a corresponding anti-particle with the same properties, only the charge-like quantum numbers¹ are reversed, e.g. the anti-up quark has an electric charge of $-2/3$. Since the neutrinos are electrically neutral, they could be their own anti-particles, but whether this is the case is still an open question in modern particle physics [6].

To describe the interactions between particles, the SM includes the symmetry group $SU(3)_c \times SU(2)_L \times U(1)_Y$, which describes the color charge, the weak isospin and the weak hypercharge, all of which get mediated by gauge bosons. From group theory it follows that there are eight gauge bosons belonging to $SU(3)_c$, namely the gluons g , three gauge bosons belonging to $SU(2)_L$, the $W^{\pm,0}$ bosons, and the B^0 boson belonging to $U(1)_Y$. Under unification of the electromagnetic and weak interactions, the W^0 and B^0 bosons mix to form the physically observable Z^0 boson and the photon γ .

The final component of the SM is the Higgs boson H , which, gives the gauge bosons their mass, through the Higgs mechanism [32–34]. Additionally, the mass of the fermions in the SM can be explained in terms of Yukawa couplings of the fermions to the Higgs boson [35]. However, this process cannot generate the mass of the neutrinos, which remain massless in the SM. Through measurements of neutrino oscillations [10–13] it was determined that neutrinos have a non-vanishing mass, which requires physics beyond the Standard Model. In the next chapter the theory of Quantum Chromodynamics which describes the strong interaction will be explained in more detail.

2.2. Quantum Chromodynamics

QCD is the part of the SM that describes the interaction between quarks and gluons [6, 37–39]. It is a non-abelian gauge theory, which means that its symmetry group $SU(3)_c$ is non-commutative, giving rise to the self-interaction of gluons. The charge described by QCD is the color charge, which is either (anti-)red, (anti-)green or (anti-)blue for (anti-)quarks, and which is a combination of a color and an anti-color for gluons. To understand the properties of systems which are bound by the strong interaction the

¹Charge-like quantum numbers are quantum numbers that correspond to conserved currents, which, according to Noether's theorem [31], are the consequences of continuous symmetries.

		three generations of matter (fermions)			interactions / forces (bosons)	
		I	II	III		
mass		$\simeq 2.16 \text{ MeV}/c^2$	$\simeq 1.27 \text{ GeV}/c^2$	$\simeq 172.6 \text{ GeV}/c^2$	0	$\simeq 125.2 \text{ GeV}/c^2$
charge		$+2/3$	$+2/3$	$+2/3$	0	0
spin		$1/2$	$1/2$	$1/2$	1	0
		u up	c charm	t top	g gluon	H Higgs
	QUARKS	$\simeq 4.70 \text{ MeV}/c^2$	$\simeq 93.5 \text{ MeV}/c^2$	$\simeq 4.18 \text{ GeV}/c^2$	0	
		$-1/3$	$-1/3$	$-1/3$	0	
		$1/2$	$1/2$	$1/2$	1	
		d down	s strange	b bottom	γ photon	
	LEPTONS	$\simeq 0.511 \text{ MeV}/c^2$	$\simeq 105.7 \text{ MeV}/c^2$	$\simeq 1.777 \text{ GeV}/c^2$	$\simeq 80.37 \text{ GeV}/c^2$	
		-1	-1	-1	± 1	
		$1/2$	$1/2$	$1/2$	1	
		e electron	μ muon	τ tau	W W boson	
		$< 0.8 \text{ eV}/c^2$	$< 0.19 \text{ MeV}/c^2$	$< 18.2 \text{ MeV}/c^2$	$\simeq 91.19 \text{ GeV}/c^2$	
		0	0	0	0	
		$1/2$	$1/2$	$1/2$	1	
		ν_e electron neutrino	ν_μ muon neutrino	ν_τ tau neutrino	Z Z boson	
						GAUGE BOSONS VECTOR BOSONS
						SCALAR BOSONS

Figure 2.1.: The particle content of the SM. It includes the quarks (blue), the leptons (green), the gauge bosons (red) and the Higgs boson (yellow). For each particle the mass, charge and spin are given according to the PDG [6]. Figure taken from [36] with changed font and updated masses.

Lagrangian density of the theory plays an important role. For QCD it can be written as [6]

$$\mathcal{L}_{\text{QCD}} = \sum_q \bar{\psi}_{q,a} \left(i\gamma^\mu \partial_\mu \delta_{ab} - g_s \gamma^\mu t_{ab}^C \mathcal{A}_\mu^C - m_q \delta_{ab} \right) \psi_{q,b} - \frac{1}{4} F_{\mu\nu}^A F^{A\mu\nu} \quad (2.3)$$

where the first part describes the quark fields $\psi_{q,a}$ of mass m_q and their interaction with the gluon fields \mathcal{A}_μ^C . These contributions are summed over the quark flavors q and the second part includes the contribution from the gluonic field tensor $F_{\mu\nu}^A$. The indices $a, b \in \{1, \dots, N_c\}$ and $A, B, C \in \{1, \dots, N_c^2 - 1\}$ are color indices, where $N_c = 3$ is the number of colors of quarks [6]. The strength of the interaction is determined by the coupling g_s , which, together with the quark masses m_q , is the only parameter of QCD [6].

2. Theory

The matrices t_{ab}^C are the generators of SU(3), while γ^μ and ∂_μ are the Dirac matrices and covariant derivative, respectively. The gluonic field tensor is given by [6]

$$F_{\mu\nu}^A = \partial_\mu \mathcal{A}_\nu^A - \partial_\nu \mathcal{A}_\mu^A - g_s f_{ABC} \mathcal{A}_\mu^B \mathcal{A}_\nu^C, \quad (2.4)$$

which includes the structure constants f_{ABC} of SU(3) defined by the commutators of the generators by

$$[t_{ab}^A, t_{ab}^B] = i f_{ABC} t_{ab}^C. \quad (2.5)$$

In addition to the Lagrangian in Equation (2.3), a CP violating term can be included without violating gauge symmetry [40]:

$$\mathcal{L}_{CP} = \theta \frac{\alpha_s}{8\pi} F_{\mu\nu}^A \tilde{F}^{A\mu\nu}. \quad (2.6)$$

Here θ is a CP violating phase and $\tilde{F}^{A\mu\nu} = \frac{1}{2} \varepsilon^{\mu\nu\rho\sigma} F_{\rho\sigma}^A$ is the dual of the gluon field, with the totally antisymmetric tensor ε . However, experimental measurements [41, 42] show that the phase is small with $|\theta| \lesssim 10^{-10}$, indicating that the strong interaction seems to conserve CP , also known as the strong CP problem [40].

As mentioned above, the strength of the interaction is governed by the QCD coupling, which is often written as $\alpha_s = \frac{g_s^2}{4\pi}$. After renormalization it follows that the coupling is not constant, but depends on the renormalization scale μ_R . This dependence is expressed in terms of a renormalization group equation as [6, 17]

$$\mu_R^2 \frac{d\alpha_s}{d\mu_R^2} = \beta(\alpha_s) = -\alpha_s^2 \sum_{n=0} \alpha_s^n \beta_n. \quad (2.7)$$

Here β_n are the $(n+1)$ -loop coefficients of the so-called β -function. For a given process, the strength of the coupling can be determined by setting $\mu_R^2 = Q^2$, where Q is the momentum transfer. By considering only the lowest term in Equation (2.7), one obtains an analytical solution for $\alpha_s(\mu_R^2)$ of

$$\alpha_s(\mu_R^2) = \left[\beta_0 \ln \left(\frac{\mu_R^2}{\Lambda^2} \right) \right]^{-1}, \quad (2.8)$$

with the 1-loop coefficient

$$\beta_0 = \frac{11C_A - 4n_f T_R}{12\pi} = \frac{33 - 2n_f}{12\pi} \quad (2.9)$$

and the QCD scale parameter Λ , which has to be determined experimentally. $C_A = 3$ and $T_R = 1/2$ are color factors associated with the emission of a gluon by another gluon and the splitting of a gluon into two quarks, respectively, and n_f is the number of quark flavors. To obtain an approximate solution for α_s for higher orders, Equation (2.7) can

be solved iteratively.

Using Equation (2.7) (or Equation (2.8)) with $\mu_R^2 = Q^2$, one can see that α_s becomes small for processes with large momentum transfer, giving rise to a phenomenon called asymptotic freedom [43,44]. For small momentum transfer, however, α_s becomes large, making the strong interaction non-perturbative in this regime. As Q^2 approaches Λ^2 , the coupling diverges, which is called the Landau pole, and a different definition of the coupling is required [17].

This divergence for small momentum transfer was thought to be the reason for another important feature of QCD, namely confinement [45]. Confinement describes the phenomenon that only color-neutral states can be observed in nature. Color-neutrality can be achieved by combining a color with its corresponding anti-color, or by combining all three (anti-)colors. Such states, bound by the strong interaction, are called hadrons. However, there is no mathematically rigorous proof that a divergent coupling leads to confinement. Rather, it has been shown that there are theories that exhibit confinement without divergent coupling [17].

2.2.1. The Quark Model

In the Quark Model, hadrons are composed of constituent quarks and gluons, which determine their quantum numbers [18,19]. Additionally, it includes sea quarks and gluons, which appear as virtual particles in the hadrons and contribute to their mass, spin, momentum and magnetic moment [46].

Depending on whether the hadron is a boson or a fermion, it is either called a baryon or a meson. Considering only the so-called conventional hadrons, (anti-)baryons are built from three (anti-)quarks and mesons are composed of a quark and an anti-quark. Considering only the three lightest quarks, baryons and mesons will be explained in more detail in Section 2.2.2 and Section 2.2.3, respectively. In addition, the constituent quark model also predicts hadrons consisting of more than three (anti-)quarks and also constituent gluons [18], these hadrons are called exotic and will be introduced in Section 2.2.5.

Since hadrons are constructed by combining (anti-)quarks and gluons, their quantum numbers play an important role in the classification of baryons and mesons [6]. Quarks have an intrinsic spin of $1/2$ and a baryon number of $\mathcal{B} = 1/3$, both of which are additive quantum numbers. Additionally, quarks carry additive quantum numbers, called flavors, which are the third component of the isospin I_3 ², strangeness S , charm \mathcal{C} , bottomness B and topness T , which are presented in Table 2.1. Each quark carries only its corresponding flavor and the sign of the quantum number is defined to be the same as the sign of its electric charge, all other flavor quantum numbers are zero. For anti-quarks the sign of the flavor quantum number is reversed. Although the topness T is defined as the flavor

²As the up and down quark have similar masses they can be described by an approximate SU(2) symmetry group called isospin.

quantum number of the top quark, it does not play a role for building up hadrons, since the top quark decays before it can hadronize [6].

Another important quantum number is the eigenvalue P of the parity operator \hat{P} (often just called parity) which describes the behavior of the particle's wave function under inversion of the spatial coordinates. For quarks the parity, which is a multiplicative quantum number, is defined as $P = +1$ and consequently for anti-quarks as $P = -1$.

When constructing the spectra of baryons and mesons, it is useful to start with the three lightest quarks (u , d and s) that have similar masses, as these can be described by an approximate $SU(3)_F$ flavor symmetry [47, 48]. This formalism can be extended to include the heavier quarks, but e.g. a $SU(4)_F$ symmetry would be strongly broken, since the c quark is much heavier than the three light quarks [6]. To construct so-called multiplets, which correspond to combinations of quarks and anti-quarks, mathematical tools of group theory can be used. In this framework, the three quark flavors are written as the triplet $\mathbf{3}$ and the anti-quarks as $\bar{\mathbf{3}}$, while e.g. a diquark would be written as $\mathbf{3} \otimes \mathbf{3}$.

In the next sections, the spectrum of baryons, which make up most of the conventional matter, and mesons will be discussed based on $SU(3)_F$.

2.2.2. Baryons

Baryons are bound states of three quarks and thus have a baryon number of $\mathcal{B} = 1$. In the Standard Model, the baryon number is an accidental symmetry of the Lagrangian [49], meaning that it is conserved in the strong interaction but it can be violated in certain weak interactions [50]. However, this violation is expected to play a role only at high temperatures and has never been measured in an experiment. These high temperatures were present in the early phases of the universe, so this effect could play a role in explaining the observed baryon asymmetry [51].

Using the notation presented in Section 2.2.1 and considering only the three lightest quarks the baryon multiplets can be constructed, e.g., using Young diagrams [6, 52] as

$$\mathbf{3} \otimes \mathbf{3} \otimes \mathbf{3} = \mathbf{10}_S \oplus \mathbf{8}_M \oplus \mathbf{8}_M \oplus \mathbf{1}_A. \quad (2.10)$$

Table 2.1.: Quantum numbers of the quarks.

	u	d	c	s	t	b
electric charge q	+2/3	-1/3	+2/3	-1/3	+2/3	-1/3
isospin I_3	+1/2	-1/2	0	0	0	0
charm \mathcal{C}	0	0	+1	0	0	0
strangeness S	0	0	0	-1	0	0
topness T	0	0	0	0	+1	0
bottomness B	0	0	0	0	0	-1

Here the $\mathbf{8}_M$ are baryon octets with mixed-symmetry flavor wave functions. Including the corresponding mixed-symmetry spin wave functions leads to the observed $J^P = 1/2^+$ baryon octet [6]. $\mathbf{10}_S$ corresponds to the baryon decuplet with $J^P = 3/2^+$ and a symmetric flavor wave function. Here, J is the total angular momentum, which is the vector sum of the baryon spin s and the orbital angular momentum l between the quarks. The ground state multiplets have an orbital momentum of $l = 0$ and therefore a total angular momentum of $1/2$ or $3/2$, respectively. $\mathbf{1}_A$ is an antisymmetric flavor singlet, which is only realized for excited multiplets due to the Pauli exclusion principle [6]. The inclusion of baryons with non-zero orbital momentum results in multiplets with all combinations of quantum numbers $J = \frac{1}{2}, \frac{3}{2}, \frac{5}{2}, \dots$ and $P = \pm 1$. The ground state octet and decuplet are depicted in Figure 2.2. They include the proton and neutron, which are responsible for building up the ordinary matter. They also include the Ω^- baryon, which was predicted when the quark model was developed [47, 48] and was later found to have exactly the predicted quantum numbers and a mass compatible with the theoretical prediction [53], which was seen as a strong validation of the quark model.

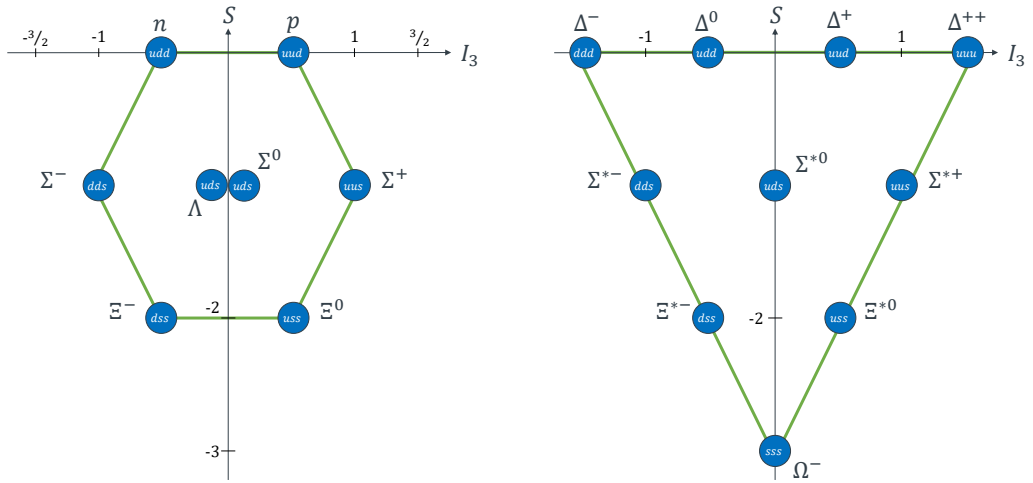


Figure 2.2.: Ground state baryon octet with $J^P = \frac{1}{2}^+$ (left) and decuplet with $J^P = \frac{3}{2}^+$ (right), sorted according to their isospin I_3 and strangeness S . Additionally, the quark content of the baryons is shown.

2.2.3. Mesons

Conventional mesons are particles composed of a quark and an anti-quark and consequently have a baryon number of $\mathcal{B} = 0$, meaning that they can be produced and annihilated individually. Since quarks and anti-quarks have opposite parities, the parity of a meson is

defined by the action of the parity operator on the spatial wave function, resulting in a factor of $(-1)^l$ [6]. Including the intrinsic parity of the quarks, the parity of a meson is

$$P = (-1)^{l+1}. \quad (2.11)$$

In addition, mesons that are their own anti-particles are eigenstates of the charge conjugation operator \hat{C} that transforms a particle into its anti-particle. For a quark-anti-quark system, this correspond to applying the parity operator with an additional factor coming from the spin s of the system. The eigenvalue C (often called C -parity) therefore results in [6]

$$C = (-1)^{l+s}. \quad (2.12)$$

Here s is zero for anti-parallel spins of the quark and anti-quark and one for parallel spins. The total angular momentum J for mesons follows from the conservation of angular momentum as

$$|l - s| < J < |l + s|. \quad (2.13)$$

The combination of Equations (2.11) to (2.13) results in quantum number combinations that are forbidden for conventional mesons:

$$J^{PC} = 0^{--}, \text{even}^{+-}, \text{odd}^{-+}. \quad (2.14)$$

If a hadron with such quantum numbers were observed in an experiment, it would have to be an exotic hadron (see Section 2.2.5).

The coupling of a quark and an anti-quark leads to the formation of multiplets. Considering only the three lightest quarks, the multiplets can be constructed as [6, 52]

$$\mathbf{3} \otimes \bar{\mathbf{3}} = \mathbf{8} \oplus \mathbf{1}. \quad (2.15)$$

The octet and the singlet are often combined into nonets, which can then be constructed for each of the allowed quantum numbers. Each nonet consists of a triplet with isospin $I = 1$, two isodoublets with $I = 1/2$ and two isosinglets with $I = 0$. In Figure 2.3 an overview of the lowest lying nonets is depicted. Experimental observations show that the mass of the particles in a nonet increases with growing angular momentum l as well as with radial excitation n of the wave function. In addition, the population of nonets becomes more sparse at higher excitations, which can be explained by the experimental difficulties in creating and identifying these states. Furthermore, the classification of the experimentally observed states into conventional meson nonets is complicated by the expected appearance of tetraquark multiplets and glueballs (see Section 2.2.5) with the same quantum numbers and similar masses.

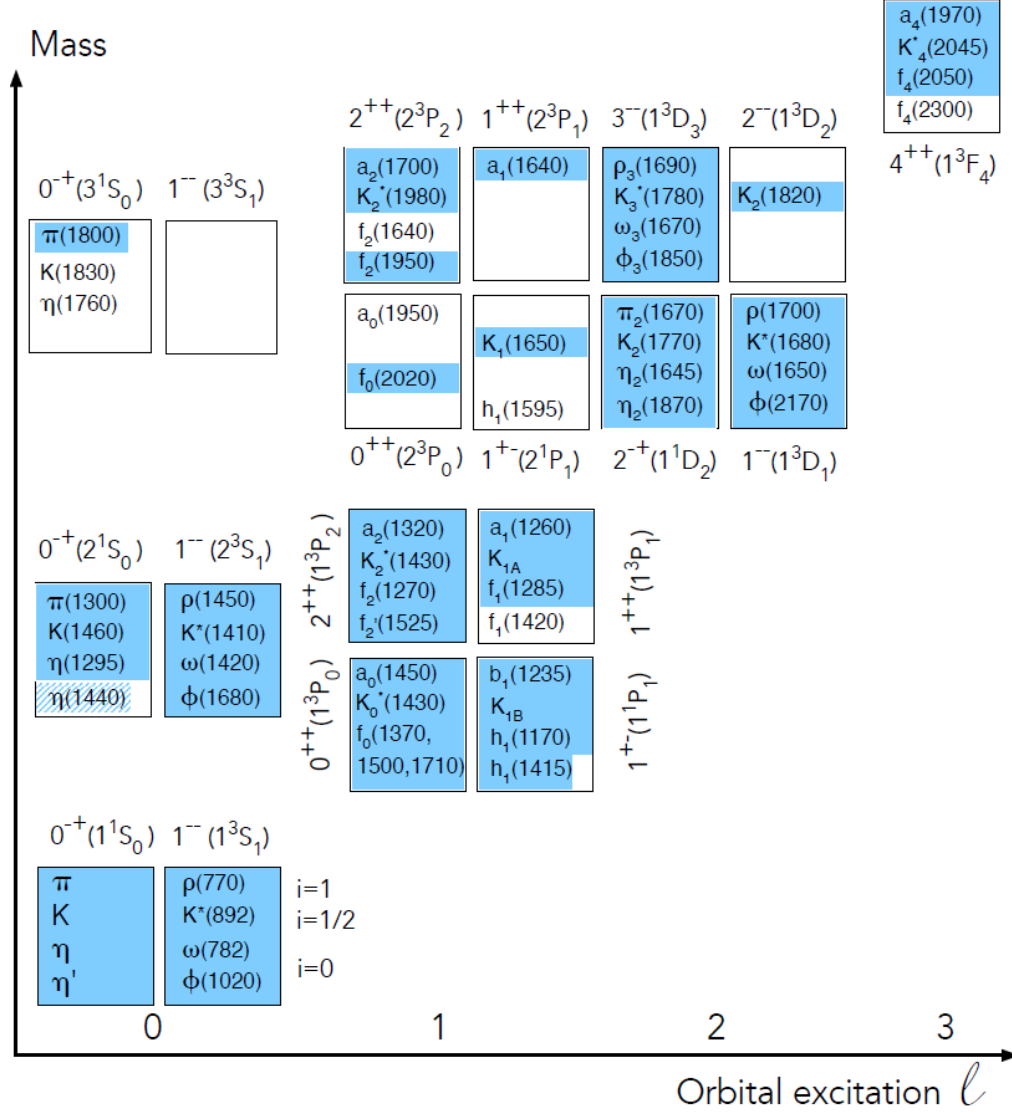


Figure 2.3.: Overview of the conventional meson nonets built from the three lightest quarks plotted with respect to their angular momentum l on the abscissa and their mass on the ordinate. Also shown are their quantum numbers in the notation $J^{PC}(n^{2s+1}l_J)$. Here, J is the total angular momentum, P and C are the eigenvalues of the \hat{P} and \hat{C} parity operators, n is the radial excitation, s is the spin and l is the angular momentum of the nonet. Each nonet contains (from top to bottom) three states with isospin $i = 1$, two doublets with $i = 1/2$ and two isosinglets with $i = 0$. Established states are marked in blue and states that are not yet classified as established or whose assignment to a nonet is still ambiguous are marked in white. Figure taken from [6], modified.

Pseudoscalar Mesons

The lightest meson nonet is the ground state pseudoscalar nonet with $J^{PC} = 0^{-+}$, presented in Figure 2.4. It contains the pions as an isospin triplet (π^\pm, π^0), the kaons in two isospin doublets (K^0, K^+ and K^-, \bar{K}^0), and the two isoscalars η and η' . Here, the quark content of the particles at the edges of the multiplet can be easily identified as

$$|\pi^-\rangle = |d\bar{u}\rangle, \quad |\pi^+\rangle = |u\bar{d}\rangle, \quad (2.16)$$

$$|K^0\rangle = |d\bar{s}\rangle, \quad |K^+\rangle = |u\bar{s}\rangle, \quad (2.17)$$

$$|K^-\rangle = |s\bar{u}\rangle, \quad |\bar{K}^0\rangle = |s\bar{d}\rangle, \quad (2.18)$$

while the three particles in the center are linear combinations of $u\bar{u}$, $d\bar{d}$ and $s\bar{s}$. They can be constructed as orthonormal wave functions:

$$|\pi^0\rangle = \frac{1}{\sqrt{2}} (|u\bar{u}\rangle - |d\bar{d}\rangle), \quad (2.19)$$

$$|\eta_8\rangle = \frac{1}{\sqrt{6}} (|u\bar{u}\rangle + |d\bar{d}\rangle - 2|s\bar{s}\rangle), \quad (2.20)$$

$$|\eta_1\rangle = \frac{1}{\sqrt{3}} (|u\bar{u}\rangle + |d\bar{d}\rangle + |s\bar{s}\rangle). \quad (2.21)$$

Here, the isovector $|u\bar{u}\rangle - |d\bar{d}\rangle$ combination is the physically observable π^0 meson, while the singlet η_1 and the octet η_8 mix to form the η and η' meson according to:

$$\begin{pmatrix} |\eta\rangle \\ |\eta'\rangle \end{pmatrix} = \begin{pmatrix} \cos\theta & -\sin\theta \\ \sin\theta & \cos\theta \end{pmatrix} \cdot \begin{pmatrix} |\eta_8\rangle \\ |\eta_1\rangle \end{pmatrix}. \quad (2.22)$$

For the pseudoscalar mesons, the mixing angle θ_p has been measured to be in the range of -10° to -20° [54–58], resulting in the approximations $|\eta\rangle \approx |\eta_8\rangle$ and $|\eta'\rangle \approx |\eta_1\rangle$, which explains the higher mass of the η' compared to the η .

Vector Mesons

Vector mesons form the first excited multiplet (shown in Figure 2.4) with quantum numbers $J^{PC} = 1^{--}$. Here, the excitation comes from the spin, which is parallel for vector mesons in contrast to the anti-parallel spins of the pseudoscalar mesons. The quark content of the vector mesons can be identified analogously to the pseudoscalar mesons ($\pi \leftrightarrow \rho, K \leftrightarrow K^*$) as

$$|\rho^-\rangle = |d\bar{u}\rangle, \quad |\rho^+\rangle = |u\bar{d}\rangle, \quad (2.23)$$

$$|K^{*0}\rangle = |d\bar{s}\rangle, \quad |K^{*+}\rangle = |u\bar{s}\rangle, \quad (2.24)$$

$$|K^{*-}\rangle = |s\bar{u}\rangle, \quad |\bar{K}^{*0}\rangle = |s\bar{d}\rangle. \quad (2.25)$$

The observable isoscalars ω and ϕ are again mixtures of the singlet and octet state. Here the mixing angle was determined to be $\theta_v = 36.5^\circ$ [6], which is quite close to the ideal mixing angle of $\theta_i = 35.3^\circ$ at which the $|u\bar{u}\rangle + |d\bar{d}\rangle$ and $|s\bar{s}\rangle$ components decouple. The quark content of the states with $I_3 = 0$ can therefore be identified as

$$|\rho^0\rangle = \frac{1}{\sqrt{2}} (|u\bar{u}\rangle - |d\bar{d}\rangle), \quad (2.26)$$

$$|\omega\rangle \approx \frac{1}{\sqrt{2}} (|u\bar{u}\rangle + |d\bar{d}\rangle), \quad (2.27)$$

$$|\phi\rangle \approx |s\bar{s}\rangle. \quad (2.28)$$

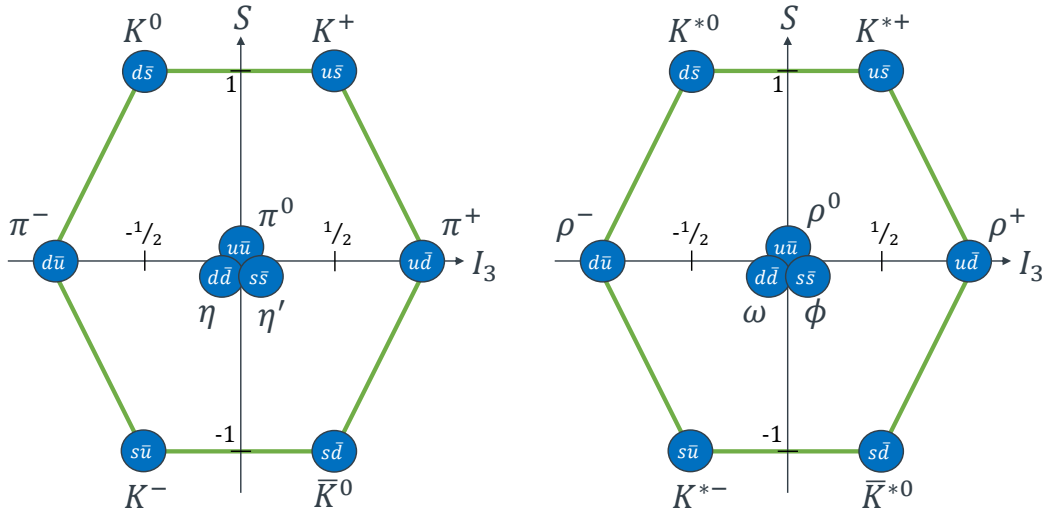


Figure 2.4.: Nonets of the pseudoscalar mesons with $J^{PC} = 0^{-+}$ (left) and vector mesons with $J^{PC} = 1^{--}$ (right), sorted according to their isospin I_3 and strangeness S . Additionally, the quark content of the mesons is shown. The $u\bar{u}$, $d\bar{d}$ and $s\bar{s}$ components mix to form the physically observable states π^0/ρ^0 , η/ω and η'/ϕ .

The Neutral Kaon System

As mentioned in Section 2.2, the strong interaction seems to conserve CP symmetry, while the weak interaction has been observed to violate it, e.g. in the decays of the neutral pseudoscalar kaons [59]. The parity of the kaons is negative, which gives

$$\hat{P}|K^0\rangle = -|K^0\rangle \quad \text{and} \quad \hat{P}|\bar{K}^0\rangle = -|\bar{K}^0\rangle. \quad (2.29)$$

Applying the C parity on the kaon states results in

$$\hat{C}|K^0\rangle = \eta_C|\bar{K}^0\rangle \quad \text{and} \quad \hat{C}|\bar{K}^0\rangle = \eta_C|K^0\rangle, \quad (2.30)$$

with the constraint $\eta_C^2 = 1$, which gets satisfied by $\eta_C = e^{i\phi}$. By choosing the convention $\phi = 0$ this results in

$$\hat{C}\hat{P}|K^0\rangle = -|\bar{K}^0\rangle \quad \text{and} \quad \hat{C}\hat{P}|\bar{K}^0\rangle = -|K^0\rangle, \quad (2.31)$$

which allows the construction of CP eigenstates as

$$|K_1\rangle = \frac{1}{\sqrt{2}}(|K^0\rangle - |\bar{K}^0\rangle) \quad \text{and} \quad |K_2\rangle = \frac{1}{\sqrt{2}}(|K^0\rangle + |\bar{K}^0\rangle) \quad (2.32)$$

with the CP transformation properties

$$\hat{C}\hat{P}|K_1\rangle = |K_1\rangle \quad \text{and} \quad \hat{C}\hat{P}|K_2\rangle = -|K_2\rangle. \quad (2.33)$$

Under the assumption of CP conservation, the K_1 decays into an even number of pions, while the K_2 decays into an odd number of pions with an angular momentum of $l = 0$. The experimentally observable mass eigenstates are the short-lived K_S and the long-lived K_L , and were thought to be the same states as K_1 and K_2 . However, after the observation of the decay $K_L \rightarrow \pi\pi$ [59], it was deduced that the K_S and K_L contain small admixtures of the opposite CP eigenstates. This phenomenon is called indirect CP violation or CP violation via mixing. The mass eigenstates are constructed as

$$|K_S\rangle = \frac{1}{\sqrt{1+|\epsilon|^2}}(|K_1\rangle + \epsilon|K_2\rangle) = \frac{1}{\sqrt{2(1+|\epsilon|^2)}}\left((1+\epsilon)|K^0\rangle - (1-\epsilon)|\bar{K}^0\rangle\right), \quad (2.34)$$

$$|K_L\rangle = \frac{1}{\sqrt{1+|\epsilon|^2}}(|K_2\rangle + \epsilon|K_1\rangle) = \frac{1}{\sqrt{2(1+|\epsilon|^2)}}\left((1+\epsilon)|K^0\rangle + (1-\epsilon)|\bar{K}^0\rangle\right), \quad (2.35)$$

with the indirect CP violation parameter $\epsilon = (2.228 \pm 0.011) \times 10^{-3}$ [6]. In addition, direct CP violation has also been measured, e.g. via the decay $K_2 \rightarrow \pi\pi$ [60, 61]. Its strength was determined to be three orders of magnitude smaller than the indirect CP violation [6].

CP violation was measured not only in the kaon sector, but also in the decays of mesons containing one of the heavier quarks c and b , such as the D [62], B [63, 64] and B_s [65] mesons. Additionally, CP violation is possible in the lepton sector due to the non-vanishing masses of the neutrinos, but so far only evidence for this effect has been seen [66].

The next section focuses on charmonia, which are mesons composed of a charm and an anti-charm quark.

2.2.4. The Charmonium System

So far, only the three lightest quarks have been considered in the construction of hadron multiplets. As mentioned in Section 2.2.1, this is motivated by the approximate $SU(3)_F$ symmetry, which would be strongly broken if extended to include heavier quarks [6].

Nevertheless, the quark model allows the construction of the quark wavefunction of such states. These are on the one hand side the D and B mesons, which consist of an (anti-)charm or (anti-)bottom quark and a lighter (anti-)quark, respectively. On the other hand, the so-called charmonia and bottomonia are systems composed of a charm and an anti-charm quark or a bottom and an anti-bottom quark, respectively.

The constituent mass of the charm quark is significantly larger than that of the lighter quarks and also much smaller than that of the bottom quark [67]:

$$\frac{m_c}{m_s} \approx 3.2 \quad \text{and} \quad \frac{m_b}{m_c} \approx 3.1 \quad (2.36)$$

This leads to the fact that the mixing with the light isoscalars and the bottomonium system can be neglected, when constructing the charmonium spectrum. In addition, the relatively high constituent mass of the charm quark $m_c \approx 1.5 \text{ GeV}/c^2$ [67, 68] causes the quarks inside the charmonium to have non-relativistic momenta. A commonly used potential to describe such systems is the sum of the Cornell potential [69] and a spin-dependent part

$$V_{c\bar{c}}(r) = V_{\text{Cornell}}(r) + V_{\text{spin}}(r). \quad (2.37)$$

The Cornell potential $V_{\text{Cornell}}(r)$ contains on the one hand side a color Coulomb term describing the one-gluon exchange, which is inspired by the Coulomb potential of the hydrogen atom. On the other hand, an additional linear term ensures the confinement of the quarks [17, 70]. The total potential has the form

$$V_{\text{Cornell}}(r) = -C_F \frac{\alpha_s}{r} + br. \quad (2.38)$$

Here $C_F = 4/3$ is the color factor for the emission of a gluon from a quark, α_s is the strong coupling constant, b is the QCD string tension [17] and r is the radius of the charmonium system. The spin-dependent part $V_{\text{spin}}(r)$ is responsible for the fine and hyperfine splitting of the states. It includes the interaction between the quark spin and the angular momentum $\vec{L} \cdot \vec{S}$ (with $\vec{S} = \vec{S}_c + \vec{S}_{\bar{c}}$), a tensor interaction between the magnetic moments of the quarks T and a spin-spin contact interaction $\vec{S}_c \cdot \vec{S}_{\bar{c}}$ [68] via

$$V_{\text{spin}}(r) = \frac{1}{m_c^2} \left[\left(\frac{2\alpha_s}{r^3} - \frac{b}{2r} \right) \vec{L} \cdot \vec{S} + \frac{4\alpha_s}{r^3} T + \frac{32\alpha_s \sigma^3}{9\sqrt{\pi}} e^{-\sigma^2 r^2} \vec{S}_c \cdot \vec{S}_{\bar{c}} \right], \quad (2.39)$$

with the mass of the charm quark m_c and a range parameter of the contact interaction σ . In total, this model includes four parameters (α_s, b, m_c, σ) that must be determined by

fitting to the charmonium spectrum. A fit to the established states $\psi(nS)$ [$n = 1, 2, 3, 4$], $\psi(nD)$ [$n = 1, 2$], $\eta_c(nS)$ [$n = 1, 2$] and $\chi_{cJ}(1P)$ [$J = 0, 1, 2$] yields values of [68]

$$\alpha_s = 0.5461, \quad b = 0.1425 \text{ GeV}^2, \quad (2.40)$$

$$m_c = 1.4794 \text{ GeV}/c^2, \quad \sigma = 1.0946 \text{ GeV}. \quad (2.41)$$

Using this fit, the masses of the higher excited charmonium states can be predicted. An extension of this model is the Godfrey-Isgur model [71], which includes relativistic corrections and is applicable not only to the charmonium system but also to lighter quarkonium systems. For the charmonium system it gives comparable results for the light S- and P-wave states, but for the highest excited states the difference goes up to $\sim 100 \text{ MeV}/c^2$ [68].

An overview of the predicted and experimentally measured charmonium states sorted by their J^{PC} quantum numbers and mass is given in Figure 2.5³. As can be seen, the calculations of the non-relativistic quark model are in good agreement with all experimentally observed states below the $D\bar{D}$ threshold and the $J^{PC} = 1^{--}$ states above the threshold. For the other quantum numbers, the experimentally established states get scarce.

Figure 2.5 also includes states that have been found in the charmonium region, but which show properties that differ from those expected for conventional charmonia. These states are being discussed as candidates for exotic hadrons, which will be presented in Section 2.2.5.

2.2.5. Exotic Hadrons

Exotic hadrons are hadrons which have a quark content of more than three (anti-)quarks or which have gluons as constituents. These are, e.g., tetraquarks ($qq\bar{q}\bar{q}$), hexaquarks ($qqqqqq$ or $qqq\bar{q}\bar{q}\bar{q}$), hybrids ($q\bar{q}g$) or glueballs (gg). For all of these theoretically predicted states, there are candidates with the corresponding properties, but the assignments are often controversial. This can be partly explained by the fact that conventional and exotic hadrons can mix, making it difficult to disentangle the inner structure of an observed state [6].

In the following, the exotic hadrons that play a role in this thesis will be discussed in more detail.

³Here and in the following the naming scheme for hadrons from the PARTICLE DATA GROUP (PDG) from 2022 will be used [72]. In 2024 the PDG introduced a new naming scheme [6], which changed the names of e.g. the $Z_c(3900)$ and $Z_{cs}(4000)$ states to $T_{c\bar{c}1}(3900)$ and $T_{c\bar{c}s1}(4000)$, respectively.

which decay into a charmonium and a charged light meson and should therefore have a quark content of $c\bar{c}q\bar{q}$. The $Z_c^\pm(3900)$ was first observed by BESIII in 2013 [77] in the decay $Z_c^\pm(3900) \rightarrow J/\psi\pi^\pm$ and later confirmed by BELLE⁴ in the same decay [78]. Assuming the $Z_c(3900)$ to be an isospin triplet, the neutral $Z_c^0(3900)$ was predicted and later found with a compatible mass and width [79,80]. It was also observed in its dominant decay $Z_c^{\pm,0}(3900) \rightarrow (D\bar{D}^*)^{\pm,0}$ [81,82].

A theoretical model that has been used to predict the existence of the $Z_c(3900)$ is the INITIAL SINGLE PION EMISSION (ISPE) mechanism [83], where the $Z_c(3900)$ is produced via pion emission in the decay of the charmonium-like state $\psi(4260)$. The ISPE mechanism was later extended to the INITIAL SINGLE CHIRAL PARTICLE EMISSION (ISChE) mechanism, which allows the emission of any chiral particle, such as a kaon [84]. Using the ISChE mechanism, the decay of the charmonium(-like) states $\psi(4415)$, $\psi(4660)$ and $\psi(4790)$ ⁵ into the J/ψ and two kaons has been studied. As can be seen in Figure 2.6, this decay could proceed through a triangle loop consisting of $D^{(*)0}$ and $D_s^{(*)+}$ mesons. The amplitude for these diagrams is calculated using an effective Lagrangian approach [87–90], by neglecting the interference with various intermediate states [84]. This calculation results in enhancements in the $J/\psi K$ system at the production thresholds for $D^*\bar{D}_s + D\bar{D}_s^*$ and $D^*\bar{D}_s^*$. These enhancements are candidates for structures with hidden charm and open strangeness [84].

This prediction is in good agreement with the states $Z_{cs}(3985)^\pm$ found by BESIII in the reaction $e^+e^- \rightarrow K^+Z_{cs}^- \rightarrow K^+(D_s^-D^{*0} + D_s^{*-}D^0)$ [27] and $Z_{cs}(4000)^\pm$ seen by LHCb⁶ in $B^+ \rightarrow Z_{cs}^+\phi \rightarrow J/\psi K^+\phi$ [91]. These states have comparable masses but significantly different widths, and it is still unclear whether they are the same state [6]. In addition to the observed decays into $D_s^{(*)}$ mesons and $J/\psi K$, the authors in [92] use QCD sum rules [93,94] to predict the decay mode $Z_{cs} \rightarrow \eta_c K^*$, assuming the Z_{cs} to be a compact tetraquark state, with a comparable partial decay width as the decay $Z_{cs} \rightarrow J/\psi K$ and a total width of the Z_{cs} of (24.9 ± 12.6) MeV. This value is in agreement with the width determined by BESIII of $(12.8_{-4.4}^{+5.3} \pm 3.0)$ MeV [27], but is significantly smaller than the width obtained by LHCb of $(131 \pm 15 \pm 26)$ MeV [91]. In addition to the charged states that were found, BESIII also found evidence for a neutral state $Z_{cs}(3985)^0$ in the processes $e^+e^- \rightarrow K_S^0 D_s^+ D^{*-}$ and $e^+e^- \rightarrow K_S^0 D_s^{*+} D^-$ [95], which is considered to be the isospin partner of the $Z_{cs}(3985)^\pm$.

In order to test the prediction in [92] and thus to investigate the assumption of a compact tetraquark, the reaction $e^+e^- \rightarrow Z_{cs}K \rightarrow \eta_c K^* K$ is analyzed in Chapter 6.

⁴Experiment at the KEKB particle accelerator at the HIGH ENERGY ACCELERATOR RESEARCH ORGANISATION.

⁵The $\psi(4790)$ was identified by [85] as the 5S charmonium in data of the reaction $e^+e^- \rightarrow \Lambda_c^+ \Lambda_c^-$ taken by the BELLE Collaboration [86].

⁶The LARGE HADRON COLLIDER BEAUTY experiment at the LARGE HADRON COLLIDER at CERN.

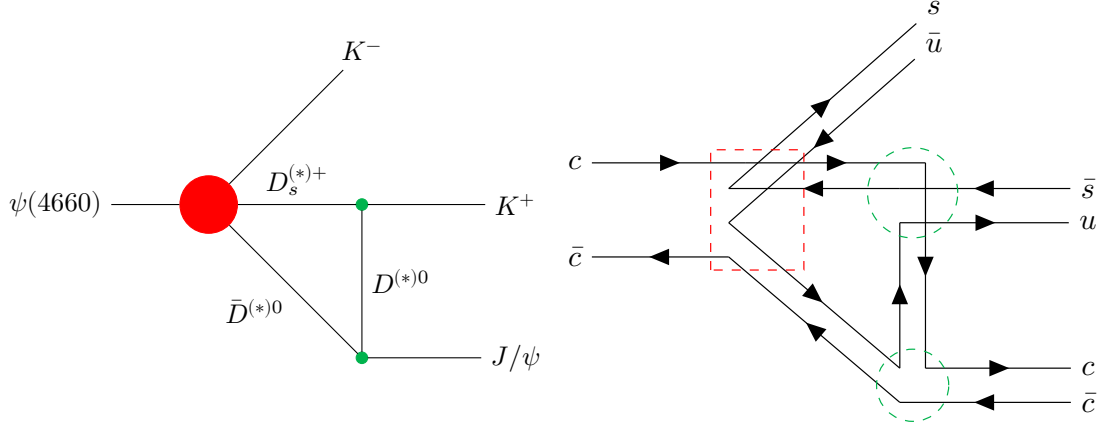


Figure 2.6.: Diagrams showing the ISChE mechanism for the decay of the charmonium-like state $\psi(4660)$ into $J/\psi K^+ K^-$ at the hadron level (left) and the quark level (right) according to [83,84]. The process includes a triangle loop consisting of $D^{(*)0}$ and $D_s^{(*)+}$ mesons.

Hexaquarks

Hexaquarks are states made up of a combination of six quarks and anti-quarks and can have either a baryon number of $\mathcal{B} = \pm 2$ with a quark content of $qqqqqq$ or $\bar{q}\bar{q}\bar{q}\bar{q}\bar{q}\bar{q}$ or a baryon number of $\mathcal{B} = 0$ with a quark content of $qqq\bar{q}\bar{q}\bar{q}$. These are then called dibaryon and baryonium, respectively.

The only established dibaryon is the deuteron, which is the nucleus of the deuterium atom, an isotope of hydrogen. Other than the deuteron, other dibaryons are not established, as they are often seen only in single experiments. An example of such a state is the $d^*(2380)$ which was seen in double-pionic fusion processes of the type $pn \rightarrow d\pi\pi$ [96–98] or in quasi-free neutron-proton scattering $dp \rightarrow np + p_{\text{spectator}}$ [99] at WASA-AT-COSY⁷.

A possible candidate for a baryonium is the state $X(1835)$ which was found by BESIII in the decay $J/\psi \rightarrow \gamma X(1835) \rightarrow \gamma\eta'\pi^+\pi^-$ [24,25] with a mass exactly at the threshold for the production of a proton and an anti-proton. It is therefore considered to be a molecular state consisting of a proton and an anti-proton. Later it was also found in decays to other light mesons such as $J/\psi \rightarrow \gamma 3(\pi^+\pi^-)$ [100], $J/\psi \rightarrow \gamma\eta K_S^0 K_S^0$ [101] and $J/\psi \rightarrow \gamma\gamma\phi$ [102]. In addition, the threshold enhancement $X(p\bar{p})$ seen by BESIII and CLEO⁸ in $J/\psi \rightarrow \gamma p\bar{p}$ and $\psi(2S) \rightarrow \gamma p\bar{p}$ [103–105], which can be explained by a state at the $p\bar{p}$ threshold, is considered to be the same state, although it has a significantly smaller width. This difference in width could be explained by interference effects in the light meson decays [105] or by final state interactions in the $p\bar{p}$ decay [106–108].

Since the $X(p\bar{p})$ has been seen in both J/ψ and $\psi(2S)$ decays, assuming it is the same state as the $X(1835)$, then the $X(1835)$ should also be observable in $\psi(2S)$ decays. So far, the $X(1835)$ has only been observed in J/ψ decays, which motivated the search for

⁷The WIDE ANGLE SHOWER APPARATUS at the COOLER SYNCHROTRON at FORSCHUNGSZENTRUM JÜLICH.

⁸Experiment at the CORNELL ELECTRON STORAGE RING (CESR) at Cornell University.

this state as an intermediate resonance in the process $\psi(2S) \rightarrow \gamma X(1835) \rightarrow \gamma \eta' \pi^+ \pi^-$ in this thesis, which is described in Section 5.5.

Hybrids

Hybrids are mesons that contain an additional constituent gluon that can contribute to the quantum numbers of the meson. Therefore, it is possible for a hybrid meson to have quantum numbers forbidden for conventional hadrons, as listed in Equation (2.14). The hybrid meson ground state nonet with the exotic quantum numbers $J^{PC} = 1^{-+}$ is predicted by flux tube models to be in the mass range $1.7 \text{ GeV}/c^2$ to $1.9 \text{ GeV}/c^2$ [109, 110], while lattice calculations yield a mass of $(2.0 \pm 0.2) \text{ GeV}/c^2$ [111, 112]. Experimental candidates for states in this nonet are the $\pi_1(1600)$ and $\eta_1(1855)$.

The isovector $\pi_1(1600)$ was observed by COMPASS⁹ in the decays to $\rho\pi$ [113, 114] and $\eta'\pi$ [115] and by E852¹⁰ in decays to $\eta'\pi$ [23], $f_1(1285)\pi$ [116], $\omega\pi\pi$ and $b_1(1235)\pi$ [117], where the particles were produced by a pion beam colliding with a hadronic target. It was also observed by CRYSTAL BARREL¹¹ in $p\bar{p}$ annihilations to $\pi^0\pi^0\eta$, $\pi^0\eta\eta$ and $K^+K^-\pi^0$ [118]. The PDG lists a mass of the $\pi_1(1600)$ of $(1645_{-17}^{+40}) \text{ MeV}/c^2$ and a width of $(370_{-60}^{+50}) \text{ MeV}$ [6], which is only slightly lighter than the predictions from lattice QCD and flux tube models. An enhancement at $\sim 1400 \text{ MeV}/c^2$, the supposed $\pi_1(1400)$, which was seen by COMPASS in $\pi^-p \rightarrow \eta\pi$ [115] can also be explained by the $\pi_1(1600)$, where the peak is shifted by kinematic effects [119].

The isoscalar $\eta_1(1855)$ was observed by BESIII in the reaction $J/\psi \rightarrow \gamma\eta_1(1885) \rightarrow \gamma\eta\eta'$ with a mass of $(1855 \pm 9_{-1}^{+6}) \text{ MeV}/c^2$ and a width of $(188 \pm 18_{-8}^{+3}) \text{ MeV}$ [120]. The resulting mass difference between the isovector $\pi_1(1600)$ and the isoscalar $\eta_1(1855)$ of $\sim 200 \text{ MeV}/c^2$ is in good agreement with lattice QCD calculations [121].

So far, the mentioned isovector hybrid candidate $\pi_1(1600)$ has been observed in $p\bar{p}$ and πp reactions, as well as in the charmonium decay $\chi_{c1} \rightarrow \eta'\pi^+\pi^-$ [122], while the isoscalar $\eta_1(1855)$ has only been observed in the decay of the charmonium J/ψ [120]. To get access to the quantum numbers of the $\pi_1(1600)$, the decays of the $\chi_{c1,2}$ into three pseudoscalar mesons can be used. This is done in this thesis in the decay $\chi_{c2} \rightarrow \pi_1(1600)^\pm \pi^\mp \rightarrow \eta'\pi^+\pi^-$, which is presented in Section 5.7. Here, the χ_{c2} has been chosen over the χ_{c1} , because of the simpler decay amplitude (see Section 5.7).

⁹The COMMON MUON PROTON APPARATUS FOR STRUCTURE AND SPECTROSCOPY at the SUPER PROTON SYNCHROTRON (SPS) at CERN.

¹⁰Experiment at the ALTERNATING GRADIENT SYNCHROTRON (AGS) at BROOKHAVEN NATIONAL LABORATORY (BNL).

¹¹Spectrometer at the LOW ENERGY ANTIPROTON RING (LEAR) at CERN.

2.3. Nonrelativistic QCD

As mentioned in Section 2.2, QCD becomes non-perturbative for small momentum transfer, making it necessary to use refined models to calculate physical properties in this energy regime. One such model is *non-relativistic QCD* (NRQCD), which is an effective field theory. It is applicable to calculations of decay and production rates of charmonia and bottomonia, since for these the relative velocity between the quarks $\beta = v/c$ is a small expansion parameter [123]. In NRQCD the QCD Lagrangian is written explicitly as

$$\mathcal{L}_{\text{QCD}} = \mathcal{L}_{\text{light}} + \bar{\Psi}(i\gamma^\mu D_\mu - m_Q)\Psi. \quad (2.42)$$

Here, $\mathcal{L}_{\text{light}}$ is the QCD Lagrangian from Equation (2.3) for the three lightest quarks $q = (u, d, s)$ and the gluonic field tensor. The second term describes the dynamics of a heavy quark with mass m_Q and Dirac spinor

$$\Psi = \begin{pmatrix} \psi \\ \chi \end{pmatrix} \quad \text{and} \quad \bar{\Psi} = \begin{pmatrix} \psi^\dagger \\ \chi^\dagger \end{pmatrix}, \quad (2.43)$$

where ψ and χ are the 2-spinors describing the heavy quark and the anti-quark, respectively. $D_\mu = \partial_\mu - ig_s t^C \mathcal{A}_\mu^C$ is the covariant derivative resulting in the coupling of the heavy quark to the gluon.

2.3.1. NRQCD Lagrangian

By a unitary transformation it can be shown that the quark and anti-quark fields approximately decouple, which allows to write down the most general effective Lagrangian [123]

$$\mathcal{L}_{\text{NRQCD}} = \mathcal{L}_{\text{light}} + \psi^\dagger \left(iD_0 + \frac{D^2}{2m_Q} \right) \psi + \chi^\dagger \left(iD_0 - \frac{D^2}{2m_Q} \right) \chi + \delta\mathcal{L} \quad (2.44)$$

with

$$D^2 = \vec{D} \cdot \vec{D} = \sum_{j=1}^3 D_j D^j = \sum_{j=1}^3 \left(\partial_j - ig_s t^C \mathcal{A}_j^C \right) \left(\partial^j - ig_s t^C \mathcal{A}^{Cj} \right). \quad (2.45)$$

This Lagrangian satisfies the $\text{SU}(3)_c$ gauge symmetry of full QCD and is invariant under charge conjugation and parity. Since it is a non-relativistic theory the Lorentz-invariance of full QCD reduces to a rotational symmetry. An additional symmetry comes from the conservation of the number of heavy quarks and anti-quarks, namely the *heavy-quark phase symmetry*, which implies that $\mathcal{L}_{\text{NRQCD}}$ is invariant under a transformation of the form [123]:

$$\psi \rightarrow e^{i\alpha} \psi \quad \text{and} \quad \chi \rightarrow e^{i\beta} \chi. \quad (2.46)$$

Setting the correction term $\delta\mathcal{L}$ in Equation (2.44) to zero leads to the minimal form of NRQCD, which includes only the two parameters m_Q and g_s [123]. In this case, the theory gets an additional symmetry, called the *heavy-quark spin symmetry*, which means that charmonia that are spin partners, such as J/ψ and η_c , are degenerate. In minimal NRQCD, the energy levels in the heavy quarkonium are accurate up to an order of $m_Q\beta^4$ [123]. To include the spin splittings and improve the accuracy of the energy levels to $m_Q\beta^6$, correction terms $\delta\mathcal{L} \neq 0$ must be added to Equation (2.44). The first of these terms are the *v²-improvement terms*, which add four additional parameters (c_1, c_2, c_3, c_4) to the theory [123].

By rescaling of the fields and the space-time coordinates and by choosing a physical gauge, an expansion of the Lagrangian in terms of powers of β can be written down. Here, the Coulomb gauge with

$$\vec{\nabla}\cdot\vec{\mathcal{A}} = \sum_{j=1}^3 \partial_j \mathcal{A}^j = 0 \quad (2.47)$$

is chosen, where $\vec{\mathcal{A}}$ is the vector component of the gluon field \mathcal{A} . The first component of the Lagrangian which is of order β^0 is then [123]

$$\mathcal{L}_0 = \mathcal{L}_{\text{light}} + \psi^\dagger \left(i\partial_0 - g_s \mathcal{A}_0 + \frac{\nabla^2}{2m_Q} \right) \psi + \chi^\dagger \left(i\partial_0 - g_s \mathcal{A}_0 - \frac{\nabla^2}{2m_Q} \right) \chi \quad (2.48)$$

and the terms of order β^1 are [123]

$$\mathcal{L}_1 = -\frac{1}{m_Q} \psi^\dagger \left(i g_s \vec{\mathcal{A}} \vec{\nabla} \right) \psi + \frac{c_4}{2m_Q} \psi^\dagger \left(g_s \vec{\nabla} \times \vec{\mathcal{A}} \right) \vec{\sigma} \psi + \text{c.c.}, \quad (2.49)$$

where $\vec{\sigma}$ are Pauli-matrices. As can be seen, \mathcal{L}_0 does not include any coupling of the heavy quarks to the vector component of the gluon field, which is responsible for the creation and annihilation of gluons. These couplings only appear at order β due to the terms included in \mathcal{L}_1 .

In order to determine the values of the parameters m_Q , g_s and c_{1-4} , a matching between NRQCD and full QCD has to be performed. For this, two different methods are used: non-perturbative and perturbative matching. For non-perturbative matching, the calculated values according to Equation (2.44) are compared either to lattice NRQCD calculations [124] or directly to experimentally determined masses [123]. However, this is only feasible for a small number of parameters and is done for the two parameters of minimal NRQCD [123]. The additional parameters are matched via perturbative matching, which relies on the asymptotic freedom of QCD. For perturbative matching the Lagrangians for full QCD (Equation (2.3)) and NRQCD (Equation (2.44)) are used to calculate the same scattering amplitudes for momenta $k \ll m_Q c$ in the perturbative regime. Both of

the amplitudes are then expanded in powers of k/m_Q and the parameters of NRQCD are adjusted so that the amplitudes match to the desired order [123].

2.3.2. Fock State Expansion

To use NRQCD to calculate the production and decay amplitudes of charmonia, the charmonium state $|H\rangle$ must be expanded in terms of Fock states¹² as

$$\begin{aligned}
 |H\rangle = & \psi^{Q\bar{Q}} |Q\bar{Q}\rangle + \sum_{\sigma,\lambda,\iota,\gamma} \psi_{\sigma,\lambda,\iota}^{Q\bar{Q}g} |Q\bar{Q}g\rangle_{\sigma,\lambda,\iota} + \psi_{\sigma,\lambda,\iota,\gamma}^{Q\bar{Q}q\bar{q}} |Q\bar{Q}q\bar{q}\rangle_{\sigma,\lambda,\iota,\gamma} \\
 & + \psi_{\sigma,\lambda,\iota,\gamma}^{Q\bar{Q}gg} |Q\bar{Q}gg\rangle_{\sigma,\lambda,\iota,\gamma} + \psi_{\sigma,\lambda,\iota,\gamma}^{Q\bar{Q}q\bar{q}g} |Q\bar{Q}q\bar{q}g\rangle_{\sigma,\lambda,\iota,\gamma} + \dots, \quad (2.50)
 \end{aligned}$$

assuming that the dominant Fock state $|Q\bar{Q}\rangle$ consists of a heavy quark anti-quark pair with defined quantum numbers $^{2S+1}L_J$ in a color-singlet state [123]. Higher Fock states include additional gluons, e.g. $|Q\bar{Q}g\rangle_{\sigma,\lambda,\iota}$, or light quark anti-quark pairs, e.g. $|Q\bar{Q}q\bar{q}\rangle_{\sigma,\lambda,\iota,\gamma}$. These higher states have spin configurations $\sigma = (S_1, S_2, \dots)$ as well as angular quantum numbers $\lambda = (L_1, L_2, \dots)$ and $\iota = (J_1, J_2, \dots)$. In addition, the particles in the Fock state can have different color configurations $\gamma = (C_1, C_2, \dots)$, which are either a singlet or an octet. Since the first excited states $|Q\bar{Q}g\rangle_{\sigma,\lambda,\iota}$ have a defined color configuration, with the $Q\bar{Q}$ being in a color-octet state, they are not summed over γ .

The amplitudes $\psi_{\sigma,\lambda,\iota,\gamma}^F$ can be calculated using the Lagrangian \mathcal{L}_1 in Equation (2.49), since the higher terms are suppressed by orders of β . It can be shown, that the first term in Equation (2.49)

$$\mathcal{L}_E = -\frac{1}{m_Q} \psi^\dagger \left(ig_s \vec{A} \vec{\nabla} \right) \psi \quad (2.51)$$

corresponds to so-called *electric transitions* that satisfy the selection rules $\Delta L = \pm 1$ and $\Delta S = 0$ for the $Q\bar{Q}$ pair [123]. The second term

$$\mathcal{L}_M = \frac{c_4}{2m_Q} \psi^\dagger \left(g_s \vec{\nabla} \times \vec{A} \right) \vec{\sigma} \psi \quad (2.52)$$

corresponds to *magnetic transitions* with $\Delta L = 0$ and $\Delta S = \pm 1$ [123]. Both transitions change a color-singlet to a color-octet and a color-octet to either a singlet or an octet. Each Fock state in Equation (2.50) can be reached by N electric and either one or zero magnetic transitions and the probability of finding it in the charmonium scales with β^{2N} and β^{2N+3} , respectively [123].

¹²Fock states are quantum states with a defined number of particles and defined creation and annihilation operators [125].

With this, the Fock state expansion of the χ_{cJ} charmonia can be written down explicitly as

$$|\chi_{cJ}\rangle = \psi_0 |c\bar{c}; {}^3P_J\rangle + \psi_1 |c\bar{c}g; {}^3S_1\rangle + \psi_2 |c\bar{c}g; {}^3D_1\rangle + \psi_3 |c\bar{c}g; {}^3D_2\rangle \\ + \psi_4 |c\bar{c}g; {}^3D_3\rangle + \psi_5 |c\bar{c}g; {}^1P_1\rangle + \mathcal{O}(\beta^2). \quad (2.53)$$

The probabilities can be calculated as an integral over the whole phase space of the particles of the square of the amplitudes, giving $P_i \sim \beta^2$ for $i \in (1, 2, 3, 4)$ and $P_5 \sim \beta^3$ and higher Fock states with probabilities of order β^4 or smaller [123].

2.3.3. NRQCD Factorization for P-Wave Charmonia

As mentioned before, the NRQCD Lagrangian in Equation (2.44) has a heavy-quark phase symmetry, which results in the conservation of the number of c and \bar{c} quarks. Therefore, the annihilation process $c\bar{c} \rightarrow gg \rightarrow \text{LH}$, where LH is any light hadron final state, is forbidden and cannot be described in NRQCD. However, by adding additional terms [126]

$$\mathcal{L}_{4\text{-fermion}} = \sum_{m,n} f_{mn} \mathcal{O}_{mn} \quad (2.54)$$

to the Lagrangian, the total decay width into light hadrons can be calculated using the optical theorem [123, 127]. These additional terms include four-fermion operators \mathcal{O}_{mn} with coefficients f_{mn} that conserve the number of c and \bar{c} quarks and have the form

$$\mathcal{O}_{mn} = \psi^\dagger \mathcal{K}_m \chi \chi^\dagger \mathcal{K}_n \psi. \quad (2.55)$$

Such an operator leads to process $Q\bar{Q} \rightarrow Q\bar{Q}$ where the initial $Q\bar{Q}$ pair, with color and angular quantum numbers determined by \mathcal{K}_n , is annihilated and a $Q\bar{Q}$ pair, with color and angular quantum numbers determined by \mathcal{K}_m , is created. \mathcal{K}_n and \mathcal{K}_m are products of different components, which can include spin matrices $\vec{\sigma}$, color matrices t_{ab}^C , and a polynomial in components of the covariant derivatives \vec{D} and $[D_0, \vec{D}]$ [123]. The coefficients f_{mn} can be calculated by perturbative matching as a power series in $\alpha_s(m_c)$ [123, 128].

The optical theorem [127] can now be used to calculate the total decay width into light hadrons $\Gamma(H)$ from the imaginary part of the scattering amplitude for $Q\bar{Q} \rightarrow Q\bar{Q}$. This results in the NRQCD factorization formula [123]

$$\Gamma(H) = \frac{1}{2M_H} \sum_{m,n} C_{mn} \langle H | \mathcal{O}_{mn} | H \rangle \quad (2.56)$$

where C_{mn} is given by $C_{mn} = 2 \text{Im} f_{mn}$ and M_H is the mass of the charmonium. Each of the summands in Equation (2.56) consists of a product of the $Q\bar{Q}$ annihilation effects

encoded in C_{mn} and the matrix element $\langle H|\mathcal{O}_{mn}|H\rangle$, which gives the probability of finding the $Q\bar{Q}$ pair in a state that can be annihilated by \mathcal{O}_{mn} [126]. While the coefficients C_{mn} can be calculated perturbatively [128], the matrix elements must be determined by non-perturbative methods such as lattice NRQCD [129].

To determine the decay width for the P-wave charmonia χ_{cJ} , the lowest order matrix elements in β must be identified. For the χ_{c0} , one of these is the color-singlet matrix element [123]

$$\begin{aligned}\langle\mathcal{O}_1\rangle &= \frac{1}{m_c^4} \left\langle \chi_{c0} \left| \psi^\dagger \left(-\frac{i}{2} \hat{D}\vec{\sigma} \right) \chi \chi^\dagger \left(-\frac{i}{2} \hat{D}\vec{\sigma} \right) \psi \right| \chi_{c0} \right\rangle \\ &= \frac{1}{m_c^4} \sum_X \left\langle \chi_{c0} \left| \psi^\dagger \left(-\frac{i}{2} \hat{D}\vec{\sigma} \right) \chi \right| X \right\rangle \left\langle X \left| \chi^\dagger \left(-\frac{i}{2} \hat{D}\vec{\sigma} \right) \psi \right| \chi_{c0} \right\rangle \\ &\approx \frac{1}{m_c^4} \left| \left\langle 0 \left| \chi^\dagger \left(-\frac{i}{2} \hat{D}\vec{\sigma} \right) \psi \right| \chi_{c0} \right\rangle \right|^2,\end{aligned}\quad (2.57)$$

where the derivative \hat{D} is defined by

$$\chi^\dagger \hat{D}\psi = \chi^\dagger \vec{D}\psi - \vec{D}\chi^\dagger \psi. \quad (2.58)$$

The approximation in Equation (2.57) is given by the *vacuum-saturation approximation*, which inserts a complete set of states $|X\rangle$ into the matrix element and then keeps only the vacuum term $|0\rangle$. This approximation is justified, since the next higher contribution comes from Fock states with two or more gluons, which are suppressed at order β^4 [126]. The second matrix element that appears at the same order in β as $\langle\mathcal{O}_1\rangle$ is the color-octet matrix element

$$\langle\mathcal{O}_8\rangle = \frac{1}{m_c^2} \left\langle \chi_{c0} \left| \psi^\dagger \vec{\sigma} t_{ab}^C \chi \chi^\dagger \vec{\sigma} t_{ab}^C \psi \right| \chi_{c0} \right\rangle, \quad (2.59)$$

for which the vacuum-saturation approximation is not applicable, as the vacuum is a color-singlet. Since the $\chi_{c1,2}$ are related to the χ_{c0} via the heavy-quark spin symmetry, their corresponding matrix elements are proportional to $\langle\mathcal{O}_1\rangle$ and $\langle\mathcal{O}_8\rangle$ [123].

As mentioned before the f_{mn} and therefore the C_{mn} can be extracted using perturbative matching [126] and in total the decay widths for the χ_{cJ} up to order α_s^2 are calculated according to Equation (2.56) as [123, 130]

$$\Gamma(\chi_{c0} \rightarrow \text{LH}) = \frac{4}{3} \pi \alpha_s^2(m_c) \langle\mathcal{O}_1\rangle + \pi \alpha_s^2(m_c) \langle\mathcal{O}_8\rangle, \quad (2.60)$$

$$\Gamma(\chi_{c1} \rightarrow \text{LH}) = \pi \alpha_s^2(m_c) \langle\mathcal{O}_8\rangle, \quad (2.61)$$

$$\Gamma(\chi_{c2} \rightarrow \text{LH}) = \frac{16}{45} \pi \alpha_s^2(m_c) \langle\mathcal{O}_1\rangle + \pi \alpha_s^2(m_c) \langle\mathcal{O}_8\rangle. \quad (2.62)$$

As can be seen, for orders up to α_s^2 , the decay width of the χ_{c0} and χ_{c2} depends on the color-singlet and color-octet terms in the same order in β , even though the first excited

Fock states have probabilities of order β^2 (see Equation (2.53)). This can be explained by the fact, that the annihilation of the dominant $|c\bar{c}; {}^3P_J\rangle$ Fock state is suppressed by β^2 due to its angular momentum, compared to the $|c\bar{c}g; {}^3S_1\rangle$ state. At this order in α_s , the χ_{c1} decay width does not depend on the color-singlet term, which can be explained by the generalized Landau-Yang theorem [123]. The Landau-Yang theorem [131, 132] states, that a massive spin-1 particle cannot annihilate into two massless bosons, which is however only true for QED. In QCD the annihilation into two gluons is allowed, but only at higher orders of α_s [133, 134].

The appearance of the color-octet terms in Equations (2.60) to (2.62) makes it clear that dynamical gluons inside the P-wave charmonia play an important role for their properties. This implies that the simple potential ansatz depending only on the quarks, as presented in Section 2.2.4, needs to be extended [135].

Using lattice QCD, the matrix elements for a charm quark mass of $m_c = 1.5 \text{ GeV}/c^2$ are determined to be [129]

$$\langle \mathcal{O}_1 \rangle_{\text{lat}} = 15.84_{-2.79}^{+3.61} \text{ MeV}, \quad (2.63)$$

$$\langle \mathcal{O}_8 \rangle_{\text{lat}} = 2.03_{-0.98}^{+1.64} \text{ MeV}. \quad (2.64)$$

These can be compared to phenomenologically determined values calculated according to [135]

$$\langle \mathcal{O}_1 \rangle_{\text{phen}} = \frac{45}{16\pi} \frac{\Gamma(\chi_{c2} \rightarrow \text{LH}) - \Gamma(\chi_{c1} \rightarrow \text{LH})}{\alpha_s^2(m_c)} = (14.9 \pm 5.5) \text{ MeV}, \quad (2.65)$$

$$\langle \mathcal{O}_8 \rangle_{\text{phen}} = \frac{1}{\pi} \frac{\Gamma(\chi_{c1} \rightarrow \text{LH})}{\alpha_s^2(m_c)} = (2.8 \pm 1.1) \text{ MeV}, \quad (2.66)$$

with the values for the $\Gamma(\chi_{cJ} \rightarrow \text{LH})$ taken from the PDG [6], under the assumption, that the χ_{cJ} decay only into light hadrons or via $\chi_{cJ} \rightarrow \gamma J/\psi$. As can be seen, these values are in good agreement, but the extracted width for the χ_{c0} of

$$\Gamma(\chi_{c0} \rightarrow \text{LH})_{\text{phen}} = (4.45 \pm 1.64) \text{ MeV} \quad (2.67)$$

differs by about 3σ from the value given by the PDG [6]

$$\Gamma(\chi_{c0} \rightarrow \text{LH})_{\text{PDG}} = (10.5 \pm 0.6) \text{ MeV}. \quad (2.68)$$

This difference indicates that the theory is still incomplete and that higher orders in β and α_s are needed to fully describe the data. However, this would introduce a significant number of additional parameters into the theory and such calculations are not yet feasible. An additional problem in comparing the experimental data with the theoretical predictions for the P-wave charmonia is the fact, that they are assumed to decay exclusively into

light hadrons or radiatively into an S-wave charmonium [135]. However, the measured branching ratios for the χ_{c0} , χ_{c1} and χ_{c2} only amount to $\sim 22\%$, $\sim 45\%$ and $\sim 32\%$, respectively [6], making it evident, that additional precise data on χ_{cJ} decays are needed. In addition, it is also possible to calculate exclusive branching ratios for heavy quarkonium decays via different extensions to NRQCD [136–138]. Although only two body decays have been calculated so far, more complex final states will hopefully be accessible in the future. This motivated the analysis of the decays $\chi_{cJ} \rightarrow \eta' \pi^+ \pi^-$ in Chapter 5 to gain insight into the contributions of the color-octet terms, and thus to explore the role of dynamical gluons within the charmonium system.

3. Experimental Setup

To obtain information on hadronic states, data from particle accelerator experiments must be collected and analyzed. In this case, the analyzed data comes from the BEIJING SPECTROMETER III (BESIII) experiment, which is located at the interaction point (IP) of the BEIJING ELECTRON POSITRON COLLIDER II (BEPCII) at the INSTITUTE OF HIGH ENERGY PHYSICS (IHEP) in Beijing. Details on the collider and the detector are given below.

3.1. BEPCII

In 1984, the predecessor of BEPCII, the BEIJING ELECTRON POSITRON COLLIDER (BEPC), was built in Beijing as the first ever high-energy accelerator in China [139]. Its first e^+e^- collision was achieved in 1988, which was accompanied by the assembly of the BEIJING SPECTROMETER (BES). BEPC was designed for center-of-mass energies from 3 GeV to 5.6 GeV and a peak luminosity of $1.7 \times 10^{31} \text{ cm}^{-2} \text{ s}^{-1}$ at a center-of-mass energy of $\sqrt{s} = 5.6 \text{ GeV}$ [140] and was operated until 2004.

In 2009, the first physics data taking with the upgraded BEPCII was started, which was designed for center-of-mass energies from 2 GeV to 4.6 GeV with a relative energy spread of 5×10^{-4} . It was planned with a peak luminosity of $1 \times 10^{33} \text{ cm}^{-2} \text{ s}^{-1}$ at a center-of-mass energy corresponding to the mass of the $\psi(3770)$ [21], which was achieved in 2016 [141] and increased to $1.1 \times 10^{33} \text{ cm}^{-2} \text{ s}^{-1}$ in 2023 [142]. Later, the maximum center-of-mass energy was increased to 4.95 GeV [143]. In contrast to its predecessor, BEPCII is a double-ring collider with a crossing angle of the two rings at the IP of $\pm 11 \text{ mrad}$. An overview of the properties of BEPCII compared to BEPC is given in Table 3.1.

BEPCII operates with 93 bunches in each of the 237.5 m-long rings, with a maximum beam current of 0.91 A, using a single radio frequency (RF) cavity in each of the rings at a frequency of 499.8 MHz [141]. Figure 3.1 shows a schematic overview of the IHEP campus around the BEPCII complex. It includes the experimental halls, one of which houses the BESIII experiment, additional accelerator facilities, the IHEP computing center, as well as the 202 m-long LINEAR ACCELERATOR (LINAC). The LINAC is used to pre-accelerate the electrons and positrons to a maximum energy of 2.5 GeV before injecting them into the storage ring at an injection rate of 50 mA/min for positrons and

200 mA/min for electrons [144, 145].

In addition to its use as a collider, BEPCII is also designed as a synchrotron radiation source, using electrons with an energy of 2.5 GeV and a beam current of 250 mA to generate 84 kW of radiation power at 14 beamlines [141].

In the future, BEPCII will be further upgraded (then called BEPCII-U), first by optimizing the accelerator for the higher energy region with a design luminosity of $1.1 \times 10^{33} \text{ cm}^{-2} \text{ s}^{-1}$ at $\sqrt{s} = 4.7 \text{ GeV}$ compared to the $3.5 \times 10^{32} \text{ cm}^{-2} \text{ s}^{-1}$ achieved with the current design. In a next step, the the maximum center-of-mass energy will be upgraded to $\sqrt{s} = 5.6 \text{ GeV}$ [22]. For these upgrades, an additional RF cavity will be installed in each of the rings and the magnets surrounding the cavities will be moved. Different designs for the positions of the cavities and magnets are currently being evaluated [146]. In addition, to accommodate the higher beam energies, the power sources of the bending magnets will be upgraded and the focusing magnets closest to the IP will be replaced. Depending on the exact configuration of these focusing magnets, the crossing angle at the IP could be increased by 2 mrad [22].

Table 3.1.: Operational parameters of BEPC, BEPCII and BEPCII-U [21, 22, 139, 140, 146].

		BEPC	BEPCII	BEPCII-U
Center-of-mass energy	[GeV]	3.0-5.6	2.0-5.0	2.0-5.6
Circumference	[m]	240.4	237.5	237.5
Number of bunches		2×1	2×93	2×120
RF cavity frequency	[MHz]	199.5	499.8	499.8
Luminosity at 3.78 GeV	$[\text{cm}^{-2} \text{ s}^{-1}]$	1×10^{31}	1.1×10^{33}	1×10^{33}
Luminosity at 4.7 GeV	$[\text{cm}^{-2} \text{ s}^{-1}]$	$< 1.7 \times 10^{31}$	3.5×10^{32}	1.1×10^{33}
Beam current	[A]	2×0.035	2×0.91	2×0.90
Crossing angle	[mrad]	0	± 11	$\pm 11 (\pm 13)$
Relative energy spread			5×10^{-4}	

3.2. BESIII

To extract data from the e^+e^- collisions taking place at BEPCII, the BESIII experiment is located at its IP. BESIII is the successor of the BES and BESII experiments, which started operating in 1989 and 1996, respectively, and were replaced by the BESIII detector in 2009. It is designed for data taking in the τ and charmonium energy region and covers a solid angle of $\Omega = 0.93 \cdot 4\pi$ [21]. Since BEPCII is a symmetric collider with only a small opening angle between the electron and positron beams, the resulting center-of-mass system is nearly at rest. Therefore, the detector is placed cylindrically symmetric around the IP, with the symmetry axis, defined as the z -axis, being the bisector

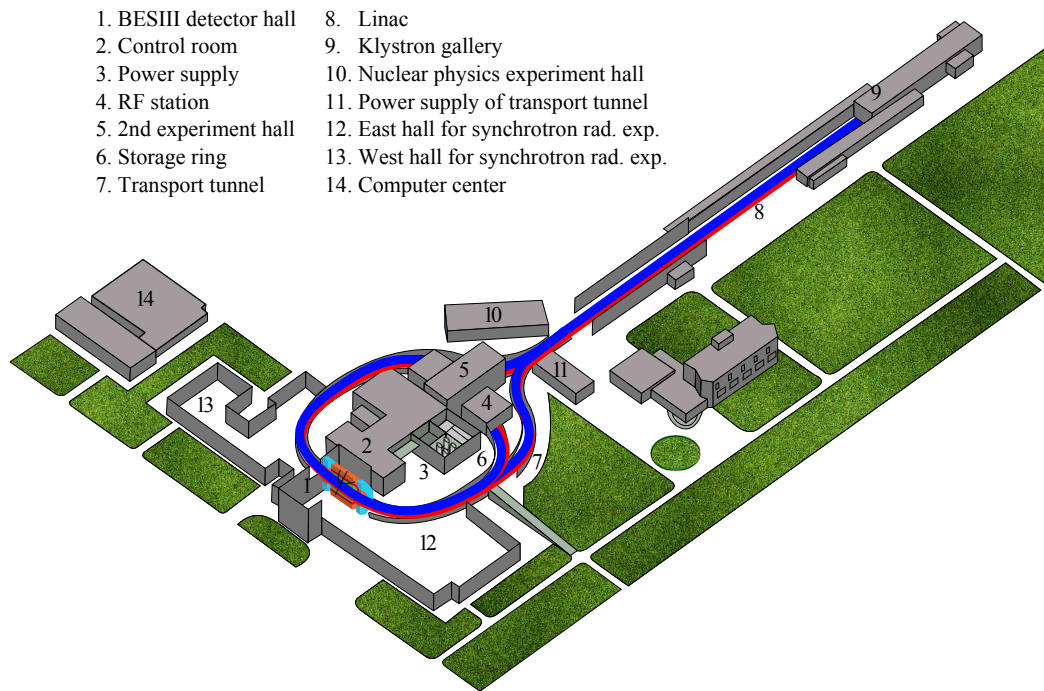


Figure 3.1.: Overview of the IHEP campus around the BEPCII complex, taken from [147]. The electron beam line is shown in red and the positron beam line in blue. Different buildings of BESIII and BEPCII are marked with numbers, which are given in the legend.

of the opening angle. From the inside out, the detector consists of the following subsystems (see Figure 3.2): a multilayer drift chamber (MDC) directly surrounding the beam pipe, a time-of-flight (TOF) system, and an electromagnetic calorimeter (EMC), all enclosed by a superconducting solenoid magnet (SSM) that produces a uniform magnetic field of 1 T [21]. An additional muon counter (MUC) is located outside of the SSM, interleaved with the flux return yoke of the magnet. Table 3.2 shows a comparison between the operational parameters achieved by BESII and BESIII for each of the subsystems. The different subsystems are presented in more detail in the following sections.

3.2.1. Multilayer Drift Chamber

The innermost part of the BESIII detector is the MDC, which is used for particle identification (PID) by measuring the energy loss dE/dx of charged particles and for momentum measurement, by reconstructing the particles' trajectories. It consists of an inner part with a stepped conical shape and an inner radius of 59 mm and an outer part with a maximum radius of 800 mm and a length of 2400 mm [21]. The stepped end region allows for the placement of focusing magnets as close as possible to the IP and limits the

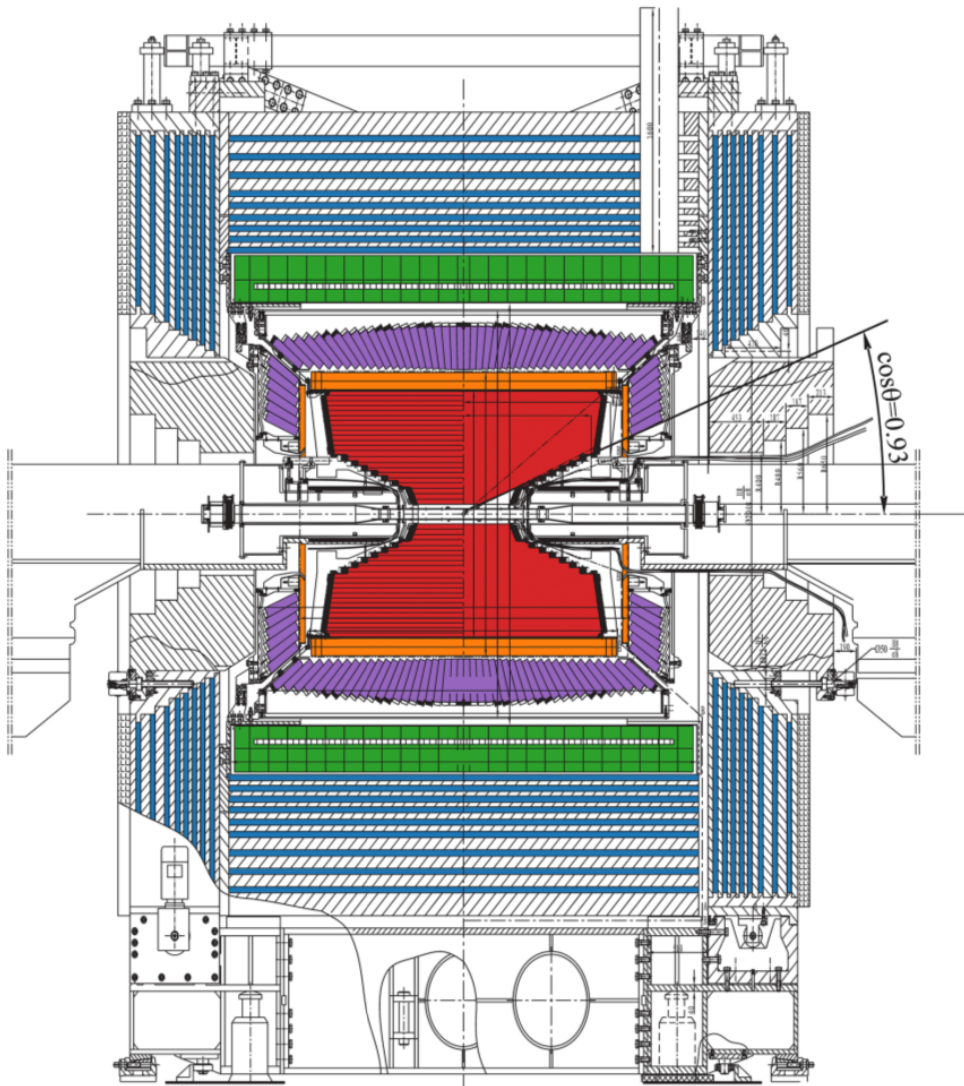


Figure 3.2.: Schematic drawing of the BESIII detector with the beam line in horizontal direction. The different detector components from the inside out are shown in red (MDC), orange (TOF), purple (EMC), green (SSM) and blue (MUC). Colored version of the figure from [21] with permission from Elsevier.

polar angle coverage to $|\cos\theta| < 0.93$. The drift chamber consists of 43 cylindrical layers of signal wires oriented parallel to the z -axis, resulting in a spatial resolution in the r - φ plane of $130\ \mu\text{m}$. About half of the layers are so-called stereo layers, which are tilted by an angle of -3.4° to 3.9° . These are used to determine the position in z -direction with a resolution of $2\ \text{mm}$ [21]. There are a total of 6796 signal wires, which are gold-plated tungsten wires with a diameter of $25\ \mu\text{m}$ [151]. These signal wires are interleaved with aluminum wires for field shaping. The chamber is filled with a gas mixture of 60% helium and 40% propane with a radiation length of $550\ \text{m}$, which gives a low probability for multiple scattering, while providing an energy loss resolution of 6% [21]. The gas is

Table 3.2.: Parameters of the subdetectors of the BESIII experiment compared with its predecessor BESII [21, 143, 148–150].

			BESII	BESIII
MDC	spatial resolution in $r - \varphi$ plane	[μm]	250	130
	spatial resolution in z direction	[mm]	8	2
	momentum resolution at $p = 1 \text{ GeV}/c^2$	[%]	2.4	0.5
	energy loss resolution	[%]	8.5	6.0
TOF	time resolution in the barrel	[ps]	180	68
	time resolution in the end caps	[ps]	350	60(110)
EMC	energy resolution at $E = 1 \text{ GeV}$	[%]	22	2.5
	spatial resolution at $E = 1 \text{ GeV}$	[mm]	30	6
MUC	spatial resolution	[mm]	45	20
	minimum muon momentum	[GeV/ c]	0.5	0.4
magnetic field		[T]	0.4	1.0

ionized along the trajectories of the charged particles passing through the detector, and the produced ions travel to the signal wires and can be detected as electrical pulses. Since the MDC is located inside the 1 T magnetic field, the trajectories of the charged particles will be helices, with the parameters of the helices depending on the momentum of the particles. In this way, the momentum of the particles can be reconstructed with a resolution of 0.5 % at a momentum of 1 GeV/ c [21].

In addition to measuring the momentum, the MDC can be used for PID by exploiting the fact that the specific energy loss dE/dx of a charged particle depends on its species. This can be seen in Figure 3.3, where the specific energy loss in the MDC for different particles is depicted. As can be seen, using only the MDC, protons and kaons can be clearly separated from muons, electrons and pions for small momenta. A 3σ separation between pions and kaons can be achieved up to a momentum of 770 MeV/ c [21]). In addition, it is not possible to distinguish between muons, electrons and pions at small momenta using only the MDC. Therefore, additional detector components have to be used, one of which is the TOF, which will be discussed in the next part.

3.2.2. Time-of-Flight System

The TOF is the detector system surrounding the MDC and is primarily used for PID. The barrel section with a polar angle coverage of $|\cos\theta| < 0.83$ consists of 88 plastic scintillators arranged in two layers. Each of the 88 scintillator bars with a length of 2.38 m, a width of 50 mm and a thickness of 50 mm is read out by two photomultiplier tubes (PMTs) mounted directly at each end [151]. The tubes are attached to the outer wall of the MDC at an inner radius of 810 mm, with the second layer being staggered with

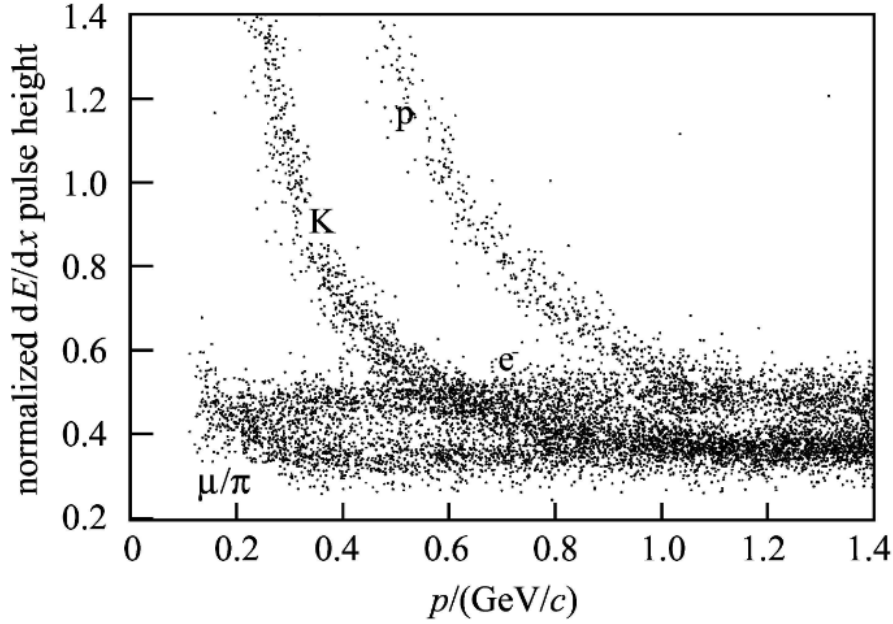


Figure 3.3.: Normalized energy loss dE/dx in the MDC for different particle species as a function of the particles' momenta p from a Monte Carlo simulation. Taken from [152].

respect to the first in order to reduce dead zones. This design results in a time-of-flight resolution of 68 ps for the double-layer barrel [143].

In its first version, the two endcaps of the TOF with a polar angle coverage of $0.85 < |\cos \theta| < 0.95$ consisted of 48 plastic scintillators each, resulting in a time resolution of 110 ps [143]. In 2015, the endcaps were upgraded with multigap resistive plate chambers (MRPC) [153]. Each endcap consists of 36 MRPC modules in two staggered layers with an inner radius of 501 mm and an outer radius of 822 mm of active area of th MRPC. This setup gives a resolution of 60 ps for Bhabha scattering events and of 70 ps for pions [154]. Using the timing information from the TOF T_{TOF} , the velocity β of a particle is calculated as

$$\beta = \frac{L}{c(T_{\text{TOF}} - T_{\text{start}})}, \quad (3.1)$$

with the speed of light c , the path length L measured in the MDC, and the event start time T_{start} , which is determined by averaging over the estimated track start times of all tracks in the event using a fast tracking and PID algorithm [155]. Together with the momentum p of the particle determined in the MDC, the mass m of the particle is calculated as

$$m^2 = \frac{1 - \beta^2}{c^2 \beta^2} p^2. \quad (3.2)$$

The calculated squared masses for different simulated particles are shown in Figure 3.4. As can be seen, protons can be unambiguously identified for all momenta from the TOF information alone, while the discrimination between kaons and pions becomes worse

for higher momenta (2σ separation up to $0.9 \text{ GeV}/c$ [156]), and electrons cannot be distinguished from pions at all.

The MDC and TOF described so far work only for charged particles. To detect photons and other uncharged particles, the EMC is used, which will be described in the next section.

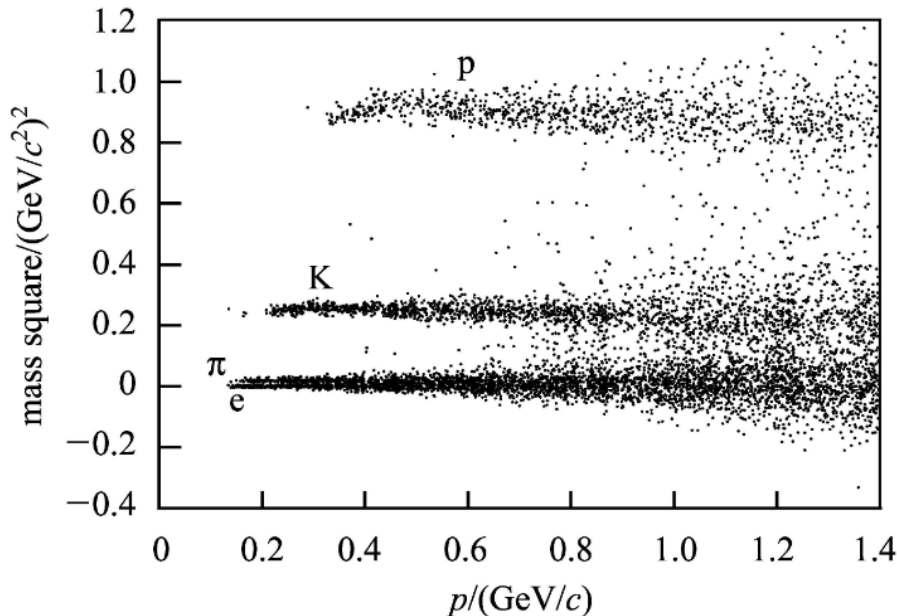


Figure 3.4.: Calculated mass squared in the TOF for different particle species as a function of the particles' momenta. Taken from [152].

3.2.3. Electromagnetic Calorimeter

The last detector component inside the SSM is the EMC, which is mainly used to reconstruct the energy and direction of photons. It is composed of 6240 cesium iodide crystals doped with thallium with a length of 280 mm, corresponding to 15 radiation lengths, and a base area of $52 \text{ mm} \times 52 \text{ mm}$ on the front side and $65 \text{ mm} \times 65 \text{ mm}$ on the back side [156]. Similar to the TOF, the EMC is divided into a barrel section with a polar angle coverage of $|\cos\theta| < 0.83$ and two end caps with $0.85 < |\cos\theta| < 0.93$, both separated by a gap of 50 mm to allow for mechanical support structures [151].

The barrel section, with a total length of 2.75 m, consists of 44 rings with an inner radius of 940 mm, each composed of 120 crystals. The crystals are tilted by 1.5° in the φ direction and additionally in the z direction to face $z = \pm 50 \text{ mm}$, depending on which side of the IP the crystal is located [151]. This tilt is added to reduce the possibility of a photon passing exactly between two crystals.

Each of the end caps consists of six rings of 80 crystals with an inner radius of 500 mm. In this case, the crystals are tilted to face a z position of $z = \pm 100 \text{ mm}$, again with a tilt

3. Experimental Setup

of 1.5° in φ direction [151]. At the end of each of the barrel and endcap crystals, two PMTs are used to collect the generated light signal [156].

Overall, this setup results in a sensitive energy range of the EMC from 0.02 GeV to 2 GeV, with a design energy resolution of

$$\sigma_E = \sqrt{\left(2.3\% \cdot \left[\frac{E}{\text{GeV}}\right]^{-0.5}\right)^2 + (1\%)^2} \quad (3.3)$$

and a design spatial resolution of

$$\sigma_r = 6 \text{ mm} \cdot \left[\frac{E}{\text{GeV}}\right]^{-0.5} \quad (3.4)$$

for an electromagnetic shower with a total energy E [151].

In addition to determining the energy and position of electromagnetic showers, the EMC can be used for PID because the shape of the electromagnetic shower depends on the species of the incident particle. Parameters describing the shape of a shower are the energy deposited in the central (or seed) crystal E_{seed} , the ratios $E_{\text{seed}}/E_{3 \times 3}$ and $E_{3 \times 3}/E_{5 \times 5}$, where $E_{3 \times 3}$ and $E_{5 \times 5}$ are the energies deposited in the 3×3 and 5×5 array around the seed, respectively. An additional parameter is the second moment

$$S = \frac{\sum_i E_i d_i^2}{\sum_i E_i}, \quad (3.5)$$

with the deposited energy E_i in crystal i at distance d_i from the center of the shower [152]. These characteristics can be used, for example, to distinguish neutrons and anti-neutrons from photons as was done in a recent BESIII measurement of the effective form factor of the neutron [157].

The last detector component of the BESIII experiment, namely the MUC, will be explained next.

3.2.4. Muon Counter

Since muons and pions have similar masses of $m_{\mu^\pm} = (105.658\,375\,5 \pm 0.000\,002\,3) \text{ MeV}/c^2$ and $m_{\pi^\pm} = (139.570\,39 \pm 0.000\,18) \text{ MeV}/c^2$ [6], respectively, they cannot be efficiently distinguished with the detector components mentioned so far. To improve the PID for this case, the BESIII detector includes a dedicated MUC, which is located outside the coil of the SSM and inside the flux return yoke. This detector component takes advantage of the fact that muons do not interact strongly and can therefore penetrate dense materials more easily than hadrons.

The barrel and end caps of the MUC contain nine and eight layers of resistive plate chambers, respectively, which are interleaved by nine layers of steel [21]. The difference in

the number of layers is due to space limitations, as the end caps must be placed as close as possible to the coil of the SSM to improve the uniformity of the magnetic field.

The barrel MUC has an inner radius of 1.7 m and an outer radius of 2.62 m with a total weight of the steel plates of 300 t, resulting in a polar angle coverage of $|\cos\theta| < 0.75$ [21]. The end caps are placed at an inner distance to the IP of 2.05 m with a total thickness of 0.75 m, a weight of 208 t and a polar angle coverage of $0.75 < |\cos\theta| < 0.89$ [21]. This design of the MUC results in a minimum momentum of $0.4 \text{ GeV}/c$ for muons to be identified by the MUC and a muon-pion misidentification rate of less than 10% for momenta greater than $0.5 \text{ GeV}/c$ [21]. To utilize the information from the MUC for PID, the hits in the MUC are used to reconstruct tracks with a spatial resolution of 20 mm [143], which is dominated by uncertainties due to multiple scattering [21].

3.3. Data Samples

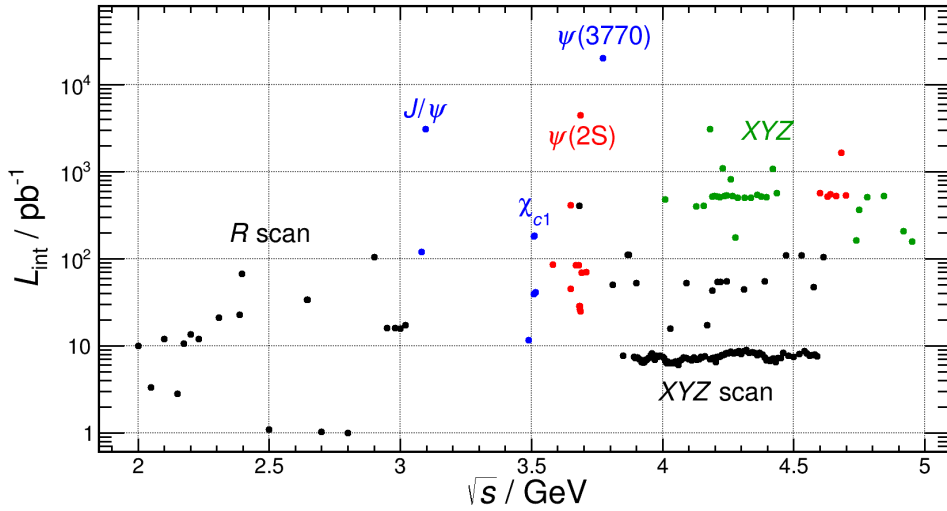


Figure 3.5.: Center-of-mass energies and luminosities of the BESIII data samples. The R scan and XYZ scan samples are shown in black, the J/ψ , $\psi(3770)$ and χ_{c1} samples are presented in blue, the XYZ samples are depicted in green and the samples that have been used in this thesis are marked in red.

Since 2009, BESIII has been collecting data in the energy range from 2 GeV to 5 GeV and has accumulated the world's largest data samples at energies corresponding to the masses of selected vector-charmonium states such as the J/ψ , the $\psi(2S)$ and the $\psi(3770)$. Figure 3.5 gives an overview of the BESIII data samples collected so far, including the resonance data sets mentioned above, scans around the χ_{c1} and $\psi(2S)$ resonances, an energy scan in the region above 4 GeV with luminosities $\mathcal{L}_{\text{int}} > 100 \text{ pb}^{-1}$ (the so-called XYZ data samples), and additional data sets over the whole range with lower luminosities,

which are used e.g. for measurements of the R value [158]. The data samples used in this thesis are marked in red. These are on the one hand side the $\psi(2S)$ samples from 2009, 2012 and 2021 (see Table 3.3) and the $\psi(2S)$ scan samples from 2009, 2018 and 2021¹³ (see Table 3.4), which are used for the analysis of $\psi(2S) \rightarrow \gamma\eta'\pi^+\pi^-$ described in Chapter 5. On the other hand the XYZ samples with energies between 4.6 GeV and 4.7 GeV (see Table 3.5) are used to search for the Z_{cs} in the reaction $e^+e^- \rightarrow \eta_c K^* K$ explained in Chapter 6. In the future, after the upgrade to BEPCII-U (see Section 3.1), additional data samples in the high energy region ($\sqrt{s} > 4.2$ GeV) will be recorded [22, 143], to give the possibility to search for heavier charmonium and charmonium-like particles.

3.4. BESIII Offline Software System

For the analysis of the mentioned data sets, the BESIII collaboration provides necessary software packages in the form of the BESIII OFFLINE SOFTWARE SYSTEM (BOSS). BOSS is mostly written in C++ and is based on the GAUDI framework [166], which was developed in the context of the LHCb experiment for the purpose of data processing for high-energy physics experiments. It includes methods for converting events from the stored raw data into ROOT [167] files, making them easier accessible for physics analysis. These methods include algorithms for PID and tracking, as well as initial event selection algorithms such as vertex and kinematic fitting. In addition, the BOSS framework contains a complete description of the BESIII detector, which is used to simulate physical events. These detector simulations are performed using the BESIII OBJECT ORIENTED SIMULATION TOOL (BOOST) [168], which is based on GEANT4 [169], and dedicated MONTE CARLO (MC) generator packages [170], which are used to simulate different physical channels. The MC simulations that have been generated in this thesis for efficiency determination, background analysis, and partial wave analysis (PWA) are presented in the next section.

3.5. Monte Carlo Simulations

In the context of this thesis, two different types of Monte Carlo (MC) simulations are used [171, 172]. These are the so-called inclusive MC samples, as well as the signal MC samples. In both cases, the simulation is split into two steps: First, the generation of the four-momenta of the involved particles according to defined production and decay models. And second, the propagation of these particles in the BESIII detector, including their reactions with the detector components, as well as the digitization of the detector responses.

¹³The data sample at $\sqrt{s} = 3.682$ GeV has not yet been calibrated and is therefore not used in this thesis.

Table 3.3.: Resonance data samples that have been used in this thesis with their integrated luminosities \mathcal{L}_{int} determined from Bhabha scattering events ($e^+e^- \rightarrow e^+e^-$) and the number of produced $\psi(2S)$ mesons $N_{\psi(2S)}$ derived from counting inclusive decays of the $\psi(2S)$ into hadrons [159, 160].

Sample	\sqrt{s} / MeV	$\mathcal{L}_{\text{int}} / \text{pb}^{-1}$	$N_{\psi(2S)} / 10^6$
		161.6 ± 1.7	107.7 ± 0.6
$\psi(2S)$	3686.1	506.9 ± 5.1	345.4 ± 2.6
		3208.5 ± 32.1	2259.3 ± 11.1
Sum		3877.0 ± 38.8	2712.4 ± 14.3

Table 3.4.: Scan data samples that have been used in this thesis. The center-of-mass energies \sqrt{s} have been measured with the beam energy measurement system (BEMS) [161, 162] and the integrated luminosities \mathcal{L}_{int} were determined from Bhabha scattering events with the same methods as in [160]. $\Delta E = \sqrt{s} - M_{\psi(2S)}c^2$ is the energy difference to the mass of the $\psi(2S)$ [6].

Sample	\sqrt{s} / MeV	$\Delta E / \text{MeV}$	$\mathcal{L}_{\text{int}} / \text{pb}^{-1}$
Scan 1	3581.54 ± 0.05	-104.56 ± 0.05	85.7 ± 0.9
Scan 2	3650.00 ± 0.05	-36.10 ± 0.05	445.5 ± 4.6
Scan 3	3670.16 ± 0.05	-15.94 ± 0.05	84.7 ± 0.9
Scan 4	3680.14 ± 0.05	-5.96 ± 0.05	84.8 ± 0.9
Scan 5	3682.75 ± 0.05	-3.35 ± 0.05	28.7 ± 0.3
Scan 6	3684.22 ± 0.05	-1.88 ± 0.05	28.7 ± 0.3
Scan 7	3685.26 ± 0.05	-0.84 ± 0.05	26.0 ± 0.3
Scan 8	3686.50 ± 0.05	0.40 ± 0.05	25.1 ± 0.3
Scan 9	3691.36 ± 0.05	5.26 ± 0.05	69.4 ± 0.7
Scan 10	3709.76 ± 0.05	23.66 ± 0.05	70.1 ± 0.8
Sum			948.9 ± 9.5

Table 3.5.: XYZ data samples that have been used in this thesis. The center-of-mass energies \sqrt{s} have been determined by analyzing the reaction $e^+e^- \rightarrow \gamma_{\text{ISR/FSR}}\mu^+\mu^-$ for the 4600 sample [163] and $e^+e^- \rightarrow \Lambda_c^+\Lambda_c^-$ for the other samples [164]. The integrated luminosities \mathcal{L}_{int} were determined from Bhabha scattering events [164, 165].

Sample	\sqrt{s} / MeV	$\mathcal{L}_{\text{int}} / \text{pb}^{-1}$
4600	4599.53 ± 0.74	586.9 ± 3.9
4620	4628.00 ± 0.33	521.5 ± 2.8
4640	4640.91 ± 0.38	551.7 ± 3.0
4660	4661.24 ± 0.30	529.4 ± 2.9
4680	4681.92 ± 0.30	1667.4 ± 8.9
4700	4698.82 ± 0.37	535.5 ± 2.9
Sum		4392.4 ± 24.1

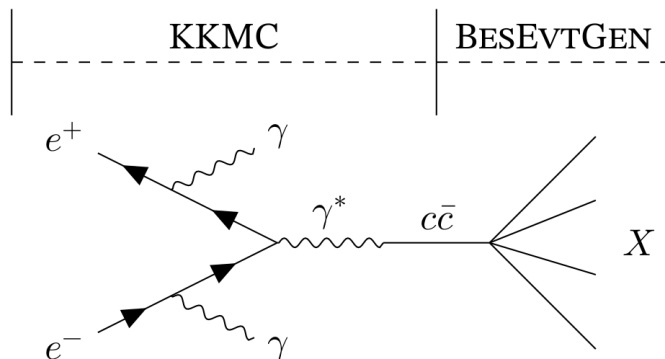


Figure 3.6.: Schematic representation of the simulated process $e^+e^- \rightarrow c\bar{c} \rightarrow X$, including ISR, in the BOSS framework using the MC generators KKMC and BESEVTGEN.

For the first step the event generators KKMC [173] and BESEVTGEN [170] are used. KKMC is a generator for processes of the type¹⁴ $e^+e^- \rightarrow f\bar{f} + n\gamma_{\text{ISR}}$, where f is any SM fermion except for the electron and top quark. In the context of the BESIII experiment, f is a c quark. KKMC includes electromagnetic processes up to second order with electro-weak corrections of first order [173]. The subsequent decay of the $c\bar{c}$ is simulated with BESEVTGEN [170], which is an extension of EVTGEN [174] for the charmonium energy regime. It allows the generation of any final state X via possible intermediate resonances. The explicit decay chain and the models used for each decay are defined by a configuration file. In addition, final state radiation (FSR) of charged particles is included via the PHOTOS algorithm [175].

In all simulations, the reconstruction is the second step and is performed using the BOOST [168] and GEANT4 [169] frameworks as described in Section 3.4. This reconstruction step is important to obtain a reliable estimate of the detector effects that may effect the reconstruction of the data samples, and to determine the acceptance of the detector. These detector effects include, for example, the production of bremsstrahlung by particles in the detector material, which can be reconstructed as electromagnetic showers in the EMC (see Equation (4.19)). Additionally, it also accounts for the energy loss of photons in the inner parts of the detector (see Equation (4.13)). All the parameters of the detector simulation are tuned to give a good description of the data, which is verified with dedicated control channels [151].

For the $\psi(2S) \rightarrow \gamma\eta'\pi^+\pi^-$ analysis, the simulated decay chains can be seen schematically in Table 3.6. A total of 2×6 (corresponding to the two different considered η' decays) signal MC simulations with 5 million events each are produced. In 2×5 of them, the first step is a radiative decay into either a lower lying charmonium state χ_{cJ} or η_c or the exotic candidate $X(1835)$. These decays are generated with the P2GCJ and JPE

¹⁴Initial state radiation (ISR) is a process where a particle in the initial state radiates a photon prior to the collision.

models, respectively, which produce an angular distribution for the helicity angle θ of the radiative photon according to

$$\frac{d\Gamma}{d\cos\theta} \propto 1 + \alpha \cos^2\theta, \quad (3.6)$$

with $\alpha = 1$ for the χ_{c0} , η_c and $X(1835)$, $\alpha = -1/3$ for the χ_{c1} , and $\alpha = 1/13$ for the χ_{c2} [176]. In each of these simulations the charmonium or $X(1835)$ decays into $\eta'\pi^+\pi^-$ according to the PHSP model. The PHSP model generates decays into n particles uniformly distributed in the n -body phase space Φ_n according to [6]

$$\frac{d\Gamma}{d\Phi_n} = \text{const.} \quad (3.7)$$

For a three-body decay this can be simplified to

$$\frac{d\Gamma}{dm_{12}^2 dm_{13}^2} = \text{const.}, \quad (3.8)$$

which corresponds to the representation often used in Dalitz plots. Here, m_{12} and m_{13} are the invariant masses of two of the two-particle subsystems. Two additional simulations include the direct decay $\psi(2S) \rightarrow \gamma\eta'\pi^+\pi^-$ again simulated according to the PHSP model. The next step in each simulation is the decay of the η' , where the decay models PHSP and EPGPP are used for $\eta' \rightarrow \eta\pi^+\pi^-$ and $\eta' \rightarrow \gamma\pi^+\pi^-$, respectively. EPGPP is a model specifically designed for the decay $\eta' \rightarrow \gamma\pi^+\pi^-$ [177], which includes the intermediate resonances ρ^0 and ω , their interference, as well as the Wess-Zumino-Witten anomaly [178, 179]. In the $\eta' \rightarrow \eta\pi^+\pi^-$ simulations the η further decays into two photons using the PHSP model.

The inclusive MC sample is prepared in advance by the BESIII collaboration and includes

Table 3.6.: Decay chain and models used in the BES-EVTGEN generator for the $\psi(2S) \rightarrow \gamma\eta'\pi^+\pi^-$ analysis.

Decay	Model
$\psi(2S) \rightarrow \gamma\chi_{cJ}$	P2GCJ
$\psi(2S) \rightarrow \gamma\eta_c$	JPE
$\psi(2S) \rightarrow \gamma X(1835)$	JPE
$\psi(2S) \rightarrow \gamma\eta'\pi^+\pi^-$	PHSP
$\chi_{cJ} \rightarrow \eta'\pi^+\pi^-$	PHSP
$\eta_c \rightarrow \eta'\pi^+\pi^-$	PHSP
$X(1835) \rightarrow \eta'\pi^+\pi^-$	PHSP
$\eta' \rightarrow \eta\pi^+\pi^-$	PHSP
$\eta' \rightarrow \gamma\pi^+\pi^-$	EPGPP
$\eta \rightarrow \gamma\gamma$	PHSP

3. Experimental Setup

all known decay modes of the $\psi(2S)$ and the subsequent decay of appearing resonances, as they are listed by the PDG. In addition, for the generation of the inclusive MC, the LUNDCHARM [180, 181] model is used to estimate branching ratios for so far unobserved decays, via the partonic hadronization model LUND [182, 183]. In this way, the inclusive MC sample is a simulation that is used to replicate the data with our current knowledge, and this can be used as a tool to analyze appearing background reactions. The number of generated events for the inclusive MC corresponds roughly to the number of measured $\psi(2S)$ events $N_{\psi(2S)} = (2712.4 \pm 14.3) \times 10^6$ [159].

4. General Event Selection

In the context of this work, the aforementioned BESIII data samples are used to search for different exotic particles, e.g., the $\pi_1(1600)$ and the $Z_{cs}(3985)$ in the reactions $\psi(2S) \rightarrow \gamma\eta'\pi^+\pi^-$ and $e^+e^- \rightarrow \eta_c K^*K$, respectively. In both analyses, multiple charged tracks and photon candidates must be reconstructed using the BOSS framework. Both analyses use standardized general selection criteria, which are described in detail in the following sections. These general selection criteria are followed by more specific ones, depending on the reaction being analyzed.

4.1. Charged Particle Selection

To select charged particles in events recorded by the BESIII detector, the information from the different subdetectors is combined. As a first step, hits in the MDC are combined to form tracks (see Section 4.1.1). The track parameters determined in this way are used together with the information from the other subdetectors to determine the corresponding particle species (see Section 4.1.2).

4.1.1. Tracking

The first step in identifying charged particles is to combine hits in the MDC into tracks. This is done using three different track-finding algorithms based on a template matching method [184], a track segment finder [185], and a Hough transformation [186], respectively. Since the efficiency of each of these algorithms depends on the momentum of the tracks, all three are used together to achieve the highest overall tracking efficiency [186]. In each of these algorithms, the tracks are first found as circles in a two-dimensional projection onto the $x - y$ plane (as can be seen in Figure 4.1), and in a second step, the information from the third dimension is added to fit the tracks with a helix parametrization. During these steps, a particle is assumed to follow a standard helix with radius ρ and pitch k parametrized as [187]

$$\begin{aligned}x &= d_\rho \cos \phi_0 + \rho [\cos \phi_0 - \cos(\phi_0 + \phi)], \\y &= d_\rho \sin \phi_0 + \rho [\sin \phi_0 - \sin(\phi_0 + \phi)], \\z &= d_z - k \frac{\phi}{2\pi}.\end{aligned}\tag{4.1}$$

Here, ϕ_0 is the angle that defines the position of the center of the helix with respect to the pivot¹⁵, and d_ρ and d_z are the distances from the pivot to the point of closest approach \vec{x}_{pca} in the $x - y$ plane and in the z direction, respectively. The position of the particle $\vec{x} = (x, y, z)$ is then defined by the turning angle ϕ measured with respect to the center of the helix \vec{x}_{cen} . Overall, the trajectory of a particle is defined by the helix parameters $\alpha = (\rho, k, d_\rho, d_z, \phi_0)^T$ and its covariance matrix V_α . From this fit, the momentum of the particle at the point of closest approach is calculated via

$$\begin{aligned} p_x &= -QB\rho \sin \phi_0, \\ p_y &= QB\rho \cos \phi_0, \\ p_z &= QBk. \end{aligned} \tag{4.2}$$

Here, Q is the electric charge of the particle and B is the magnetic flux density in the MDC. In these fits, the particle is assumed to follow an ideal helical trajectory, but in the real detector, its trajectory is perturbed by several effects. On the one hand, there are material effects such as energy loss, which reduces the momentum of the particle, and multiple scattering, which is responsible for many small-angle deflections. These effects can be calculated using the Bethe-Bloch equation [188,189] or Molière theory [6,190], respectively. On the other hand, the non-uniformity of the magnetic field, which has been mapped using specially designed Hall sensors [21,191], must be taken into account. In addition, the wire sag, which can be estimated from the properties of the wire used [187], must be considered. All these effects are incorporated using a Kalman filter method [187,192], which uses the result of the intermediate helix parametrization in Equation (4.1) as a starting point and then updates the helix parameters to account for these effects. As a first selection step, the distance of closest approach of each of the tracks not originating from the decay of a K_s ¹⁶ meson must satisfy the conditions:

$$d_\rho < 1 \text{ cm}, \tag{4.3}$$

$$|d_z| < 10 \text{ cm}. \tag{4.4}$$

This reduces the background from particles that do not come from the e^+e^- collision, such as cosmic rays. In addition, charged tracks must satisfy a geometric condition (see Section 3.2.1) on the polar angle of

$$|\cos \theta| < 0.93 \tag{4.5}$$

¹⁵Here, the nominal interaction point, which in this case is set to $\vec{0}$, is used as the pivot.

¹⁶To determine if a track comes from the decay of a K_s , a secondary vertex fit is used, which is described in Section 4.3.

to exclude tracks that have been erroneously reconstructed in a region without detector coverage.

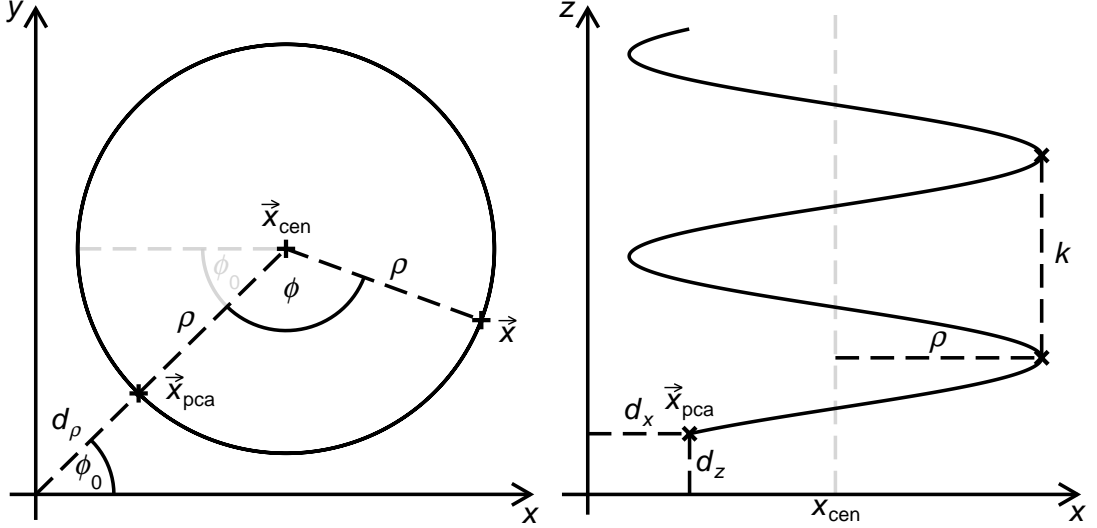


Figure 4.1.: Schematic illustration of the helix parametrization $\vec{x}(\phi)$ with radius ρ in the $x - y$ plane (left) and $x - z$ plane (right). It includes the point of closest approach \vec{x}_{pca} from the helix to the pivot and the center of the helix \vec{x}_{cen} . The distances from \vec{x}_{pca} to the pivot are $d_x = d_\rho \cos \phi_0$, $d_y = d_\rho \sin \phi_0$ and d_z in x -, y - and z -directions, respectively. ϕ_0 defines the position of \vec{x}_{cen} with respect to the pivot.

4.1.2. Particle Identification

The next step in the reconstruction process is the determination of a particle species for each of the reconstructed tracks using the PID system of BESIII. As mentioned in Section 3.2, each subdetector of the BESIII experiment can be used for particle identification. In this work, however, only the energy loss dE/dx in the MDC and the time-of-flight T_{TOF} extracted with the TOF are used, since these have the highest discriminating power for charged hadrons [151], which are the only charged particles of relevance for the analyzed channels. In both subdetectors, the difference $\chi_i(H)$ of the measured PID criterion i_{meas} from the expected value $i_{\text{exp}}(p, H)$ for a particle with momentum p of species H is calculated via:

$$\chi_i(H) = \frac{i_{\text{meas}} - i_{\text{exp}}(p, H)}{\sigma_i(p, H)} \quad \text{with } i \in \{dE/dx, T_{\text{TOF}}\}. \quad (4.6)$$

Here, the expected energy loss dE/dx_{exp} and the resolution of the energy loss $\sigma_{dE/dx}$ are calculated using a semi-empirical model [193]. This model is based on the Bethe-Bloch formula [188, 189] and is calibrated using dedicated control data samples [193]. The energy loss dE/dx_{meas} is calculated from the measured energy deposited in the MDC after accounting for several corrections [193]. These corrections include effects

due to environmental changes in the gas and the wire geometry, as well as space charge effects [193]. According to Equations (3.1) and (3.2), the expected time-of-flight $T_{\text{TOF,exp}}$ for a particle of mass m_H is given by

$$T_{\text{TOF,exp}}(p, H) = T_{\text{start}} + \frac{L}{c} \frac{\sqrt{p^2 + m_H^2 c^2}}{p}, \quad (4.7)$$

which is compared to a weighted average $T_{\text{TOF,meas}}$ of the measured time-of-flight in each of the TOF layers and each of the PMTs [151]. This weighted average takes into account the correlations between the different measurements coming from the common event start time T_{start} [155].

Finally, the PID measurements are combined to calculate a total χ_{PID}^2 via

$$\chi_{\text{PID}}^2(H) = \chi_{\text{dE/dx}}^2(H) + \chi_{T_{\text{TOF}}}^2(H), \quad (4.8)$$

which is used to calculate the so-called p -value P . The p -value indicates the probability of observing a χ^2 greater than or equal to the observed $\chi_{\text{PID}}^2(H)$, assuming the particle is of species H . Thus, a small p -value indicates that the hypothesis, that the particle is of species H , can be rejected [6]. For a χ^2 -distributed $\chi_{\text{PID}}^2(H)$ with n_{DOF} degrees of freedom the p -value is calculated according to

$$P(H) = 1 - F\left(\chi_{\text{PID}}^2(H); n_{\text{DOF}}\right). \quad (4.9)$$

Here, $n_{\text{DOF}} = 2$ corresponds to the number of independent PID criteria and $F(x; n)$ is the cumulative distribution function of a χ^2 -distributed variable x with n degrees of freedom, which is calculated via

$$F(x; n) = \frac{\gamma\left(\frac{n}{2}, \frac{x}{2}\right)}{\Gamma\left(\frac{n}{2}\right)}, \quad (4.10)$$

with the lower incomplete gamma function γ and the gamma function Γ [194].

For each charged particle, the calculated p -values are compared to assign a species $H \in \{\pi^\pm, K^\pm, p/\bar{p}\}$. This is done by requiring that the p -value $P(\pi^\pm)$ for an assumed pion is greater than the p -value for all other considered hadrons and vice versa:

$$\begin{aligned} \pi^\pm : & \quad P(\pi^\pm) > P(K^\pm) \quad \text{and} \quad P(\pi^\pm) > P(p/\bar{p}), \\ K^\pm : & \quad P(K^\pm) > P(\pi^\pm) \quad \text{and} \quad P(K^\pm) > P(p/\bar{p}), \\ p/\bar{p} : & \quad P(p/\bar{p}) > P(K^\pm) \quad \text{and} \quad P(p/\bar{p}) > P(\pi^\pm). \end{aligned} \quad (4.11)$$

In addition, a minimum p -value of 10^{-5} is required for all particles to reduce the background from track candidates that do not originate from actual particles or from particles coming from outside the detector.

After assigning a particle species to a track and calculating its momentum using Equation (4.2), its energy E can be calculated as

$$E = \sqrt{c^2(p_x^2 + p_y^2 + p_z^2) + m_H^2 c^4} = \sqrt{Q^2 B^2 c^2(\rho^2 + k^2) + m_H^2 c^4}. \quad (4.12)$$

Here, the mass m_H is taken from the PDG [6]. Thus, the total four-momentum of each of the charged tracks can be calculated and used for further analysis.

4.2. Photon Selection

Photons hitting the scintillators in the EMC produce electromagnetic showers through pair production and bremsstrahlung and can therefore be reconstructed as clusters of hits in the EMC. These clusters are identified using a cluster-finding algorithm [195] that searches for local maxima in the deposited energy of single crystals and then combines these so-called *seeds* with neighboring crystals. The energy of the shower E_{shower} is then calculated as the sum of the N highest energy losses E_i in the crystals associated with the shower. Here, N depends on the total energy of all crystals in the shower E_{total} and is defined to optimize the energy resolution [195, 196]. The shower energy E_{shower} is then corrected to account for losses in the inner part of the detector, mainly in the MDC and TOF, corresponding to about 30% of the radiation length X_0 [21]. Therefore, the deposited energy $E_{\text{TOF},j}$ in the three TOF counters closest to the path of the photon candidate is added to the deposited energy in the EMC to determine the final energy of a shower [21]:

$$E_{\text{shower}} = \sum_{i=1}^N E_i + \sum_{j=1}^3 E_{\text{TOF},j}. \quad (4.13)$$

In addition to the energy of the shower, its position \vec{x}_{shower} is calculated as a weighted sum over the positions of all crystals i in a shower via [195]

$$\vec{x}_{\text{shower}} = \frac{\sum_i W(E_i) \vec{x}_i}{\sum_i W(E_i)}. \quad (4.14)$$

Here, \vec{x}_i is the position of the crystal center on the front face and $W(E_i)$ is a logarithmic weighting function

$$W(E_i) = \max \left\{ 0, a_0 + \ln \left(\frac{E_i}{E_{\text{total}}} \right) \right\} \quad (4.15)$$

with a threshold constant a_0 calibrated using MC simulations [197].

As a first selection criterion, any shower with an energy below a certain threshold is

discarded to reduce the number of false photons due to electronic noise and radiative losses of the e^+ or e^- beam. These thresholds are defined as

$$E_{\text{shower}} > 25 \text{ MeV} \quad \text{for} \quad |\cos \theta| < 0.8, \quad (4.16)$$

$$E_{\text{shower}} > 50 \text{ MeV} \quad \text{for} \quad 0.86 < |\cos \theta| < 0.92 \quad (4.17)$$

with the ranges of the polar angle corresponding to the angular coverage of the barrel EMC and end cap EMC, respectively.

Additional general event selection criteria include a cut on the shower time T_{shower} , which is defined as the time difference between the first detection of a shower and the calculated event start time (see Section 3.2.2). This criterion removes background photons that are unrelated to the event under consideration and is defined as

$$0 \text{ ns} < T_{\text{shower}} < 700 \text{ ns}. \quad (4.18)$$

Another type of background photons come from charged particles that produce bremsstrahlung near the EMC. Since these photons are in close distance to the track of the charged particle, they can be identified by the angle α_i between the position of the shower and the extrapolated track of the charged particle i . Therefore, all photon candidates with a minimum separation angle α_{sep} smaller than 10° are rejected:

$$\alpha_{\text{sep}} = \min(\alpha_i) > 10^\circ. \quad (4.19)$$

After the charged particles and photons in an event have been identified as described above, they are combined into a final state according to the reaction being analyzed (see Chapters 5 and 6). If more than the wanted number of photons are successfully reconstructed, every combination of them is considered in the analysis. For each of the analyzed final states, different vertex and kinematic fits are performed, as described in the next section.

4.3. Vertex and Kinematic Fit

For each of the considered final states, the first analysis step consists of a vertex fit based on the Kalman filter [192,198]. The filter determines the common primary vertex of all charged tracks, which are assumed not to originate from decays of K_S mesons, since K_S mesons have a lifetime of $(8.954 \pm 0.004) \times 10^{-11}$ s [6], meaning that their decay vertex (also called *secondary vertex*) could be at a measurable distance (a few cm) from the primary vertex.

The primary vertex fit uses the two tracks with the smallest distance between their respective helices as a starting point, and then subsequently adds one of the not yet

included tracks in each of the Kalman filter steps to update the position of the primary vertex. At each step, the helix parameters of the tracks are recalculated using the updated primary vertex as the pivot [198]. After the last filter step, the position of the primary vertex and the updated helix parameters, as well as their covariance matrix, are extracted and are used for further analysis. Only events for which the primary vertex fit converges are considered for further analysis.

As mentioned above, for final states containing a K_S^0 , a secondary vertex can be identified for each K_S^0 . This is done by using a secondary vertex fit, which is again based on the Kalman filter [192, 198]. The fit takes as input the primary vertex and the helix parametrization of the two supposed daughter tracks. At the end, the fit returns a $\chi_{2\text{nd}}^2$, updated track parameters, and the flight length L of the K_S^0 . Here, L is calculated as the distance between the primary and secondary vertex and $\chi_{2\text{nd}}^2$ is a measure of how far the track parameters have been shifted. To reduce the background in final states containing a K_S , both the flight length and the $\chi_{2\text{nd}}^2$ of the secondary vertex fit are limited by

$$\chi_{2\text{nd}}^2 < 100 \quad \text{and} \quad (4.20)$$

$$L > 2\sigma_L, \quad (4.21)$$

where σ_L is the uncertainty of the determined flight length.

The next step in the analysis is a kinematic fit, which ensures that the measured four-momenta satisfy energy and momentum conservation. In the fit, the momenta of the particles in a final state are adjusted to obey the considered constraints, and the quadratic difference between the adjusted (β) and initial values (β_0) is minimized. This is done using the Lagrange multiplier method [199] by constructing the χ^2 as [151]

$$\chi^2 = (\beta - \beta_0)^T V_{\beta_0}^{-1} (\beta - \beta_0) + 2\lambda^T H(\beta). \quad (4.22)$$

Here, $\beta = (\vec{p}_1, \dots, \vec{p}_n)^T$ and $\beta_0 = (\vec{p}_{01}, \dots, \vec{p}_{0n})^T$ are the fitted and initial four-momenta of the n final state particles, respectively, and the $3n \times 3n$ covariance matrix V_{β_0} is constructed from the covariance matrices after the vertex fit. $\lambda = (\lambda_1, \dots, \lambda_r)^T$ is the vector of Lagrange multipliers λ_i , one for each of the r constraints given by $H(\beta) = (H_1(\beta), \dots, H_r(\beta))^T = 0$.

Four constraints are given by the conservation of energy and momentum between the initial state and the final state under consideration:

$$H(\beta) = \begin{pmatrix} E_{e^+e^-} \\ \vec{p}_{e^+e^-} \cdot c \end{pmatrix} - \sum_{i=1}^n \begin{pmatrix} \sqrt{p_i^2 c^2 + m_i^2 c^4} \\ \vec{p}_i \cdot c \end{pmatrix} = 0 \quad (4.23)$$

Since the e^+ and e^- collide under a small crossing angle of $\alpha_{\text{cross}} = \pm 11$ mrad [140], the e^+e^- system has a momentum in the x -direction¹⁷ of [151]

$$p_{x,e^+e^-}c = \sqrt{s} \tan \alpha_{\text{cross}} \sqrt{1 - 4 \frac{m_e^2 c^2}{s}} \approx \sqrt{s} \tan \alpha_{\text{cross}}, \quad (4.24)$$

an energy of

$$E_{e^+e^-} = \sqrt{s} \frac{1}{\cos \alpha_{\text{cross}}} \sqrt{1 - 4 \frac{m_e^2 c^2}{s} \sin^2 \alpha_{\text{cross}}} \approx \sqrt{s} \frac{1}{\cos \alpha_{\text{cross}}}, \quad (4.25)$$

and no momentum in the y - and z - direction:

$$p_{y,e^+e^-} = p_{z,e^+e^-} = 0. \quad (4.26)$$

Here, $m_e = 511 \text{ keV}/c^2$ is the mass of the electron, which is small compared to the considered center-of-mass energies \sqrt{s} justifying the approximation used in Equations (4.24) and (4.25).

Additional constraints are used for final states containing one or more $\pi^0 \rightarrow \gamma\gamma$, $\eta \rightarrow \gamma\gamma$ or $K_S \rightarrow \pi^+\pi^-$ decays, where the invariant mass of the system of the two daughter particles m_{12} is constrained to the PDG mass of the parent particle m_{PDG} :

$$m_{12}c^2 - m_{\text{PDG}}c^2 = \sqrt{(E_1 + E_2)^2 - (\vec{p}_1 + \vec{p}_2)^2 c^2} - m_{\text{PDG}}c^2 = 0. \quad (4.27)$$

To find the optimal solution for β , the χ^2 in Equation (4.22) is minimized with respect to β and λ . Since the constraints used here are nonlinear in \vec{p}_i , this can be done iteratively using a Kalman filter [192].

In the end, the fit returns the updated momenta β , an updated covariance matrix V_β , and the minimized χ^2 . It can be shown, that the diagonal elements of the updated covariance matrix are smaller than those of the initial covariance matrix [151], resulting in an improved resolution. Additionally, the resulting χ^2 can be written as a sum of r terms, one for each of the constraints [151]:

$$\chi^2 = \lambda^T H(\beta_0) = \sum_{i=1}^r \lambda_i H_i(\beta_0). \quad (4.28)$$

The terms $H_i(\beta_0)$ are a measure of how well the initial four-momenta satisfy the given constraints, and thus the χ^2 can be used to distinguish between events with the desired final state and events with additional, missing, or misidentified particles. This is done

¹⁷The x -axis is defined as the flight direction of the e^+e^- system. Together with the z axis defined as the bisector of the e^+e^- opening, the y axis is then defined to be perpendicular to both.

by placing cuts on the χ^2 of kinematic fits with different hypotheses as described in Sections 5.2 and 6.1.

5. Analysis of the Decay

$$\psi(2S) \rightarrow \gamma\eta'\pi^+\pi^-$$

In the first analysis part of this thesis, the study of the decay $\psi(2S) \rightarrow \gamma\eta'\pi^+\pi^-$ is presented. The main motivation, presented in detail in Section 2.3.3, comes from the production and subsequent decay of the P-wave charmonia χ_{cJ} , as well as the S-wave charmonium η_c via:

$$\psi(2S) \rightarrow \gamma\chi_{cJ}/\eta_c \rightarrow \gamma\eta'\pi^+\pi^-. \quad (5.1)$$

As the η' meson is short-lived, it cannot be detected directly with the BESIII detector. Therefore its two most common decays are used for reconstruction [6]:

$$\eta' \rightarrow \eta\pi^+\pi^- \quad \text{with} \quad \text{Br}(\eta' \rightarrow \eta\pi^+\pi^-) = (42.5 \pm 0.5) \%, \quad (5.2)$$

$$\eta' \rightarrow \gamma\pi^+\pi^- \quad \text{with} \quad \text{Br}(\eta' \rightarrow \gamma\pi^+\pi^-) = (29.5 \pm 0.4) \%, \quad (5.3)$$

whereby the η meson is detected in its dominant decay [6]

$$\eta \rightarrow \gamma\gamma \quad \text{with} \quad \text{Br}(\eta \rightarrow \gamma\gamma) = (39.36 \pm 0.18) \%, \quad (5.4)$$

resulting in the final states

$$\gamma(\eta \rightarrow \gamma\gamma)\pi^+\pi^-\pi^+\pi^- \quad \text{for} \quad \eta' \rightarrow \eta\pi^+\pi^-, \quad (5.5)$$

$$\gamma\gamma\pi^+\pi^-\pi^+\pi^- \quad \text{for} \quad \eta' \rightarrow \gamma\pi^+\pi^-. \quad (5.6)$$

Therefore, in total for both decay chains, each event must have two positively and two negatively charged pions, whereas each track is considered as a pion that fulfills the criteria described in Section 4.1. In addition, each event must have at least two or three photons that satisfy the conditions given in Section 4.2 for the $\eta' \rightarrow \gamma\pi^+\pi^-$ and $\eta' \rightarrow \eta\pi^+\pi^-$ channel, respectively. The reason for defining a lower bound for the number of photons, rather than imposing an exact condition, is that in most events additional photons are detected that are electronic noise, which is interpreted as a detector signal and reconstructed as a photon. In addition, cosmic radiation might produce additional background photons..

As explained in Section 4.3 for each event a kinematic fit is performed, which ensures energy and momentum conservation and improves the resolution of the measured momenta.

In the $\eta' \rightarrow \eta\pi^+\pi^-$ case the kinematic fit includes an additional constraint on the invariant mass of two of the photons, which are constrained to form an η meson. The kinematic fits are performed for each combination of photons in the event, and the combination that yields the smallest χ^2 is selected for further analysis. This includes the assignment of the photons coming from the $\eta \rightarrow \gamma\gamma$ decay, since the additional constraint in the kinematic fit gives a penalty if the assigned photons have an invariant mass far from the PDG mass of the η meson. Unless explicitly mentioned, the spectra shown below are always filled using the four-vectors after the 5C and 4C kinematic fit for the $\eta' \rightarrow \eta\pi^+\pi^-$ and $\eta' \rightarrow \gamma\pi^+\pi^-$ channel, respectively.

Having found the combination of particles that gives the smallest χ^2 , the next step is the treatment of η' combinatorics. In the $\eta' \rightarrow \eta\pi^+\pi^-$ case, each of the two π^+ and π^- is combined with the η to form an η' candidate, resulting in four possible combinations, and the one with the mass closest to the PDG mass $m_{\eta',\text{PDG}}$ of the η' is selected for the further analysis:

$$\min_{i,j \in \{1,2\}} \left| m_{\pi_i^+ \pi_j^- \eta} - m_{\eta',\text{PDG}} \right|. \quad (5.7)$$

Here, $m_{\pi_i^+ \pi_j^- \eta}$ is the invariant mass of the corresponding $\pi^+\pi^-\eta$ system. Similarly, for the $\eta' \rightarrow \gamma\pi^+\pi^-$ case, every combination of the two photons, two π^+ and two π^- is considered, giving eight combinations, and again the one with the smallest difference to the PDG value is chosen:

$$\min_{i,j,k \in \{1,2\}} \left| m_{\pi_i^+ \pi_j^- \gamma_k} - m_{\eta',\text{PDG}} \right|. \quad (5.8)$$

To estimate how often this assignment gives the correct combination, the signal MC sample with the direct decay $\psi(2S) \rightarrow \gamma\eta'\pi^+\pi^-$ is used. In this simulation, the generated values for the four-vectors of the initial pions (and the photon) can be matched to the reconstructed values and thus the true combination can be determined. This results in a misidentification rate of 0.4 % for $\eta' \rightarrow \eta\pi^+\pi^-$ and 2.3 % for $\eta' \rightarrow \gamma\pi^+\pi^-$, after considering all of the following selection criteria. It has to be noted, that this determination has an uncertainty, since the matching is not always correct. The effect of misidentification is discussed in the context of the determination of the systematic uncertainties in Section 5.6. After the combinatorial assignments according to Equations (5.7) and (5.8), the resulting spectra for the invariant mass of the η' candidates can be seen in Figure 5.1. Clear peaks at the PDG mass of the η' [6] can be seen in data, the signal MC sample and inclusive MC sample. In both channels, the inclusive MC sample slightly exceeds the data in signal and background, while the overall shape is quite well described. For the $\eta' \rightarrow \gamma\pi^+\pi^-$ channel the background shows a shape that rises from both sides towards the η' mass. This unusual shape can be explained by the procedure used for the η' combinatorics, since for events without an η' there is a high probability that at least one combination

lies close to the η' mass, which is then included in this spectrum. The background in the $\eta' \rightarrow \eta\pi^+\pi^-$ channel does not show this shape, which can be explained by the smaller number of combinations and the lower misidentification rate.

For the $\eta' \rightarrow \eta\pi^+\pi^-$ channel, the two-dimensional distribution of the invariant mass of the η candidate plotted against the invariant mass of the selected η' candidate can be seen in Figure 5.2. Here, the four-momenta are taken from before the kinematic fit, since otherwise the $\gamma\gamma$ spectrum would be a line at the η mass. It shows a significant clustering at the intersection of the lines given by the PDG masses of the corresponding particles [6]. The projection onto the $m_{\gamma\gamma}$ axis (left in Figure 5.2) shows that this peak is accompanied by a declining background.

As can be seen in Figures 5.1 and 5.2, a large number of background events are still visible after the initial event selection. In addition, the presence of background reactions contributing to the peak in the presented spectra cannot be excluded. Therefore, dedicated background studies are carried out, which are presented in the next section.

5.1. Background Analysis

In order to gain a better insight into the distribution of possible background reactions contributing to the data, and to identify and optimize corresponding selection criteria, the inclusive MC is used. The identified possible selection criteria are further discussed in Section 5.2.

For the inclusive MC the reactions leading to each event can be determined and therefore the amount of individual contributions can be estimated. For this purpose, any event that produces the correct final state and proceeds via the wanted η' (and η) decay is considered to be a signal event and all other events are classified as background. A list of

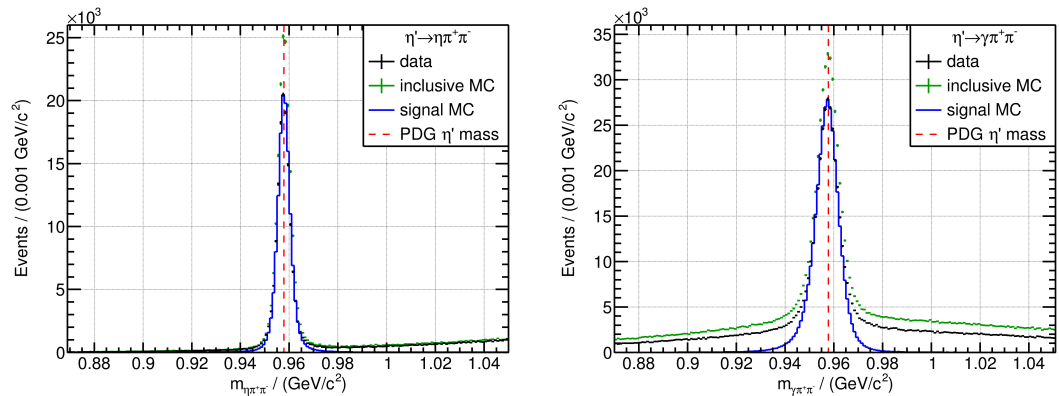


Figure 5.1.: Invariant mass spectrum of η' candidates for $\eta' \rightarrow \eta\pi^+\pi^-$ (left) and $\eta' \rightarrow \gamma\pi^+\pi^-$ (right) in data (black), inclusive MC (green) and signal MC (blue). The signal MC is scaled so that its maximum is at the same height as in the data. In all spectra clear peaks at the PDG mass [6] of the η' meson can be seen, which is marked by the red dashed line.

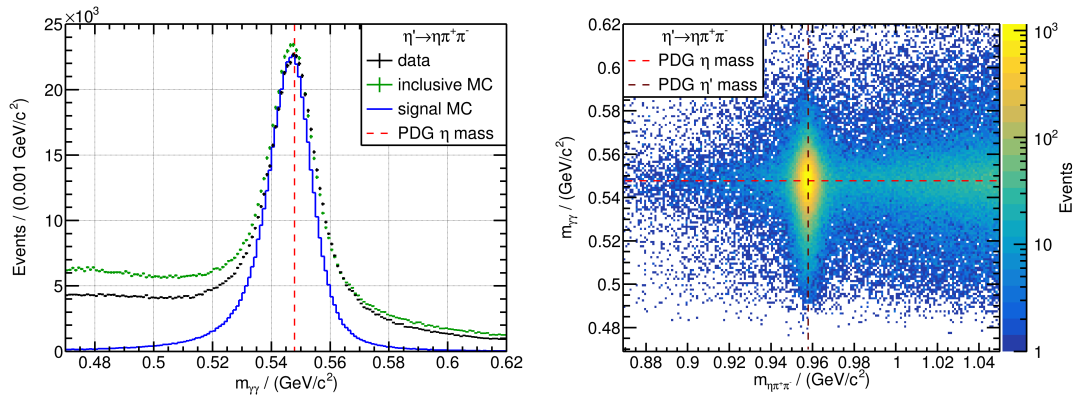


Figure 5.2.: Invariant mass spectrum of η candidates (left) and two-dimensional distribution of the invariant mass of the two-photon system $m_{\gamma\gamma}$ against the invariant mass of the $\eta\pi^+\pi^-$ system $m_{\eta\pi^+\pi^-}$ for data (right), both for the $\eta' \rightarrow \eta\pi^+\pi^-$ channel. In this case, the four-momenta from before the kinematic fit are used. The signal MC is scaled so that its maximum is at the same height as in the data. The PDG masses [6] of the η and η' mesons are marked with red and purple dashed lines, respectively.

the involved signal and background reactions after applying the general event selection criteria for the $\eta' \rightarrow \eta\pi^+\pi^-$ and $\eta' \rightarrow \gamma\pi^+\pi^-$ channel is given in Tables 5.1 and 5.2 and Tables 5.3 and 5.4, respectively. In addition, the inclusive MC can be used to plot the contributions to different spectra, which is shown for the invariant mass of η' candidates in Figures 5.3 and 5.4 and for the $\eta'\pi^+\pi^-$ system in Figures 5.5 and 5.6, respectively. As can be seen, the invariant mass spectrum of η' candidates is quite well described in both channels. However, in the $\eta'\pi^+\pi^-$ spectrum larger differences exist, especially in the mass region between $2 \text{ GeV}/c^2$ and $3 \text{ GeV}/c^2$. This is a mass region in which no sharp resonances are known, which can be produced in the analyzed decays. As will be discussed in Section 5.5 this region might actually get contributions from a number of resonances which were seen by BESIII in the reaction $J/\psi \rightarrow \gamma\eta'\pi^+\pi^-$ [25] and which are also expected to be present in the corresponding $\psi(2S)$ decay.

In both channels, the main contributions come from the reaction $\psi(2S) \rightarrow J/\psi\pi^+\pi^-$, which is the largest decay mode of the $\psi(2S)$ with a branching fraction of $(34.69 \pm 0.34) \%$ [6]. The J/ψ then decays further (via possible intermediate resonances) mainly into pions and η mesons, which are needed to produce a final state which is similar to the ones of interest. All these reactions are background reactions, except for when the J/ψ decays via $J/\psi \rightarrow \gamma\eta'$, which is the largest signal contribution in both channels. However, as we are mainly interested in the decay of resonances into $\eta'\pi^+\pi^-$, these reactions are considered as background in the following. This is particularly important in the search for the $X(1835)$ presented in Section 5.5, as the reactions $\psi(2S) \rightarrow J/\psi\pi^+\pi^-$ contribute mainly in the mass region $m_{\eta'\pi^+\pi^-} < 2 \text{ GeV}$, which can be seen in Figures 5.5 and 5.6. To reduce this background, a cut on the invariant mass $m_{\pi^+\pi^-}^{\text{rec}}$ of the system recoiling

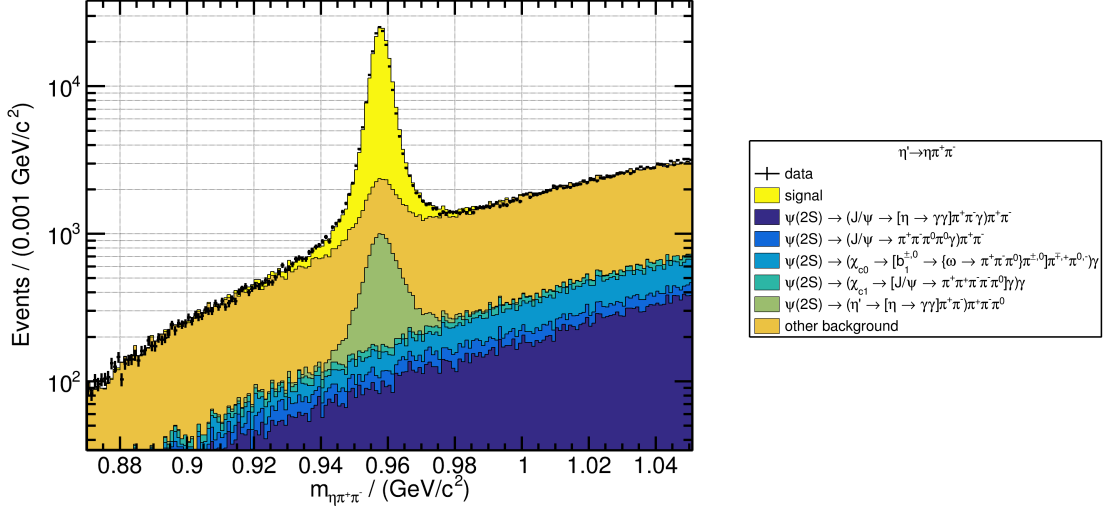


Figure 5.3.: Invariant mass spectrum of η' candidates in the $\eta' \rightarrow \eta\pi^+\pi^-$ channel for data (black) and various contributions from the inclusive MC as stacked histograms. Explicitly shown are the signal contribution, five of the largest background contributions, and the rest of the background. The inclusive MC is scaled to have the same number of events as the data over the entire range.

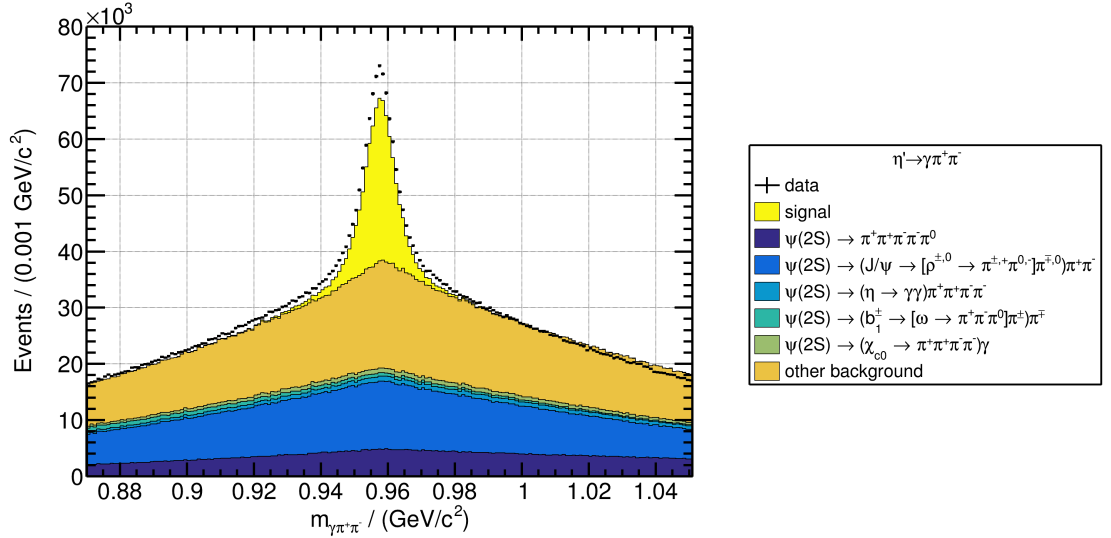


Figure 5.4.: Invariant mass spectrum of η' candidates in the $\eta' \rightarrow \gamma\pi^+\pi^-$ channel for data (black) and various contributions from the inclusive MC as stacked histograms. Explicitly shown are the signal contribution, five of the largest background contributions, and the rest of the background. The inclusive MC is scaled to have the same number of events as the data over the entire range.

against the $\pi^+\pi^-$ system is used. In addition, the J/ψ also appears in the background reactions $\psi(2S) \rightarrow \gamma(\chi_{cJ} \rightarrow \gamma[J/\psi \rightarrow \pi^+\pi^-\pi^+\pi^-])$ and $\psi(2S) \rightarrow \eta(J/\psi \rightarrow \pi^+\pi^-\pi^+\pi^-)$, which can be identified by the invariant mass of the 4π system.

It is also noteworthy that the inclusive MC includes the signal reaction $\chi_{c0} \rightarrow \eta'\pi^+\pi^-$, which is forbidden by the conservation of the J^{PC} quantum numbers. For this

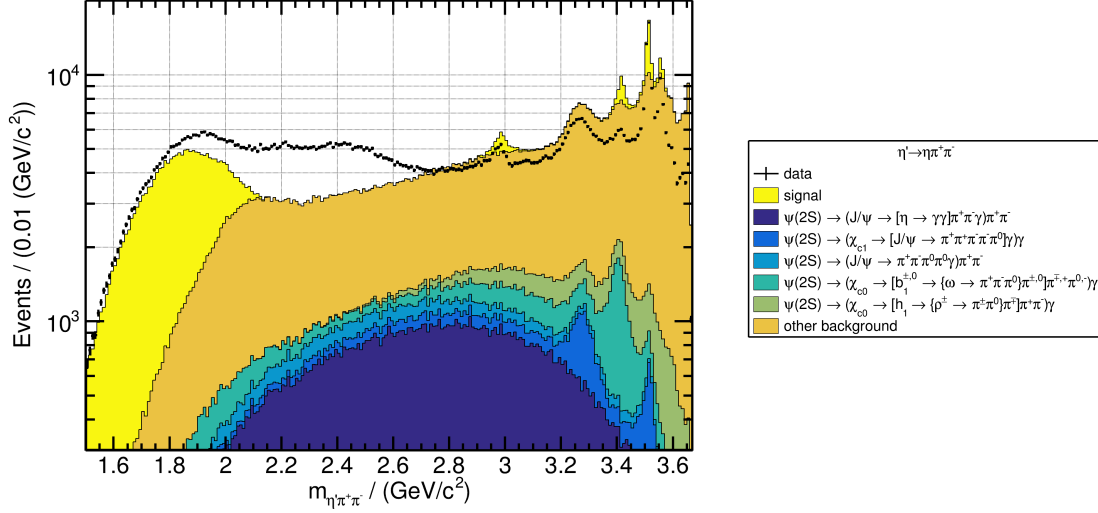


Figure 5.5.: Invariant mass spectrum of the $\eta'\pi^+\pi^-$ system in the $\eta' \rightarrow \eta\pi^+\pi^-$ channel for data (black) and various contributions from the inclusive MC as stacked histograms. Explicitly shown are the signal contribution, five of the largest background contributions, and the rest of the background. The inclusive MC is scaled to have the same number of events as the data over the entire range.

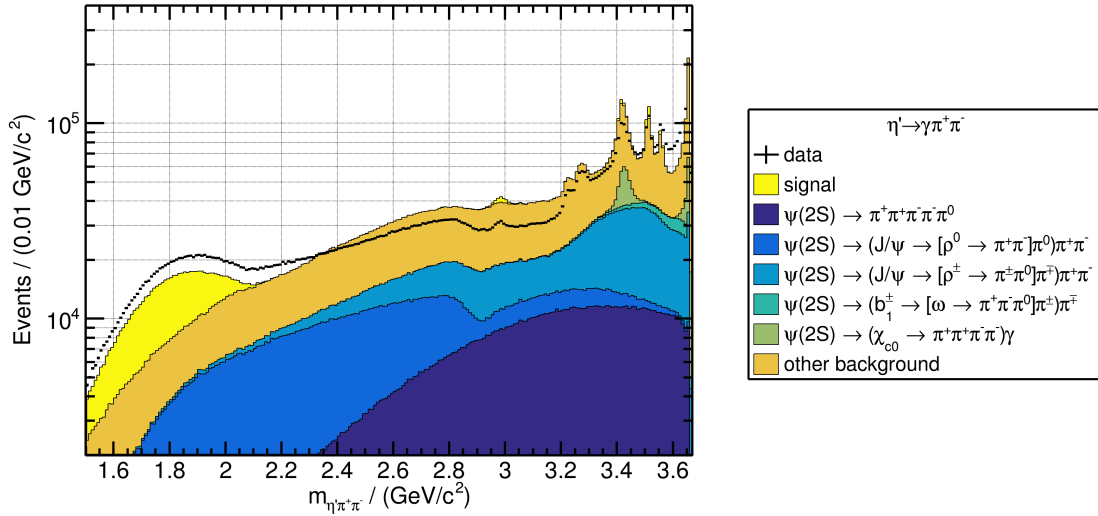


Figure 5.6.: Invariant mass spectrum of the $\eta'\pi^+\pi^-$ system in the $\eta' \rightarrow \gamma\pi^+\pi^-$ channel for data (black) and various contributions from the inclusive MC as stacked histograms. Explicitly shown are the signal contribution, five of the largest background contributions, and the rest of the background. The inclusive MC is scaled to have the same number of events as the data over the entire range.

reaction, the CLEO collaboration determined an upper limit on the branching ratio of $\text{Br}(\chi_{c0} \rightarrow \eta'\pi^+\pi^-) < 0.38 \times 10^{-3}$ at the 90% confidence level [200]. In such cases, where only an upper limit for a branching ratio exists, this value is taken as the actual

value when generating the inclusive MC. This also explains why the inclusive MC includes a large number of background events originating from reactions involving the intermediate axial vector mesons $h_1(1170)$ and $b_1(1235)$. Their corresponding branching ratios are either measured with large uncertainties or only upper limits exist [6], which seems to lead to a large overestimation of these contributions.

Overall, it can be seen that many of the background contributions include the production of unwanted neutral pions and η mesons. These background events can be reduced by placing dedicated cuts around their nominal mass for every possible $\gamma\gamma$ system. In addition, in the $\eta' \rightarrow \eta\pi^+\pi^-$ channel, these reactions often involve an additional photon in the final state. If this additional photon has been detected, such reactions can be identified by comparing the χ^2 of the nominal kinematic fit presented in Section 4.3 with a kinematic fit that includes an additional photon in its hypothesis.

Another kind of background are reactions with a missing photon compared to the number of wanted photons, such as $\psi(2S) \rightarrow \gamma(\chi_{c0} \rightarrow \pi^+\pi^-\pi^+\pi^-)$ in the $\eta' \rightarrow \gamma\pi^+\pi^-$ channel, which can be seen as the light green histogram in Figure 5.6. For such events to survive the initial event selection, a photon unrelated to the event must be reconstructed as a final state photon. As these photons are mostly low energetic, these events produce a rising structure towards the end of the available phase space at $m_{\text{end}} = m_{\psi(2S)} - E_{\gamma,\text{min}}/c^2$, where $m_{\psi(2S)}$ is the mass of the $\psi(2S)$ meson according to the PDG [6]. In order to veto these events, either the minimum photon energy $E_{\gamma,\text{min}}$ can be increased from the nominal thresholds given in Equations (4.16) and (4.17), or via another additional kinematic fit, which includes one less photon in its hypothesis.

In the next section, the identified selection criteria will be analyzed for their effectiveness and applied if found to be useful.

5.2. Background Reduction

The overall goal of the event selection is to obtain a high statistical significance of the wanted signal reaction over the remaining background. Since all applied event selection criteria will inevitably lead to a loss of efficiency for the signal reaction, this can be interpreted as an optimization problem. To find the optimal selection criteria, the inclusive MC is used to estimate the effect of the applied selection criteria. This optimization, which will be explained in detail in Section 5.2.1, relies on a good agreement between data and inclusive MC in the spectra of interest. A known problem of the BESIII simulation is the distribution of the number of photons in an event, which tend to produce too many photons. Therefore, the selection criteria that are effected by the number of photons are not included in the optimization.

The first of these selection criteria to be applied is a cut on the minimum energy of the appearing photons. While the lowest energy photon coming from the radiative

5. Analysis of the Decay $\psi(2S) \rightarrow \gamma\eta'\pi^+\pi^-$

Table 5.1.: Signal reactions with their corresponding number of events N_{reac} for the $\eta' \rightarrow \eta\pi^+\pi^-$ channel after the general event selection and the additional cut on the minimum photon energy in Equation (5.9). Shown are the contributions with more than ten events.

Nr.	Reaction	N_{reac}
1	$\psi(2S) \rightarrow (J/\psi \rightarrow [\eta' \rightarrow \{\eta \rightarrow \gamma\gamma\}\pi^+\pi^-]\gamma)\pi^+\pi^-$	173 178
2	$\psi(2S) \rightarrow (\chi_{c1} \rightarrow [\eta' \rightarrow \{\eta \rightarrow \gamma\gamma\}\pi^+\pi^-]\pi^+\pi^-)\gamma$	17 534
3	$\psi(2S) \rightarrow (\chi_{c0} \rightarrow [\eta' \rightarrow \{\eta \rightarrow \gamma\gamma\}\pi^+\pi^-]\pi^+\pi^-)\gamma$	8 791
4	$\psi(2S) \rightarrow (\eta_c \rightarrow [\eta' \rightarrow \{\eta \rightarrow \gamma\gamma\}\pi^+\pi^-]\pi^+\pi^-)\gamma$	7 314
5	$\psi(2S) \rightarrow (\chi_{c2} \rightarrow [\eta' \rightarrow \{\eta \rightarrow \gamma\gamma\}\pi^+\pi^-]\pi^+\pi^-)\gamma$	3 631
6	$\psi(2S) \rightarrow (b_1^- \rightarrow \pi^-\gamma)(\eta' \rightarrow [\eta \rightarrow \gamma\gamma]\pi^+\pi^-)\pi^+$	48
7	$\psi(2S) \rightarrow (b_1^+ \rightarrow \pi^+\gamma)(\eta' \rightarrow [\eta \rightarrow \gamma\gamma]\pi^+\pi^-)\pi^-$	44
8	$\psi(2S) \rightarrow (\eta' \rightarrow [\eta \rightarrow \gamma\gamma]\pi^+\pi^-)(\rho^0 \rightarrow \pi^+\pi^-\gamma)$	16
9	$\psi(2S) \rightarrow (\eta_c(2S) \rightarrow [\eta' \rightarrow \{\eta \rightarrow \gamma\gamma\}\pi^+\pi^-]\pi^+\pi^-)\gamma$	13
10	Other	20
Sum		210 589

Table 5.2.: Background reactions with their corresponding number of events N_{reac} for the $\eta' \rightarrow \eta\pi^+\pi^-$ channel after the general event selection and the additional cut on the minimum photon energy in Equation (5.9). Shown are the fifteen largest contributions.

Nr.	Reaction	N_{reac}
1	$\psi(2S) \rightarrow (J/\psi \rightarrow [\eta \rightarrow \gamma\gamma]\pi^+\pi^-\gamma)\pi^+\pi^-$	139 842
2	$\psi(2S) \rightarrow (\chi_{c1} \rightarrow [J/\psi \rightarrow \pi^+\pi^+\pi^-\pi^-\pi^0]\gamma)\gamma$	22 837
3	$\psi(2S) \rightarrow (J/\psi \rightarrow \pi^+\pi^-\pi^0\pi^0\gamma)\pi^+\pi^-$	21 428
4	$\psi(2S) \rightarrow (J/\psi \rightarrow [\eta \rightarrow \gamma\gamma]\pi^+\pi^-\pi^0)\pi^+\pi^-$	19 304
5	$\psi(2S) \rightarrow (\chi_{c0} \rightarrow [b_1^0 \rightarrow \{\omega \rightarrow \pi^+\pi^-\pi^0\}\pi^0]\pi^+\pi^-)\gamma$	19 184
6	$\psi(2S) \rightarrow (\chi_{c0} \rightarrow [h_1 \rightarrow \{\rho^- \rightarrow \pi^-\pi^0\}\pi^+]\pi^+\pi^-)\gamma$	18 808
7	$\psi(2S) \rightarrow (\chi_{c0} \rightarrow [h_1 \rightarrow \{\rho^+ \rightarrow \pi^+\pi^0\}\pi^-]\pi^+\pi^-)\gamma$	18 430
8	$\psi(2S) \rightarrow (J/\psi \rightarrow \pi^+\pi^+\pi^-\pi^-\pi^0)(\eta \rightarrow \gamma\gamma)$	15 657
9	$\psi(2S) \rightarrow (\chi_{c0} \rightarrow [b_1^- \rightarrow \{\omega \rightarrow \pi^+\pi^-\pi^0\}\pi^-]\pi^+\pi^0)\gamma$	15 448
10	$\psi(2S) \rightarrow (\chi_{c0} \rightarrow [b_1^+ \rightarrow \{\omega \rightarrow \pi^+\pi^-\pi^0\}\pi^+]\pi^-\pi^0)\gamma$	15 327
11	$\psi(2S) \rightarrow (J/\psi \rightarrow [\omega \rightarrow \pi^0\gamma]\pi^+\pi^-)\pi^+\pi^-$	15 100
12	$\psi(2S) \rightarrow (J/\psi \rightarrow \pi^+\pi^-\pi^0\pi^0\pi^0)\pi^+\pi^-$	13 078
13	$\psi(2S) \rightarrow (\eta' \rightarrow [\eta \rightarrow \gamma\gamma]\pi^+\pi^-)\pi^+\pi^-\pi^0$	12 770
14	$\psi(2S) \rightarrow (\chi_{c2} \rightarrow [b_1^0 \rightarrow \{\omega \rightarrow \pi^+\pi^-\pi^0\}\pi^0]\pi^+\pi^-)\gamma$	12 610
15	$\psi(2S) \rightarrow (\chi_{c1} \rightarrow [b_1^0 \rightarrow \{\omega \rightarrow \pi^+\pi^-\pi^0\}\pi^0]\pi^+\pi^-)\gamma$	12 514
16	Other	695 687
Sum		1 068 024

Table 5.3.: Signal reactions with their corresponding number of events N_{reac} for the $\eta' \rightarrow \gamma\pi^+\pi^-$ channel after the general event selection and the additional cut on the minimum photon energy in Equation (5.9). Shown are the contributions with more than ten events.

Nr.	Reaction	N_{reac}
1	$\psi(2S) \rightarrow (J/\psi \rightarrow [\eta' \rightarrow \pi^+\pi^-\gamma]\gamma)\pi^+\pi^-$	396 108
2	$\psi(2S) \rightarrow (\chi_{c1} \rightarrow [\eta' \rightarrow \pi^+\pi^-\gamma]\pi^+\pi^-)\gamma$	40 633
3	$\psi(2S) \rightarrow (\chi_{c0} \rightarrow [\eta' \rightarrow \pi^+\pi^-\gamma]\pi^+\pi^-)\gamma$	21 309
4	$\psi(2S) \rightarrow (\eta_c \rightarrow [\eta' \rightarrow \pi^+\pi^-\gamma]\pi^+\pi^-)\gamma$	18 891
5	$\psi(2S) \rightarrow (\chi_{c2} \rightarrow [\eta' \rightarrow \pi^+\pi^-\gamma]\pi^+\pi^-)\gamma$	8 330
6	$\psi(2S) \rightarrow (b_1^+ \rightarrow \pi^+\gamma)(\eta' \rightarrow \pi^+\pi^-\gamma)\pi^-$	123
7	$\psi(2S) \rightarrow (b_1^- \rightarrow \pi^-\gamma)(\eta' \rightarrow \pi^+\pi^-\gamma)\pi^+$	109
8	$\psi(2S) \rightarrow (\eta_c(2S) \rightarrow [\eta' \rightarrow \pi^+\pi^-\gamma]\pi^+\pi^-)\gamma$	40
9	$\psi(2S) \rightarrow (\eta' \rightarrow \pi^+\pi^-\gamma)(\rho^0 \rightarrow \pi^+\pi^-\gamma)$	25
10	Other	30
Sum		485 598

Table 5.4.: Background reactions with their corresponding number of events N_{reac} for the $\eta' \rightarrow \gamma\pi^+\pi^-$ channel after the general event selection and the additional cut on the minimum photon energy in Equation (5.9). Shown are the fifteen largest contributions.

Nr.	Reaction	N_{reac}
1	$\psi(2S) \rightarrow \pi^+\pi^+\pi^-\pi^-\pi^0$	1 382 428
2	$\psi(2S) \rightarrow (J/\psi \rightarrow [\rho^0 \rightarrow \pi^+\pi^-]\pi^0)\pi^+\pi^-$	1 142 984
3	$\psi(2S) \rightarrow (J/\psi \rightarrow [\rho^+ \rightarrow \pi^+\pi^0]\pi^-)\pi^+\pi^-$	853 569
4	$\psi(2S) \rightarrow (J/\psi \rightarrow [\rho^- \rightarrow \pi^-\pi^0]\pi^+)\pi^+\pi^-$	853 045
5	$\psi(2S) \rightarrow (J/\psi \rightarrow \pi^+\pi^-\pi^0)\pi^+\pi^-$	337 949
6	$\psi(2S) \rightarrow (\eta \rightarrow \gamma\gamma)\pi^+\pi^+\pi^-\pi^-$	265 621
7	$\psi(2S) \rightarrow (\chi_{c0} \rightarrow \pi^+\pi^+\pi^-\pi^-)\gamma$	218 146
8	$\psi(2S) \rightarrow (b_1^+ \rightarrow [\omega \rightarrow \pi^+\pi^-\pi^0]\pi^+)\pi^-$	121 650
9	$\psi(2S) \rightarrow (b_1^- \rightarrow [\omega \rightarrow \pi^+\pi^-\pi^0]\pi^-)\pi^+$	121 457
10	$\psi(2S) \rightarrow (\chi_{c0} \rightarrow \pi^+\pi^-[\rho^0 \rightarrow \pi^+\pi^-])\gamma$	120 495
11	$\psi(2S) \rightarrow (\chi_{c2} \rightarrow \pi^+\pi^+\pi^-\pi^-)\gamma$	109 054
12	$\psi(2S) \rightarrow (J/\psi \rightarrow [f_4(2050) \rightarrow \pi^+\pi^-]\gamma)\pi^+\pi^-$	103 890
13	$\psi(2S) \rightarrow (\chi_{c0} \rightarrow [\rho^0 \rightarrow \pi^+\pi^-][\rho^0 \rightarrow \pi^+\pi^-])\gamma$	102 281
14	$\psi(2S) \rightarrow (J/\psi \rightarrow \mu^-\mu^+)(\eta \rightarrow \pi^+\pi^-\pi^0)$	92 249
15	$\psi(2S) \rightarrow (\chi_{c1} \rightarrow \pi^+\pi^+\pi^-\pi^-)\gamma$	91 138
16	Other	3 214 833
Sum		9 130 789

$\psi(2S) \rightarrow \gamma X$ decay is that of the χ_{c2} with an energy of 128 MeV, the photons coming from the $\eta' \rightarrow \gamma\pi^+\pi^-$ and $\eta \rightarrow \gamma\gamma$ decays tend to have higher energies, as they are Lorentz-boosted due to the momentum of the decaying particle. Taking these factors into account, a cut on the minimum photon energy is set as

$$E_\gamma > 80 \text{ MeV}. \quad (5.9)$$

This cut is approximately 6σ away from the energy of the radiative photon of the reaction $\psi(2S) \rightarrow \gamma\chi_{c2}$, where σ is the width of the χ_{c2} determined in Section 5.3. This criterion is not optimized with the inclusive MC due to the mentioned problem with the generated number of photons. The next selection criterion is the comparison of the χ^2 of the nominal kinematic fit with the $\chi_{+1\gamma}^2$ of the kinematic fit with an additional photon and with the $\chi_{-1\gamma}^2$ of the kinematic fit with one less photon. This comparison is shown in Figure 5.7 for $\chi_{+1\gamma}^2$ and it can be seen, that especially in the $\eta' \rightarrow \eta\pi^+\pi^-$ channel a large number of events accumulate at $\chi_{+1\gamma}^2$ below 10. However, for the $\eta' \rightarrow \gamma\pi^+\pi^-$ channel, most of the events have a $\chi_{+1\gamma}^2$ greater than 10. These observations are consistent with the findings from Tables 5.2 and 5.4, with all reactions except numbers 1, 6, 7 and 11 for $\eta' \rightarrow \eta\pi^+\pi^-$ having additional photons, in most cases coming from the decay of π^0 mesons.

The comparison with one less photon in Figure 5.8 shows only a small number of events at low $\chi_{-1\gamma}^2$ for both channels. This can be explained by the applied cut on the minimum photon energy, which already significantly reduces the background events with a missing photon. However, especially in the $\eta' \rightarrow \gamma\pi^+\pi^-$ channel, there is still an enhancement visible at small $\chi_{-1\gamma}^2$, which corresponds to reactions 7, 10-13 and 15 in Table 5.4. For the further analysis, only the events that fulfill the selection criteria

$$\chi^2 < \chi_{+1\gamma}^2, \quad (5.10)$$

$$\chi^2 < \chi_{-1\gamma}^2 \quad (5.11)$$

are considered. These criteria are also marked as red lines in Figures 5.7 and 5.8, where all events, which lie below these lines, are excluded.

5.2.1. Multidimensional Cut Optimization

To optimize the remaining selection criteria, a multidimensional optimization of the signal significance over the background is performed. To do this, a figure of merit $\mathcal{F}(\xi)$ is defined

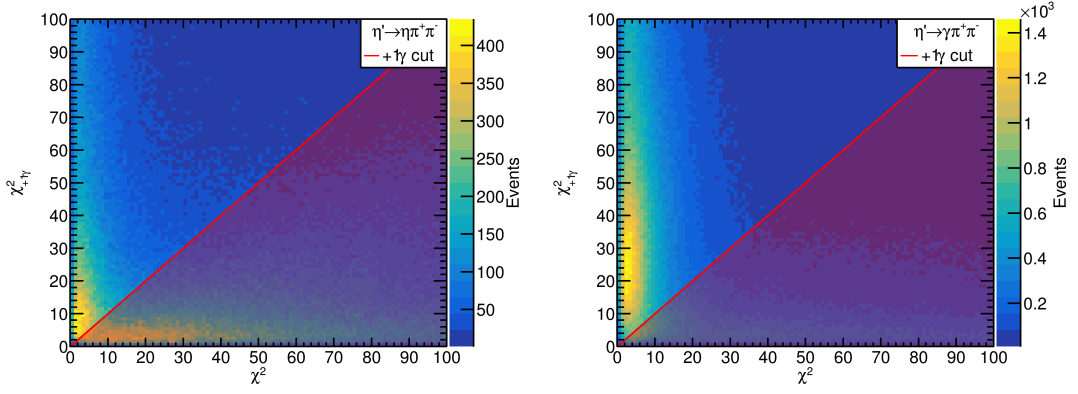


Figure 5.7.: Two-dimensional distribution of the $\chi^2_{+1\gamma}$ of the kinematic fit with one additional photon plotted against the χ^2 of the nominal fit for the $\eta' \rightarrow \eta\pi^+\pi^-$ channel (left) and the $\eta' \rightarrow \gamma\pi^+\pi^-$ channel (right) in the data. The applied cut is marked with the red line and all events below this line are discarded.

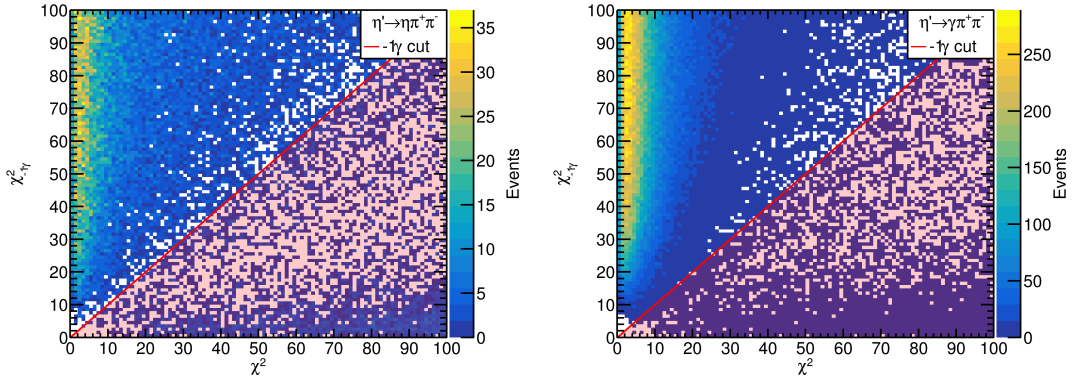


Figure 5.8.: Two-dimensional distribution of the $\chi^2_{-1\gamma}$ of the kinematic fit with one less photon plotted against the χ^2 of the nominal fit for the $\eta' \rightarrow \eta\pi^+\pi^-$ channel (left) and the $\eta' \rightarrow \gamma\pi^+\pi^-$ channel (right) in the data. The applied cut is marked with the red line and all events below this line are discarded.

that depends on the predicted number of signal events $N_S(\xi)$ and background events $N_B(\xi)$ that survive a set of selection criteria ξ :

$$\mathcal{F}(\xi) = \frac{N_S(\xi)}{\sqrt{N_S(\xi) + N_B(\xi)}}. \quad (5.12)$$

Here, the denominator is the predicted statistical uncertainty of the remaining sample assuming a Poisson-distributed number of signal and background events [201]. The number of signal and background events is estimated from the inclusive MC. To obtain the optimal solution for ξ , Equation (5.12) is maximized using MINUIT [202] and the

resulting values for the selection criteria ξ are used for further analysis¹⁸. For both channels the considered selection criteria ξ include a χ^2 cut, a veto on the background resonances $\pi^0 \rightarrow \gamma\gamma$ and $\psi(2S) \rightarrow J/\psi\pi^+\pi^-$, and a signal region around the η' resonances. In addition, for the $\eta' \rightarrow \gamma\pi^+\pi^-$ channel, a veto on the background processes $\eta \rightarrow \gamma\gamma$, $\omega \rightarrow \gamma\pi^0$ and $J/\psi \rightarrow \pi^+\pi^-\pi^+\pi^-$ and a signal region for $\rho^0 \rightarrow \pi^+\pi^-$ are examined. For each of the resonances the selection criterion is defined symmetrically around the mass of the particle given by the PDG [6]. These criteria and the resulting optimized values are discussed next.

To reduce the background with additional, missing, or misidentified particles the χ^2 of the kinematic fit, is limited by

$$\chi_{5C}^2 < 81.4 \quad \text{for} \quad \eta' \rightarrow \eta\pi^+\pi^-, \quad (5.13)$$

$$\chi_{4C}^2 < 27.8 \quad \text{for} \quad \eta' \rightarrow \gamma\pi^+\pi^-. \quad (5.14)$$

The χ^2 distributions with the resulting cuts are plotted in Figure 5.9. It can be seen that the inclusive MC describes the shape of the data quite well, while the signal MC gives much smaller values on average.

The background containing unwanted π^0 and η resonances can be reduced by looking at the invariant mass spectrum of each combination of two photons measured in an event. This is shown in Figure 5.10 and for both channels the data and the inclusive MC show clear peaks at the mass of the π^0 and η . For the $\eta' \rightarrow \gamma\pi^+\pi^-$ channel there is also a peak slightly below the ω mass, which comes from the decay $\omega \rightarrow \gamma\pi^0$. This decay produces a peak in the $\gamma\gamma$ spectrum for events where one of the three photons coming from the decay

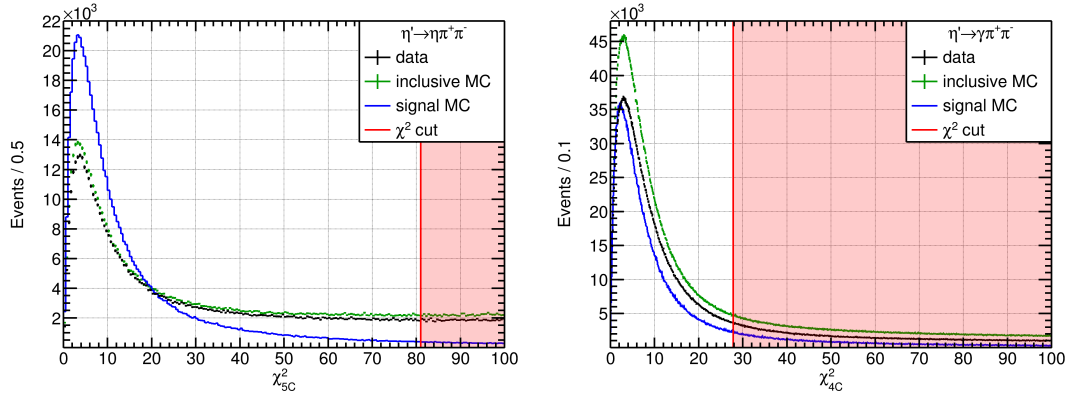


Figure 5.9.: χ^2 distribution for the $\eta' \rightarrow \eta\pi^+\pi^-$ channel (left) and the $\eta' \rightarrow \gamma\pi^+\pi^-$ channel (right) for data in black, the inclusive MC in green and the signal MC in blue. The signal MC is arbitrarily scaled. Additionally, the optimized cut is shown as the red line and the vetoed region is shown as the red shaded area.

¹⁸In the context of this thesis an alternative method for background rejection was tested, which is presented in Appendix C.

is low energetic and is discarded by the event selection procedure. This also explains why the peak is shifted towards lower masses. In the $\eta' \rightarrow \eta\pi^+\pi^-$ channel, the step at $\sim 440 \text{ MeV}/c^2$ in the $\gamma\gamma$ invariant mass comes from background events without an $\eta \rightarrow \gamma\gamma$ decay, which was verified using the inclusive MC sample. The optimization shows that vetoes on all resonances appearing in the $\gamma\gamma$ spectrum actually decrease the overall figure of merit, so no veto is applied here. This can be explained by the fact, that these background reactions can also be suppressed by the cuts on χ_{5C}^2 and $\chi_{+1\gamma}^2$, but also on $m_{\pi^+\pi^-}^{\text{rec}}$, as many of them involve a J/ψ decay. In addition, a veto here would lead to a significant loss of efficiency due to the large number of photon combinations, with a high probability, that at least one of them falls into the veto region by chance.

To reduce the amount of J/ψ background, the invariant mass of the system recoiling against the $\pi^+\pi^-$ system $m_{\pi^+\pi^-}^{\text{rec}}$ is vetoed in a region around the mass of the J/ψ given by the PDG [6]. In both channels, the optimized veto region is given by

$$\left| m_{\pi^+\pi^-}^{\text{rec}} - m_{J/\psi, \text{PDG}} \right| > 20 \text{ MeV}/c^2, \quad (5.15)$$

as shown in Figure 5.11.

As the kinematic limit is lower in the $\eta' \rightarrow \gamma\pi^+\pi^-$ channel, additional peaks are visible at the masses of the η and ω mesons. These come from the reactions $\psi(2S) \rightarrow (J/\psi \rightarrow \mu^+\mu^-)(\eta \rightarrow \pi^+\pi^-\pi^0)$, where the muons are misidentified as pions, and $\psi(2S) \rightarrow \pi^+\pi^-(\omega \rightarrow \pi^+\pi^-\pi^0)$. As these reactions are only small contributions and do not contain an η' or any of the searched resonances in the $\eta'\pi^+\pi^-$ system, no veto is placed on their masses in the $m_{\pi^+\pi^-}^{\text{rec}}$ spectrum.

The second spectrum that shows a contribution from a J/ψ is the invariant mass of the 4π

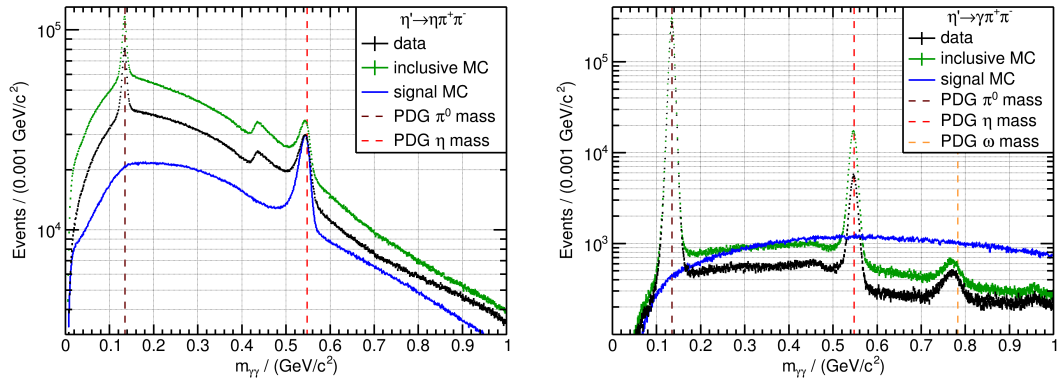


Figure 5.10.: Invariant mass spectrum of each combination of two photons, for the $\eta' \rightarrow \eta\pi^+\pi^-$ channel (left) and the $\eta' \rightarrow \gamma\pi^+\pi^-$ channel (right). The data is shown in black, the inclusive MC in green and the signal MC in blue. The masses of the appearing resonances, according to the PDG [6], are marked as dashed lines.

5. Analysis of the Decay $\psi(2S) \rightarrow \gamma\eta'\pi^+\pi^-$

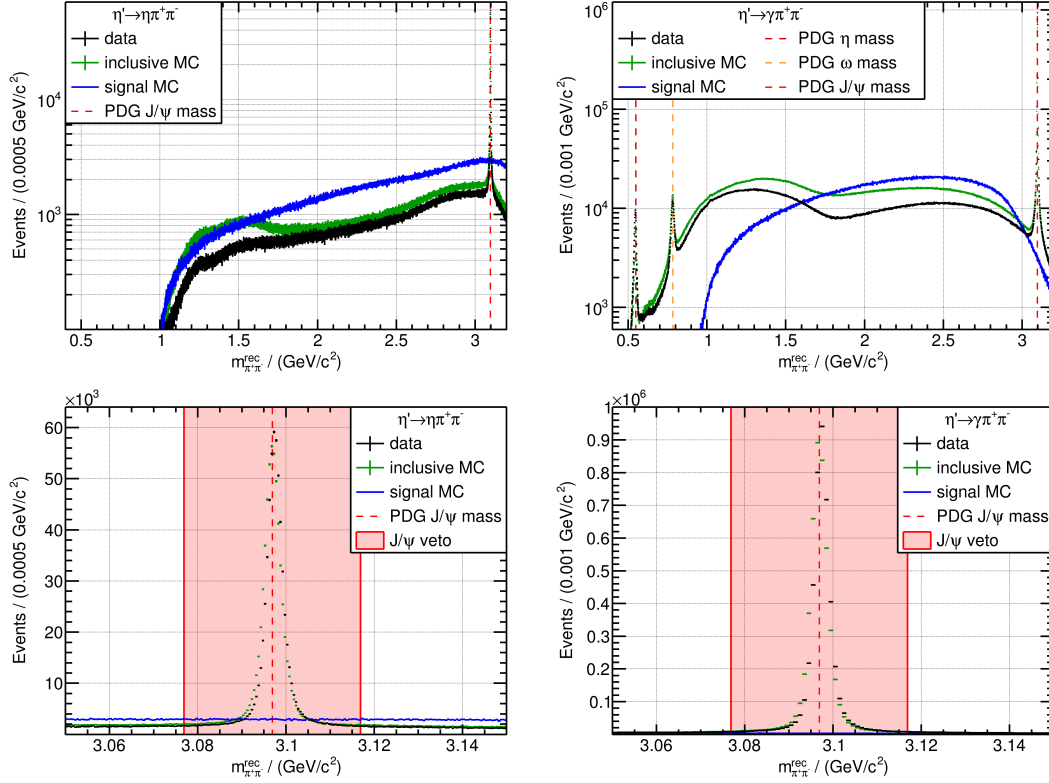


Figure 5.11.: Invariant mass $m_{\pi^+\pi^-}^{\text{rec}}$ of the system recoiling against the $\pi^+\pi^-$ system for the $\eta' \rightarrow \eta\pi^+\pi^-$ channel (left) and the $\eta' \rightarrow \gamma\pi^+\pi^-$ channel (right) in a wide range (top) and around the J/ψ peak (bottom). The data is shown in black, the inclusive MC in green and the signal MC in blue. The PDG masses [6] of the visible resonances are indicated as dashed lines while the veto region around the J/ψ peak is marked by the red solid lines. The spectrum for the signal MC is arbitrarily scaled, but with the same factor for the top and bottom spectra.

system in the $\eta' \rightarrow \gamma\pi^+\pi^-$ channel, depicted in Figure 5.12. In this case, the optimization results in a veto region of

$$\left| m_{\pi^+\pi^-\pi^+\pi^-} - m_{J/\psi, \text{PDG}} \right| > 20 \text{ MeV}/c^2. \quad (5.16)$$

In the $\eta' \rightarrow \eta\pi^+\pi^-$ channel no J/ψ can be seen, which can be explained by the cut on the minimum photon energy, since this limits the available phase space in the 4π system to below the J/ψ mass. In this channel, however, the data shows a small enhancement at the mass of the axial vector meson $f_1(1285)$, which is neglected. In addition, the inclusive MC shows a clear peak at the mass of the $\eta(1405)$, which is a candidate for the first radial excitation of the η' or the lightest pseudoscalar glueball [203]. For the $\eta(1405) \rightarrow \rho\rho \rightarrow 4\pi$ decay, only an upper limit of 58% has been determined [204], and the contribution is overestimated in the inclusive MC as there is no visible enhancement in the data. The enhancement between $1 \text{ GeV}/c^2$ to $2 \text{ GeV}/c^2$ in the $\eta' \rightarrow \gamma\pi^+\pi^-$ comes from the reaction $\psi(2S) \rightarrow J/\psi\pi^+\pi^-$.

For the $\eta' \rightarrow \gamma\pi^+\pi^-$ channel, the invariant mass spectrum of the $\pi^+\pi^-$ system from the

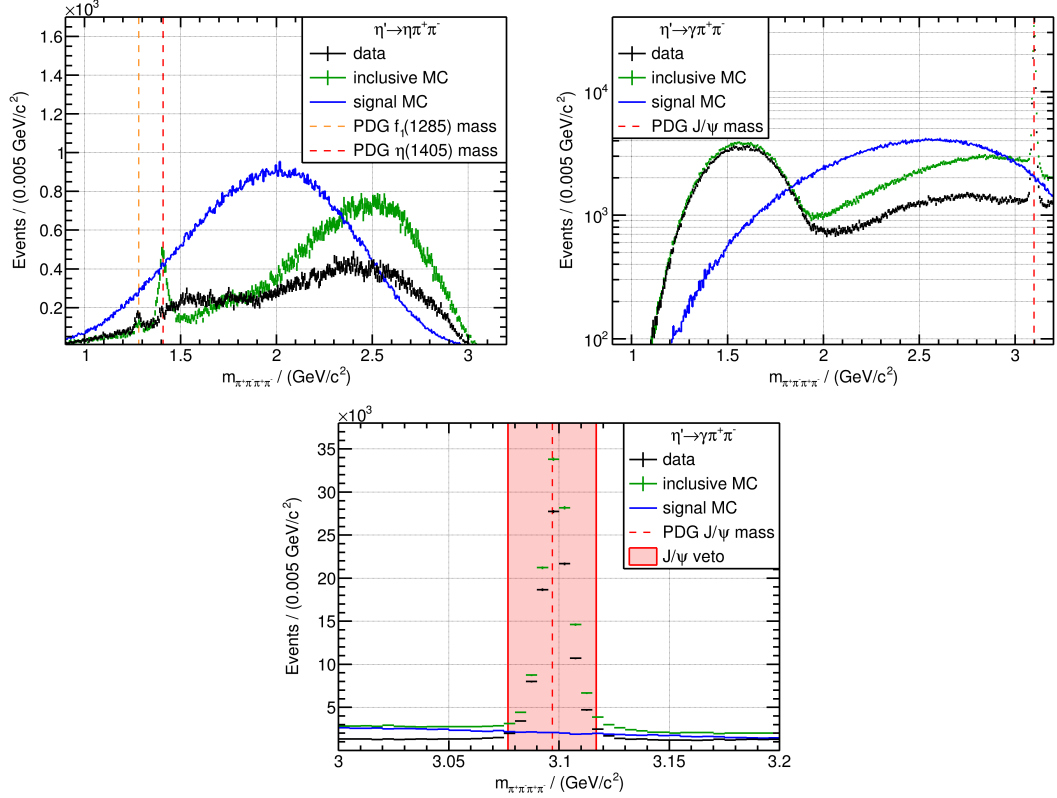


Figure 5.12.: Invariant mass $m_{\pi^+\pi^-\pi^+\pi^-}$ of the 4π system for the $\eta' \rightarrow \eta\pi^+\pi^-$ channel (left) and the $\eta' \rightarrow \gamma\pi^+\pi^-$ channel (right) in a wide range (top) and around the J/ψ peak (bottom). The data is shown in black, the inclusive MC in green and the signal MC in blue. The masses of the appearing resonances, according to the PDG [6], are indicated as dashed lines and the veto around the J/ψ peak is marked by the red solid lines.

η' decay, depicted in Figure 5.13, is another way of increasing the signal significance. This is due to the fact that the decay $\eta' \rightarrow \gamma\pi^+\pi^-$ dominantly occurs via an intermediate ρ^0 , which is not easily distinguishable from the direct decay. The data and the inclusive MC show a similar behavior, with a distribution that peaks slightly below the ρ^0 mass. The signal MC shows a clear peak at the ρ^0 mass, which can be explained by the model used to generate the decay $\eta' \rightarrow \gamma\pi^+\pi^-$ (see Section 3.5). The structure at low $m_{\pi^+\pi^-}$ again comes from the background reaction $\psi(2S) \rightarrow J/\psi\pi^+\pi^-$, which limits the phase space of the $\pi^+\pi^-$ system to $m_{\psi(2S)} - m_{J/\psi} = 589 \text{ MeV}/c^2$. The optimization yields a cut window of

$$\left| m_{\pi^+\pi^-} - m_{\rho^0, \text{PDG}} \right| < 198 \text{ MeV}/c^2. \quad (5.17)$$

The last selection criterion considered is that of a signal region around the η' resonances

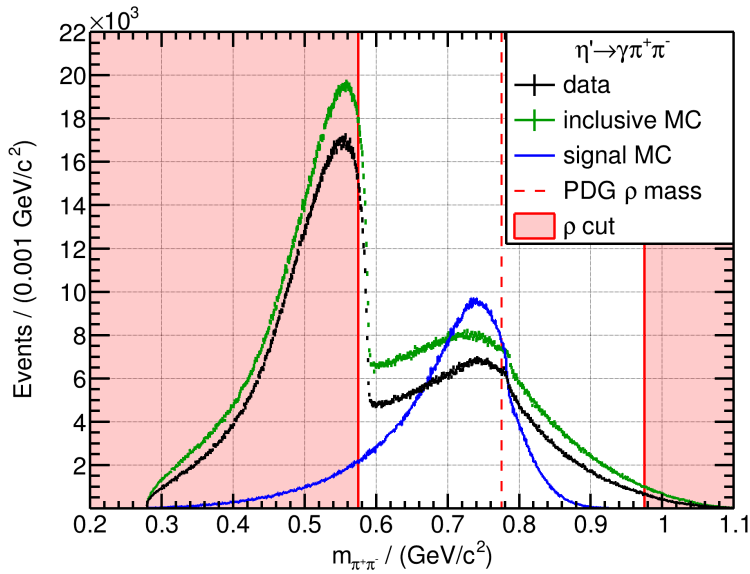


Figure 5.13.: Invariant mass of the $\pi^+\pi^-$ system resulting from the $\eta' \rightarrow \gamma\pi^+\pi^-$ decay. The data is shown in black, the inclusive MC in green and the signal MC in blue. The mass of the ρ^0 , according to the PDG [6], is indicated as a dashed line and the selection around it is marked with the red solid lines.

to reduce the amount of non- η' background, resulting in

$$\left| m_{\eta\pi^+\pi^-} - m_{\eta',\text{PDG}} \right| < 9.3 \text{ MeV}/c^2 \quad \text{for } \eta' \rightarrow \eta\pi^+\pi^-, \quad (5.18)$$

$$\left| m_{\gamma\pi^+\pi^-} - m_{\eta',\text{PDG}} \right| < 10.1 \text{ MeV}/c^2 \quad \text{for } \eta' \rightarrow \gamma\pi^+\pi^-. \quad (5.19)$$

However, a simple cut, is not sufficient to remove the background which lies below the resonance itself. Therefore, a more sophisticated method is presented in the next section.

5.2.2. Sideband Subtraction

To remove the background in the data that does not contain an η' , a sideband subtraction method is applied. This method is based on the assumption that any non- η' background behaves similarly in the η' signal region and in the so-called sidebands. If this assumption holds, the non- η' background in the η' signal region can be estimated from events in the sidebands. The sideband regions are defined in the invariant mass of the η' candidate. This is shown in Figures 5.14 and 5.15 for the $\eta' \rightarrow \eta\pi^+\pi^-$ and $\eta' \rightarrow \gamma\pi^+\pi^-$ channels, respectively.

The signal region is defined by the optimal value obtained from the optimization given in Equations (5.18) and (5.19). The sidebands are chosen so that they are far enough away from the η' signal and do not contain any signal, in this case a distance between the

signal and sideband regions of $\Delta_m = 40 \text{ MeV}$ is chosen. This results in the definition of the sidebands for the $\eta' \rightarrow \eta\pi^+\pi^-$ channel as

$$\text{left: } m_{\eta\pi^+\pi^-} \in [0.8992 \text{ MeV}/c^2, 0.9085 \text{ MeV}/c^2], \quad (5.20)$$

$$\text{right: } m_{\eta\pi^+\pi^-} \in [1.0071 \text{ MeV}/c^2, 1.0163 \text{ MeV}/c^2], \quad (5.21)$$

and for the $\eta' \rightarrow \gamma\pi^+\pi^-$ channel as

$$\text{left: } m_{\gamma\pi^+\pi^-} \in [0.8976 \text{ MeV}/c^2, 0.9077 \text{ MeV}/c^2], \quad (5.22)$$

$$\text{right: } m_{\gamma\pi^+\pi^-} \in [1.0079 \text{ MeV}/c^2, 1.0180 \text{ MeV}/c^2]. \quad (5.23)$$

According to the signal MC sample the sidebands chosen this way include less than 0.3% of the signal. The signal region is marked with a green box and the sideband regions are marked with blue boxes in Figures 5.14 and 5.15. Since the background in both channels is not constant, the events in the sideband regions must be weighted to obtain an accurate estimate for the signal region.

To determine the weights, the invariant mass spectra of the η' candidates are fitted using the method of least squares. In the fit, the model function consists of a sum of the signal and background contribution $\mathcal{M}(m) = \mathcal{S}(m) + \mathcal{B}(m)$. In both channels the signal is described by a sum of two Gaussian functions with the same mean m_{peak} :

$$\mathcal{S}(m) = N_{\text{obs}} \left[\frac{f}{\sqrt{2\pi}\sigma_1} \exp\left(-\frac{(m - m_{\text{peak}})^2}{2\sigma_1^2}\right) + \frac{1-f}{\sqrt{2\pi}\sigma_2} \exp\left(-\frac{(m - m_{\text{peak}})^2}{2\sigma_2^2}\right) \right]. \quad (5.24)$$

Here, N_{obs} is the number of signal events, f is the ratio of events in the first Gaussian compared to the total number of signal events and σ_1 and σ_2 are the widths of the two Gaussians. This model is chosen to account for the resolution of the detector, which is significantly larger than the natural width of the η' of $\Gamma_{\eta', \text{PDG}} = (0.188 \pm 0.006) \text{ MeV}$ [6], as can be seen in Table 5.5. For the $\eta' \rightarrow \eta\pi^+\pi^-$ channel the background is rising smoothly towards higher invariant masses, which is described by a second order polynomial¹⁹:

$$\mathcal{B}_{\eta' \rightarrow \eta\pi^+\pi^-}(m) = a_0 + a_1 (m - m_{\eta', \text{PDG}}) + a_2 (m - m_{\eta', \text{PDG}})^2. \quad (5.25)$$

For the $\eta' \rightarrow \gamma\pi^+\pi^-$ channel, the background rises in both directions towards the η' mass, which results from the chosen method of determining the best η' combination (see Equation (5.8)). This shape is reproduced by the inclusive MC with only small deviations,

¹⁹Here and in the following the background polynomials are always shifted by a typical value of the spectra it describes. This is in most cases the mass of the fitted resonances. This way correlations between the background parameters are reduced.

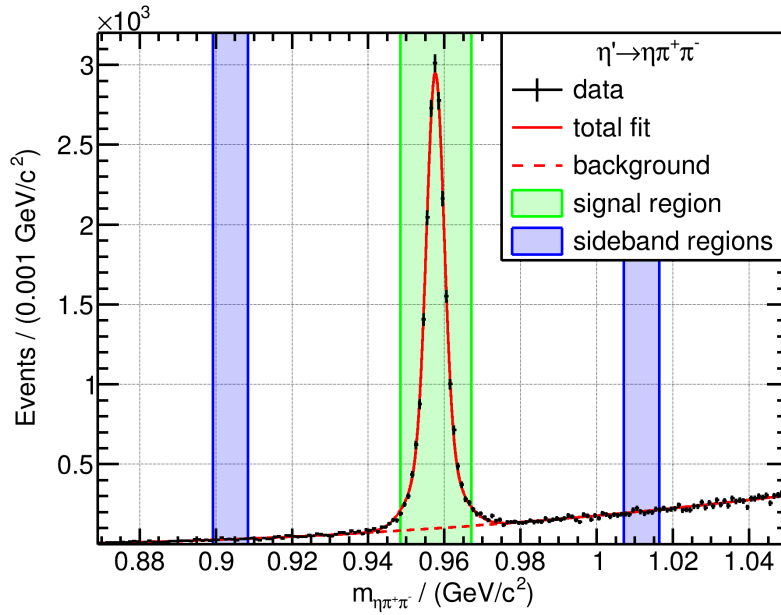


Figure 5.14.: Invariant mass of the $\eta\pi^+\pi^-$ system, with the definition of the signal and sideband regions. The data is shown as black dots with uncertainties, the total fit is shown as a solid red line, and the background component as a dashed red line. The signal and sideband regions are indicated by green and blue boxes, respectively. The fit is described in the text and the resulting parameters are listed in Table 5.5.

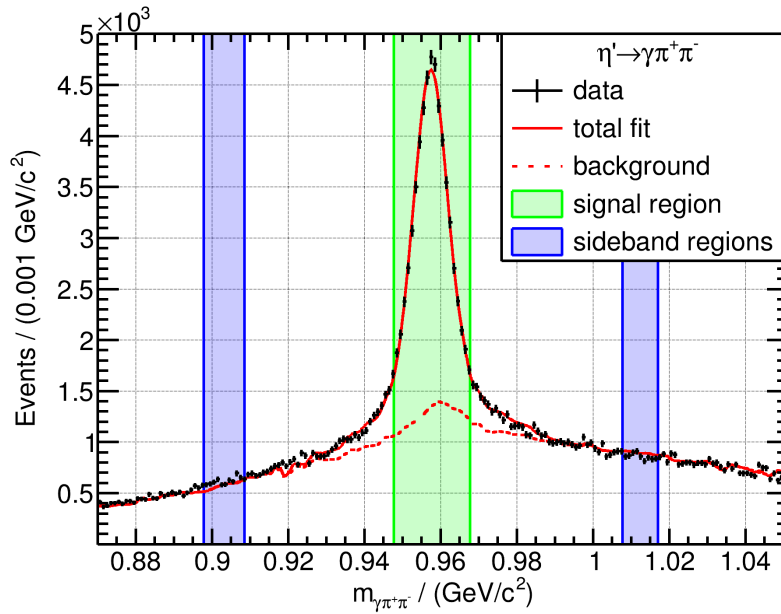


Figure 5.15.: Invariant mass of the $\gamma\pi^+\pi^-$ system, with the definition of the signal and sideband regions. The data is shown as black dots with uncertainties, the total fit is shown as the solid red line and the background component as a dashed red line. The signal and sideband regions are marked with green and blue boxes, respectively. The fit is described in the text and the resulting parameters are listed in Table 5.5.

so it is used to describe the background in the fit to the data. To account for the slightly different slope, an additional linear function is added to the background function:

$$\mathcal{B}_{\eta' \rightarrow \gamma \pi^+ \pi^-}(m) = b \cdot \text{INCL}(m) + a_0 + a_1 (m - m_{\eta', \text{PDG}}). \quad (5.26)$$

Here, $\text{INCL}(m)$ is the histogram of the $\gamma \pi^+ \pi^-$ invariant mass for the inclusive MC background after applying the smoothing algorithm 353QH TWICE [205] five times and b is a scaling factor. The resulting fits are displayed in Figures 5.14 and 5.15 as a red solid line and the corresponding background component as a red dashed line. The fitted parameters are listed in Table 5.5. As can be seen, the fit describes the data well in both channels with a $\chi^2 / \text{ndf} = 1.00$ in the $\eta' \rightarrow \eta \pi^+ \pi^-$ channel and $\chi^2 / \text{ndf} = 1.73$ in the $\eta' \rightarrow \gamma \pi^+ \pi^-$ channel. The difference in the $\eta' \rightarrow \gamma \pi^+ \pi^-$ channel comes mainly from the background to the left of the peak. In both channels the fit gives a peak position that is smaller than the value taken from the PDG $m_{\eta', \text{PDG}} = (957.78 \pm 0.06) \text{ MeV}/c^2$ [6], considering only the statical uncertainties. However, the difference is explainable by the detector resolution (see Table 3.2), which is on the order of a few MeV/c^2 considering that four charged tracks are reconstructed.

Using the background contribution $\mathcal{B}(m)$ of the fits, the weights of the sidebands are calculated according to

$$w_{l,r} = \int_{m_{l,r}^{\min}}^{m_{l,r}^{\max}} \mathcal{B}(m) dm \cdot \left(\int_{m_{\text{signal}}^{\min}}^{m_{\text{signal}}^{\max}} \mathcal{B}(m) dm \right)^{-1}, \quad (5.27)$$

where $m_i^{\min, \max}$ are the minimum and maximum of the corresponding signal or sideband regions defined in Equations (5.18) to (5.23). For further analysis, the events in the sidebands are subtracted from the events in the signal region weighted by their respective factor. This can be seen for the $\eta' \pi^+ \pi^-$ spectrum in Figure 5.16, where clear peaks are visible at the invariant mass of the η_c , χ_{c1} and χ_{c2} . In addition, an enhancement can be seen in the mass region below $2 \text{ GeV}/c^2$, which can be associated with the $X(1835)$. One disadvantage of the sideband subtraction procedure is that it can produce a negative number of events in certain bins. This can happen due to statistical fluctuations or if the assumption that the background behaves similar in the signal and sideband regions is not fulfilled. In this case, for both channels negative event numbers are indeed observed. However, these are explainable by statistical fluctuations and are therefore no problem for the further analysis.

As clear peaks are observed at the masses of expected charmonia, the contents of these can be used to determine their corresponding branching ratios, which will be presented in the next section.

5. Analysis of the Decay $\psi(2S) \rightarrow \gamma\eta'\pi^+\pi^-$

Table 5.5.: Parameters of the fits to the invariant mass of the η' candidate and the resulting weighting factors. The uncertainties are statistical only.

	$\eta' \rightarrow \eta\pi^+\pi^-$	$\eta' \rightarrow \gamma\pi^+\pi^-$
Observed Events N_{obs}	$20\,256 \pm 158$	$46\,506 \pm 656$
Mass $m_{\text{peak}} / (\text{MeV}/c^2)$	957.621 ± 0.023	957.245 ± 0.040
Factor $f / \%$	67.4 ± 2.2	67.6 ± 1.5
Width $\sigma_1 / (\text{MeV}/c^2)$	2.271 ± 0.048	4.335 ± 0.075
Width $\sigma_2 / (\text{MeV}/c^2)$	5.77 ± 0.24	14.66 ± 0.97
$a_0 / \text{a.u.}$	97.7 ± 0.9	247.1 ± 13.3
$a_1 / \text{a.u.}$	1620 ± 16	-346 ± 18
$a_2 / \text{a.u.}$	6745 ± 166	
$b / \text{a.u.}$		1.123 ± 0.009
χ^2 / ndf	$192.41 / 192 = 1.00$	$607.78 / 352 = 1.73$
Weight w_1	3.26	2.22
Weight w_r	0.48	1.42

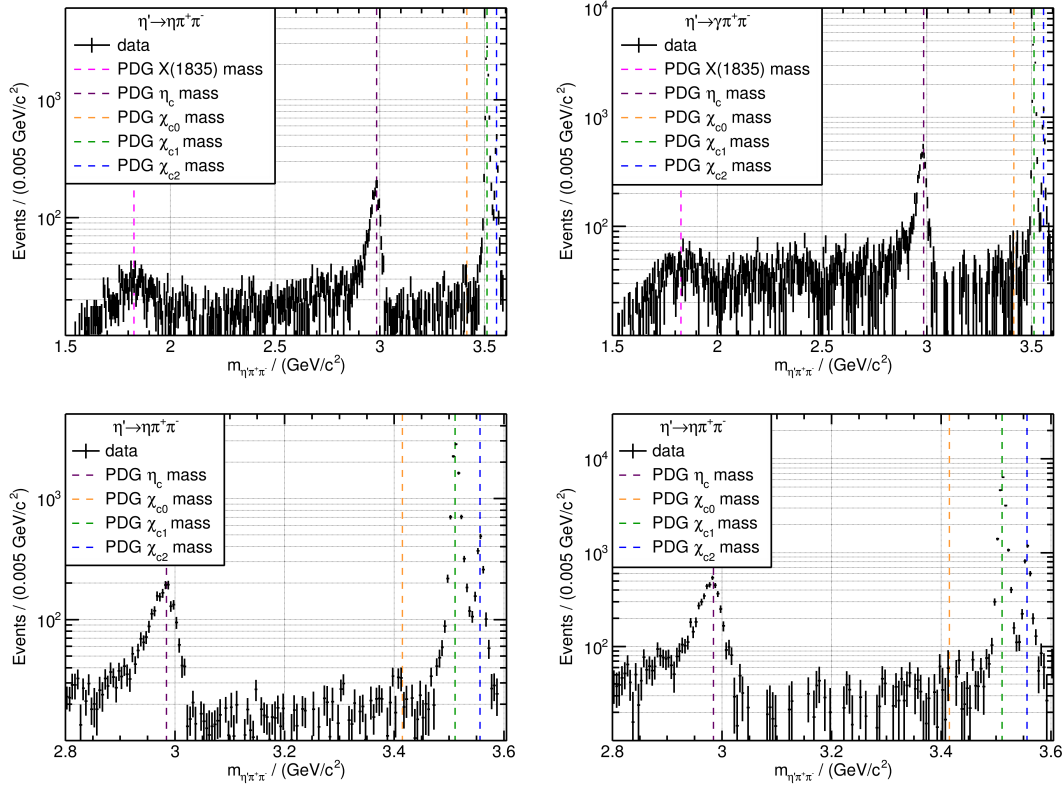


Figure 5.16.: Invariant mass of the $\eta'\pi^+\pi^-$ system for the $\eta' \rightarrow \eta\pi^+\pi^-$ channel (left) and the $\eta' \rightarrow \gamma\pi^+\pi^-$ channel (right) over the whole range (top) and as a zoom into the charmonium region (bottom). The data is shown in black and the masses of appearing resonances, according to the PDG [6], are indicated as colored dashed lines.

5.3. Determination of $\chi_{cJ} \rightarrow \eta' \pi^+ \pi^-$ Branching Ratios

The branching ratios of the χ_{cJ} can be calculated according to

$$\text{Br}(\chi_{cJ} \rightarrow \eta' \pi^+ \pi^-) = \frac{N_{\chi_{cJ} \rightarrow \eta' \pi^+ \pi^-}}{N_{\chi_{cJ}}}, \quad (5.28)$$

where $N_{\chi_{cJ}}$ is the number of produced χ_{cJ} which is calculated as

$$N_{\chi_{cJ}} = N_{\psi(2S)} \cdot \text{Br}(\psi(2S) \rightarrow \gamma \chi_{cJ}), \quad (5.29)$$

from the number of recorded $\psi(2S)$ events and the branching ratio for the corresponding radiative decay. The number $N_{\chi_{cJ} \rightarrow \eta' \pi^+ \pi^-}$ of χ_{cJ} decaying into $\eta' \pi^+ \pi^-$ can be extracted by fitting the data, after taking into account the efficiency of the analysis procedure ε and the branching ratios of the subsequent decays $\text{Br}_{\text{sub}} = \text{Br}(\eta' \rightarrow \eta \pi^+ \pi^-) \cdot \text{Br}(\eta \rightarrow \gamma \gamma)$ for the $\eta' \rightarrow \eta \pi^+ \pi^-$ channel and $\text{Br}_{\text{sub}} = \text{Br}(\eta' \rightarrow \gamma \pi^+ \pi^-)$ for the $\eta' \rightarrow \gamma \pi^+ \pi^-$ channel:

$$N_{\chi_{cJ} \rightarrow \eta' \pi^+ \pi^-} = \frac{N_{\chi_{cJ}, \text{obs}}}{\varepsilon_{\chi_{cJ}} \cdot \text{Br}_{\text{sub}}}. \quad (5.30)$$

Here, $N_{\chi_{cJ}, \text{obs}}$ is the number of observed χ_{cJ} events. Inserting Equations (5.29) and (5.30) into Equation (5.28) gives

$$\text{Br}(\chi_{cJ} \rightarrow \eta' \pi^+ \pi^-) = \frac{N_{\chi_{cJ}, \text{obs}}}{\varepsilon_{\chi_{cJ}} \cdot N_{\psi(2S)} \cdot \text{Br}(\psi(2S) \rightarrow \gamma \chi_{cJ}) \cdot \text{Br}_{\text{sub}}}. \quad (5.31)$$

The number of $\psi(2S)$ events was determined by the BESIII collaboration to [159]

$$N_{\psi(2S)} = (2.712 \pm 0.014) \times 10^9 \quad (5.32)$$

and the branching ratios of the radiative decays are taken from the PDG [6]:

$$\text{Br}(\psi(2S) \rightarrow \gamma \chi_{c0}) = (9.77 \pm 0.23) \%, \quad (5.33)$$

$$\text{Br}(\psi(2S) \rightarrow \gamma \chi_{c1}) = (9.75 \pm 0.27) \%, \quad (5.34)$$

$$\text{Br}(\psi(2S) \rightarrow \gamma \chi_{c2}) = (9.36 \pm 0.23) \%, \quad (5.35)$$

as well as the branching ratios of the subsequent decays

$$\text{Br}(\eta' \rightarrow \eta \pi^+ \pi^-) = (42.5 \pm 0.5) \%, \quad (5.36)$$

$$\text{Br}(\eta \rightarrow \gamma \gamma) = (39.36 \pm 0.18) \%, \quad (5.37)$$

$$\text{Br}(\eta' \rightarrow \gamma \pi^+ \pi^-) = (29.5 \pm 0.4) \%. \quad (5.38)$$

To estimate the efficiency ε resulting from the event selection criteria and the detector acceptance, the signal MC (see Table 3.6) is used. The efficiency is calculated as

$$\varepsilon_{\chi_{cJ}} = \frac{N_{\text{rec},\chi_{cJ}}}{N_{\text{gen},\chi_{cJ}}}, \quad (5.39)$$

with the number of reconstructed events $N_{\text{rec},\chi_{cJ}}$ in the signal MC and the number of generated events $N_{\text{gen},\chi_{cJ}} = 5 \times 10^6$. This is done for both η' channels and the resulting efficiencies are presented in Table 5.6. All efficiencies lie in the range of 10% to 17% and for each resonance the efficiency in the $\eta' \rightarrow \gamma\pi^+\pi^-$ channel is slightly higher than in the $\eta' \rightarrow \eta\pi^+\pi^-$ channel, which can be explained by the additional photon that needs to be reconstructed in the $\eta' \rightarrow \eta\pi^+\pi^-$ channel.

The next step is the determination of the number of observed χ_{cJ} events $N_{\chi_{cJ},\text{obs}}$, which is done using a fit²⁰ to the $\eta'\pi^+\pi^-$ spectrum, as can be seen in Figures 5.17 and 5.18 for the $\eta' \rightarrow \eta\pi^+\pi^-$ and $\eta' \rightarrow \gamma\pi^+\pi^-$ channels, respectively. For both channels the total fit consists of a signal contribution from the χ_{c1} and χ_{c2} and a background contribution: $\mathcal{M} = \mathcal{S}_{\chi_{c1}} + \mathcal{S}_{\chi_{c2}} + \mathcal{B}$. Both signal contributions are described by a sum of two Gaussian functions with the same mean, according to Equation (5.24), and the background is a linear function

$$\mathcal{B} = a_0 + a_1 \left(m - m_{\chi_{c1},\text{PDG}} \right). \quad (5.40)$$

This is done, again under the assumption that the natural width is negligible compared to the detector resolution. The resulting parameters are listed in Tables 5.7 and 5.8 for the $\eta' \rightarrow \eta\pi^+\pi^-$ and $\eta' \rightarrow \gamma\pi^+\pi^-$ channels, respectively.

Both fits give a reasonable description of the data, with the largest deviations occurring on the right flank of the χ_{c1} peak, which shows a slight asymmetry that is not

Table 5.6.: Determined efficiencies ε in % for all considered resonances and for both η' channels determined with the corresponding signal MC simulations. The uncertainties are the statistical uncertainties from the number of reconstructed events, they are negligible compared to the other systematic uncertainties (see Section 5.6).

	$\eta' \rightarrow \eta\pi^+\pi^-$	$\eta' \rightarrow \gamma\pi^+\pi^-$
χ_{c1}	11.83 ± 0.02	13.50 ± 0.02
χ_{c2}	11.39 ± 0.02	12.71 ± 0.02
χ_{c0}	10.91 ± 0.02	12.86 ± 0.02
η_c	11.92 ± 0.02	16.57 ± 0.02
$X(1835)$	10.28 ± 0.01	16.20 ± 0.02

²⁰Unless explicitly mentioned, the fits presented in this chapter are always least- χ^2 fits, as on the one hand side the number of events is large and on the other hand the appearance of negative bin contents makes a likelihood fit not applicable.

reproduced by the chosen fit model. This asymmetry is also responsible for the measured distances of $1.40 \text{ MeV}/c^2$ and $1.02 \text{ MeV}/c^2$ between the peak position of the χ_{c1} and the value taken from the PDG of $m_{\chi_{c1},\text{PDG}} = (3510.67 \pm 0.05) \text{ MeV}/c^2$ [6]. In the case of the χ_{c2} , the deviations are $0.07 \text{ MeV}/c^2$ and $0.64 \text{ MeV}/c^2$ from the PDG mass of $m_{\chi_{c2},\text{PDG}} = (3556.17 \pm 0.07) \text{ MeV}/c^2$ [6] explainable by the momentum resolution. To determine the significance of a possible χ_{c0} signal, a fit is performed to the $\eta' \pi^+ \pi^-$ spectrum in the χ_{c0} mass region. For this fit, the background is described by a linear function and the signal contribution is described by a Voigt function

$$\mathcal{S}(m) = N_{\text{obs}} \int_{-\infty}^{\infty} \frac{1}{\pi} \frac{\Gamma/2}{(m - m_{\text{peak}} - m')^2 c^4 + \Gamma^2/4} \cdot \frac{1}{\sqrt{2\pi}\sigma} \exp\left(-\frac{m'^2}{2\sigma^2}\right) dm', \quad (5.41)$$

which is a convolution of a non-relativistic Breit-Wigner function and a Gaussian function. The reason for this choice is the measurable width of the χ_{c0} of $\Gamma_{\chi_{c0},\text{PDG}} = (10.7 \pm 0.6) \text{ MeV}$ [6], which is fixed to its central value in the fit. To estimate the detector resolution σ for the χ_{c0} , the widths of the χ_{c1} and χ_{c2} are averaged. The widths of the χ_{c1} and χ_{c2} are the averages of σ_1 and σ_2 weighted by the factor f , resulting in a detector resolution of

$$\sigma = \frac{f_{\chi_{c1}} \sigma_{1,\chi_{c1}} + (1 - f_{\chi_{c1}}) \sigma_{2,\chi_{c1}}}{2} + \frac{f_{\chi_{c2}} \sigma_{1,\chi_{c2}} + (1 - f_{\chi_{c2}}) \sigma_{2,\chi_{c2}}}{2}, \quad (5.42)$$

which is fixed in the fit. The position of the peak m_{peak} is fixed to the mass of the χ_{c0} taken from the PDG $m_{\chi_{c0},\text{PDG}} = (3414.71 \pm 0.30) \text{ MeV}/c^2$ [6]. In both channels no significant contribution of the χ_{c0} is visible, which is expected since the decay $\chi_{c0} \rightarrow \eta' \pi^+ \pi^-$ violates the conservation of the J^{PC} quantum numbers. To determine the significance, the fit is repeated with only the background component, resulting in a change of the χ^2 of 7.86 and 0.34 for the $\eta' \rightarrow \eta \pi^+ \pi^-$ and $\eta' \rightarrow \gamma \pi^+ \pi^-$ channels, respectively. These changes in χ^2 combined with the one additional degree of freedom correspond to a statistical significance of 2.80σ and 0.58σ , respectively.

Since no significant signal is observed, an upper limit for the number of observed χ_{c0} events $N_{\chi_{c0},\text{obs}}$ is calculated by performing a χ^2 scan. To do this, N_{obs} is fixed at values around the determined central value and the corresponding χ^2 is calculated. The χ^2 is then used to calculate a relative likelihood according to

$$L = \frac{e^{-\chi^2/2}}{e^{-\chi_{\text{min}}^2/2}}, \quad (5.43)$$

where χ_{min}^2 is the χ^2 value of the best fit. The resulting likelihood scans are presented in Figure 5.19. To determine an upper limit, the likelihood scans are fitted with a Gaussian

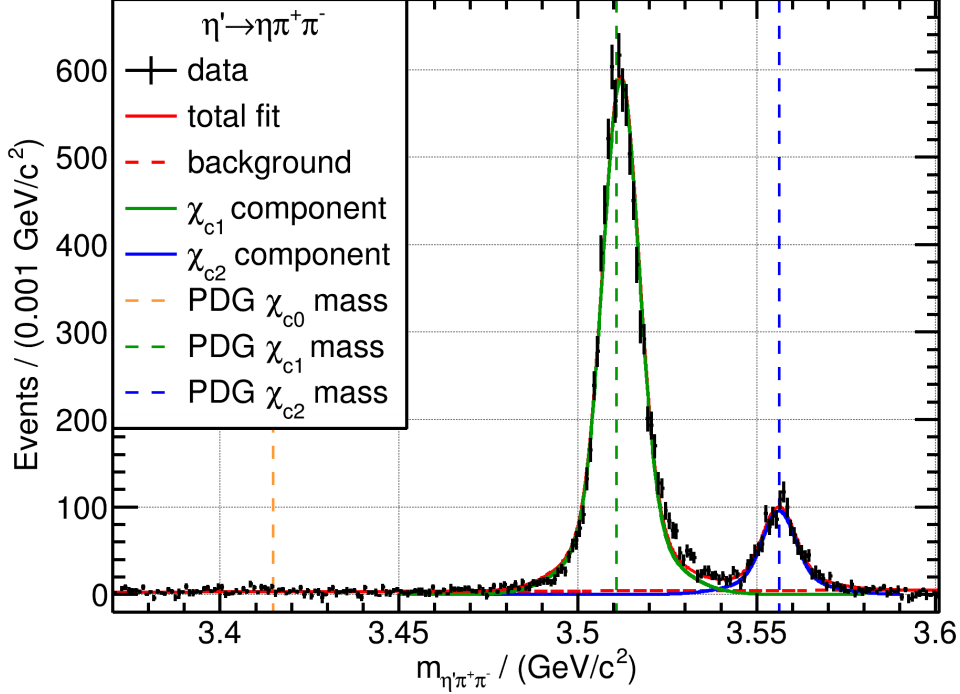


Figure 5.17.: Invariant mass of the $\eta'\pi^+\pi^-$ system, with the fit to the χ_{c1} and χ_{c2} for the $\eta' \rightarrow \eta\pi^+\pi^-$ channel. The data is shown as black dots with uncertainties, the total fit is shown as the solid red line and the background component as the dashed red line. The χ_{c1} and χ_{c2} components are indicated with the green and the blue solid line, respectively. The fit is described in the text and the resulting parameters are listed in Table 5.7. Additionally, the masses of the χ_{cJ} according to the PDG [6] are marked with dashed lines.

Table 5.7.: Parameters of the fits to the invariant mass of the χ_{c1} and χ_{c2} candidates in the $\eta' \rightarrow \eta\pi^+\pi^-$ channel. The uncertainties are statistical only.

	χ_{c1}	χ_{c2}
Observed Events N_{obs}	8729 ± 99	1409 ± 49
Mass $m_{\text{peak}} / (\text{MeV}/c^2)$	3512.072 ± 0.076	3556.243 ± 0.220
Factor $f / \%$	73.1 ± 3.1	61.0 ± 9.5
Width $\sigma_1 / (\text{MeV}/c^2)$	4.97 ± 0.14	4.48 ± 0.41
Width $\sigma_2 / (\text{MeV}/c^2)$	12.30 ± 0.78	11.54 ± 1.74
$a_0 / \text{a.u.}$	4.18 ± 0.66	
$a_1 / \text{a.u.}$	10.5 ± 4.3	
χ^2 / ndf	$525.17 / 296 = 1.77$	

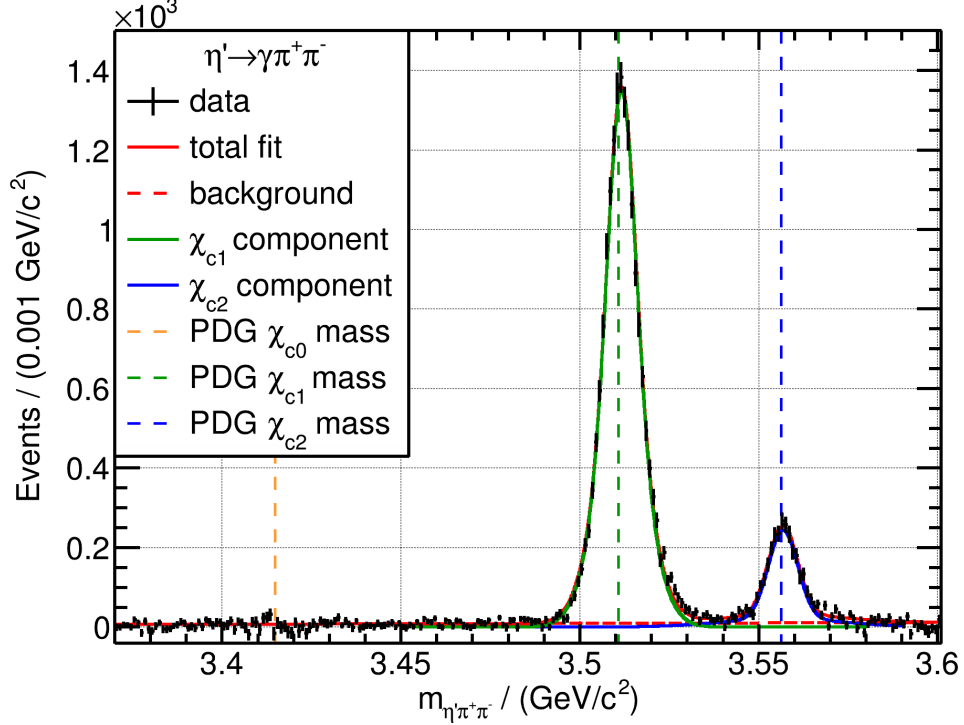


Figure 5.18.: Invariant mass of the $\eta' \pi^+ \pi^-$ system, with the fit to the χ_{c1} and χ_{c2} for the $\eta' \rightarrow \gamma \pi^+ \pi^-$ channel. The data is shown as black dots with uncertainties, the total fit is shown as the solid red line and the background component as the dashed red line. The χ_{c1} and χ_{c2} components are indicated with the green and the blue solid line, respectively. The fit is described in the text and the resulting parameters are listed in Table 5.8. Additionally, the masses of the χ_{cJ} according to the PDG [6] are marked with dashed lines.

Table 5.8.: Parameters of the fits to the invariant mass of the χ_{c1} and χ_{c2} candidates in the $\eta' \rightarrow \gamma \pi^+ \pi^-$ channel. The uncertainties are statistical only.

	χ_{c1}	χ_{c2}
Observed Events N_{obs}	$17\,005 \pm 150$	3167 ± 114
Mass $m_{\text{peak}} / (\text{MeV}/c^2)$	3511.686 ± 0.049	3556.808 ± 0.152
Factor $f / \%$	48.1 ± 7.6	72.6 ± 4.0
Width $\sigma_1 / (\text{MeV}/c^2)$	3.85 ± 0.20	4.10 ± 0.20
Width $\sigma_2 / (\text{MeV}/c^2)$	7.04 ± 0.36	17.03 ± 2.95
$a_0 / \text{a.u.}$	9.6 ± 1.7	
$a_1 / \text{a.u.}$	22 ± 12	
χ^2 / ndf	$349.42 / 296 = 1.18$	

5. Analysis of the Decay $\psi(2S) \rightarrow \gamma\eta'\pi^+\pi^-$

function $\mathcal{G}(N_{\chi_{c0}})$ and the upper limit N^{UL} at a confidence level of 90% is determined using a Bayesian approach [206] via the integral:

$$\int_{-\infty}^{N^{\text{UL}}} \mathcal{G}(N_{\chi_{c0}})\pi(N_{\chi_{c0}}) dN_{\chi_{c0}} \cdot \left(\int_{-\infty}^{\infty} \mathcal{G}(N_{\chi_{c0}})\pi(N_{\chi_{c0}}) dN_{\chi_{c0}} \right)^{-1} = 0.9. \quad (5.44)$$

Here, $\pi(N_{\chi_{c0}})$ is a prior chosen as a step function at $N_{\chi_{c0}} = 0$ to exclude the unphysical region:

$$\pi(N_{\chi_{c0}}) = \begin{cases} 1, & \text{for } N_{\chi_{c0}} \geq 0 \\ 0, & \text{for } N_{\chi_{c0}} < 0 \end{cases} \quad (5.45)$$

From this, the upper limits are extracted as

$$N_{\eta' \rightarrow \eta\pi^+\pi^-}^{\text{UL}} = 88.2, \quad (5.46)$$

$$N_{\eta' \rightarrow \gamma\pi^+\pi^-}^{\text{UL}} = 117.6. \quad (5.47)$$

With the determined values for the number of observed events and for the efficiencies the branching ratios for the decays $\chi_{cJ} \rightarrow \eta'\pi^+\pi^-$ can be calculated and the resulting values with their statistical uncertainties are listed in Table 5.9. Taking only the statistical uncertainties into account, the differences between the $\eta' \rightarrow \eta\pi^+\pi^-$ and $\eta' \rightarrow \gamma\pi^+\pi^-$ channels for the χ_{c1} and χ_{c2} are 2.2σ and 2.6σ , respectively.

As mentioned above, the data sample also includes a significant contribution from the $\eta_c \rightarrow \eta'\pi^+\pi^-$ decay, and the corresponding branching ratios are determined in the next section.

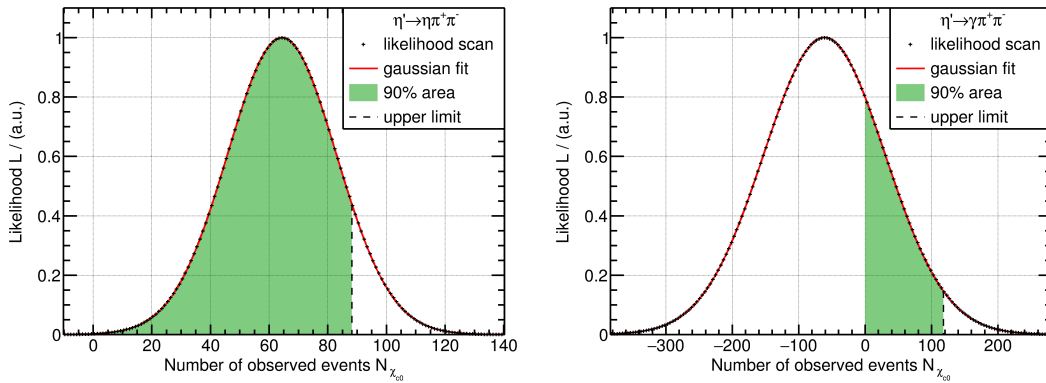


Figure 5.19.: Likelihood scans for the number of χ_{c0} events. The scan values are shown as the black markers, the fit with a Gaussian function is shown as the solid red line, the 90% area under the peak is shown in green and the resulting upper limit is marked with the black dashed line.

Table 5.9.: Determined branching ratios for the decays $\chi_{cJ} \rightarrow \eta' \pi^+ \pi^-$. The uncertainties are statistical only.

		N_{obs}	$\varepsilon / \%$	$\text{Br}(\chi_{cJ} \rightarrow \eta' \pi^+ \pi^-)$
χ_{c0}	$\eta' \rightarrow \eta \pi^+ \pi^-$	< 88.2	10.91	$< 1.91 \times 10^{-5}$
	$\eta' \rightarrow \gamma \pi^+ \pi^-$	< 117.6	12.86	$< 1.23 \times 10^{-5}$
χ_{c1}	$\eta' \rightarrow \eta \pi^+ \pi^-$	8729 ± 99	11.83	$(1.664 \pm 0.019) \times 10^{-3}$
	$\eta' \rightarrow \gamma \pi^+ \pi^-$	17005 ± 150	13.50	$(1.611 \pm 0.015) \times 10^{-3}$
χ_{c2}	$\eta' \rightarrow \eta \pi^+ \pi^-$	1409 ± 49	11.39	$(2.798 \pm 0.099) \times 10^{-4}$
	$\eta' \rightarrow \gamma \pi^+ \pi^-$	3167 ± 114	12.71	$(3.194 \pm 0.116) \times 10^{-4}$

5.4. Determination of the $\eta_c \rightarrow \eta' \pi^+ \pi^-$ Branching Ratio

Using a similar approach as for the χ_{cJ} , the branching ratio of the decay $\eta_c \rightarrow \eta' \pi^+ \pi^-$ is calculated according to

$$\text{Br}(\eta_c \rightarrow \eta' \pi^+ \pi^-) = \frac{N_{\eta_c, \text{obs}}}{\varepsilon_{\eta_c} \cdot N_{\psi(2S)} \cdot \text{Br}(\psi(2S) \rightarrow \gamma \eta_c) \cdot \text{Br}_{\text{sub}}}. \quad (5.48)$$

In this case, the branching ratio for the radiative decay into the η_c is given by the PDG [6] as

$$\text{Br}(\psi(2S) \rightarrow \gamma \eta_c) = (3.6 \pm 0.5) \times 10^{-3}. \quad (5.49)$$

The invariant mass spectra of the $\eta' \pi^+ \pi^-$ system around the η_c mass are depicted in Figure 5.20 for the $\eta' \rightarrow \eta \pi^+ \pi^-$ channel. The η_c peak shows a clear asymmetry with a tail to the left side of the peak. This asymmetry could be a result of the energy dependence of the transition matrix element for the radiative decay $\psi(2S) \rightarrow \gamma \eta_c$ [207]. To describe the asymmetry, the CLEO collaboration used a Breit-Wigner function with a pre-factor \mathcal{C} defined as [208]

$$\mathcal{C}(m) = E_\gamma(m)^3 \exp\left(-\frac{E_\gamma(m)^2}{8\beta^2}\right), \quad (5.50)$$

with the energy of the radiative photon given by

$$E_\gamma(m) = \frac{m_{\psi(2S)}^2 c^4 - m^2 c^4}{2m_{\psi(2S)} c^2} \quad (5.51)$$

and a normalization constant $\beta = (65.0 \pm 2.5) \text{ MeV}$ [208]. The E_γ^3 term comes from the hindered magnetic dipole transition in $\psi(2S) \rightarrow \gamma \eta_c$ [207], which diverges at high photon energies. To dampen this divergence, an exponential factor is introduced, inspired by the overlap of two ground state wave functions [208]. To test this model, a fit consisting of

a linear function for the background and a relativistic Breit-Wigner function with the CLEO pre-factor is used:

$$S(m) = I \cdot \mathcal{C}(m) \cdot \frac{m_{\text{peak}} c^2 \Gamma}{(m^2 c^4 - m_{\text{peak}}^2 c^4)^2 + m_{\text{peak}}^2 c^4 \Gamma^2}. \quad (5.52)$$

Here, I is the intensity of the signal, m_{peak} is the position and Γ is the width of the peak. The result of this fit is also displayed in Figure 5.20 and the resulting parameters are listed in Table 5.10. As can be seen, the fit fails to adequately describe the asymmetry of the peak, giving a reduced $\chi^2 / \text{ndf} = 313.53 / 155 = 2.02$, with the deviations coming mainly from the flanks of the peak. In addition, the fit returns a peak position of $m_{\text{peak}} = (2976.33 \pm 0.85) \text{ MeV}/c^2$, which is significantly smaller than the PDG value of $m_{\eta_c, \text{PDG}} = (2984.1 \pm 0.4) \text{ MeV}/c^2$ [6], and a width of $\Gamma = (36.8 \pm 1.7) \text{ MeV}$, which is significantly larger than the PDG width $\Gamma_{\eta_c, \text{PDG}} = (30.5 \pm 0.5) \text{ MeV}$ [6]. However, this overestimation is to be expected, since the model neglects the detector resolution that broadens the peak.

In order to overcome the shortcomings of the presented fit, an alternative model is tested, which considers a possible interference of the η_c with the non-resonant background with

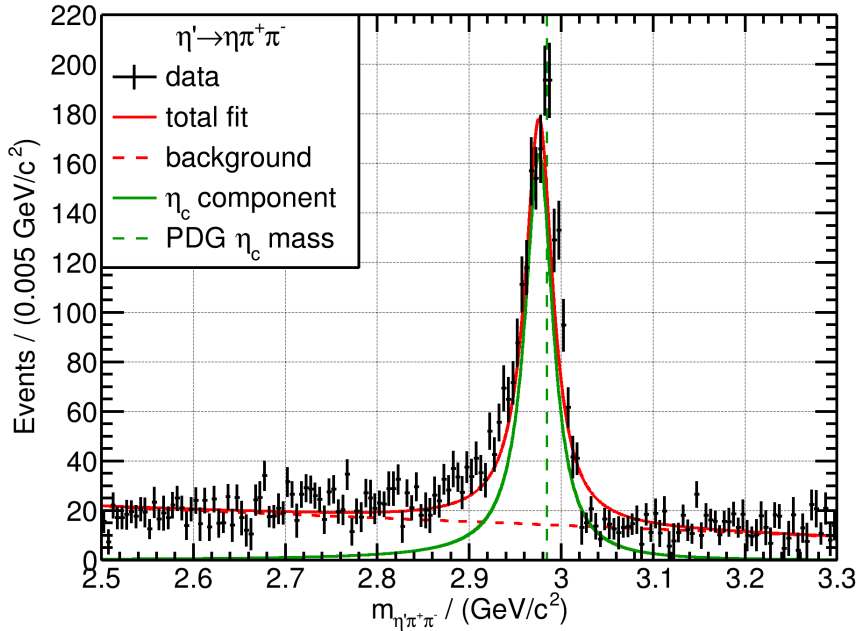


Figure 5.20.: Invariant mass of the $\eta'\pi^+\pi^-$ system, with a Breit-Wigner fit to the η_c for the $\eta' \rightarrow \eta\pi^+\pi^-$ channel. The data is shown as black dots with uncertainties, the total fit is shown as the solid red line and the background component as the dashed red line. The η_c component is indicated with the green solid line. The fit is described in the text and the resulting parameters are listed in Table 5.10. Additionally, the mass of the η_c according to the PDG [6] is marked with a dashed line.

Table 5.10.: Values determined by the fit to the η_c in the $\eta' \rightarrow \eta \pi^+ \pi^-$ channel using a relativistic Breit-Wigner function with the CLEO pre-factor. The uncertainties are statistical only.

Intensity I / a.u.	19.32 ± 0.66
Mass $m_{\text{peak}} / (\text{MeV}/c^2)$	2976.33 ± 0.85
Width Γ / MeV	36.8 ± 1.7
a_0 / a.u.	14.23 ± 0.55
a_1 / a.u.	-15.0 ± 1.9
χ^2 / ndf	$313.53 / 155 = 2.02$

a phase ϕ . This interference might also produce an asymmetric peak and therefore no additional pre-factor is needed. For this, the total model is defined as [209]

$$\mathcal{M}(m) = \left| \mathcal{B}(m) + e^{i\phi} \mathcal{S}(m) \right|^2. \quad (5.53)$$

This model is a reasonable description of the physics if the non-resonant background consists mainly of contributions with the same J^{PC} quantum numbers as the η_c given by $J^{PC} = 0^{-+}$. Since the decay of a pseudoscalar meson into three pseudoscalar mesons is possible without any angular momenta, this is a reasonable assumption, since higher angular momenta are suppressed. The background intensity $|\mathcal{B}|^2$ is defined as a first order polynomial

$$\mathcal{B}(m) = \sqrt{a_0 + a_1(m - m_{\eta_c})}, \quad (5.54)$$

and the signal intensity $|\mathcal{S}|^2$ is given as a relativistic Breit-Wigner function:

$$\mathcal{S}(m) = \sqrt{\frac{N_{\text{obs}}}{C_{\text{norm}}}} \frac{\sqrt{m_{\text{peak}} c^2 \Gamma}}{m^2 c^4 - m_{\text{peak}}^2 c^4 + im_{\text{peak}} c^2 \Gamma}. \quad (5.55)$$

Here, N_{obs} is the number of observed η_c events and C_{norm} is a normalization factor given by

$$C_{\text{norm}} = \int_0^\infty \frac{m_{\text{peak}} c^2 \Gamma}{(m'^2 c^4 - m_{\text{peak}}^2 c^4)^2 + m_{\text{peak}}^2 c^4 \Gamma^2} dm'. \quad (5.56)$$

With the model defined in this way, it is mathematically expected that the fit has two solutions that give exactly the same χ^2 , with the same parameters, except for the number of events N_{obs} and the phase ϕ [210]. These two solutions are shown for both channels in Figure 5.21 and the resulting parameters are listed in Table 5.11. In both channels the fit gives an excellent description of the data, with both χ^2 / ndf being close to one. The extracted mass of the η_c lies within 2σ and within 1σ of the mass given by the PDG for the $\eta' \rightarrow \eta \pi^+ \pi^-$ and $\eta' \rightarrow \gamma \pi^+ \pi^-$ channels, respectively. Again, the determined widths are significantly higher than the PDG value, although they are closer compared to the fit with the CLEO prefactor in Table 5.10.

5. Analysis of the Decay $\psi(2S) \rightarrow \gamma\eta'\pi^+\pi^-$

Another interesting observation is the fact that the extracted phases for the solutions with constructive and destructive interference agree with the phases extracted by a previous BESIII analysis of different decays of the type $\psi(2S) \rightarrow \gamma\eta_c \rightarrow \gamma P$, where $P \in \{K_S^0 K^+ \pi^-, K^+ K^- \pi^0, \eta \pi^+ \pi^-, K_S^0 K^+ \pi^+ \pi^- \pi^-, K^+ K^- \pi^+ \pi^- \pi^0, 3(\pi^+ \pi^-)\}$ [209]:

$$\phi_{\text{constr}} = (2.40 \pm 0.07 \pm 0.47) \text{ rad}, \quad (5.57)$$

$$\phi_{\text{destr}} = (4.19 \pm 0.03 \pm 0.47) \text{ rad}. \quad (5.58)$$

There is no known physical reason for this possible common phase yet [209].

With the determined values for the number of observed η_c events and the efficiencies from Table 5.6, the branching ratio of the decay $\eta_c \rightarrow \eta' \pi^+ \pi^-$ can be calculated. This is done for the fit with constructive and destructive interference and the results are presented in Table 5.12. Considering only the statistical uncertainties, there is a discrepancy of 4.1σ for the constructive interference and 3.7σ for the destructive interference between

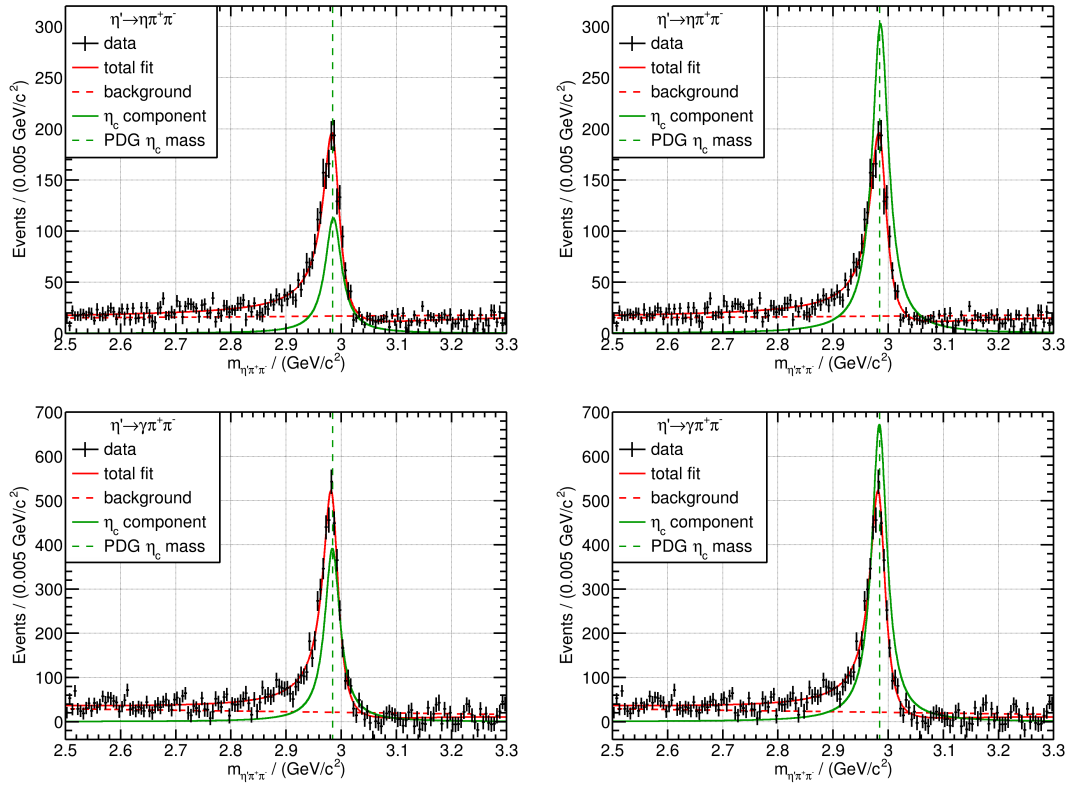


Figure 5.21.: Invariant mass of the $\eta'\pi^+\pi^-$ system for the $\eta' \rightarrow \eta\pi^+\pi^-$ channel (top) and the $\eta' \rightarrow \gamma\pi^+\pi^-$ channel (bottom) for the solution with constructive interference (left) and destructive interference (right). The data is shown as black points with uncertainties, the total fit as the red solid line, the background component with the red dashed line and the signal contribution with the green solid line. The fit is described in the text and the resulting parameters are listed in Table 5.11. Additionally, the mass of the η_c according to the PDG [6] is shown as the dashed green line.

Table 5.11.: Parameters of the fit to the η_c candidates in the $\eta' \rightarrow \eta\pi^+\pi^-$ channel (top) and the $\eta' \rightarrow \gamma\pi^+\pi^-$ channel (bottom). The uncertainties are statistical only.

	Constructive interference	Destructive interference	
$\eta' \rightarrow \eta\pi^+\pi^-$	Observed Events N_{obs}	1283 ± 54	3446 ± 106
	Mass $m_{\text{peak}} / (\text{MeV}/c^2)$	2986.00 ± 0.96	
	Width $\Gamma / (\text{MeV})$	36.2 ± 1.6	
	Phase ϕ / rad	2.364 ± 0.060	4.265 ± 0.034
	$a_0 / \text{a.u.}$	16.86 ± 0.61	
	$a_1 / \text{a.u.}$	3.6 ± 2.3	
χ^2 / ndf	$151.10 / 154 = 0.98$		
$\eta' \rightarrow \gamma\pi^+\pi^-$	Observed Events N_{obs}	4132 ± 203	7094 ± 260
	Mass $m_{\text{peak}} / (\text{MeV}/c^2)$	2984.14 ± 0.72	
	Width $\Gamma / (\text{MeV})$	33.6 ± 1.3	
	Phase ϕ / rad	2.569 ± 0.107	4.006 ± 0.082
	$a_0 / \text{a.u.}$	21.2 ± 1.9	
	$a_1 / \text{a.u.}$	-16.2 ± 6.3	
χ^2 / ndf	$167.57 / 154 = 1.09$		

the two η' channels. Comparing the calculated values and taking isospin symmetry into account, the values for the destructive interference are in agreement with the value for $\text{Br}(\eta_c \rightarrow \eta'\pi^+\pi^-) = (1.3 \pm 0.3) \%$ from the PDG within 1.5σ .

The last peak that is visible in the $\eta'\pi^+\pi^-$ spectrum in Figure 5.16 is an enhancement

Table 5.12.: Determined branching ratios for the decay $\eta_c \rightarrow \eta'\pi^+\pi^-$. The uncertainties are statistical only.

	N_{obs}	$\varepsilon / \%$	$\text{Br}(\eta_c \rightarrow \eta'\pi^+\pi^-) / \%$
constructive $\eta' \rightarrow \eta\pi^+\pi^-$	1283 ± 54	11.92	0.659 ± 0.028
interference $\eta' \rightarrow \gamma\pi^+\pi^-$	4132 ± 203	16.57	0.866 ± 0.043
destructive $\eta' \rightarrow \eta\pi^+\pi^-$	3446 ± 106	11.92	1.770 ± 0.055
interference $\eta' \rightarrow \gamma\pi^+\pi^-$	7094 ± 260	16.57	1.486 ± 0.055

below $2 \text{ GeV}/c^2$, which will be analyzed in the next section.

5.5. Search for the $X(1835)$

While all peaks in the $\eta'\pi^+\pi^-$ spectrum analyzed so far originate from the decay of known charmonia, the enhancement in the mass range of the $X(1835)$ suggests light quark

5. Analysis of the Decay $\psi(2S) \rightarrow \gamma\eta'\pi^+\pi^-$

constituents. As the decay $\psi(2S) \rightarrow \gamma X(1835)$ has not yet been measured, only a product branching ratio can be calculated for the $X(1835)$:

$$\text{Br}(\psi(2S) \rightarrow \gamma X(1835)) \cdot \text{Br}(X(1835) \rightarrow \eta'\pi^+\pi^-) = \frac{N_{X(1835),\text{obs}}}{\varepsilon_{X(1835)} \cdot N_{\psi(2S)} \cdot \text{Br}_{\text{sub}}}. \quad (5.59)$$

To do this, different models for the $X(1835)$ are considered.

The first model to describe the enhancement in the $X(1835)$ mass region of Figure 5.16 is a relativistic Breit-Wigner

$$\mathcal{S}(m) = \frac{N_{\text{obs}}}{C_{\text{norm}}} \frac{m_{\text{peak}} c^2 \Gamma}{(m^2 c^4 - m_{\text{peak}}^2 c^4)^2 + m_{\text{peak}}^2 c^4 \Gamma^2}, \quad (5.60)$$

with the normalization constant C_{norm} from Equation (5.56) and a linear background. In order for this fit to converge, a fit using only the background component is first applied by excluding the region $m_{\eta'\pi^+\pi^-} \in [1.4 \text{ GeV}/c^2, 2.2 \text{ GeV}/c^2]$. The resulting background parameters are then fixed in the total fit, which is shown in Figure 5.22 for both η' channels, and the resulting fit parameters are listed in Table 5.13. In both channels the fit gives a reasonable χ^2/ndf , although it produces an unphysical result, as the fitted background function becomes negative at low invariant masses. This can be explained by the fact, that the current fit does not include the effect of the opening of the $\eta'\pi^+\pi^-$ phase space at $m_{\eta'\pi^+\pi^-} = (1236.92 \pm 0.06) \text{ MeV}/c^2$.

To consider this effect, the fit model is adjusted according to [25]

$$\mathcal{B}(m) = a_0 \mathcal{P}(m) \quad (5.61)$$

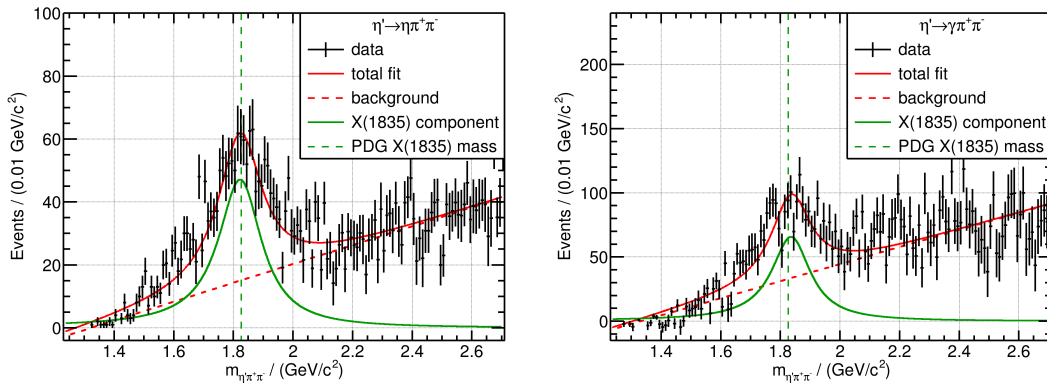


Figure 5.22.: Invariant mass of the $\eta'\pi^+\pi^-$ system, with a Breit-Wigner fit to the $X(1835)$ for the $\eta' \rightarrow \eta\pi^+\pi^-$ channel (left) and the $\eta' \rightarrow \gamma\pi^+\pi^-$ channel (right). The data is shown as black dots with uncertainties, the total fit is shown as the solid red line and the background component as the dashed red line. The $X(1835)$ component is indicated with the green solid line and the mass of the $X(1835)$ according to the PDG [6] is marked with a dashed line. The fit is described in the text and the resulting parameters are listed in Table 5.13.

and

$$\mathcal{S}(m) = \frac{N_{\text{obs}}}{C_{\text{norm}}} \mathcal{P}(m) \frac{m_{\text{peak}} c^2 \Gamma}{(m^2 c^4 - m_{\text{peak}}^2 c^4)^2 + m_{\text{peak}}^2 c^4 \Gamma^2}, \quad (5.62)$$

with the modified normalization constant

$$C_{\text{norm}} = \int_0^\infty \mathcal{P}(m') \frac{m_{\text{peak}} c^2 \Gamma}{(m'^2 c^4 - m_{\text{peak}}^2 c^4)^2 + m_{\text{peak}}^2 c^4 \Gamma^2} dm'. \quad (5.63)$$

Here, $\mathcal{P}(m)$ is the three-body phase space for the decay $X(1835) \rightarrow \eta' \pi^+ \pi^-$, calculated in Appendix A.1. The resulting fits are presented in Figure 5.23, with the parameters also given in Table 5.13. These fits give a similar χ^2 to that of the first model and significantly larger widths for the $X(1835)$, consistent with the width given by the PDG of $\Gamma_{X(1835),\text{PDG}} = 242_{-15}^{+14}$ MeV. However, the curvature of the background shifts the position of the peak to values, which are significantly smaller than the PDG value $m_{X(1835),\text{PDG}} = 1826.5_{-3.4}^{+13.0}$ MeV. In addition, the extracted number of events differs significantly between the two models.

Looking at the $\eta' \pi^+ \pi^-$ mass spectrum in the region from $2.1 \text{ GeV}/c^2$ to $2.7 \text{ GeV}/c^2$, a slight oscillatory behavior can be seen. Exactly in this mass region, some structures were visible in the BESIII analysis of the decay $J/\psi \rightarrow \gamma \eta' \pi^+ \pi^-$ [25], which have been identified with the $X(2120)$ and $X(2370)$. Including these structures in the fit model would influence the extracted values for the $X(1835)$, but with the present data sample such contributions are expected to be insignificant.

Using the determined values for N_{obs} from these fits, results in the product branching ratios $\text{Br}(\psi(2S) \rightarrow \gamma X(1835)) \cdot \text{Br}(X(1835) \rightarrow \eta' \pi^+ \pi^-)$ presented in Table 5.14. Considering only the statistical uncertainties, the values differ by more than 7σ between the two η' channels.

In order to reliably interpret the determined values for the branching ratios of the χ_{cJ} , η_c and $X(1835)$, the systematic uncertainties are calculated in the next section.

5.6. Systematic Uncertainties

In the context of the present analysis, several sources of systematic uncertainties have to be considered. Possible systematic effects arise mainly from differences between the data and the signal MC samples which are used to estimate the efficiencies. These effects come from the efficiency of the reconstruction and identification of the particles on the one hand and from the applied event selection criteria on the other hand. Another form of systematic uncertainty comes from the arbitrarily chosen signal regions and the chosen description of signal and background components in the fits, which are used to determine the number of observed events. Additional uncertainties come from the branching ratios taken from the PDG and the number of $\psi(2S)$ events.

5. Analysis of the Decay $\psi(2S) \rightarrow \gamma\eta'\pi^+\pi^-$

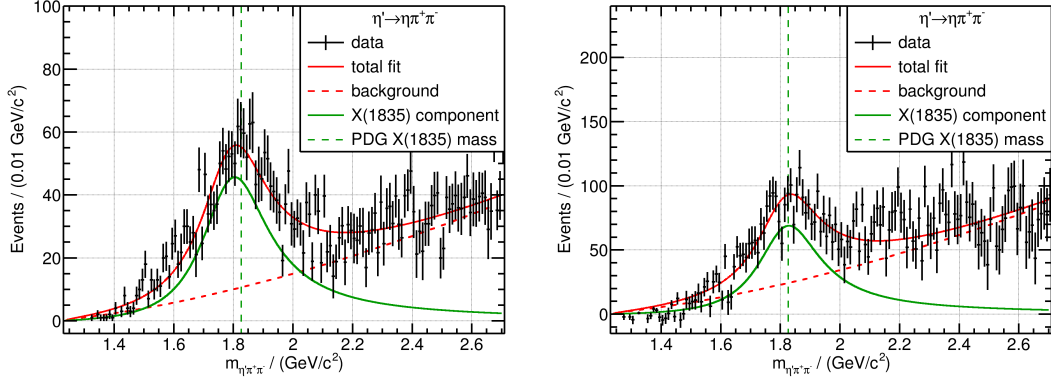


Figure 5.23.: Invariant mass of the $\eta'\pi^+\pi^-$ system, with a Breit-Wigner fit to the $X(1835)$ considering the three-particle phase space for the $\eta' \rightarrow \eta\pi^+\pi^-$ channel (left) and the $\eta' \rightarrow \gamma\pi^+\pi^-$ channel (right). The data is shown as black dots with uncertainties, the total fit is shown as the solid red line and the background component as the dashed red line. The $X(1835)$ component is indicated with the green solid line and the mass of the $X(1835)$ according to the PDG [6] is marked with a dashed line. The fit is described in the text and the resulting parameters are listed in Table 5.13.

Table 5.13.: Parameters of the fits to the $X(1835)$ candidates in the $\eta' \rightarrow \eta\pi^+\pi^-$ channel (top) and the $\eta' \rightarrow \gamma\pi^+\pi^-$ channel (bottom). The uncertainties are statistical only.

	relativistic BW linear BG	PHSP relativistic BW PHSP constant BG
$\eta' \rightarrow \eta\pi^+\pi^-$		
Observed Events N_{obs}	1299 ± 57	1972 ± 104
Mass $m_{\text{peak}} / (\text{MeV}/c^2)$	1822.9 ± 5.8	1784.0 ± 6.7
Width $\Gamma / (\text{MeV})$	176 ± 10	271 ± 18
$a_0 / \text{a.u.}$	15.06 ± 0.49	10.59 ± 0.43
$a_1 / \text{a.u.}$	29.95 ± 1.01	
χ^2 / ndf	$194.97 / 133 = 1.47$	$170.23 / 132 = 1.29$
$\eta' \rightarrow \gamma\pi^+\pi^-$		
Observed Events N_{obs}	1623 ± 100	2801 ± 217
Mass $m_{\text{peak}} / (\text{MeV}/c^2)$	1836.1 ± 7.8	1810.9 ± 7.7
Width $\Gamma / (\text{MeV})$	158 ± 12	256 ± 23
$a_0 / \text{a.u.}$	32.87 ± 1.17	24.24 ± 1.07
$a_1 / \text{a.u.}$	66.54 ± 2.39	
χ^2 / ndf	$239.46 / 136 = 1.76$	$245.55 / 135 = 1.82$

Table 5.14.: Determined product branching ratios for the decay $\psi(2S) \rightarrow \gamma X(1835) \rightarrow \gamma\eta'\pi^+\pi^-$. The uncertainties are statistical only.

	N_{obs}	$\varepsilon / \%$	$\text{Br} / 10^{-5}$
$\eta' \rightarrow \eta\pi^+\pi^-$	1972 ± 104	10.28	4.23 ± 0.23
$\eta' \rightarrow \gamma\pi^+\pi^-$	2801 ± 217	16.20	2.16 ± 0.17

The uncertainty on the number of $\psi(2S)$ events was determined to be 0.53% [159] by counting $\psi(2S)$ inclusive decays, and the efficiency of the particle identification was determined to be 1% per track using the control sample $J/\psi \rightarrow \pi^+\pi^-\pi^0$ [211]. Similarly, the uncertainty on the tracking efficiency of a single charged pion was determined using the reactions $J/\psi \rightarrow p\bar{p}\pi^+\pi^-$ and $J/\psi \rightarrow \pi^+\pi^-\pi^0$ for different momentum ranges, and the uncertainty was determined to be 1% per track [212, 213]. The photon reconstruction efficiency was determined using the three control samples $\psi(2S) \rightarrow \pi^+\pi^- (J/\psi \rightarrow \rho^0\pi^0)$, $\psi(2S) \rightarrow \pi^0\pi^0 (J/\psi \rightarrow l^+l^-)$ and $J/\psi \rightarrow \rho^0\pi^0$ giving a consistent uncertainty of 1% per photon [214]. Additional uncertainties come from the branching ratios of the $\eta' \rightarrow \eta\pi^+\pi^-$, $\eta' \rightarrow \gamma\pi^+\pi^-$ and $\eta \rightarrow \gamma\gamma$ decays, which are 1.2%, 1.4% and 0.5%, respectively [6]. Also the radiative decays $\psi(2S) \rightarrow \gamma X$ cause a systematic uncertainty of 2.4%, 2.8%, 2.5% and 13.9% for the χ_{c0} , χ_{c1} , χ_{c2} and η_c , respectively [6]. Table 5.15 gives an overview of all the mentioned uncertainties, which are all independent of the specific event selection, including the total uncertainty coming from these sources.

All other systematic uncertainties arise from the chosen event selection criteria, and the corresponding uncertainties are estimated by varying the criteria around their optimized values. A Barlow test [215, 216] is performed to check whether any observed difference in the determined branching ratios can be explained by statistical effects. In this test, the difference between the branching ratio Br_{alt} , obtained with an alternative selection criterion and the nominal value Br_{nom} is weighted by the uncorrelated uncertainty of the difference:

$$\mathcal{D} = \frac{|\text{Br}_{\text{nom}} - \text{Br}_{\text{alt}}|}{\sqrt{|\sigma_{\text{nom}}^2 - \sigma_{\text{alt}}^2|}} \quad (5.64)$$

An alternative selection criterion is considered to give a significant systematic uncertainty if any of the alternative cuts results in $\mathcal{D} > 2$.

In a case where a test gives a significant deviation, a systematic uncertainty for this

Table 5.15.: Systematic uncertainties from the number of $\psi(2S)$ events, tracking efficiency, particle identification, photon reconstruction and branching ratios in %.

	$\eta' \rightarrow \eta\pi^+\pi^-$					$\eta' \rightarrow \gamma\pi^+\pi^-$				
	χ_{c0}	χ_{c1}	χ_{c2}	η_c	X	χ_{c0}	χ_{c1}	χ_{c2}	η_c	X
Number of $\psi(2S)$			0.6					0.6		
PID			4.0					4.0		
Tracking			4.0					4.0		
γ Reconstruction			3.0					2.0		
Br_{sub}			1.3					1.4		
$\text{Br}(\psi(2S) \rightarrow \gamma X)$	2.4	2.8	2.5	13.9	–	2.4	2.8	2.5	13.9	–
Total External	7.0	7.2	7.0	15.4	6.6	6.7	6.8	6.7	15.2	6.2

criterion is calculated by considering the ratios R_i between the nominal value and the alternative values Br_i

$$R_i = \frac{\text{Br}_i}{\text{Br}_{\text{nom}}}, \quad (5.65)$$

which have a relative uncertainty of

$$\frac{\Delta R_i}{R_i} = \sqrt{\left(\frac{\Delta \text{Br}_i}{\text{Br}_i}\right)^2 + \left(\frac{\Delta \text{Br}_{\text{nom}}}{\text{Br}_{\text{nom}}}\right)^2 - 2\rho_i \left(\frac{\Delta \text{Br}_i}{\text{Br}_i}\right) \left(\frac{\Delta \text{Br}_{\text{nom}}}{\text{Br}_{\text{nom}}}\right)}. \quad (5.66)$$

Here, ρ_i is the correlation between the two branching ratios, coming from the common number of events between the two samples. This correlation factor is calculated as

$$\rho_i = \sqrt{\min\left(\frac{N_{\text{obs},i}}{N_{\text{obs,nom}}}, \frac{N_{\text{obs,nom}}}{N_{\text{obs},i}}\right)}. \quad (5.67)$$

The systematic uncertainty for the criterion under consideration is then defined by the standard deviation of a weighted average over the ratios R_i , given by

$$\sigma_R^2 = \frac{\sum_i (\Delta R_i)^{-2} (1 - R_i)^2}{\sum_i (\Delta R_i)^{-2}}. \quad (5.68)$$

This procedure is applicable for all the considered resonances with a significant observation. For the χ_{c0} case, the largest uncertainty between the χ_{c1} and χ_{c2} is taken as the systematic uncertainty. For the η_c , the systematic uncertainty is determined separately for the constructive and destructive interference, and the larger of the two is used in the end. In the following, the performed systematic checks for the selection criteria are presented and the resulting values are listed in Table 5.16.

5.6.1. Assignment of the η' Candidate

As mentioned before, every possible combination of pions and photons is considered when defining the η' candidate. To estimate an uncertainty for this procedure, the signal MC is used, where the generated and reconstructed four momenta of the participating particles can be matched. As this procedure can give a false match for events with large differences between the reconstructed and generated momenta the estimated misidentification rate has an uncertainty. As a conservative estimate, 1.5 times the misidentification rate is chosen as the systematic uncertainty, resulting in an uncertainty of 0.6 % and 3.5 % for the $\eta' \rightarrow \eta\pi^+\pi^-$ and $\eta' \rightarrow \gamma\pi^+\pi^-$ channels, respectively.

Table 5.16.: Systematic uncertainties coming from the event selection criteria in %. Entries marked with "-" are not applicable and entries marked with "*" show no systematic effect according to the Barlow test.

	$\eta' \rightarrow \eta\pi^+\pi^-$					$\eta' \rightarrow \gamma\pi^+\pi^-$				
	χ_{c0}	χ_{c1}	χ_{c2}	η_c	X	χ_{c0}	χ_{c1}	χ_{c2}	η_c	X
External	7.0	7.2	7.0	15.4	6.6	6.7	6.8	6.7	15.2	6.2
η' Combinatoric	0.6	0.6	0.6	0.6	0.6	3.5	3.5	3.5	3.5	3.5
χ^2 Cut	1.3	0.4	1.3	0.7	1.8	2.0	0.5	2.0	3.8	11.7
Min. γ Energy	0.5	0.2	0.5	*	1.8	5.1	0.7	5.1	2.0	2.2
J/ψ Recoil Veto	1.2	*	1.2	0.6	20.5	0.2	0.2	*	*	23.7
J/ψ Veto 4π	-	-	-	-	-	0.8	0.1	0.8	*	*
ρ^0 Cut	-	-	-	-	-	0.4	0.1	0.4	0.7	0.9
η' Cut	1.3	0.5	1.3	1.8	5.2	2.4	0.2	2.4	2.9	10.5
SB distance	2.7	0.2	2.7	0.9	0.4	2.7	0.3	2.7	5.0	5.6
Continuum	*	*	*	*	*	2.6	1.8	2.6	4.9	7.8
Fitting Models	-	0.7	6.9	1.6	8.2	-	0.2	4.4	4.4	16.4
PWA	4.8	4.8	4.8	4.8	4.8	4.8	4.8	4.8	4.8	4.8
Total	8.9	8.7	11.5	16.4	24.2	11.1	9.3	12.2	19.0	35.3

5.6.2. Kinematic Fit χ^2 Cut

The applied cut on the χ^2 of the kinematic fit might introduce a systematic uncertainty, if the χ^2 distribution has significant differences between the signal MC and the signal component in the real data. To estimate this, the value of the cut on the χ^2 is changed from the nominal values $\chi_{\text{cut},\eta' \rightarrow \eta\pi^+\pi^-}^2 = 81.4$ and $\chi_{\text{cut},\eta' \rightarrow \gamma\pi^+\pi^-}^2 = 27.8$ to values in the intervals [55; 110] and [13; 50], respectively. The Barlow test shows a significant effect for all considered resonances and the systematic uncertainties are calculated according to Equation (5.68) to be in the range of 0.4% to 11.7%. The ratios of the variation to the nominal value for the branching ratio of the decay $\chi_{c1} \rightarrow \eta'\pi^+\pi^-$ are shown in Figure 5.24 and for the other resonances in Figure A.1.

5.6.3. Minimum Photon Energy

To estimate the systematic uncertainty introduced by the cut on the minimum photon energy, the cut is varied from the nominal value of $E_{\gamma,\text{min}} = 80$ MeV to values in the range [50 MeV; 110 MeV]. Again, according to the Barlow test, a systematic effect is visible for all resonances and the systematic uncertainties are calculated in the range of 0.2% to 5.1%. The systematic studies for the χ_{c2} decay are shown in Figure 5.25 and for the other decays in Figure A.2. By far the largest effect is seen for the χ_{c2} in the $\eta' \rightarrow \gamma\pi^+\pi^-$ channel, which can be explained by the fact, that the χ_{c2} has a mass near the edge of the available phase space. The phase space at this edge is directly influenced

5. Analysis of the Decay $\psi(2S) \rightarrow \gamma\eta'\pi^+\pi^-$

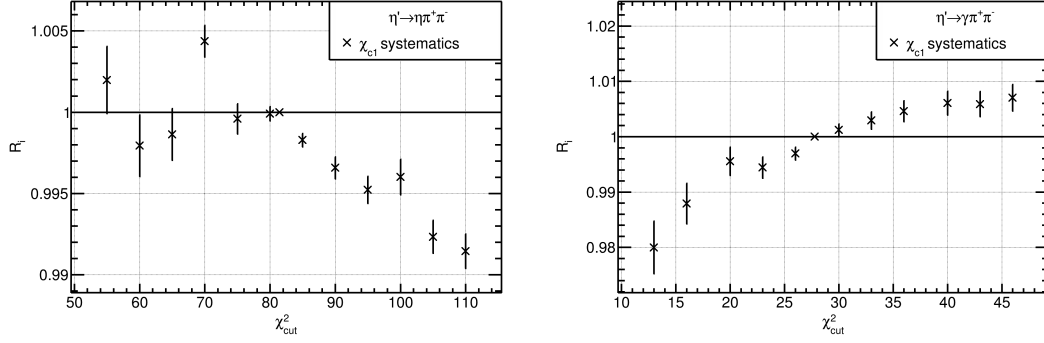


Figure 5.24.: Ratio of the variation and the nominal value for the branching ratio of the decay $\chi_{c1} \rightarrow \eta'\pi^+\pi^-$ for the cut on the χ^2 of the kinematic fit, in the $\eta' \rightarrow \eta\pi^+\pi^-$ channel (left) and the $\eta' \rightarrow \gamma\pi^+\pi^-$ channel (right).

by the minimum photon energy, with the maximum for $m_{\eta'\pi^+\pi^-}$ given by $m_{\psi(2S)} - E_{\gamma,\text{min}}$.

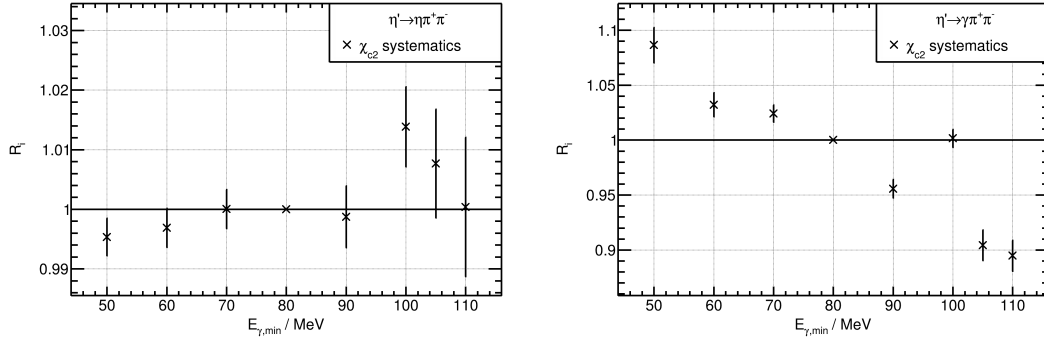


Figure 5.25.: Ratio of the variation and the nominal value for the branching ratio of the decay $\chi_{c1} \rightarrow \eta'\pi^+\pi^-$ for the minimum photon energy, in the $\eta' \rightarrow \eta\pi^+\pi^-$ channel (left) and the $\eta' \rightarrow \gamma\pi^+\pi^-$ channel (right).

5.6.4. J/ψ Veto in the $\pi^+\pi^-$ Recoil System

In both channels, a cut is applied to the J/ψ in the system recoiling against the $\pi^+\pi^-$ system of $m_{J/\psi}^{\text{rec veto}} = 20 \text{ MeV}/c^2$ and this value is varied in the range $[15 \text{ MeV}/c^2; 25 \text{ MeV}/c^2]$ in steps of $1 \text{ MeV}/c^2$. This is shown for the χ_{c1} in Figure 5.26 and for the other resonances in Figure A.3. The Barlow test shows no significant effect for the χ_{c1} in the $\eta' \rightarrow \eta\pi^+\pi^-$ channel and no effect for the χ_{c2} and η_c in the $\eta' \rightarrow \gamma\pi^+\pi^-$ channel. By far the largest systematic effect of 20.5% and 23.7% is determined for the $X(1835)$, which comes from the correlation between the background reaction $\psi(2S) \rightarrow J/\psi\pi^+\pi^-$ and the decay $X(1835) \rightarrow \eta'\pi^+\pi^-$ (described in Section 5.1). For the other resonances the systematic uncertainties lie in the range of 0.2% to 1.2%.

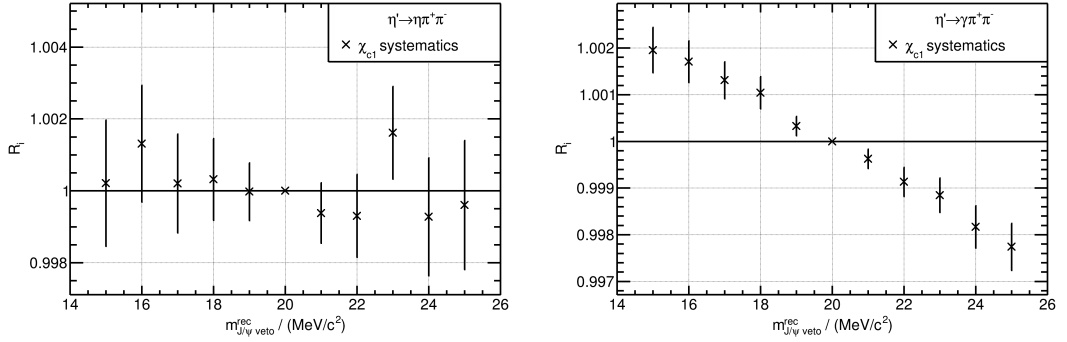


Figure 5.26.: Ratio of the variation and the nominal value for the branching ratio of the decay $\chi_{c1} \rightarrow \eta'\pi^+\pi^-$ for the veto on the J/ψ in the system recoiling against the $\pi^+\pi^-$ system, in the $\eta' \rightarrow \eta\pi^+\pi^-$ channel (left) and the $\eta' \rightarrow \gamma\pi^+\pi^-$ channel (right).

5.6.5. J/ψ Veto in the 4π System and ρ^0 Cut

In the $\eta' \rightarrow \gamma\pi^+\pi^-$ channel, an additional veto on the J/ψ in the 4π system is applied with a nominal value of $m_{J/\psi \text{ veto}} = 20 \text{ MeV}/c^2$, which is changed to values in the range $[15 \text{ MeV}/c^2; 25 \text{ MeV}/c^2]$ in steps of $1 \text{ MeV}/c^2$. This cut has no systematic effect for the η_c and $X(1835)$. In addition, the cut on the ρ^0 in the $\pi^+\pi^-$ system coming from the $\eta' \rightarrow \gamma\pi^+\pi^-$ decay is changed from its nominal value $m_{\rho^0 \text{ cut}} = 198 \text{ MeV}/c^2$ in the range $[150 \text{ MeV}/c^2; 250 \text{ MeV}/c^2]$ in steps of $10 \text{ MeV}/c^2$, which shows a systematic effect for all resonances. The systematic studies are shown in Figure 5.27 for the χ_{c1} decay and for the other decays in Figure A.4 and the resulting uncertainties are calculated to be in the range 0.1 % to 0.9 %.

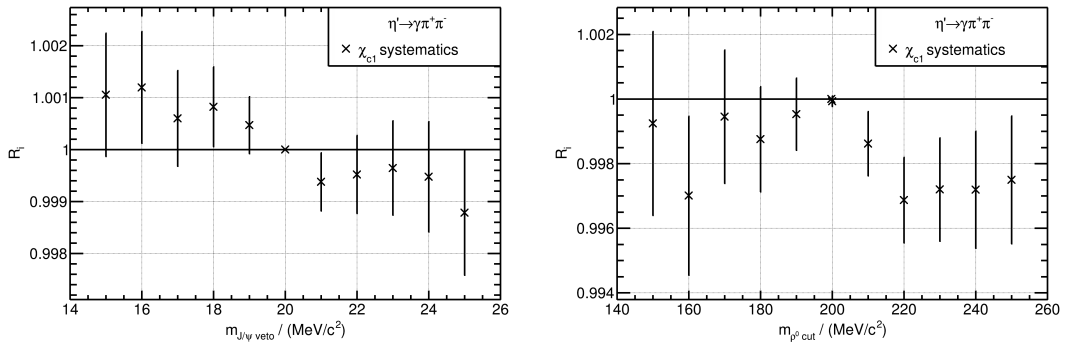


Figure 5.27.: Ratio of the variation and the nominal value for the branching ratio of the decay $\chi_{c1} \rightarrow \eta'\pi^+\pi^-$ for the veto on the J/ψ in the 4π system (left) and the cut on the ρ^0 in the $\pi^+\pi^-$ system coming from the $\eta' \rightarrow \gamma\pi^+\pi^-$ decay (right).

5.6.6. Sideband Subtraction

For the sideband subtraction it is assumed, that the non- η' background behaves in the same way in the phase space of the signal region and the sideband region. If this is not the case, the arbitrary definition of the signal and sideband regions could introduce a systematic effect. The regions are defined as

$$\text{signal: } m \in [m_{\eta',\text{PDG}} - \sigma, m_{\eta',\text{PDG}} + \sigma], \quad (5.69)$$

$$\text{left: } m \in [m_{\eta',\text{PDG}} - 2\sigma - \Delta_m, m_{\eta',\text{PDG}} - \sigma - \Delta_m], \quad (5.70)$$

$$\text{right: } m \in [m_{\eta',\text{PDG}} + \sigma + \Delta_m, m_{\eta',\text{PDG}} + 2\sigma + \Delta_m]. \quad (5.71)$$

To estimate the systematic uncertainty regarding the choice of the signal and sideband regions, the values for the η' cut, given by σ , are changed from the nominal value $\sigma_{\eta' \rightarrow \eta\pi^+\pi^-} = 9.3 \text{ MeV}/c^2$ in the range $[5 \text{ MeV}/c^2; 13 \text{ MeV}/c^2]$ and from the nominal value $\sigma_{\eta' \rightarrow \gamma\pi^+\pi^-} = 10.1 \text{ MeV}/c^2$ in the range $[5 \text{ MeV}/c^2; 15 \text{ MeV}/c^2]$. In addition, the distance between the signal and sideband regions is varied from $\Delta_m = 40 \text{ MeV}/c^2$ in the range $[30 \text{ MeV}/c^2; 60 \text{ MeV}/c^2]$. In both cases the Barlow test shows a significant effect for all considered resonances and the uncertainties are determined to lie in the range from 0.2 % to 10.5 %. The systematic variations are shown in Figure 5.28 for the χ_{c1} and in Figures A.5 and A.6 for the other resonances.

5.6.7. Continuum Background

A possible source of background that has been neglected so far is the continuum production $e^+e^- \rightarrow \gamma R$. To estimate an uncertainty for this, the scan data samples listed in Table 3.4 are used. Excluded are the samples that are close to the mass of the $\psi(2S)$ meson, compared to the BEPCII energy spread of $\sigma_{\sqrt{s}} = 1.3 \text{ MeV}$. These are the scan samples numbered six, seven and eight, with a difference of less than 2 MeV. The scan data samples are subject to the same selection criteria as the $\psi(2S)$ data sample and in the end weighted by a scaling factor w_i given by

$$w_i = \frac{\mathcal{L}_{\text{int}}^{\psi(2S)}}{\mathcal{L}_{\text{int}}^{\text{scan},i}} \cdot \left[\frac{\sqrt{\mathcal{S}_{\text{scan},i}}}{\sqrt{\mathcal{S}_{\psi(2S)}}} \right]^\lambda. \quad (5.72)$$

Here, \mathcal{L}_{int} and \sqrt{s} are the integrated luminosity and center-of-mass energy of the corresponding data sample, respectively. The exponent λ is given by an assumed line shape for the continuum cross section of the reaction $e^+e^- \rightarrow \gamma R$ given by a power law [217, 218]

$$\sigma(e^+e^- \rightarrow \gamma R) \propto (\sqrt{s})^{-\lambda}. \quad (5.73)$$

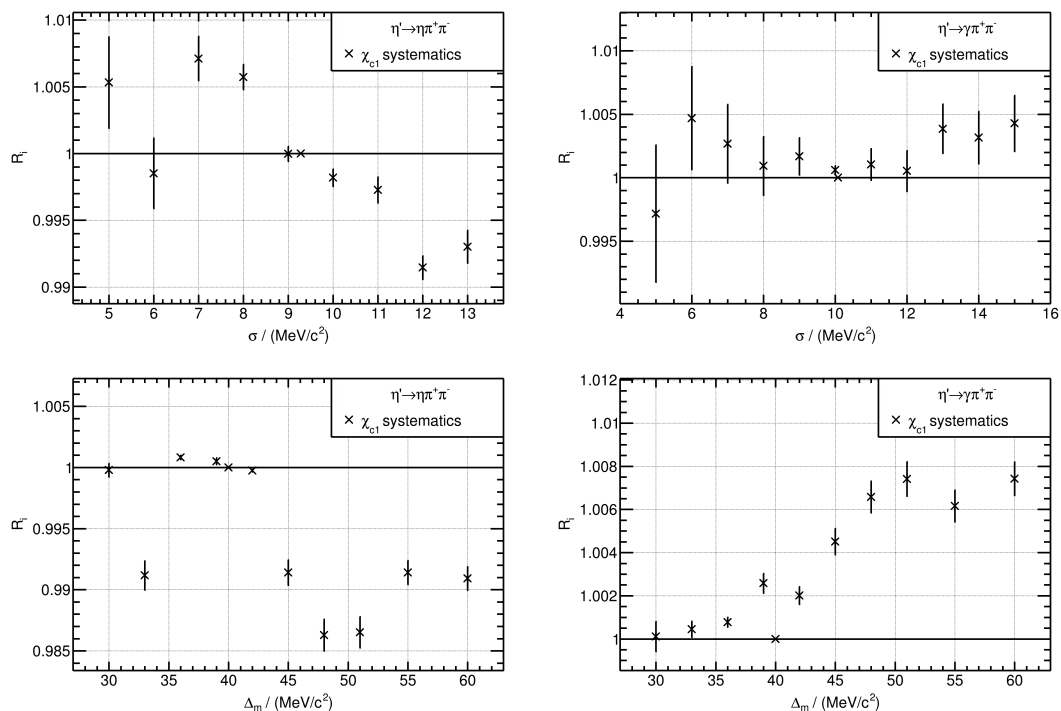


Figure 5.28.: Ratio of the variation and the nominal value for the branching ratio of the decay $\chi_{c1} \rightarrow \eta' \pi^+ \pi^-$ for the width of the signal region (top) and the distance between the signal and sideband regions (bottom), in the $\eta' \rightarrow \eta \pi^+ \pi^-$ channel (left) and the $\eta' \rightarrow \gamma \pi^+ \pi^-$ channel (right).

Using the weighted samples, the number of events in the corresponding signal regions for all considered resonances is determined for each $\lambda \in \{-5, -4, \dots, 4, 5\}$. As a conservative estimate, the largest number of continuum events is then used to determine the systematic uncertainty as the ratio of continuum events to signal events. This results in a negligible uncertainty in the $\eta' \rightarrow \eta \pi^+ \pi^-$ channel and an uncertainty of 1.8% to 7.8% in the $\eta' \rightarrow \gamma \pi^+ \pi^-$ channel.

5.6.8. Fitting Models

To estimate the systematic uncertainty arising from the chosen models used to fit the different resonances in the $\eta' \pi^+ \pi^-$ spectrum, they are replaced by alternative models. For the χ_{cJ} and η_c fits, the background polynomials are changed from linear functions to constants and quadratic functions. In addition, for the χ_{c0} , the detector resolution is adjusted within its uncertainty determined according to Equation (5.42). In the case of the η_c , the signal function is exchanged by the Breit-Wigner function with the CLEO pre-factor in Equation (5.50). For the $X(1835)$ the background is changed from the pure phase space distribution to a background given by the phase space multiplied by a linear function. Additionally, the effect of adding another Breit-Wigner function to the fit was tested, to account for a possible contribution from the $X(2120)$ or $X(2370)$.

For the resonances with a significant contribution, the systematic uncertainties are defined by the average of the relative changes in the extracted number of events. In the case of the χ_{c0} , the largest upper limit among all the considered variations is taken as the new upper limit.

5.6.9. PWA

In the determination of the branching ratios, the efficiencies were determined using the signal MC simulations presented in Section 3.5. These simulations do not include any resonances in the $\chi_{cJ} \rightarrow \eta'\pi^+\pi^-$ decay, which could affect the efficiency. Therefore, to determine a systematic uncertainty due to possible resonances, the PWA for the decay $\chi_{c2} \rightarrow \eta'\pi^+\pi^-$ with $\eta' \rightarrow \gamma\pi^+\pi^-$ presented in the next section is used. Different PWA results are compared and the weighted average of the differences of the estimated efficiencies compared to the nominal one is taken as the systematic uncertainty. This results in an uncertainty of 4.8% and this uncertainty is then also used for the other resonances as well as for the $\eta' \rightarrow \eta\pi^+\pi^-$ channel.

5.7. Search for the $\pi_1(1600)$

As mentioned in Section 2.2.5 the decay $\chi_{c1,2} \rightarrow \eta'\pi^+\pi^-$ could contain contributions from the exotic candidate $\pi_1(1600)$. To search for the $\pi_1(1600)$, the data sample resulting from the event selection has to be decomposed into contributions from different partial waves. To do this, a partial wave analysis (PWA) [26] is performed for the $\chi_{c2} \rightarrow \eta'\pi^+\pi^-$ decay. The reason for choosing the χ_{c2} over the χ_{c1} is the fact that in the χ_{c2} decay no intermediate $J^{P(C)} = 0^{+(+)}$ resonances are allowed, which reduces the complexity of the fit model. To select events coming from the decay of the χ_{c2} , only events with $m_{\eta'\pi^+\pi^-} > 3.54$ GeV are considered in the PWA. Also only the $\eta' \rightarrow \gamma\pi^+\pi^-$ channel is used, resulting in a number of events of 6129 in the signal region and 1451 in the sideband regions. According to the fit in Table 5.8, the resulting data sample still contains about 14% of non- χ_{c2} background, which is neglected in the fit.

5.7.1. PWA Amplitude

For the PWA, the so-called isobar formalism is used [219], which describes a decay amplitude \mathcal{A} as a product of two-particle decay amplitudes, which in this case can be written as

$$\mathcal{A}_{\psi(2S) \rightarrow \gamma\eta'\pi^+\pi^-} = \mathcal{A}_{\psi(2S) \rightarrow \gamma\chi_{c2}} \left(\sum_R \mathcal{A}_{\chi_{c2} \rightarrow \eta'R} \mathcal{A}_{R \rightarrow \pi^+\pi^-} + \sum_S \mathcal{A}_{\chi_{c2} \rightarrow S^\pm\pi^\mp} \mathcal{A}_{S^\pm \rightarrow \eta'\pi^\pm} \right). \quad (5.74)$$

In this way, possible resonances R and S are allowed in the $\pi^+\pi^-$ and $\eta'\pi$ system, respectively. As mentioned before, the advantage of considering the χ_{c2} decay is, that no $0^{+(+)}$ resonances are allowed. Therefore, the remaining possible quantum numbers for R are

$$J^{PC} = 2^{++}, 4^{++}, \dots \quad (5.75)$$

and for S are

$$J^P = 1^-, 2^+, 3^-, 4^+, \dots \quad (5.76)$$

Considering only resonances with $J < 3$ and demanding isospin conservation leaves the possible resonances²¹

$$R = f_2 \quad \text{and} \quad S = \pi_1, a_2. \quad (5.77)$$

To describe a general two-body decay amplitude for a decay $a \rightarrow bc$, the helicity formalism is used. In the helicity formalism, the coordinate system is chosen such that the quantization axis of the spin is aligned with the particle's momentum, which means that a particle can be identified by its total angular momentum J and its helicity λ . In this formalism, the amplitude for the decay of the particle a with total angular momentum J_a and helicity λ_a into the particles b and c with helicities λ_b and λ_c and $\bar{\lambda} = \lambda_a - \lambda_b$ can be written as [220]

$$\mathcal{A}_{a \rightarrow bc}^{J_a, \lambda_a, \lambda_b, \lambda_c} = \sqrt{\frac{2J_a + 1}{4\pi}} D_{\lambda_a, \bar{\lambda}}^{J_a*}(\varphi_b^a, \theta_b^a, -\varphi_c^a) \mathcal{F}_{\lambda_a, \lambda_b}^{J_a} \mathcal{D}(s_a). \quad (5.78)$$

Here, $D_{m', m}^{j*}$ is the complex conjugate of the Wigner D-matrix [221], $\mathcal{F}_{\lambda_b, \lambda_c}^{J_a}$ is the amplitude of the corresponding decay and $\mathcal{D}(s_a)$ is the dynamical part of the amplitude depending on the center-of-mass energy s_a of the parent particle. The appearing helicity angles ϕ_b^a and θ_b^a define the direction of the daughter particle b with respect to the momentum direction of the parent particle a in the rest frame of its parent particle [220]. To obtain the total amplitude of the two-body decay, Equation (5.78) must be summed over all occurring helicities. If the corresponding particle is part of the initial or final state the summation must be incoherent and otherwise coherent.

Since all decays considered in the PWA are either electromagnetic or strong decays, the angular momentum and spin are good quantum numbers. Therefore, the amplitudes $\mathcal{F}_{\lambda_b, \lambda_c}^{J_a}$ can be expanded in terms of the relative angular momentum L between the daughter particles and their total spin S by using Clebsch-Gordon coefficients [220]:

$$\mathcal{F}_{\lambda_b, \lambda_c}^{J_a} = \sum_{L, S} \sqrt{\frac{2L + 1}{2J_a + 1}} \langle L, 0; S, \bar{\lambda} | J_a, \bar{\lambda} \rangle \langle S_b, \lambda_b; S_c, -\lambda_c | S, \bar{\lambda} \rangle \alpha_{LS}^{J_a}, \quad (5.79)$$

²¹Considering only the J^{PC} quantum numbers and the isospin allows also resonances $S = \rho$. However, these are forbidden by the conservation of the G parity.

Here, $\alpha_{LS}^{J_a}$ is the complex amplitude of the corresponding decay and determines the strength of the individual contribution.

Although this expansion is also possible for the radiative decay $\psi(2S) \rightarrow \gamma\chi_{c2}$, it could lead to additional parameters in the fit that need to be constrained due to symmetries arising from the conservation of C and P parity. An alternative expansion that already takes this into account, is given by the multipole expansion, which for this case reads [222]:

$$\mathcal{F}_{\lambda_\gamma, \lambda_{\chi_{c2}}}^{J_{\psi(2S)}} = \sum_{J_\gamma} \sqrt{\frac{2J_\gamma + 1}{2J_{\psi(2S)} + 1}} \langle J_\gamma, \lambda_\gamma; J_{\psi(2S)}, \bar{\lambda} | J_{\chi_{c2}}, \lambda_{\chi_{c2}} \rangle \alpha_{J_\gamma}^{J_{\psi(2S)}}. \quad (5.80)$$

The sum over J_γ corresponds to different allowed multipole transitions, which in this case are the electric dipole and octupole transitions, as well as, the magnetic quadrupole transition. For the $\psi(2S) \rightarrow \gamma\chi_{c2}$ decay, the fractions of the magnetic quadrupole amplitude and the electric octupole amplitude with respect to the total amplitude were determined to be $(1.9 \pm 0.9)\%$ and $(1.0 \pm 0.6)\%$ [6], respectively. These contributions cannot be identified with the statistics of the present data sample and are therefore neglected in the PWA.

Inserting Equations (5.78) to (5.80) into Equation (5.74) and inserting the quantum numbers of the initial and final state particles gives the total intensity

$$\mathcal{I}_{\psi(2S) \rightarrow \gamma\eta'\pi^+\pi^-} = \sum_{\lambda_{\psi(2S)}} \sum_{\lambda_\gamma} \left| \sum_{\lambda_{\chi_{c2}}} \sum_{X, \lambda_X} \sum_{L, S} \mathcal{M}_{\psi(2S)} \cdot \mathcal{M}_{\chi_{c2}} \cdot \mathcal{M}_X \right|^2 \quad (5.81)$$

with the substitution $X = \{R, S\}$ and

$$\begin{aligned} \mathcal{M}_{\psi(2S)} &= \sqrt{\frac{3}{4\pi}} \langle 1, \lambda_\gamma; 1, \bar{\lambda} | 2, \lambda_{\chi_{c2}} \rangle D_{\lambda_{\psi(2S)}, \bar{\lambda}}^{1*}(\varphi_\gamma^{\psi(2S)}, \theta_\gamma^{\psi(2S)}, -\varphi_\gamma^{\psi(2S)}) \alpha_{\psi(2S)}, \\ \mathcal{M}_{\chi_{c2}} &= \sqrt{\frac{2L+1}{4\pi}} \langle L, 0; S, \lambda_X | 2, \lambda_X \rangle \langle S_X, \lambda_X; 0, 0 | S, \lambda_X \rangle \\ &\quad \cdot D_{\lambda_{\chi_{c2}}, \lambda_X}^{2*}(\varphi_X^{\chi_{c2}}, \theta_X^{\chi_{c2}}, -\varphi_X^{\chi_{c2}}) \mathcal{D}(s_{\chi_{c2}}) \alpha_{LS}^2, \\ \mathcal{M}_X &= \sqrt{\frac{2J_X+1}{4\pi}} D_{\lambda_X, 0}^{J_X*}(\varphi_{\eta', \pi^+}^X, \theta_{\eta', \pi^+}^X, -\varphi_{\eta', \pi^+}^X) \mathcal{D}(s_X) \alpha_{J_X S}^{J_X}. \end{aligned} \quad (5.82)$$

The only missing part is the description of the dynamical part, which in this simple ansatz is given for all resonances X by a relativistic Breit-Wigner function [6]

$$\mathcal{D}(s_X) = \frac{m_X \Gamma_X \cdot p(s_X)^L B_L(p(s_X)/p_0)}{m_X^2 - s_X - im_X \Gamma(s_X)} \quad (5.83)$$

with the energy-dependent width given by [6]

$$\Gamma(s_X) = \Gamma_X \frac{1}{8\pi} \frac{p(s_X)^{2L+1}}{\sqrt{s_X}} B_L(p(s_X)/p_0)^2. \quad (5.84)$$

Here, L is the angular momentum and $p(s_X)$ is the absolute momentum of the daughter particles b and c , given by [6]

$$p(s_X) = \frac{1}{2\sqrt{s_X}} \sqrt{(s_X - (m_b + m_c)^2)(s_X - (m_b - m_c)^2)}. \quad (5.85)$$

The Blatt-Weisskopf barrier factors [223] $B_L(p(s_X)/p_0)$ are given with respect to a momentum scale chosen to be $p_0 = 0.3 \text{ GeV}/c$, and they are listed for different angular momenta L in Appendix A.2. For the χ_{c2} , the dynamical part is a constant, since the decay of the χ_{c2} is already included in the signal MC sample that is used for the normalization of the PWA model.

In the PWA, the masses m_X and widths Γ_X of all participating resonances are fixed to the values taken from the PDG [6] and the amplitudes of charge conjugate decays (e.g. $\chi_{c2} \rightarrow a_2^+ \pi^-$ and $\chi_{c2} \rightarrow a_2^- \pi^+$) are constrained to be equal. The free parameters in the fit are then the products of the complex amplitudes for any given decay chain.

5.7.2. Likelihood Construction

To determine the best values for the amplitudes, an extended maximum likelihood fit is performed using the AMPTOOLS library [224]. The extended likelihood for a data sample consisting of N_{data} events with observations \vec{x}_i and parameters $\vec{\theta}$ is defined as

$$\mathcal{L}(\vec{\theta}) = \frac{e^{-\mu} \mu^{N_{\text{data}}}}{N_{\text{data}}!} \prod_{i=1}^{N_{\text{data}}} \mathcal{P}(\vec{x}_i; \vec{\theta}), \quad (5.86)$$

with the predicted number of events μ and the probability density function $\mathcal{P}(\vec{x}_i; \vec{\theta})$. The predicted number of events is given by an integral of the intensity $\mathcal{I}(\vec{x}, \vec{\theta})$ over the whole available phase space R as [224]

$$\mu = \int_R \mathcal{I}(\vec{x}, \vec{\theta}) \varepsilon(\vec{x}) d\vec{x}, \quad (5.87)$$

taking into account the efficiency $\varepsilon(\vec{x})$. The probability density function is defined by [224]

$$\mathcal{P}(\vec{x}_i; \vec{\theta}) = \frac{1}{\mu} \mathcal{I}(\vec{x}_i, \vec{\theta}) \varepsilon(\vec{x}_i) \quad (5.88)$$

and the intensity is given by Equation (5.81). In order to maximize \mathcal{L} , the integral in Equation (5.87) must be calculated, which is impossible to do analytically as the efficiency

function $\varepsilon(\vec{x}_i)$ is not known a priori. However, it can be solved by using the mean value theorem for integrals [224, 225]:

$$\mu = \int_{\mathcal{R}} \mathcal{I}(\vec{x}, \vec{\theta}) \varepsilon(\vec{x}) d\vec{x} = \mathcal{R} \langle \mathcal{I}(\vec{x}, \vec{\theta}) \varepsilon(\vec{x}) \rangle \approx \frac{\mathcal{R}}{N_{\text{gen}}} \sum_{i=1}^{N_{\text{acc}}} \mathcal{I}(\vec{x}_i, \vec{\theta}). \quad (5.89)$$

Here, \mathcal{R} is the Lebesgue measure of the phase space [226]. The approximation in Equation (5.89) is given by a random sampling of the intensity over the phase space using a MC sample with N_{gen} generated and N_{acc} accepted events. The factor \mathcal{R} can be eliminated by rescaling the intensity, which introduces an additional factor into the likelihood. However, this factor does not affect the maximization of the likelihood.

So far, the likelihood construction assumed that the data sample contains only signal events. However, as described in Section 5.2.2, the data sample still contains non- η' background that can be estimated from the sidebands. To account for this in the PWA, the likelihood in Equation (5.86) must be adjusted according to [224]

$$\mathcal{L}(\vec{\theta}) = \frac{e^{-(\mu+\beta)} (\mu + \beta)^{N_{\text{sig}}}}{N_{\text{sig}}!} \prod_{i=1}^{N_{\text{sig}}} \mathcal{P}(\vec{x}_i; \vec{\theta}) \cdot \prod_{j=1}^{N_{\text{bg}}} \mathcal{P}(\vec{x}_j; \vec{\theta})^{-w_j}. \quad (5.90)$$

Here, N_{sig} is the number of events in the signal region, N_{bg} is the number of events in the sideband regions and w_j is the weight of the j -th sideband event. The predicted number of background events β is given by a sum over the weights of the events in the sidebands as

$$\beta = \sum_{j=1}^{N_{\text{bg}}} w_j. \quad (5.91)$$

Instead of maximizing the likelihood, it is often computationally useful to minimize the negative logarithm of the likelihood (NLL) instead, which is given by [224]

$$-\ln[\mathcal{L}(\vec{\theta})] = -\sum_{i=1}^{N_{\text{sig}}} \ln \mathcal{I}(\vec{x}_i; \vec{\theta}) + \sum_{j=1}^{N_{\text{bg}}} w_j \ln \mathcal{I}(\vec{x}_j; \vec{\theta}) + \mu - N_{\text{sig}} \ln(\mu + \beta) + (N_{\text{sig}} - \beta) \ln \mu, \quad (5.92)$$

after inserting Equation (5.88) into Equation (5.90) and dropping the terms that do not depend on $\vec{\theta}$ and therefore do not play a role in minimizing $-\ln(\mathcal{L})$.

The NLL in Equation (5.92) is minimized using MINUIT [202] for a total of 50 randomized initial amplitude parameters and the result with the best NLL is chosen as the nominal result. The results of the PWA are presented in the next section.

5.7.3. PWA Results

In Figure 5.29 the invariant masses of the $\pi^+\pi^-$ and $\eta'\pi^+$ systems are shown. In the $\pi^+\pi^-$ spectrum there is a distinct peak around $1.3 \text{ GeV}/c^2$, corresponding to the mass of

the $f_2(1270)$ included in the fit. There is also an enhancement at high masses around $2.3 \text{ GeV}/c^2$, which is in the mass range of several possible f_2 states. Systematic tests showed that at least three resonances are needed to describe this peak. These are the $f_2(2150)$ and $f_2(1950)$ on the one hand, and either the $f_2(2300)$ or the $f_2(2340)$ on the other, both of which result in a similar NLL. The η'/π spectrum shows no clear resonances and testing the established $a_2(1320)$ and $a_2(1700)$ shows no significant improvement of the NLL. Including the $\pi_1(1600)^\pm$ in the fit gives a change of the NLL of $2\Delta \ln(\mathcal{L}) = 6.01$ with two additional parameters, corresponding to a statistical significance of 1.96σ .

In Figures 5.29 to 5.31 the best result with all significant resonances as well as the $\pi_1(1600)$ is shown as projections onto the kinematic variables of interest. These are on the one hand side the helicity angles needed to describe the radiative decay $\psi(2S) \rightarrow \gamma\chi_{c2}$ given by $\phi_{\gamma_{\text{rad}}}$ and $\theta_{\gamma_{\text{rad}}}$. On the other hand, the two decay chains $\chi_{c2} \rightarrow \eta' R, R \rightarrow \pi^+\pi^-$ and $\chi_{c2} \rightarrow S^\pm\pi^\mp, S^\pm \rightarrow \eta'\pi^\pm$ are described by the angles $(\phi_{\eta'\pi^+\pi^-}, \theta_{\eta'\pi^+\pi^-}, \phi_{\pi^+\pi^-}, \theta_{\pi^+\pi^-})$ and $(\phi_{\pi^+\pi^-}, \theta_{\pi^+\pi^-}, \phi_{\eta'\pi^+}, \theta_{\eta'\pi^+})$, respectively. The ϕ helicity angles are presented in Figure 5.30 and in each case the fit gives a reasonable description of the data with a χ^2/nbins close to one. While the overall differences between the fit and the data are larger for the θ angles, depicted in Figure 5.31, the fit still gives a reasonable description of the data. The largest differences are present in the projections onto the invariant masses in Figure 5.29, although the overall shape of the data is well described. The differences in the $m_{\eta'\pi^+\pi^-}$ spectrum are mainly due to the neglected background. Since this background may have different quantum numbers than the χ_{c2} , it could also influence the other spectra, by giving possible contributions from additional partial waves.

As the $\pi_1(1600)^\pm$ contribution is found to be insignificant, a likelihood scan is performed to determine an upper limit on the number of $\pi_1(1600)^\pm$ events. This scan is shown in Figure 5.32. The scan is fitted with a Gaussian function and the upper limit at a confidence level of 90% is extracted according to Equation (5.44), resulting in

$$N_{\pi_1(1600)^\pm}^{\text{UL, stat.}} = 237.8. \quad (5.93)$$

This upper limit only includes the statistical uncertainty coming from the PWA fit. To determine the uncertainty due to the choice of the PWA model, the results of different tested models are compared and a weighted average is taken as the systematic uncertainty. This results in a systematic uncertainty on the efficiency of 4.8% and on the number of extracted $\pi_1(1600)^\pm$ events of 79.5%. To account for this in the determination of the upper limit, the fitted likelihood profile is convolved with a Gaussian function with a

Table 5.17.: List of resonances that were included in the PWA (top) and additional tested resonances that were not included in the nominal result (bottom). Listed are the $J^{P(C)}$ quantum numbers, the mass m_{PDG} and width Γ_{PDG} taken from the PDG [6], as well as the fit fraction f .

Resonance	Subsystem	$J^{P(C)}$	Mass	Width	Fit Fraction
			$m_{\text{PDG}} / (\text{MeV}/c^2)$	$\Gamma_{\text{PDG}} / \text{MeV}$	
$f_2(1270)$	$\pi^+\pi^-$	2^{++}	1275.4 ± 0.8	$186.6^{+2.8}_{-2.2}$	19.5
$f_2(1950)$	$\pi^+\pi^-$	2^{++}	1936 ± 12	464 ± 24	23.3
$f_2(2150)$	$\pi^+\pi^-$	2^{++}	2157 ± 12	152 ± 30	61.8
$f_2(2300)$	$\pi^+\pi^-$	2^{++}	2297 ± 28	150 ± 40	18.9
$\pi_1(1600)^\pm$	$\eta'\pi^\pm$	1^-	1645^{+40}_{-17}	370^{+50}_{-60}	3.9
sum					127.4
$f'_2(1525)$	$\pi^+\pi^-$	2^{++}	1517.3 ± 2.4	72^{+7}_{-6}	
$f_2(1565)$	$\pi^+\pi^-$	2^{++}	1571 ± 13	132 ± 23	
$f_2(2010)$	$\pi^+\pi^-$	2^{++}	2010^{+60}_{-80}	200 ± 60	
$f_2(2340)$	$\pi^+\pi^-$	2^{++}	2346^{+21}_{-10}	331^{+27}_{-18}	
$a_2(1320)^\pm$	$\eta'\pi^\pm$	2^+	1318.2 ± 0.6	107 ± 5	
$a_2(1700)^\pm$	$\eta'\pi^\pm$	2^+	1706 ± 14	380^{+60}_{-50}	

width given by the systematic uncertainty. The convolved likelihood is also shown in Figure 5.32 and the upper limit at a confidence level of 90 % is calculated as

$$N_{\pi_1(1600)^\pm}^{\text{UL}} = 322.9. \quad (5.94)$$

From this, the product of the branching ratios of the decays $\chi_{c2} \rightarrow \pi_1(1600)^\pm\pi^\mp$ and $\pi_1(1600)^\pm \rightarrow \eta'\pi^\pm$ is determined to be

$$\text{Br}(\chi_{c2} \rightarrow \pi_1(1600)^\pm\pi^\mp) \cdot \text{Br}(\pi_1(1600)^\pm \rightarrow \eta'\pi^\pm) < 3.26 \times 10^{-5} \quad (5.95)$$

at a 90 % confidence level. This value can be compared with the results from a CLEO analysis of the decay $\chi_{c1} \rightarrow \eta'\pi^+\pi^-$ [122], which determined

$$\text{Br}(\chi_{c1} \rightarrow \pi_1(1600)^\pm\pi^\mp) \cdot \text{Br}(\pi_1(1600)^\pm \rightarrow \eta'\pi^\pm) = (2.9 \pm 0.8) \times 10^{-4}. \quad (5.96)$$

Combining these two results gives the ratio of the production branching ratios

$$R = \frac{\text{Br}(\chi_{c2} \rightarrow \pi_1(1600)^\pm\pi^\mp) \cdot \text{Br}(\pi_1(1600)^\pm \rightarrow \eta'\pi^\pm)}{\text{Br}(\chi_{c1} \rightarrow \pi_1(1600)^\pm\pi^\mp) \cdot \text{Br}(\pi_1(1600)^\pm \rightarrow \eta'\pi^\pm)} \quad (5.97)$$

$$= \frac{\text{Br}(\chi_{c2} \rightarrow \pi_1(1600)^\pm\pi^\mp)}{\text{Br}(\chi_{c1} \rightarrow \pi_1(1600)^\pm\pi^\mp)} < 7.8 \% \quad (5.98)$$

at a confidence level of 90 %.

In addition, the projections on the invariant mass spectra obtained in this thesis can be

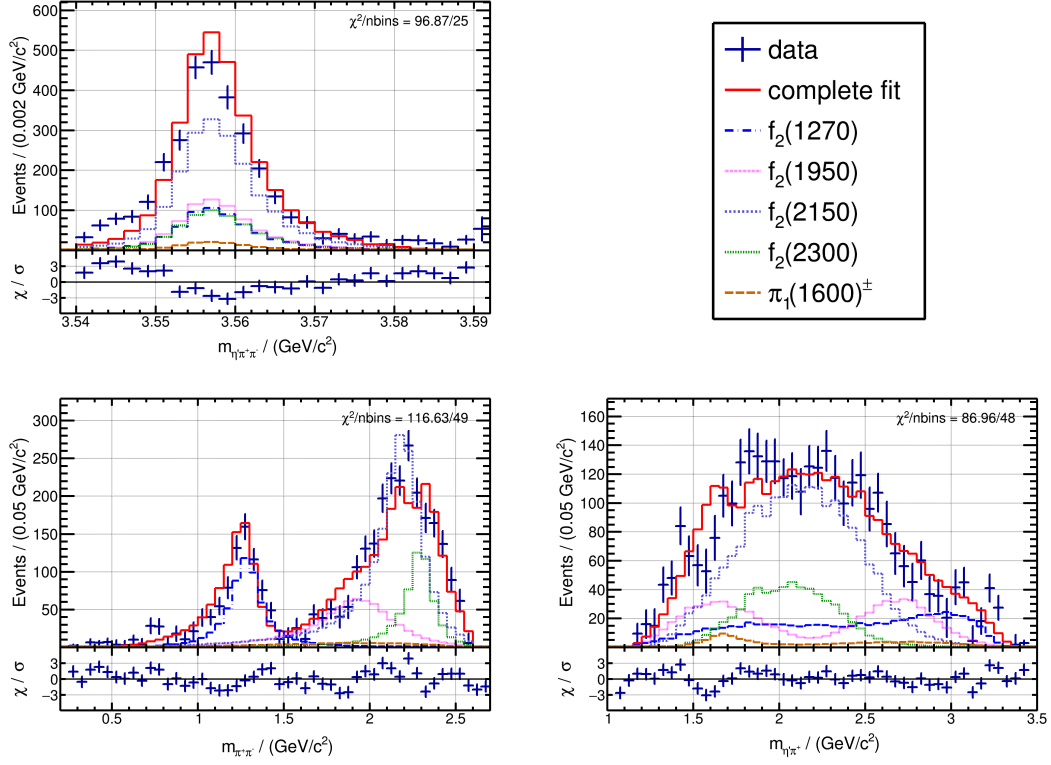


Figure 5.29.: Results of the PWA for the decay $\chi_{c2} \rightarrow \eta' \pi^+ \pi^-$ for the projections on the invariant masses of the $\eta' \pi^+ \pi^-$ (top left), $\pi^+ \pi^-$ (bottom left) and $\eta' \pi^+$ (bottom right) system. The data is shown as the blue points with uncertainties, the total fit is shown as the red solid line and the different contributions are shown with the colors given in the legend. On the bottom of each plot the difference between the fit and the data χ divided by the uncertainty of the data σ is shown.

compared with a recent BESIII PWA of the decay $\chi_{c1} \rightarrow \eta' \pi^+ \pi^-$ [227]. As can be seen in Figure 5.33, the projections show significantly different features. The biggest difference comes from the contributions of the $f_0(500)$ and $f_0(980)$ (referred to as "pipiswave η' " in the legend) in the low $m_{\pi^+ \pi^-}$ region for the χ_{c1} , while for the χ_{c2} there are basically no events in this region. In both PWA results, a major contribution comes from the $f_2(1270)$, which is known to have a large branching ratio for the decay into $\pi^+ \pi^-$ of $84.3^{+2.8}_{-1.0} \%$. While in the χ_{c2} PWA several f_2 resonances are needed to describe the structure at high $m_{\pi^+ \pi^-}$ masses, in the χ_{c1} case this region is described by a few small f_0 resonances. Also the projections onto the $\eta' \pi$ mass look significantly different, with the maximum in the middle for the χ_{c1} and rising structures towards both edges in the χ_{c2} case. In addition, a clear peak around 1.7 GeV is visible for the χ_{c2} , which is described by the contribution from the $\pi_1(1600)$. A possible reason why the $\pi_1(1600)$ is needed in the case of the χ_{c1} is that the production $\chi_{c1} \rightarrow \pi_1(1600)^\pm \pi^\mp$ is possible in S-wave, while $\chi_{c2} \rightarrow \pi_1(1600)^\pm \pi^\mp$ requires D-wave production.

5. Analysis of the Decay $\psi(2S) \rightarrow \gamma\eta'\pi^+\pi^-$

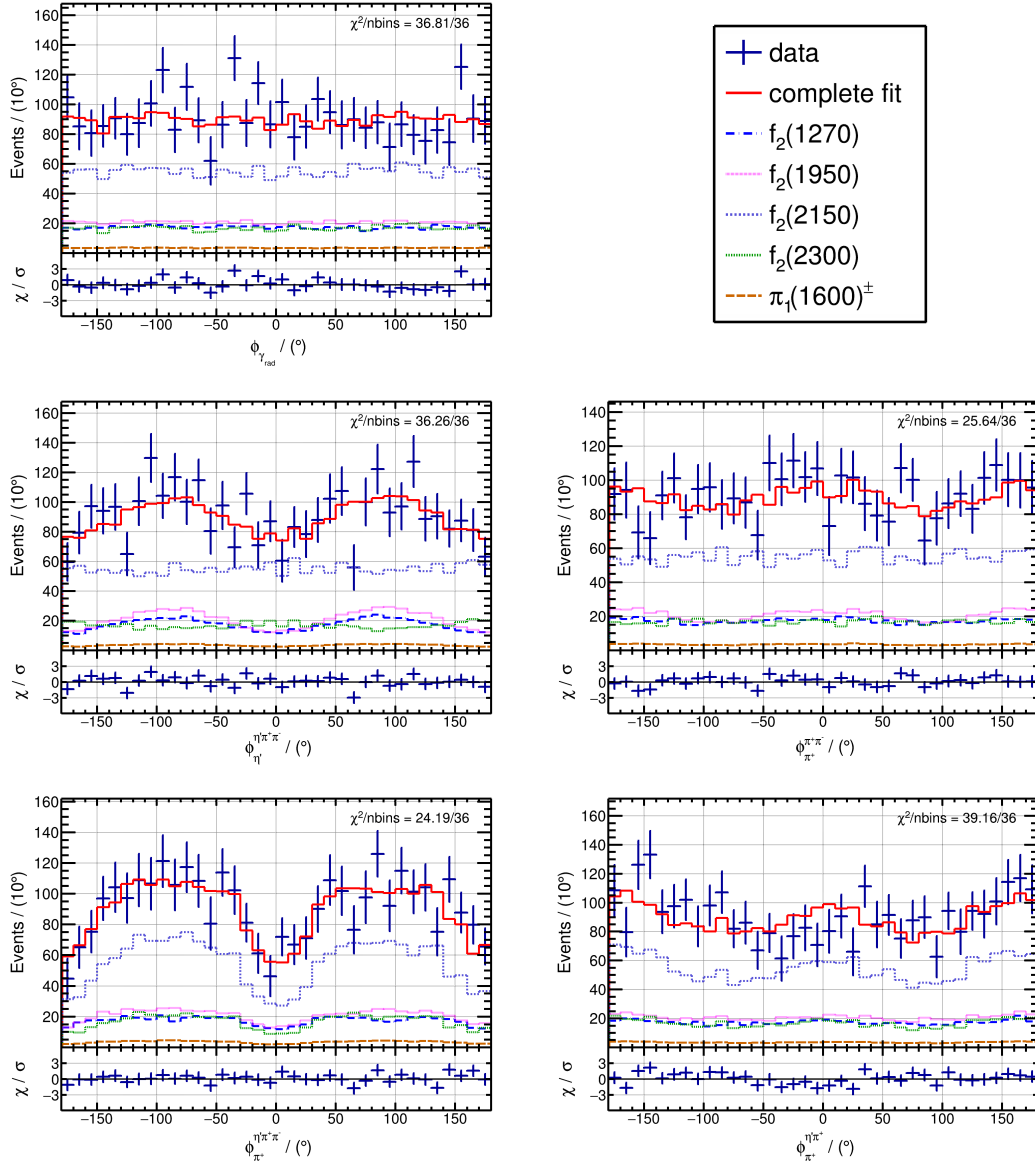


Figure 5.30.: Results of the PWA for the decay $\chi_{c2} \rightarrow \eta'\pi^+\pi^-$ for the projections on the azimuthal angle of the radiative photon in the center-of-mass system (top left), of the η' in the $\eta'\pi^+\pi^-$ system (middle left), of the π^+ in the $\pi^+\pi^-$ system (middle right), of the π^+ in the $\eta'\pi^+\pi^-$ system (bottom left) and of the π^+ in the $\eta'\pi^+$ system (bottom right). The data is shown as the blue points with uncertainties, the total fit is shown as the red solid line and the different contributions are shown with the colors given in the legend. On the bottom of each plot the difference between the fit and the data χ divided by the uncertainty of the data σ is shown.

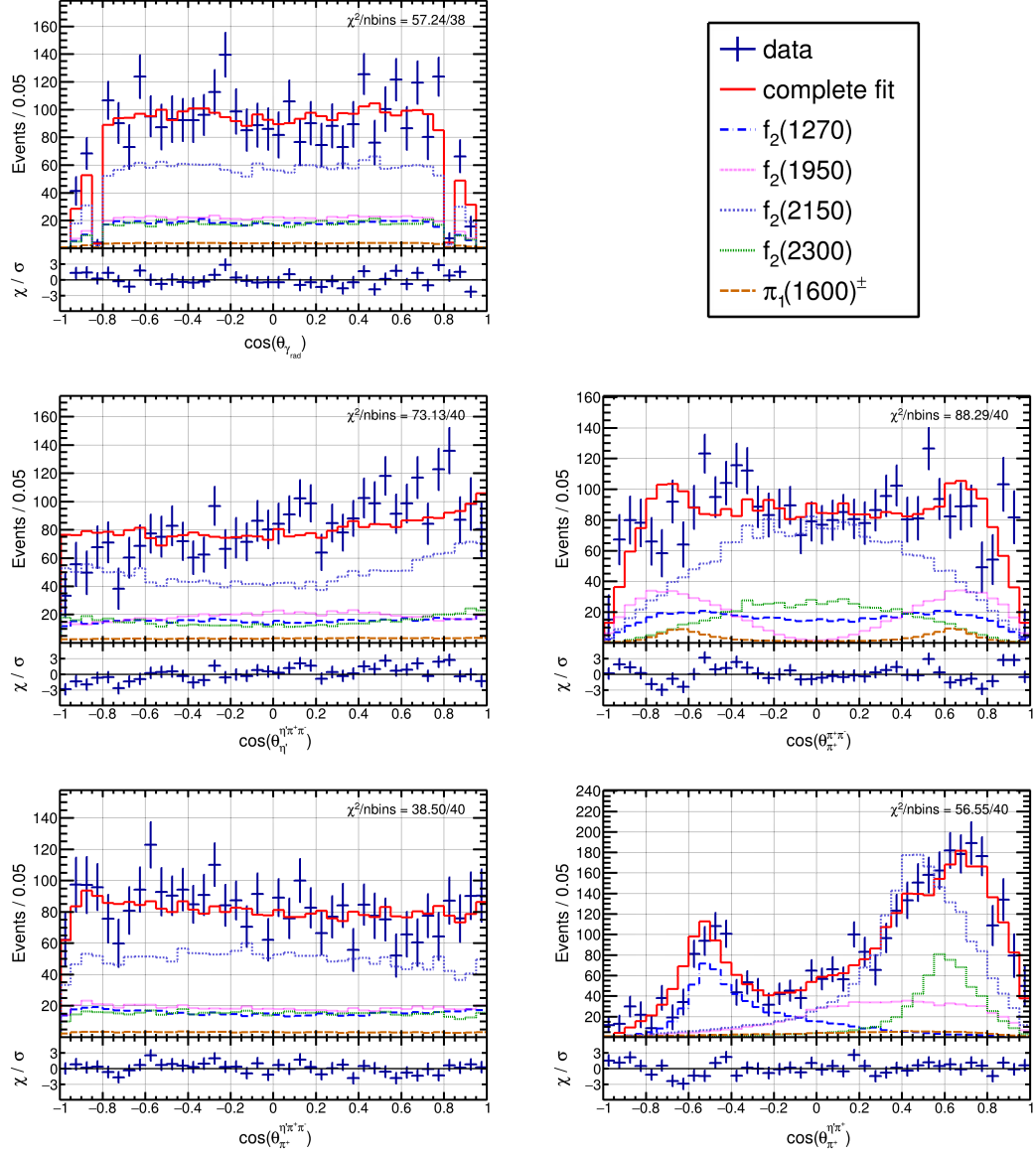


Figure 5.31.: Results of the PWA for the decay $\chi_{c2} \rightarrow \eta' \pi^+ \pi^-$ for the projections on the polar angle of the radiative photon in the center-of-mass system (top left), of the η' in the $\eta' \pi^+ \pi^-$ system (middle left), of the π^+ in the $\pi^+ \pi^-$ system (middle right), of the π^+ in the $\eta' \pi^+ \pi^-$ system (bottom left) and of the π^+ in the $\eta' \pi^+$ system (bottom right). The data is shown as the blue points with uncertainties, the total fit is shown as the red solid line and the different contributions are shown with the colors given in the legend. On the bottom of each plot the difference between the fit and the data χ divided by the uncertainty of the data σ is shown.

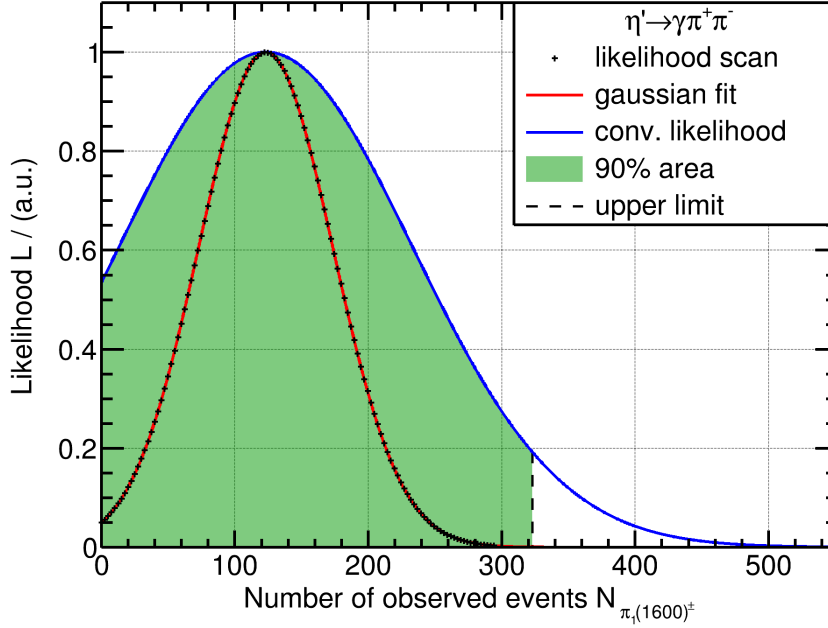


Figure 5.32.: Likelihood scan for the $\pi_1(1600)$. The scan values are shown as the black markers and the fit with a Gaussian function is shown as the red solid line. The fitted profile is convolved with a Gaussian function to consider the systematic uncertainty and the convolved likelihood is shown as the blue solid line. The 90 % area under the convolved likelihood is shown in green and the resulting upper limit is marked with the black dashed line.

5.8. Results

In the context of this analysis, branching ratios were determined for the decays $\chi_{cJ} \rightarrow \eta'\pi^+\pi^-$, $\eta_c \rightarrow \eta'\pi^+\pi^-$ and $X(1835) \rightarrow \eta'\pi^+\pi^-$ using the two decay modes of the $\eta' \rightarrow \eta\pi^+\pi^-$ and $\eta' \rightarrow \gamma\pi^+\pi^-$. To combine the information from the two decay modes, a weighted average is calculated for the product branching ratio $\text{Br}_R = \text{Br}(\psi(2S) \rightarrow \gamma R) \cdot \text{Br}(R \rightarrow \eta'\pi^+\pi^-)$. This is done according to [228]

$$\overline{\text{Br}}_R = \left(\sum_{i=0}^1 \text{Br}_{R,i} \cdot \sum_{j=0}^1 (V_R^{-1})_{ij} \right) \left(\sum_{i=0}^1 \sum_{j=0}^1 (V_R^{-1})_{ij} \right)^{-1}, \quad (5.99)$$

with an uncertainty of

$$\Delta \overline{\text{Br}}_R = \left(\sum_{i=0}^1 \sum_{j=0}^1 (V_R^{-1})_{ij} \right)^{-0.5}. \quad (5.100)$$

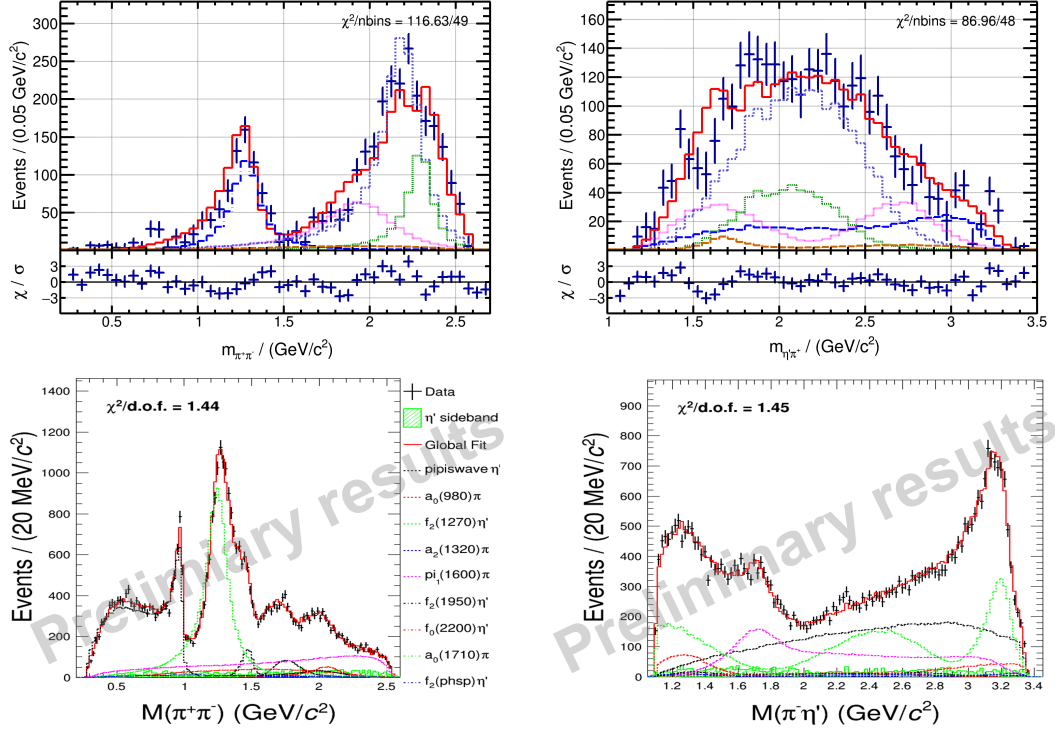


Figure 5.33.: Comparison of the results of the PWA for the decays $\chi_{c2} \rightarrow \eta' \pi^+ \pi^-$ obtained in this work (top) and $\chi_{c1} \rightarrow \eta' \pi^+ \pi^-$ [227] (bottom). Shown are the projections on the invariant masses of the $\pi^+ \pi^-$ (left) and $\eta' \pi^+$ (right) systems. In both cases the data is shown as points with uncertainties and the total fit is shown as the red solid line. For each PWA the single contributions are given by the individual legends.

Here, $\text{Br}_{R,i}$ is the branching ratio for the resonance $R \in \{\chi_{c1}, \chi_{c2}, \eta_c, X(1835)\}$ determined in the two η' channels $i \in \{\eta, \gamma\}$ and V_R is the covariance matrix given by [229]

$$V_R = \begin{pmatrix} \sigma_{R,\text{tot},\eta}^2 & \text{cov}_R \\ \text{cov}_R & \sigma_{R,\text{tot},\gamma}^2 \end{pmatrix}. \quad (5.101)$$

$\sigma_{R,\text{tot},i}$ is the total uncertainty, calculated by quadratically adding the statistical and systematic uncertainties, and cov_R is the covariance between the two different η' channels, calculated as

$$\text{cov}_R = \text{Br}_{R,\eta} \text{Br}_{R,\gamma} \rho_R^2. \quad (5.102)$$

The correlated relative uncertainty ρ_R between the two channels is given by the uncertainties due to the number of $\psi(2S)$ events, PID and tracking. In addition, the photon reconstruction is partially correlated, due to the two/three photons in the two channels. It should be noted, that this procedure can lead to biased results, if the correlated uncertainties are large in combination with a significant difference between the averaged values [229]. In such a case, this procedure leads to an average that is

smaller compared to the case without correlation. This has been tested for all calculated branching ratios, and the difference between the average with and without correlation is found to be negligible compared to the total uncertainty for all resonances.

For the χ_{c1} the product branching ratios are given by

$$\text{Br}_{\chi_{c1},\eta} = (1.623 \pm 0.018_{\text{stat}} \pm 0.090_{\text{uncor}} \pm 0.098_{\text{cor}}) \times 10^{-4} \quad (5.103)$$

$$\text{Br}_{\chi_{c1},\gamma} = (1.571 \pm 0.014_{\text{stat}} \pm 0.101_{\text{uncor}} \pm 0.095_{\text{cor}}) \times 10^{-4}, \quad (5.104)$$

which are consistent within 1σ . The first uncertainty is statistical, the second is the uncorrelated part of the systematic uncertainty and the third is the correlated systematic uncertainty. The application of the weighting procedure according to Equations (5.99) and (5.100) results in a combined branching ratio of

$$\overline{\text{Br}}_{\chi_{c1}} = (1.599 \pm 0.118) \times 10^{-4}. \quad (5.105)$$

Here, the uncertainty is the total uncertainty, since the averaging procedure combines the uncertainties and does not allow for an independent determination of the statistical and systematic uncertainties. In the case of the χ_{c2} , the ratios are calculated to be

$$\text{Br}_{\chi_{c2},\eta} = (2.619 \pm 0.093_{\text{stat}} \pm 0.248_{\text{uncor}} \pm 0.158_{\text{cor}}) \times 10^{-5} \quad (5.106)$$

$$\text{Br}_{\chi_{c2},\gamma} = (2.989 \pm 0.108_{\text{stat}} \pm 0.309_{\text{uncor}} \pm 0.180_{\text{cor}}) \times 10^{-5}. \quad (5.107)$$

These are also consistent within 1σ and result in a combined branching ratio of

$$\overline{\text{Br}}_{\chi_{c2}} = (2.757 \pm 0.265) \times 10^{-5}. \quad (5.108)$$

For the η_c , the branching ratios are calculated separately for the solutions with constructive interference

$$\text{Br}_{\eta_c,\text{constr},\eta} = (2.374 \pm 0.100_{\text{stat}} \pm 0.144_{\text{uncor}} \pm 0.143_{\text{cor}}) \times 10^{-5} \quad (5.109)$$

$$\text{Br}_{\eta_c,\text{constr},\gamma} = (3.116 \pm 0.153_{\text{stat}} \pm 0.357_{\text{uncor}} \pm 0.188_{\text{cor}}) \times 10^{-5} \quad (5.110)$$

and destructive interference

$$\text{Br}_{\eta_c,\text{destr},\eta} = (6.373 \pm 0.198_{\text{stat}} \pm 0.387_{\text{uncor}} \pm 0.384_{\text{cor}}) \times 10^{-5} \quad (5.111)$$

$$\text{Br}_{\eta_c,\text{destr},\gamma} = (5.349 \pm 0.196_{\text{stat}} \pm 0.613_{\text{uncor}} \pm 0.322_{\text{cor}}) \times 10^{-5}, \quad (5.112)$$

which are consistent within 1.9σ and 1.4σ , respectively. From this the combined branching ratios are calculated as

$$\overline{\text{Br}}_{\eta_c, \text{constr}} = (2.473 \pm 0.219) \times 10^{-5} \quad (5.113)$$

$$\overline{\text{Br}}_{\eta_c, \text{destr}} = (6.015 \pm 0.512) \times 10^{-5}. \quad (5.114)$$

The same procedure yields for the $X(1835)$

$$\text{Br}_{X(1835), \eta} = (4.228 \pm 0.225_{\text{stat}} \pm 0.989_{\text{uncor}} \pm 0.255_{\text{cor}}) \times 10^{-5} \quad (5.115)$$

$$\text{Br}_{X(1835), \gamma} = (2.161 \pm 0.168_{\text{stat}} \pm 0.750_{\text{uncor}} \pm 0.130_{\text{cor}}) \times 10^{-5}. \quad (5.116)$$

Consistency is achieved within 1.7σ and the combined branching ratio is determined to be

$$\overline{\text{Br}}_{X(1835)} = (2.887 \pm 0.637) \times 10^{-5}. \quad (5.117)$$

As mentioned in Section 5.6.8, in order to account for the additive systematic uncertainty of the chosen fit models, the upper limit was determined for each variation. To additionally include all other uncertainties, the corresponding likelihood profiles are convolved according to the procedure described in Section 5.7.3. This results in upper limits of

$$\text{Br}_{\chi_{c0}, \eta} < 2.20 \times 10^{-5} \quad (5.118)$$

$$\text{Br}_{\chi_{c0}, \gamma} < 1.46 \times 10^{-5}. \quad (5.119)$$

After combining the two decay modes the results can be compared to the values given by the PDG [6], as shown in Table 5.18, after dividing the product branching ratios by the corresponding measured production ratios [6]. As can be seen, the values obtained in this thesis are more precise by a factor of ~ 3 , ~ 6 and ~ 2 for the χ_{c1} , χ_{c2} and η_c , respectively. Also, the upper limit for the decay $\chi_{c0} \rightarrow \eta' \pi^+ \pi^-$ is improved by more than one order of magnitude. For the χ_{c1} and χ_{c2} , the determined values are both smaller than the existing value, with a difference of 1.2σ and 1.4σ , respectively.

In the case of the η_c , only the branching ratios obtained for the destructive interference is in agreement with the value given by the PDG, which could be an indication that this result is the physically realized result. However, it should be noted, that the PDG value is calculated from different analyses, all of which did not include the interference in the fit to the η_c [230, 231], or the inclusion of the interference did not give a significant improvement [232].

As mentioned in Section 2.2.5, the $X(1835)$ has so far only been seen in the decay of the J/ψ charmonium, and the first observation of this particle in the decay of the $\psi(2S)$ is further evidence for the existence of this particle. Using the value for the product branching ratio determined in this thesis and the value for the branching ratio in the

Table 5.18.: Determined branching ratios for the decays $\chi_{cJ}, \eta_c \rightarrow \eta'\pi^+\pi^-$ compared to the values given by the PDG [6], which are rescaled values from a CLEO measurement for the χ_{cJ} decays [200]. The value given for the $X(1835)$ is the product branching ratio, which was not measured before.

	This Work	PDG
χ_{c0}	$< 1.46 \times 10^{-5}$	$< 4 \times 10^{-4}$
χ_{c1}	$(1.64 \pm 0.12) \times 10^{-3}$	$(2.2 \pm 0.4) \times 10^{-3}$
χ_{c2}	$(2.95 \pm 0.29) \times 10^{-4}$	$(5.1 \pm 1.9) \times 10^{-4}$
η_c constr. int.	$(0.69 \pm 0.07) \times 10^{-2}$	$(1.6 \pm 0.3) \times 10^{-2}$
η_c destr. int.	$(1.67 \pm 0.14) \times 10^{-2}$	$(1.6 \pm 0.3) \times 10^{-2}$
$X(1835)$	$(2.89 \pm 0.64) \times 10^{-5}$	–

decay of a J/ψ [25], the ratio between the two production branching ratios is calculated as²²

$$\begin{aligned}
 R_{\text{Flatté}} &= \frac{\text{Br}(\psi(2S) \rightarrow \gamma X(1835))}{\text{Br}(J/\psi \rightarrow \gamma X(1835))} = \frac{\text{Br}(\psi(2S) \rightarrow \gamma X(1835))\text{Br}(X(1835) \rightarrow \eta'\pi^+\pi^-)}{\text{Br}(J/\psi \rightarrow \gamma X(1835))\text{Br}(X(1835) \rightarrow \eta'\pi^+\pi^-)} \\
 &= \frac{(2.86 \pm 0.63) \times 10^{-5}}{(3.93 \pm 0.38_{-0.84}^{+0.31}) \times 10^{-4}} = 7.3_{-1.8}^{+2.4} \%. \tag{5.120}
 \end{aligned}$$

This ratio is calculated for an assumed line shape of the $X(1835)$ given by a Flatté distribution [233]. The fit is also performed using a sum of two interfering Breit-Wigner functions, which has two solutions, which result in alternative values for the ratio given by [25]

$$R_{\text{BW,constr}} = \frac{(2.86 \pm 0.63) \times 10^{-5}}{(3.01 \pm 0.17_{-0.28}^{+0.26}) \times 10^{-4}} = (9.5 \pm 2.4) \%, \tag{5.121}$$

$$R_{\text{BW,destr}} = \frac{(2.86 \pm 0.63) \times 10^{-5}}{(3.72 \pm 0.21_{-0.35}^{+0.18}) \times 10^{-4}} = 7.7_{-1.8}^{+1.9} \%. \tag{5.122}$$

These values can now be compared with the corresponding results for the $X(p\bar{p})$ (see Section 2.2.5) determined in the $J/\psi \rightarrow \gamma p\bar{p}$ and $\psi(2S) \rightarrow \gamma p\bar{p}$ analyses [105]:

$$R_{p\bar{p}} = \frac{\text{Br}(\psi(2S) \rightarrow \gamma X(p\bar{p}))}{\text{Br}(J/\psi \rightarrow \gamma X(p\bar{p}))} = 5.1_{-3.6}^{+1.0} \%. \tag{5.123}$$

The values determined this way are compatible within 1.7σ , providing further evidence, that the $X(p\bar{p})$ and $X(1835)$ are indeed the same state.

²²The systematic uncertainties for the two measurements are slightly correlated, due to the same basic event selection. However, in both analyses the uncertainties are dominated by the uncertainties coming from the fitting models or specific event selection criteria and the correlation is negligible. Therefore, for this calculation it is assumed, that the uncertainties between the two measurements are uncorrelated.

6. Analysis of the Reaction $e^+e^- \rightarrow \eta_c K^* K$

The second part of this work is the analysis of the reaction $e^+e^- \rightarrow \eta_c K^* K$, which was performed in parts together with Sascha Lennartz in the context of his Master's thesis [28]. The main motivation is given by a possible contribution of the exotic candidate $Z_{cs}(3985)/Z_{cs}(4000)$ via the reactions (see Section 2.2.5)

$$\begin{aligned} e^+e^- &\rightarrow Z_{cs}^\pm K^\mp \rightarrow \eta_c K^{*\pm} K^\mp, \\ e^+e^- &\rightarrow Z_{cs}^0 \bar{K}^0 \rightarrow \eta_c K^{*0} \bar{K}^0, \\ e^+e^- &\rightarrow \bar{Z}_{cs}^0 K^0 \rightarrow \eta_c \bar{K}^{*0} K^0. \end{aligned} \quad (6.1)$$

The appearing K^* mesons are reconstructed via their decay into a kaon and a pion, which are [6]

$$K^{*\pm} \rightarrow K^\pm \pi^0 \quad \text{with} \quad \text{Br}(K^{*\pm} \rightarrow K^\pm \pi^0) = 1/3 \cdot (99.902 \pm 0.009) \%, \quad (6.2)$$

$$K^{*+} \rightarrow K^0 \pi^+ \quad \text{with} \quad \text{Br}(K^{*+} \rightarrow K^0 \pi^+) = 2/3 \cdot (99.902 \pm 0.009) \%, \quad (6.3)$$

$$K^{*-} \rightarrow \bar{K}^0 \pi^- \quad \text{with} \quad \text{Br}(K^{*-} \rightarrow \bar{K}^0 \pi^-) = 2/3 \cdot (99.902 \pm 0.009) \%, \quad (6.4)$$

for the charged K^* mesons and [6]

$$K^{*0} \rightarrow K^- \pi^+ \quad \text{with} \quad \text{Br}(K^{*0} \rightarrow K^- \pi^+) = 2/3 \cdot (99.754 \pm 0.021) \%, \quad (6.5)$$

$$\bar{K}^{*0} \rightarrow K^+ \pi^- \quad \text{with} \quad \text{Br}(\bar{K}^{*0} \rightarrow K^+ \pi^-) = 2/3 \cdot (99.754 \pm 0.021) \%, \quad (6.6)$$

for the neutral ones. The appearing factors of 1/3 and 2/3 are given by isospin Clebsch-Gordon coefficients for the corresponding decays. As mentioned in Section 2.2.3, the K^0 and \bar{K}^0 are not mass eigenstates, but compositions of the K_S^0 and K_L^0 . Neglecting CP violation results in both K^0 and \bar{K}^0 being 50% K_S^0 and 50% K_L^0 , with only the K_S^0 being detectable in the BESIII experiment, as it can be reconstructed via [6]

$$K_S^0 \rightarrow \pi^+ \pi^- \quad \text{with} \quad \text{Br}(K_S^0 \rightarrow \pi^+ \pi^-) = (69.20 \pm 0.05) \%. \quad (6.7)$$

Considering the additional kaon in Equation (6.1), the six decays of the K^* in Equations (6.2) to (6.6) result in a total of three distinct systems recoiling against the η_c given by

$$K^+ K^- \pi^0, \quad K^+ K_S^0 \pi^-, \quad K^- K_S^0 \pi^+. \quad (6.8)$$

Looking at the isospin Clebsch-Gordon coefficients, the factor of 1/2 for each K_S^0 and neglecting the small difference between the branching ratios of the charged and uncharged K^* mesons leads to an equal number of expected produced events for each recoil system. The reactions considered in Equation (6.1) also include the η_c , which, unlike all other appearing resonances, does not have a dominant decay mode. Therefore, the η_c is reconstructed in a total of 13 decay modes, which are listed in Table 6.1. The decay modes are chosen to include the decay modes with the highest branching ratios, while still having a large expected efficiency. The selected decay modes cover a total branching ratio of the η_c of $(37.2 \pm 2.7)\%$ ²³. Combining the 13 decay modes with the three recoil systems results in 39 final states. However, considering the decay $\eta_c \rightarrow K \bar{K} \pi$, which is the same as the recoil system, results in three of the 39 final states being reachable by exchanging the η_c decay mode and the recoil system. Therefore, in total 36 different final states are investigated in this analysis.

Appearing π^0 and η resonances are both reconstructed in their decay to two photons:

$$\pi^0 \rightarrow \gamma\gamma \quad \text{with} \quad \text{Br}(\pi^0 \rightarrow \gamma\gamma) = (98.823 \pm 0.034)\%, \quad (6.9)$$

$$\eta \rightarrow \gamma\gamma \quad \text{with} \quad \text{Br}(\eta \rightarrow \gamma\gamma) = (39.36 \pm 0.18)\%. \quad (6.10)$$

Depending on the final state, a different number of charged tracks must be reconstructed, ranging from four tracks (e.g. $\eta_c \rightarrow p\bar{p}$ with the $K^+K^-\pi^0$ recoil system) to ten tracks (e.g. $\eta_c \rightarrow K^+K^-2(\pi^+\pi^-)$ with the $K^+K_S^0\pi^-$ recoil system). Each of the charged tracks must satisfy the selection criteria given in Section 4.1. Additionally, for an event to be included in the analysis, a minimum number of photons must be detected, determined by the number of π^0 and η resonances appearing, ranging from zero photons, e.g. $\eta_c \rightarrow K^+K^-\pi^+\pi^-$ with the $K^+K_S^0\pi^-$ recoil system, to six photons, e.g. $\eta_c \rightarrow \pi^+\pi^-\pi^0\pi^0$ with the $K^+K^-\pi^0$ recoil system. These photon candidates must meet the requirements defined in Section 4.2. For each event in which the appropriate number of charged tracks and photons have been found, a kinematic fit is performed according to Section 4.3. In addition to imposing energy and momentum conservation, an additional constraint is added, for each participating K_S^0 , π^0 and η resonance. In this analysis, the kinematic fit is used to find the correct photon assignments for the π^0 and η mesons and to assign $\pi^+\pi^-$ candidates to a K_S^0 by constraining the invariant mass of the $\pi^+\pi^-$ system. Then the combination that yields the smallest χ^2 of the resulting kinematic fit is used for further analysis.

After finding the best combination, the next step is to assign the particles in the final state to either the η_c decay or the recoil system. In contrast to the procedure for the

²³For the calculation of the uncertainty on the total branching ratio, it is assumed that the individual values are uncorrelated. However, some of the values are determined by a combined fit [6] and partially come from the same experiments. This results in correlations that should be small, since most measurements are dominated by statistical uncertainties. Additionally, the extracted correlations from the combined fit are all negligible compared to the total uncertainty [6].

Table 6.1.: Considered decays of the η_c with their branching ratios taken from the PDG [6] and the resulting final states. The final states marked with * appear twice.

η_c Decay Channel	Branching Ratio Br / %	Final State
$p\bar{p}$	0.133 ± 0.011	$p\bar{p} K^+ K^- \pi^0$ $p\bar{p} K^+ K_S^0 \pi^-$ $p\bar{p} K^- K_S^0 \pi^+$
$\pi^+ \pi^- \pi^0 \pi^0$	4.6 ± 1.0	$K^+ K^- \pi^+ \pi^- 3\pi^0$ $K^+ K_S^0 \pi^+ 2\pi^- 2\pi^0$ $K^- K_S^0 2\pi^+ \pi^- 2\pi^0$
$2(\pi^+ \pi^- \pi^0)$	15.9 ± 2.0	$K^+ K^- 2\pi^+ 2\pi^- 3\pi^0$ $K^+ K_S^0 2\pi^+ 3\pi^- 2\pi^0$ $K^- K_S^0 3\pi^+ 2\pi^- 2\pi^0$
$2(K^+ K^-)$	1.4 ± 0.4	$3K^+ 3K^- \pi^0$ $3K^+ 2K^- K_S^0 \pi^-$ $2K^+ 3K^- K_S^0 \pi^+$
$K\bar{K}\pi$	$1/2 \cdot (7.1 \pm 0.4)$	$2K^+ 2K^- 2\pi^0$ $2K^+ K^- K_S^0 \pi^- \pi^0 *$ $K^+ 2K^- K_S^0 \pi^+ \pi^0 *$ $2K^+ 2K_S^0 2\pi^-$ $K^+ K^- 2K_S^0 \pi^+ \pi^- *$ $2K^- 2K_S^0 2\pi^+$
$K^+ K^- \pi^+ \pi^-$	0.83 ± 0.18	$2K^+ 2K^- \pi^+ \pi^- \pi^0$ $2K^+ K^- K_S^0 \pi^+ 2\pi^-$ $K^+ 2K^- K_S^0 2\pi^+ \pi^-$
$K^+ K^- \pi^+ \pi^- \pi^0$	3.4 ± 0.6	$2K^+ 2K^- \pi^+ \pi^- 2\pi^0$ $2K^+ K^- K_S^0 \pi^+ 2\pi^- \pi^0$ $K^+ 2K^- K_S^0 2\pi^+ \pi^- \pi^0$
$K^+ K^- 2(\pi^+ \pi^-)$	0.84 ± 0.24	$2K^+ 2K^- 2\pi^+ 2\pi^- \pi^0$ $2K^+ K^- K_S^0 2\pi^+ 3\pi^-$ $K^+ 2K^- K_S^0 3\pi^+ 2\pi^-$
$\eta \pi^+ \pi^-$	1.6 ± 0.4	$\eta K^+ K^- \pi^+ \pi^- \pi^0$ $\eta K^+ K_S^0 \pi^+ 2\pi^-$ $\eta K^- K_S^0 2\pi^+ \pi^-$
$\eta 2(\pi^+ \pi^-)$	4.3 ± 1.3	$\eta K^+ K^- 2\pi^+ 2\pi^- \pi^0$ $\eta K^+ K_S^0 2\pi^+ 3\pi^-$ $\eta K^- K_S^0 3\pi^+ 2\pi^-$
$\eta K^+ K^-$	0.66 ± 0.08	$\eta 2K^+ 2K^- \pi^0$ $\eta 2K^+ K^- K_S^0 \pi^-$ $\eta K^+ 2K^- K_S^0 \pi^+$
Sum	37.21 ± 2.74	

$\psi(2S) \rightarrow \gamma \eta' \pi^+ \pi^-$ analysis, choosing the combination, which is closest to the mass of the η_c introduces a significant bias. The reason for this is the large number of possible combinations in final states with a large number of particles. Therefore, in this analysis, every combination of particles that can form an η_c is considered. After assigning the particles to an η_c candidate, for each of them the recoil system $K \bar{K} \pi$ remains, with two possible combinations to form a K^* . Here, the combination is chosen that is closest to the mass of the K^* given by the PDG [6]:

$$\min_{i \in \{0,1\}} \left| m_{K_i \pi} - m_{K^{*\pm,0}, \text{PDG}} \right|, \quad (6.11)$$

where the comparison is made with the mass of the K^* , which has the same charge as the $K_i \pi$ system under consideration [6]:

$$m_{K^{*\pm}} = (891.67 \pm 0.26) \text{ MeV}/c^2, \quad (6.12)$$

$$m_{K^{*0}} = (895.55 \pm 0.20) \text{ MeV}/c^2. \quad (6.13)$$

This also defines the charge of the K^* for each η_c candidate. By comparing the results with and without selecting the best K^* , it was determined that the bias is negligible.

As a first selection criterion, mass cuts are applied around the nominal masses of the appearing π^0 , η and K_S^0 candidates, which are plotted in Figure 6.1 for arbitrarily chosen final states²⁴. Here, the candidates are the ones that were determined by choosing the combination giving the best χ^2 , and they are already subject to the cut on the χ^2 , which will be presented in Section 6.1. As can be seen, the spectra appear to be almost background free, with the data being well described by both the signal MC and the inclusive MC, which are both scaled to have the same number of events as the data. The mass windows are defined as

$$m_{\pi^+ \pi^-} \in [0.460 \text{ GeV}/c^2, 0.530 \text{ GeV}/c^2], \quad (6.14)$$

$$m_{\gamma \gamma, \pi^0} \in [0.120 \text{ GeV}/c^2, 0.144 \text{ GeV}/c^2], \quad (6.15)$$

$$m_{\gamma \gamma, \eta} \in [0.500 \text{ GeV}/c^2, 0.570 \text{ GeV}/c^2]. \quad (6.16)$$

These windows correspond to $\sim 90\%$ of the signal according to the signal MC, depending on the final state under consideration.

In addition, the invariant mass of the K^* candidate is restricted to a range of

$$m_{K\pi} \in [0.7 \text{ GeV}/c^2, 1.1 \text{ GeV}/c^2], \quad (6.17)$$

²⁴In this section and in Section 6.1, the final states presented are arbitrarily chosen and all come from the samples at $\sqrt{s} \approx 4.68 \text{ GeV}$. The corresponding spectra for the other final states and center-of-mass energies were all inspected and analyzed in the same way. Unless explicitly mentioned, no additional significant features are visible in them.

which can be seen in Figure 6.2. This mass window around the nominal mass of the K^* [6] is approximately four times its width given by the PDG [6] as

$$\Gamma_{K^{*\pm}} = (51.4 \pm 0.8) \text{ MeV}/c^2, \quad (6.18)$$

$$\Gamma_{K^{*0}} = (47.3 \pm 0.5) \text{ MeV}/c^2. \quad (6.19)$$

These spectra are filled for each possible η_c combination with the $K\pi$ combination yielding the best K^* according to Equation (6.11). It is clearly visible that the number of possible combinations plays a significant role in the shape of the spectrum. While in the case of $\eta_c[\rightarrow p\bar{p}]K^-K_S^0\pi^+$ there is only one possible combination, in the $\eta_c[\rightarrow 2(\pi^+\pi^-\pi^0)]K^+K^-\pi^0$ final state there are already three. These combinations produce a large combinatorial background that is also visible in the signal MC, which is not easily distinguishable from the background coming from events without a K^* .

6.1. Background Reduction

Similar to the $\psi(2S) \rightarrow \gamma\eta'\pi^+\pi^-$ analysis, after the initial event selection there are still unwanted background reactions present in the data sample, which can be reduced by applying additional selection criteria. However, due to the large number of final states, each with only a small number of events, a multidimensional cut optimization is not feasible. Instead, the only selection criterion that is optimized is the cut on the χ^2 of the kinematic fit using the figure of merit definition from Equation (5.12), in this case depending only on the cut on the χ^2 of the kinematic fit:

$$\mathcal{F}(\chi_{\text{cut}}^2) = \frac{N_S(\chi_{\text{cut}}^2)}{\sqrt{N_S(\chi_{\text{cut}}^2) + N_B(\chi_{\text{cut}}^2)}}. \quad (6.20)$$

Here, N_S and N_B are the number of signal and background events satisfying the χ^2 condition calculated as

$$N_S(\chi_{\text{cut}}^2) = \int_0^{\chi_{\text{cut}}^2} p_{\text{sig}}(\chi^2) d\chi^2, \quad (6.21)$$

$$N_B(\chi_{\text{cut}}^2) = \int_0^{\chi_{\text{cut}}^2} p_{\text{bg}}(\chi^2) d\chi^2, \quad (6.22)$$

where $p_{\text{sig/bg}}(\chi^2)$ is the χ^2 distribution of signal and background in the inclusive MC, respectively. In this case, the signal component is defined as all reactions that lead to the correct final state without requiring intermediate resonances. Two of the resulting figures of merit are shown in Figure 6.3. If the figure of merit has a maximum, the corresponding value is used as the cut on the χ^2 . This is done separately for each analyzed final state using the inclusive MC simulation for the data sample at $\sqrt{s} \approx 4.6 \text{ GeV}$. While

6. Analysis of the Reaction $e^+e^- \rightarrow \eta_c K^* K$

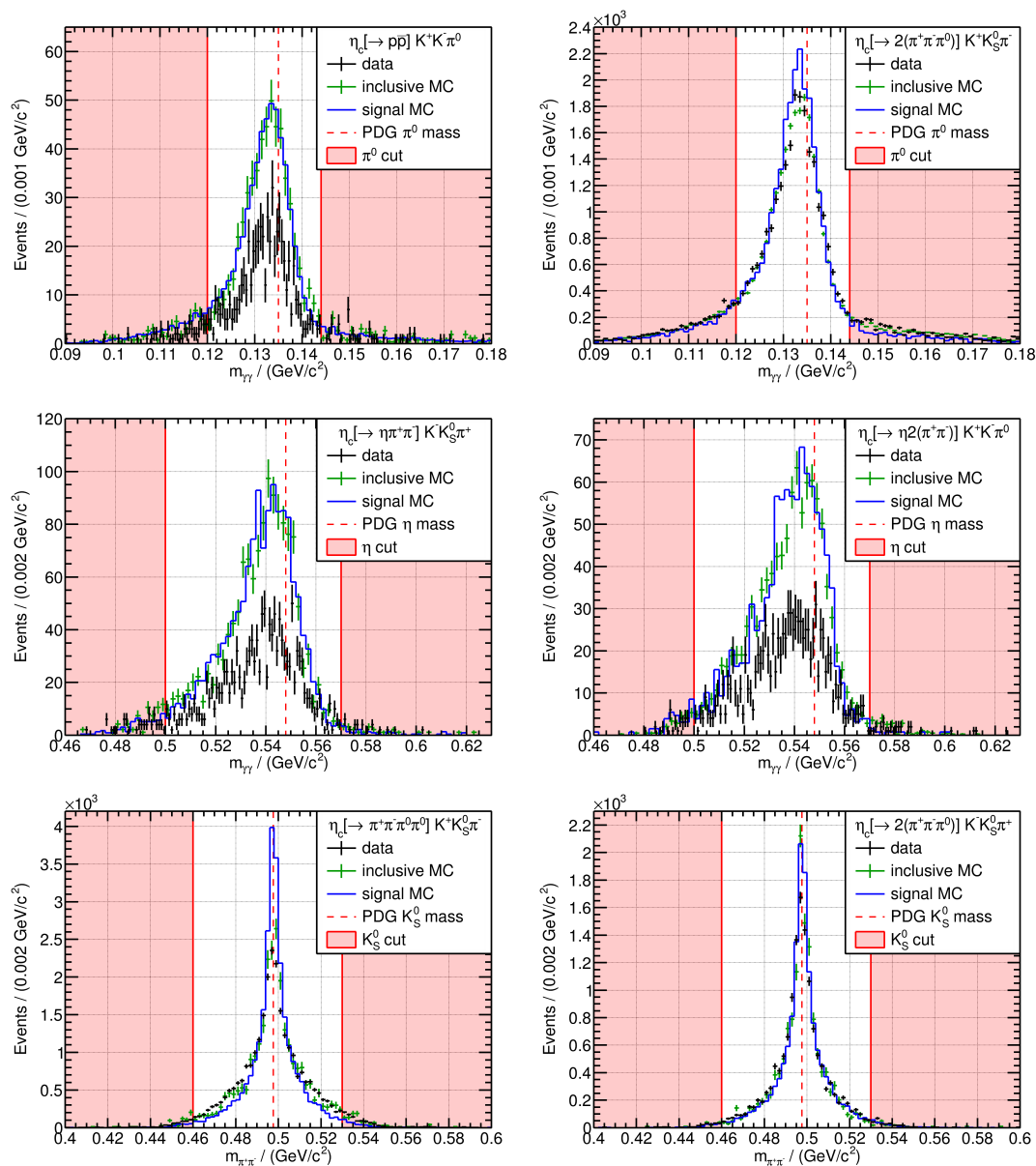


Figure 6.1.: Invariant mass spectra of π^0 candidates for the $\eta_c[\rightarrow p\bar{p}]K^+K^-\pi^0$ (top left) and $\eta_c[\rightarrow 2(\pi^+\pi^-\pi^0)]K^+K_S^0\pi^-$ (top right) final states. Invariant mass spectra of η candidates for the $\eta_c[\rightarrow \eta\pi^+\pi^-]K^-K_S^0\pi^+$ (middle left) and $\eta_c[\rightarrow \eta 2(\pi^+\pi^-)]K^+K^-\pi^0$ (middle right) final states. Invariant mass spectra of K_S^0 candidates for the $\eta_c[\rightarrow \pi^+\pi^-\pi^0\pi^0]K^+K_S^0\pi^-$ (bottom left) and $\eta_c[\rightarrow 2(\pi^+\pi^-\pi^0)]K^-K_S^0\pi^+$ (bottom right) final states. The data is shown in black, the inclusive MC in green and the signal MC in blue. The mass of the signal resonances, according to the PDG [6], are indicated as a red dashed line and the cuts are marked with the red solid lines. The signal MC and inclusive MC are scaled to have the same integral as the data.

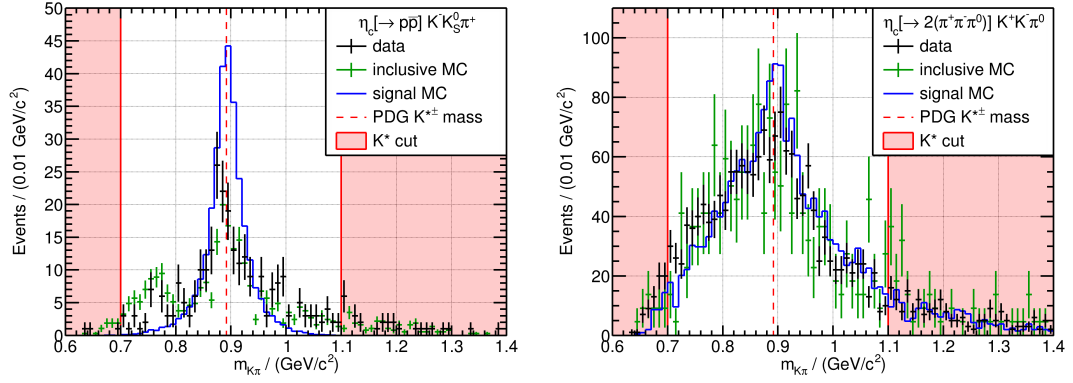


Figure 6.2.: Invariant mass spectra of K^* candidates for the $\eta_c[\rightarrow p\bar{p}]K^-K_S^0\pi^+$ (left) and $\eta_c[\rightarrow 2(\pi^+\pi^-\pi^0)]K^+K^-\pi^0$ (right) final states. The data is shown in black, the inclusive MC in green and the signal MC in blue. The mass of the K^{*+} , according to the PDG, is indicated as a red dashed line and the cut on the K^* is marked with the red solid lines. The signal MC and inclusive MC are scaled to have the same integral as the data.

in principle the background composition can depend on the center-of-mass energy, the analyzed data samples are in such a small energy range that no large differences are expected. Therefore, the cut values determined for the $\sqrt{s} \approx 4.6$ GeV data sample are also used for the other samples. If the figure of merit does not show a maximum, the χ^2 is still restricted to exclude events where the kinematic fit had problems finding a reasonable minimum. In such a case the cut on the χ^2 is given by $\chi^2_{\text{cut}} = 50 \cdot N_c$, where N_c is the number of constraints in the corresponding final state.

In addition, appearing unwanted resonances are excluded by mass vetoes, which are defined by hand. These vetoes are applied to every combination of final state particles,

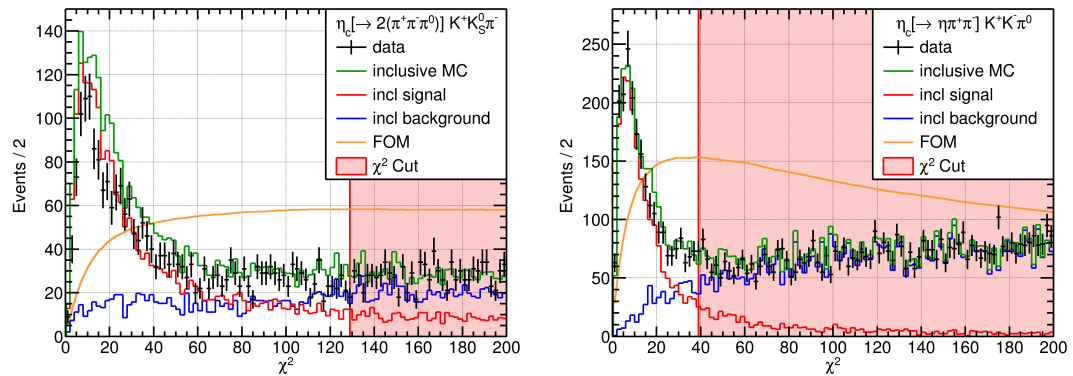


Figure 6.3.: Figure of merit for the cut on the χ^2 of the kinematic fit for the $\eta_c[\rightarrow 2(\pi^+\pi^-\pi^0)]K^+K_S^0\pi^-$ (left) and $\eta_c[\rightarrow \eta\pi^+\pi^-]K^+K^-\pi^0$ (right) final states. The data is presented in black, the total inclusive MC in green, the signal component of the inclusive MC in red and the background component in blue. The calculated figure of merit is given as the orange solid line and the resulting χ^2 is shown with the red box.

6. Analysis of the Reaction $e^+e^- \rightarrow \eta_c K^* K$

in which such an unwanted resonance appears and which contains at least one particle from the recoil system. This distinction is made, to allow for resonances in the decay of the η_c meson, e.g., in the decay $\eta_c \rightarrow \phi \pi^+ \pi^- \rightarrow K^+ K^- \pi^+ \pi^-$. Significantly contributing background resonances are on the one hand the light mesons η and ω found in the invariant mass of $\pi^+ \pi^- \pi^0$ systems and the ϕ meson in $K^+ K^-$ systems, both presented in Figure 6.4. The mass vetoes are defined symmetrically around the PDG masses [6] of the resonances:

$$|m_{\pi^+ \pi^- \pi^0} - m_{\eta, \text{PDG}}| > 10 \text{ MeV}/c^2, \quad (6.23)$$

$$|m_{\pi^+ \pi^- \pi^0} - m_{\omega, \text{PDG}}| > 20 \text{ MeV}/c^2, \quad (6.24)$$

$$|m_{K^+ K^-} - m_{\phi, \text{PDG}}| > 10 \text{ MeV}/c^2. \quad (6.25)$$

On the other hand, large background contributions come from D mesons, which is to be

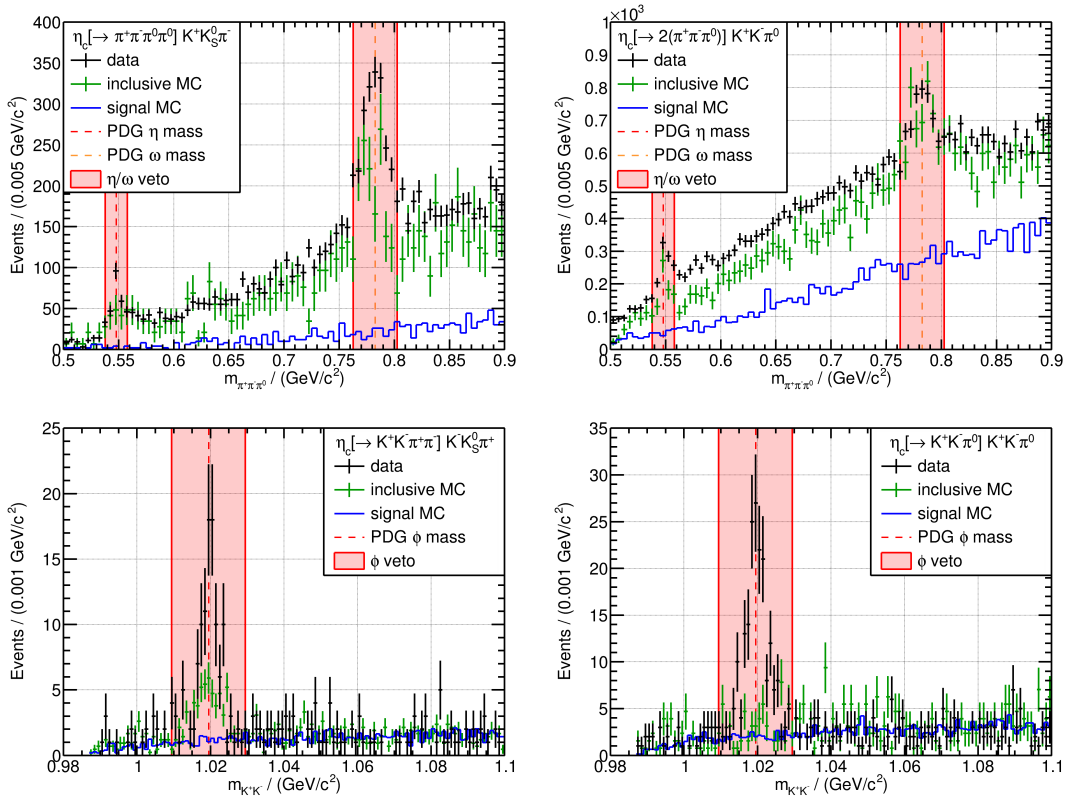


Figure 6.4.: Invariant mass spectra of the $\pi^+ \pi^- \pi^0$ system with appearing η and ω background resonances for the $\eta_c[\rightarrow \pi^+ \pi^- \pi^0 \pi^0] K^+ K_S^0 \pi^-$ (top left) and $\eta_c[\rightarrow 2(\pi^+ \pi^- \pi^0)] K^+ K^- \pi^0$ (top right) final states. Invariant mass spectra of the $K^+ K^-$ system with appearing ϕ background resonances for the $\eta_c[\rightarrow K^+ K^- \pi^+ \pi^-] K^- K_S^0 \pi^+$ (bottom left) and $\eta_c[\rightarrow K^+ K^- \pi^0] K^+ K^- \pi^0$ (bottom right) final states. The data is presented in black, the inclusive MC in green and the signal MC in blue. The mass of the background resonances according to the PDG [6] are indicated as dashed lines and the applied vetoes are marked with red solid lines.

expected, since the analyzed data samples are above the threshold for the production of a $D\bar{D}$ pair. For the D mesons the dominant hadronic decays are given by the decay into a kaon and a number n of pions [6]

$$D^{\pm,0} \rightarrow (K n\pi)^{\pm,0}, \quad (6.26)$$

with a combined branching ratio of $\sim 35\%$ for the charged and $\sim 55\%$ for the uncharged D meson. Therefore, the invariant mass spectra of systems containing one kaon and any number of pions are investigated for possible $D^{\pm,0}$ contributions. In addition, the D mesons can also decay into $K\bar{K}$, but these decays are suppressed by the corresponding off-diagonal element of the Cabibbo-Kobayashi-Maskawa (CKM) matrix (also called quark mixing matrix) [234, 235]. However, this is different for the D_s^{\pm} mesons, where the dominant hadronic decays are given by [6]

$$D_s^{\pm} \rightarrow (K\bar{K} n\pi)^{\pm}, \quad (6.27)$$

with a combined branching ratio of $\sim 40\%$ and the single kaon decays are suppressed by the CKM matrix element. Therefore, D_s mesons are searched for in systems containing two kaons and any number of pions. In addition, excited $D_{(s)}^*$ mesons may play a role, which almost exclusively decay into their respective ground states via [6]

$$D^{*0} \rightarrow D^0\pi^0 \quad \text{with} \quad \text{Br}(D^{*0} \rightarrow D^0\pi^0) = (64.7 \pm 0.9)\%, \quad (6.28)$$

$$D^{*0} \rightarrow D^0\gamma \quad \text{with} \quad \text{Br}(D^{*0} \rightarrow D^0\gamma) = (35.3 \pm 0.9)\%, \quad (6.29)$$

for the uncharged D^{*0} meson and via [6]

$$D^{*+} \rightarrow D^0\pi^+ \quad \text{with} \quad \text{Br}(D^{*+} \rightarrow D^0\pi^+) = (67.7 \pm 0.5)\%, \quad (6.30)$$

$$D^{*+} \rightarrow D^+\pi^0 \quad \text{with} \quad \text{Br}(D^{*+} \rightarrow D^+\pi^0) = (30.7 \pm 0.5)\%, \quad (6.31)$$

for the charged D^{*+} . The \bar{D}^{*0} and D^{*-} decay modes are the charge conjugates of the above modes. Since the excited D mesons decay to their respective ground states, no additional veto is needed to reduce their contribution.

The invariant mass spectra of various final states with appearing $D_{(s)}^{(*)}$ resonances are shown in Figure 6.5. The $D^{\pm,0}$ mesons are clearly visible in almost all final states, while the $D^{*\pm,0}$ and D_s^{\pm} are only weakly visible in selected final states. The mass veto around the $D^{\pm,0}$ is defined asymmetrically around its nominal mass [6] with the excluded region given by

$$m_{(K n\pi)^{\pm,0}} \notin [1.82 \text{ GeV}/c^2, 1.94 \text{ GeV}/c^2]. \quad (6.32)$$

6. Analysis of the Reaction $e^+e^- \rightarrow \eta_c K^* K$

For the D_s^\pm it is defined symmetrically around its nominal mass [6] via

$$|m_{(K\bar{K}n\pi)^\pm} - m_{D_s^\pm, \text{PDG}}| > 20 \text{ MeV}/c^2. \quad (6.33)$$

The vetoes are applied only to systems in which the D mesons are allowed to appear. The D mesons can only appear in combinations with the correct charge and special attention has to be paid to the recoil systems containing a K_S^0 . For these, the other kaon in the recoil system defines the strangeness of the K_S^0 (corresponding to it being produced as either a K^0 or a \bar{K}^0). This results in the fact that for these final states either $D_{(s)}^+ \rightarrow K_S^0[(K)n\pi]^+$ or $D_{(s)}^- \rightarrow K_S^0[(K)n\pi]^-$ is allowed, but not both. After applying all event selection criteria, four resulting η_c spectra are presented in Figure 6.6. As can be seen, no clear peaks at the invariant mass of the η_c are visible in any of the spectra. However, the combination of all η_c channels considered provides

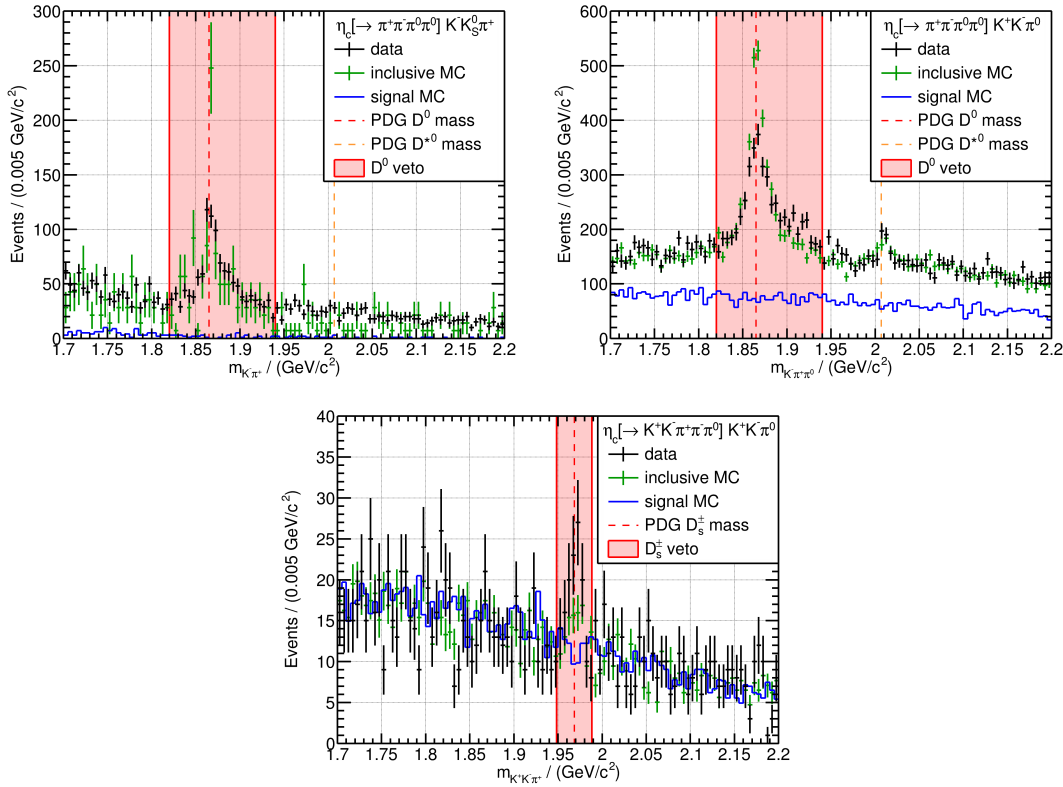


Figure 6.5.: Invariant mass spectra of systems with appearing $D_{(s)}^{(*)}$ background resonances. Shown are the $D^0 \rightarrow K^- \pi^+$ decay in the $\eta_c[\rightarrow \pi^+ \pi^- \pi^0 \pi^0] K^- K_S^0 \pi^+$ final state (top left), the $D^0 \rightarrow K^- \pi^+ \pi^0$ and $D^{*0} \rightarrow D^0 \pi^0 \rightarrow K^- \pi^+ \pi^0$ decay in the $\eta_c[\rightarrow \pi^+ \pi^- \pi^0 \pi^0] K^+ K^- \pi^0$ final state (top right) and the $D_s^+ \rightarrow K^+ K^- \pi^+$ decay in the $\eta_c[\rightarrow K^+ K^- \pi^+ \pi^- \pi^0] K^+ K^- \pi^0$ final state (bottom). The data is presented in black, the inclusive MC in green and the signal MC in blue. The masses of $D_{(s)}^{(*)}$ mesons according to the PDG [6] are indicated as a red/orange dashed line and the applied vetoes are marked with a red solid line.

additional information, as the relative strength of the η_c in the different channels can be fixed by the relevant branching ratios and the efficiency. This combination of the final states is done by a combined fit, which will be presented in the next section.

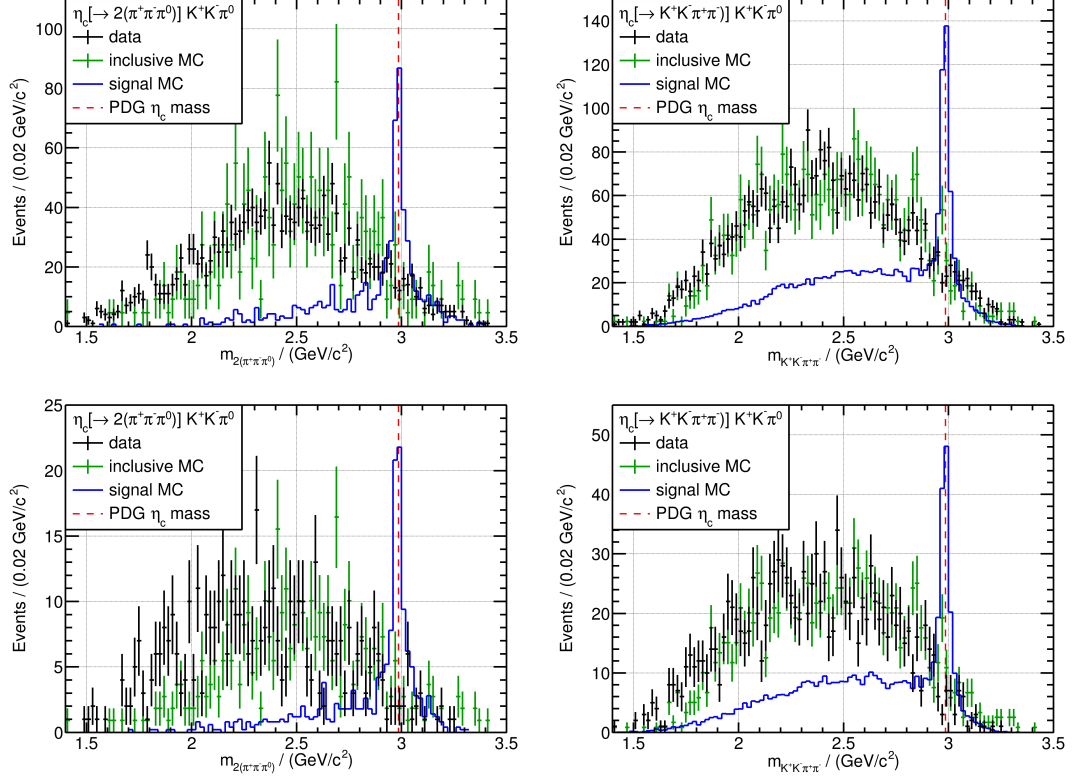


Figure 6.6.: Invariant mass spectra of η_c candidates for the $\eta_c[\rightarrow 2(\pi^+\pi^-\pi^0)]K^+K^-\pi^0$ (left) and $\eta_c[\rightarrow K^+K^-\pi^+\pi^-]K^+K^-\pi^0$ (right) final states. Shown are the spectra for the data sample at $\sqrt{s} \approx 4.68$ GeV (top) and for the data sample at $\sqrt{s} \approx 4.60$ GeV (bottom). The data is presented in black, the inclusive MC in green and the signal MC in blue. The mass of the η_c meson according to the PDG [6] is indicated as a red dashed line.

6.2. Combined Fit to the η_c

As mentioned above, the η_c yield in any single final state is not significant. However, additional information is obtained by combining the information from all the final states. This is done with a method inspired by [236], which determined the number of produced η_c mesons in the reactions $e^+e^- \rightarrow \eta_c\pi^+\pi^-\pi^0, \eta_c\pi^+\pi^-$ and $\eta_c\pi^0\gamma$. This method was adapted to include the final states in this analysis and to consider the different recoil systems. The method was then applied by Sascha Lennartz [28] to all of the data samples analyzed and the results are presented in Section 6.2.3.

The fit to the different final states is done as a combined extended unbinned maximum likelihood fit, and the likelihood is defined similarly to Equation (5.86), by considering

the different final states and by approximating the Poisson distribution with a Gaussian distribution:

$$\mathcal{L}(\vec{\theta}) = \prod_{i=1}^c \exp \left[-\frac{(\mu_i - N_i)^2}{2N_i} \right] \cdot \prod_{i_1=1}^{N_1} \mathcal{P}_1(\vec{x}_{i_1}; \vec{\theta}) \cdot \prod_{i_2=1}^{N_2} \mathcal{P}_2(\vec{x}_{i_2}; \vec{\theta}) \cdots \prod_{i_c=1}^{N_c} \mathcal{P}_c(\vec{x}_{i_c}; \vec{\theta}). \quad (6.34)$$

Here, $c = 36$ is the number of channels, N_j is the number of events, μ_j is the predicted number of events, and \mathcal{P}_j is the PDF, each for channel j . After taking the negative logarithm of the likelihood and dropping terms that do not influence the minimization, the NLL is defined as

$$-\ln [\mathcal{L}(\vec{\theta})] = \sum_{j=1}^c (\mu_j - N_j)^2 + \sum_{i_1=1}^{N_1} \mathcal{P}_1(\vec{x}_{i_1}; \vec{\theta}) + \sum_{i_2=1}^{N_2} \mathcal{P}_2(\vec{x}_{i_2}; \vec{\theta}) + \dots + \sum_{i_c=1}^{N_c} \mathcal{P}_c(\vec{x}_{i_c}; \vec{\theta}). \quad (6.35)$$

The model for each channel is defined by

$$\mathcal{P}_j(m_j) = \mathcal{S}_j(m_j) + \mathcal{B}_j(m_j), \quad (6.36)$$

where \mathcal{S}_j is the signal shape and \mathcal{B}_j is the background. The background is parametrized by modified Chebyshev polynomials of order $N_{\text{ord},j} \leq 2$, which are written as

$$\mathcal{B}_j(m_j) = \frac{1}{m_u - m_l} \cdot \sum_{k=0}^{N_{\text{ord},j}} a_{k,j} \mathcal{T}_k(x_j). \quad (6.37)$$

The Chebyshev polynomials are modified so that their integral over the fitting range from the lower limit m_l to the upper limit m_u is zero (except for the zeroth order):

$$\begin{aligned} \mathcal{T}_0(x_j) &= 1 \\ \mathcal{T}_1(x_j) &= x_j \\ \mathcal{T}_2(x_j) &= 6x_j^2 - 2, \end{aligned} \quad (6.38)$$

with x_j given by

$$x_j = 2 \frac{m_j - \frac{m_u + m_l}{2}}{m_u - m_l}. \quad (6.39)$$

With this definition, the number of predicted background events for channel j is simply given by $a_{0,j}$. The signal function is given by

$$\mathcal{S}_j(m_j) = s_j \cdot \text{MC}_j(m_j), \quad (6.40)$$

where $\text{MC}_j(m_j)$ is the normalized signal shape taken from a MC simulation, presented in Section 6.2.1 and s_j determines the number of predicted signal events. Thus, the

predicted number of events μ_j in Equation (6.35) is given by $\mu_j = s_j + a_{0,j}$. While the background parameters $a_{k,j}$ are independent for each channel, the number of predicted signal events s_j is calculated from a common fit parameter \mathcal{N} via:

$$s_j = \text{Br}_j \cdot \varepsilon_j \cdot \mathcal{N}. \quad (6.41)$$

Here, ε_j is the efficiency and Br_j is the product of all appearing branching ratios for channel j , given by the decay of the K^* (Equations (6.2) to (6.6)) and appearing intermediate π^0 , η and K_S^0 mesons (Equations (6.7), (6.9) and (6.10)), including the necessary Clebsch-Gordon coefficients. The physical interpretation of the common parameter \mathcal{N} is, that it gives the total number of η_c mesons produced via the reaction $e^+e^- \rightarrow \eta_c K^* K$.

As mentioned above, the combined fit requires the signal shape as well as the efficiency for each channel, both of which are determined from MC simulations, which are presented next.

6.2.1. Signal Shape and Efficiency

For the $e^+e^- \rightarrow \eta_c K^* K$ analysis, for each of the analyzed final states presented in Table 6.1, two signal MC samples are generated for each of the center-of-mass energies (four samples for the final states that occur twice). The two samples correspond to the two different $K^* K$ combinations that yield the same recoil system for each η_c decay:

$$e^+e^- \rightarrow \left\{ \begin{array}{l} \eta_c [K^{*-} \rightarrow K_S^0 \pi^-] K^+ \\ \eta_c [K^{*0} \rightarrow K^+ \pi^-] K_S^0 \end{array} \right\} \rightarrow \eta_c K^+ K_S^0 \pi^- \quad (6.42)$$

$$e^+e^- \rightarrow \left\{ \begin{array}{l} \eta_c [K^{*+} \rightarrow K_S^0 \pi^+] K^- \\ \eta_c [\bar{K}^{*0} \rightarrow K^- \pi^+] K_S^0 \end{array} \right\} \rightarrow \eta_c K^- K_S^0 \pi^+ \quad (6.43)$$

$$e^+e^- \rightarrow \left\{ \begin{array}{l} \eta_c [K^{*+} \rightarrow K^+ \pi^-] K^- \\ \eta_c [K^{*-} \rightarrow K^- \pi^0] K^+ \end{array} \right\} \rightarrow \eta_c K^+ K^- \pi^0 \quad (6.44)$$

At each center-of-mass energy 10^5 events are generated for each final state, with each decay generated according to the PHSP model.

In addition to the decays mentioned above, these simulations also include the production of initial state radiation (ISR). ISR describes the process, where either the electron or the positron (or both) emit a number of photons prior to the collision, resulting in a reduced center-of-mass energy for that collision. The probability for ISR to occur depends on the cross section line shape for the process under consideration, and here the cross section for $e^+e^- \rightarrow J/\psi K^+ K^-$ is used [237].

The MC samples are treated in the same way as the data, and the resulting η_c spectra are used as the signal shape. This includes the combinatorial background introduced by the different η_c combinations. The spectra are normalized such that the integral over

the fitted range equals one. Additionally, the efficiency is calculated as the number of η_c candidates that survive the selection criteria divided by the number of generated events.

6.2.2. Input-Output Check

To check the reliability of the chosen method, the presented fit is tested for a cocktail MC sample, which includes a known number of signal and background events. This sample consists of 2.5×10^7 total events, whereby 1.723×10^6 (6.9%) are signal events, evenly distributed over the four signal reactions

$$\begin{aligned} e^+e^- &\rightarrow Z_{cs}^\pm K^\mp \rightarrow \eta_c K^{*\pm} K^\mp, \\ e^+e^- &\rightarrow Z_{cs}^0 \bar{K}^0 \rightarrow \eta_c K^{*0} \bar{K}^0, \\ e^+e^- &\rightarrow \bar{Z}_{cs}^0 K^0 \rightarrow \eta_c \bar{K}^{*0} K^0. \end{aligned} \quad (6.45)$$

The decay of the η_c is simulated with the branching ratios taken from Table 6.1 scaled to 100%. The background consist of 1.155×10^7 (46.2%) events with open-charm production of the type

$$e^+e^- \rightarrow D_{(s)}^{(*)} \bar{D}_{(s)}^{(*)} n\pi \quad \text{with } n = 0, 1, 2 \quad (6.46)$$

and of 1.172×10^7 (46.9%) events with the direct production of light hadrons. All appearing $D_{(s)}^{(*)}$ mesons and light hadrons decay with their branching ratios given by the PDG and unmeasured decays are estimated using the LUNDCHARM [180,181] model.

The resulting invariant mass spectra of η_c candidates with the corresponding fit are shown in Figures 6.7 and 6.8. As can be seen, the fit accurately describes the sample for all final states, with the biggest deviations seen for the decay $\eta_c \rightarrow K^+ K^- 2(\pi^+ \pi^-)$. It has to be noted, that the background composition was chosen as an educated guess, by taking into account the measured cross sections for different possible background reactions [6,238–243]. Therefore the shape of the background does not necessarily have to correspond to the shape of the background in data. From the fit, the number of produced η_c mesons is calculated as

$$\mathcal{N}_{\text{IO}} = (1.709 \pm 0.024) \times 10^6, \quad (6.47)$$

which is consistent with the number of generated signal events.

This test is now repeated 1200 times for different toy MC samples with varying numbers of generated signal and background events. For each test, the number of produced η_c mesons extracted by the fit is compared to the number of generated signal events, as shown in Figure 6.9. As can be seen, the extracted number of events is distributed around the number of generated events, with a small offset. These results are fitted with a Gaussian function, resulting in a peak position of 0.191 ± 0.030 and a width of 0.941 ± 0.030 with a

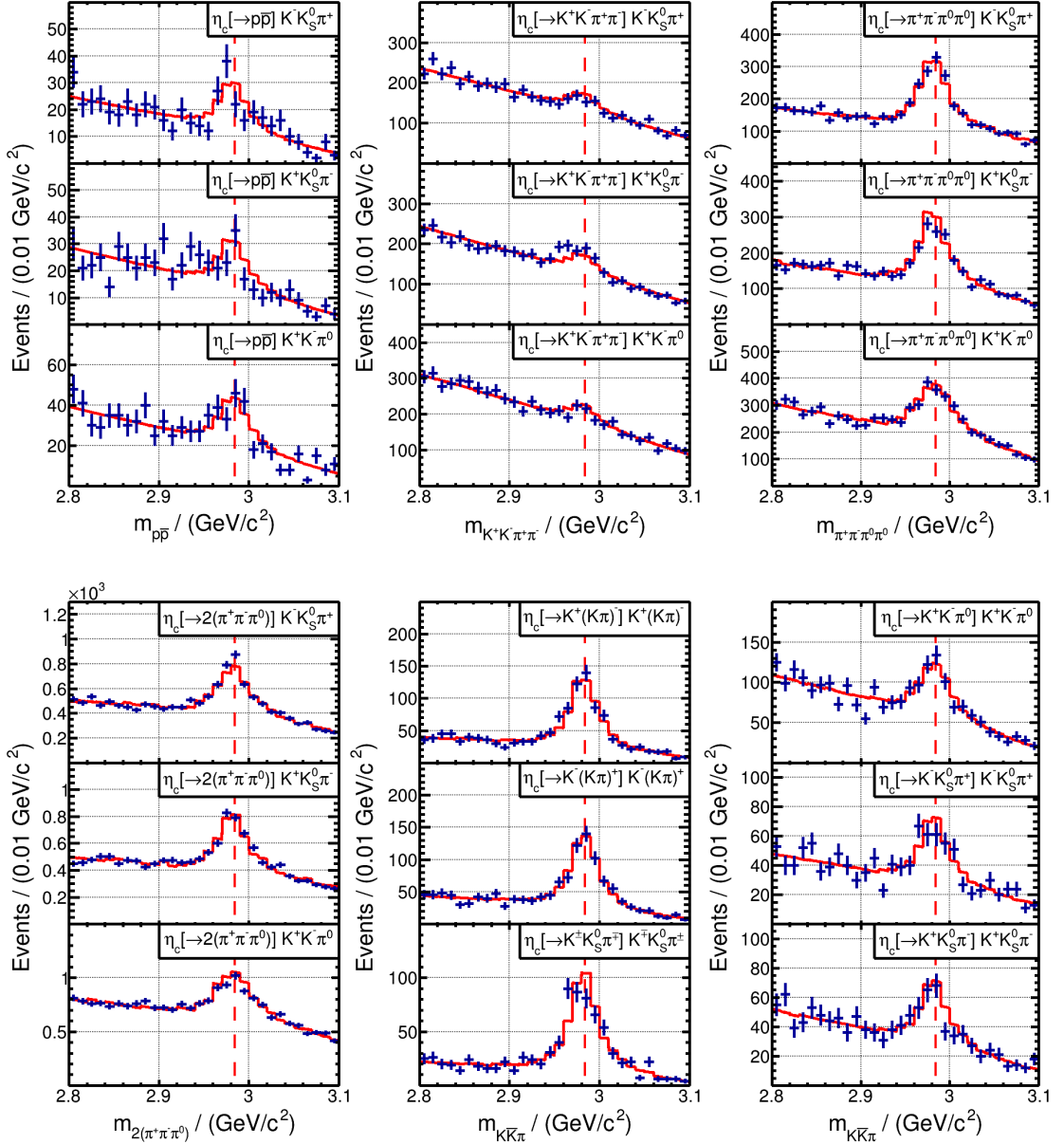


Figure 6.7.: Combined fit to the cocktail MC sample for the decays $\eta_c \rightarrow p\bar{p}$ (top left), $\eta_c \rightarrow K^+K^-\pi^+\pi^-$ (top middle), $\eta_c \rightarrow \pi^+\pi^-\pi^0\pi^0$ (top right), $\eta_c \rightarrow 2(\pi^+\pi^-\pi^0)$ (bottom left) and $\eta_c \rightarrow K\bar{K}\pi$ (bottom middle and right). The cocktail MC is presented in blue, the total fit as the red solid line and the mass of the η_c according to the PDG as the red dashed line.

6. Analysis of the Reaction $e^+e^- \rightarrow \eta_c K^* K$

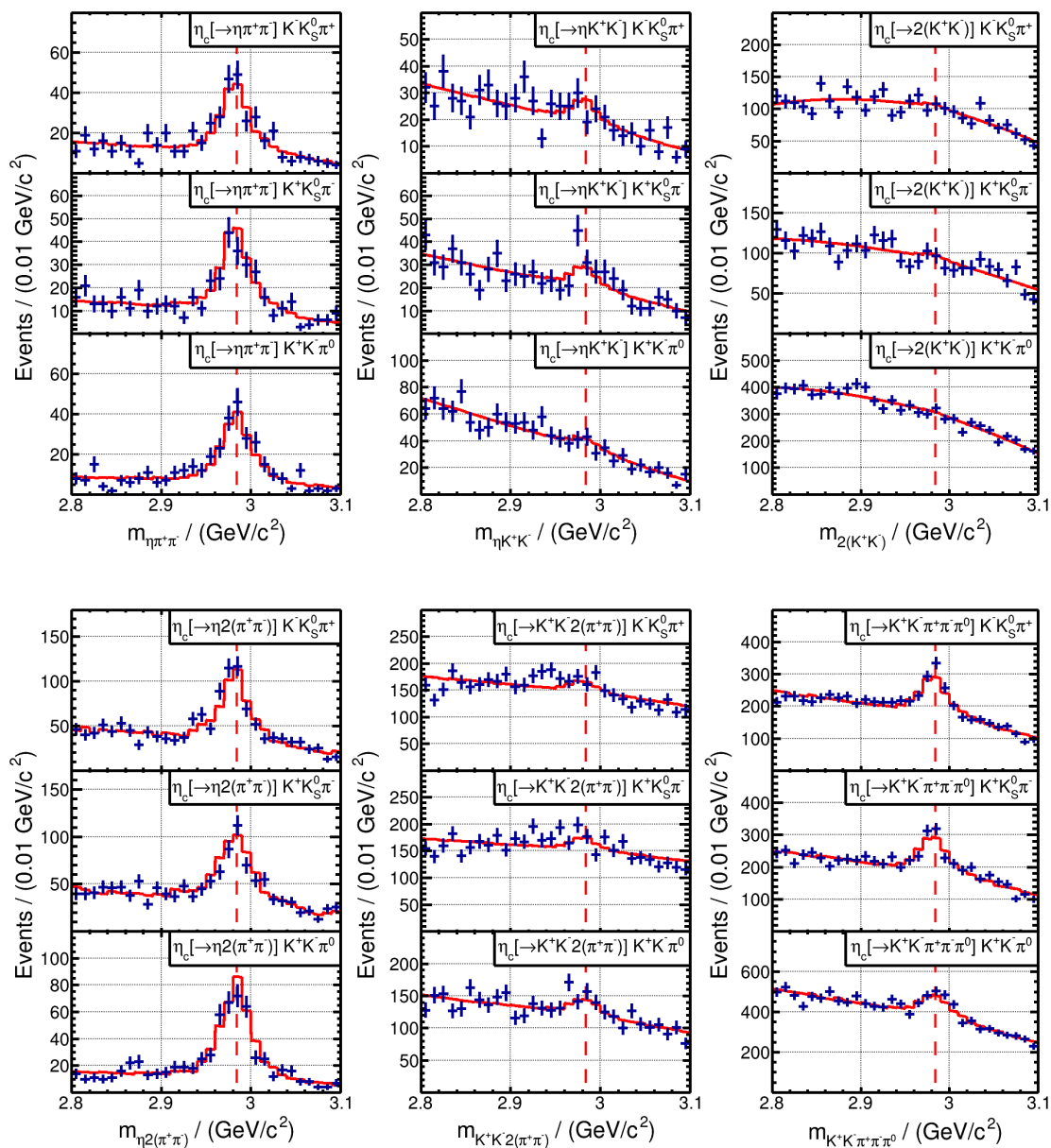


Figure 6.8.: Combined fit to the cocktail MC sample for the decays $\eta_c \rightarrow \eta\pi^+\pi^-$ (top left), $\eta_c \rightarrow \eta K^+K^-$ (top middle), $\eta_c \rightarrow 2(K^+K^-)$ (top right), $\eta_c \rightarrow \eta 2(\pi^+\pi^-)$ (bottom left), $\eta_c \rightarrow K^+K^- 2(\pi^+\pi^-)$ (bottom middle) and $\eta_c \rightarrow K^+K^- \pi^+\pi^-\pi^0$ (bottom right). The cocktail MC is presented in blue, the total fit as the red solid line and the mass of the η_c according to the PDG as the red dashed line.

goodness-of-fit of $\chi^2/\text{ndf} = 144.37/104 = 1.39$. The position of the peak corresponds to the bias of the combined fitting procedure, which shows a small deviation from zero, but this difference is negligible compared to the width of the peak, which corresponds to the uncertainty of the fitting procedure. The fit determines a width of the peak close to one, which is the expected value for a reasonable model.

After checking the validity of the presented method, it can be applied to the data samples, which is presented in the next section.

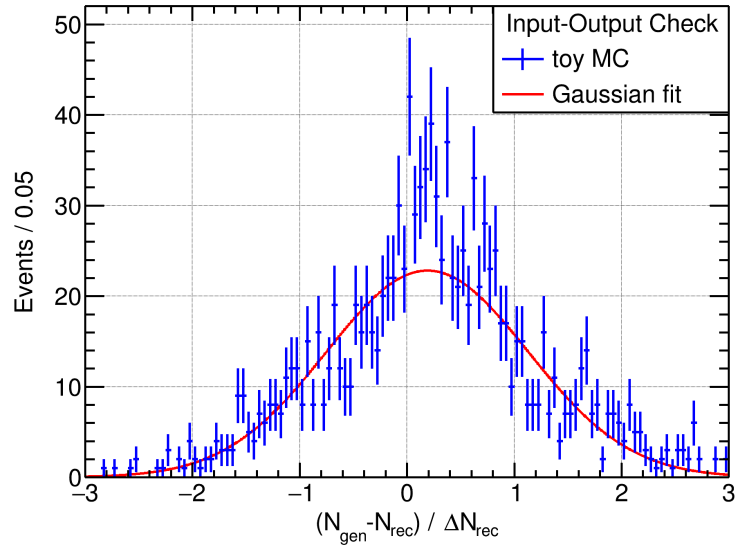


Figure 6.9.: Results of the 1200 input-output checks. Plotted is the difference between the generated number of η_c events and the number of η_c events determined with the combined fit, divided by the uncertainty of the number of reconstructed events. In blue the fit results to the toy MC are shown, and in red a fit with a Gaussian function is shown.

6.2.3. Results

The results of the combined fit to the 4680 data sample are presented in Figures 6.10 and 6.11 and the results for the other data samples are shown in Appendix B.1. As mentioned before, the number of events which survive the event selection is quite small in some of the final states and even in the final states with a significant number of events no clear η_c peak is visible. However, the background is described well for all final states and data samples. This is also true after summing all individual final states, which results in the spectra presented in Figure 6.12 for the 4640 and 4680 data sample. The other data samples are shown in Figure B.11. The fit determines a statistical significance of the η_c signal of 0.8σ and 1.5σ for the 4600 and 4640 samples, respectively, while for all other samples the significance is zero, if the number of produced η_c mesons is limited to positive values.

Since no significant signals are present an upper limit on the number \mathcal{N} of produced η_c mesons is calculated according to the method presented in Section 5.3. The resulting likelihood profile for the 4680 sample is presented in Figure 6.13 and for the other samples the profiles are found in Appendix B.2. The likelihood profiles are fitted with an asymmetric Gaussian function defined as

$$\mathcal{G}(\mathcal{N}) = \begin{cases} \exp\left[-\frac{(\mathcal{N}-\mathcal{N}_{\max})^2}{2\sigma_l^2}\right] & \text{for } \mathcal{N} \geq \mathcal{N}_{\max} \\ \exp\left[-\frac{(\mathcal{N}-\mathcal{N}_{\max})^2}{2\sigma_r^2}\right] & \text{for } \mathcal{N} < \mathcal{N}_{\max} \end{cases}, \quad (6.48)$$

where \mathcal{N}_{\max} is maximum of the peak and σ_l and σ_r are the left and right width of the peak, respectively. As can be seen, the profiles differ significantly from the Gaussian functions, which shows that the uncertainties are non-Gaussian. Therefore, these fits are not used to determine the upper limits. Instead the upper limit is determined by discretely integrating the determined likelihood values until 90% of the area is reached. The resulting upper limits are presented in Table 6.2.

6.3. Calculation of the Cross Section

With the determined upper limits for the number of produced η_c mesons, the cross section for the reaction $e^+e^- \rightarrow \eta_c K^* K$ can be determined. The first step is the calculation of the observed cross section which is given by

$$\sigma_{\text{obs}}(e^+e^- \rightarrow \eta_c K^* K) = \frac{\mathcal{N}}{\mathcal{L}_{\text{int}}}. \quad (6.49)$$

The resulting upper limits are presented in Table 6.2. From the observed cross section the Born cross section can be calculated, which only includes the production of the final state via the lowest order Feynman diagrams. For this, the observed cross section has to be corrected for initial-state radiation and vacuum polarization, which are shown in Figure 6.14. This results in the cross section being calculated as

$$\sigma_{\text{Born}}(e^+e^- \rightarrow \eta_c K^* K) = \frac{\mathcal{N}}{\mathcal{L}_{\text{int}}(1 + \delta_r)(1 + \delta_v)}. \quad (6.50)$$

Here, $(1 + \delta_r)$ and $(1 + \delta_v)$ are the correction factors for ISR and vacuum polarization, respectively. The correction factor for vacuum polarization is calculated with the program ALPHAQED [244] and the correction factor for ISR is taken from the MC generator [173], which was used to generate the MC samples for the combined fit. As mentioned before, the ISR correction factor depends on the line shape of the studied reaction and in this case the cross section for $e^+e^- \rightarrow J/\psi K K$ was used, which is expected to have a similar cross

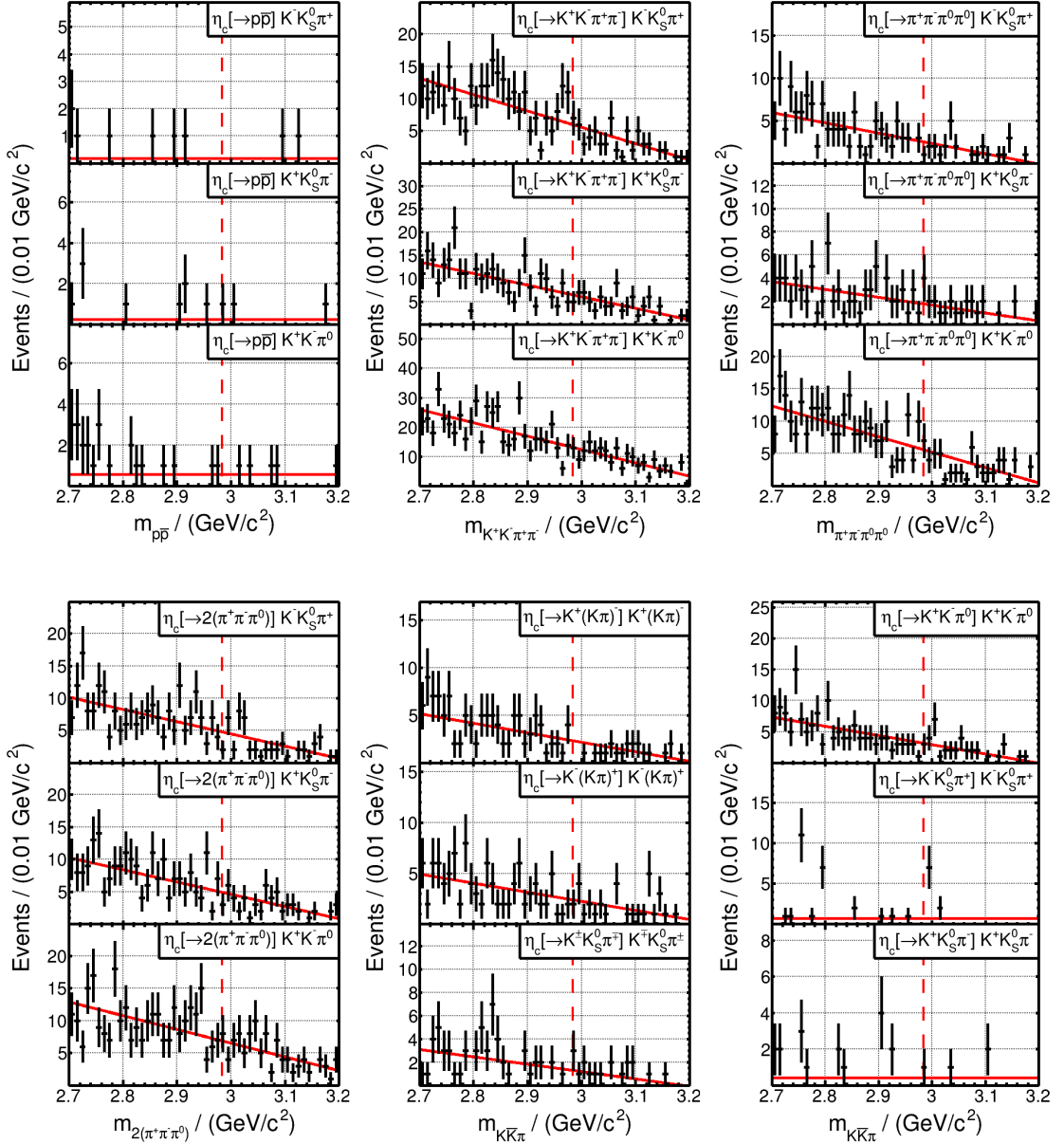


Figure 6.10.: Combined fit to the 4680 data sample for the decays $\eta_c \rightarrow p\bar{p}$ (top left), $\eta_c \rightarrow K^+ K^- \pi^+ \pi^-$ (top middle), $\eta_c \rightarrow \pi^+ \pi^- \pi^0 \pi^0$ (top right), $\eta_c \rightarrow 2(\pi^+ \pi^- \pi^0)$ (bottom left) and $\eta_c \rightarrow K\bar{K}\pi$ (bottom middle and right). The data is presented in black, the total fit as the red solid line and the mass of the η_c according to the PDG as the red dashed line.

6. Analysis of the Reaction $e^+e^- \rightarrow \eta_c K^* K$

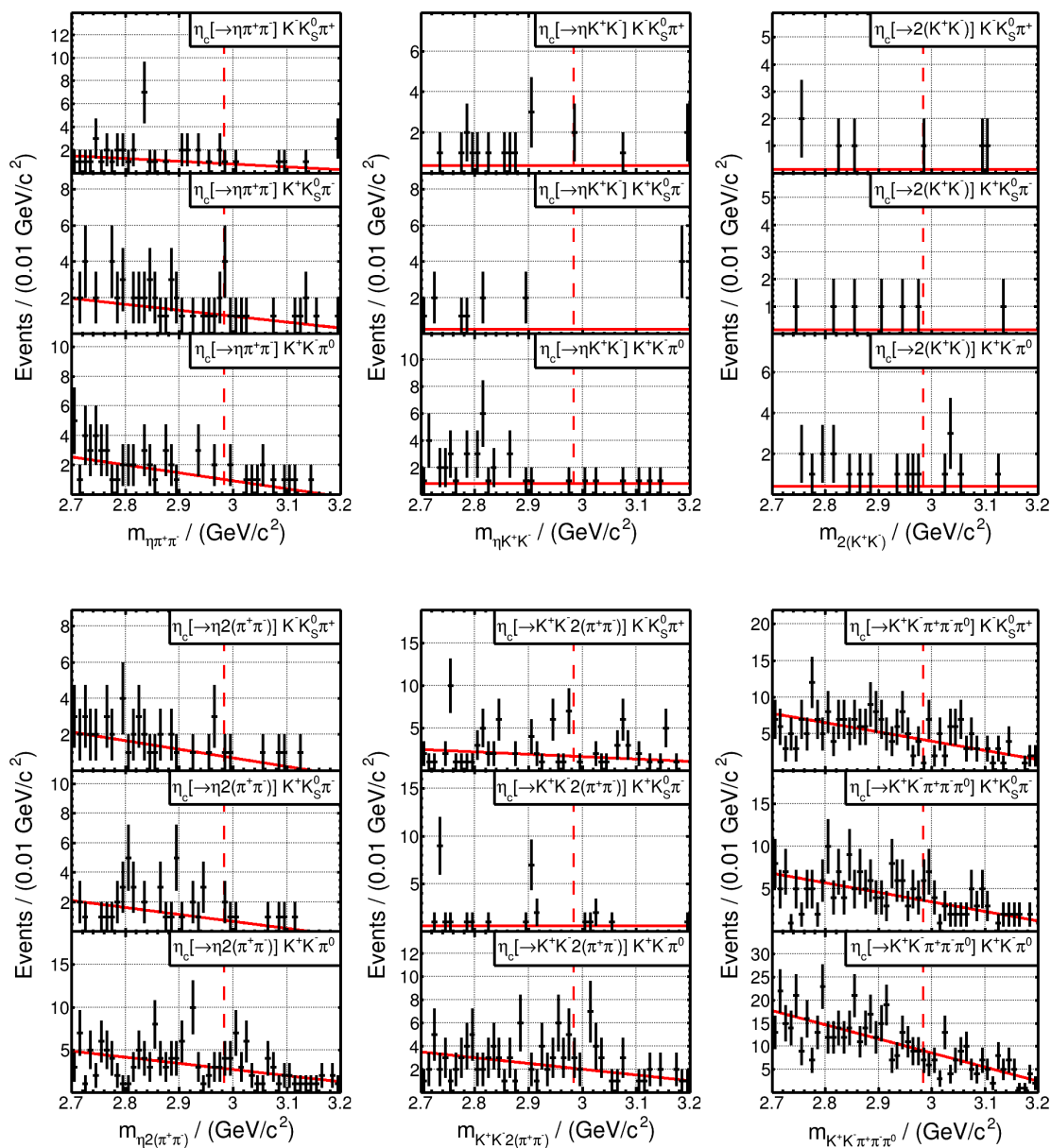


Figure 6.11.: Combined fit to the 4680 data sample for the decays $\eta_c \rightarrow \eta \pi^+ \pi^-$ (top left), $\eta_c \rightarrow \eta K^+ K^-$ (top middle), $\eta_c \rightarrow 2(K^+ K^-)$ (top right), $\eta_c \rightarrow \eta 2(\pi^+ \pi^-)$ (bottom left), $\eta_c \rightarrow K^+ K^- 2(\pi^+ \pi^-)$ (bottom middle) and $\eta_c \rightarrow K^+ K^- \pi^+ \pi^- \pi^0$ (bottom right). The data is presented in black, the total fit as the red solid line and the mass of the η_c according to the PDG as the red dashed line.

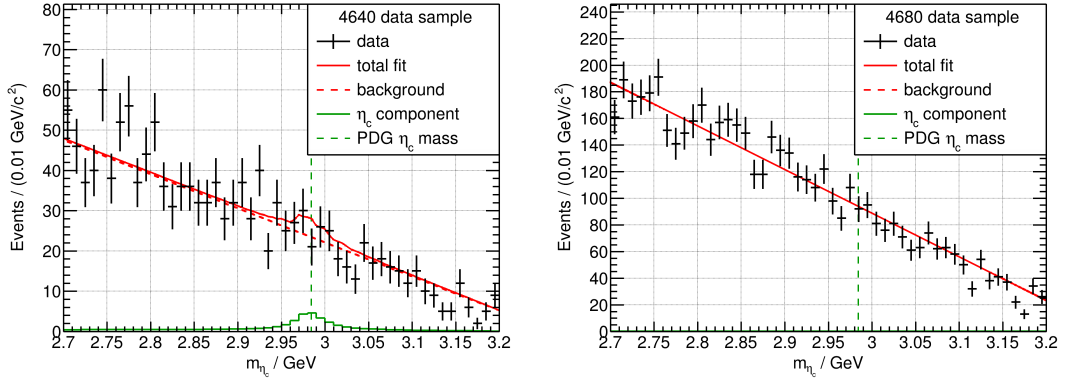


Figure 6.12.: Invariant mass spectrum of η_c candidates summed over all final states for the 4640 data sample (left) and the 4680 data sample (right). The data is presented in black, the sum of all fitted functions for each final state as the red solid line, the sum of all background components as the dashed red line, the sum of all signal components as the solid green line and the mass of the η_c according to the PDG as the green dashed line.

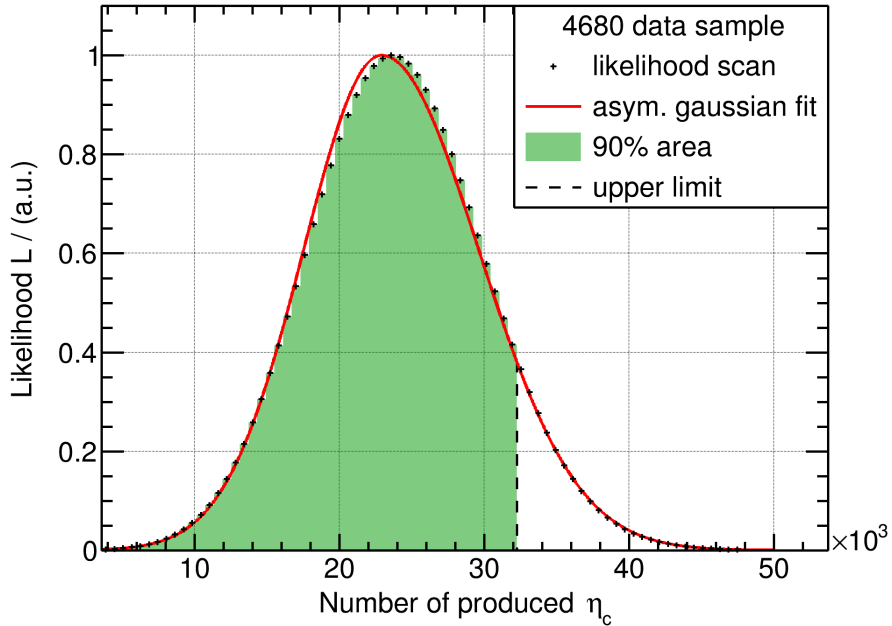


Figure 6.13.: Likelihood profile of the η_c fit for the 4680 data sample. The scan values are shown as the black markers, the fit with an asymmetric Gaussian function is shown as the solid red line, the 90% area under the peak is shown in green and the resulting upper limit is marked with the black dashed line.

section shape as $e^+e^- \rightarrow \eta_c K^* K$ [236, 245]. Since no significant signal was observed, it is not possible to use the actual cross section value of $e^+e^- \rightarrow \eta_c K^* K$ for ISR correction. However, the effect from this on the determined upper limits on the Born cross sections is negligible.

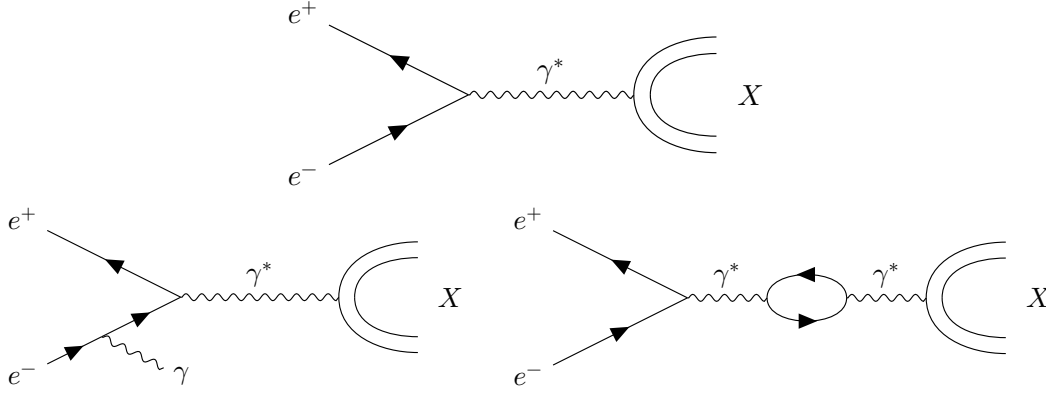


Figure 6.14.: Feynman diagrams for $e^+e^- \rightarrow \gamma^* \rightarrow X$ for the tree-level (top) and with the higher order corrections ISR (bottom left) and vacuum polarization (bottom right).

Table 6.2.: List of values needed for the calculation of the observed cross section $\sigma_{\text{obs}}(e^+e^- \rightarrow \eta_c K^* K)$ and Born cross section $\sigma_{\text{Born}}(e^+e^- \rightarrow \eta_c K^* K)$ at each center-of-mass energy \sqrt{s} : the determined upper limit on the number of produced η_c mesons \mathcal{N} , the integrated luminosity of the data sample \mathcal{L}_{int} , the ISR correction factor $(1 + \delta_r)$ and the vacuum polarization correction factor $(1 + \delta_v)$. All upper limits are determined at a confidence level of 90% and the included uncertainties are only statistical.

\sqrt{s} / MeV	$\mathcal{L}_{\text{int}} / \text{pb}^{-1}$	$\mathcal{N}_{\text{UL}} / 10^3$	$\sigma_{\text{obs}}^{\text{UL}} / \text{pb}$	$(1 + \delta_r)$	$(1 + \delta_v)$	$\sigma_{\text{Born}}^{\text{UL}} / \text{pb}$
4599.53 ± 0.74	586.9 ± 3.9	16.0	27.3	1.102	1.055	23.4
4628.00 ± 0.33	521.5 ± 2.8	7.9	15.1	1.181	1.055	12.2
4640.91 ± 0.38	551.7 ± 3.0	22.3	40.4	1.200	1.054	33.7
4661.24 ± 0.30	529.4 ± 2.9	10.3	19.5	1.158	1.054	15.9
4681.92 ± 0.30	1667.4 ± 8.9	21.1	12.7	1.043	1.054	11.5
4698.82 ± 0.37	535.5 ± 2.9	12.7	23.7	0.953	1.055	23.6

6.4. Search for Contributions of the Z_{cs}

As the final step in this analysis, the invariant mass spectrum of the $\eta_c K^*$ system is analyzed to search for possible contributions from Z_{cs} mesons. To do so, all η_c candidates are considered which have an invariant mass m_{η_c} close to the mass of the η_c according to the PDG [6]:

$$m_{\eta_c} \in [m_{\eta_c, \text{PDG}} - 2\Gamma_{\eta_c, \text{PDG}}; m_{\eta_c, \text{PDG}} + 2\Gamma_{\eta_c, \text{PDG}}]. \quad (6.51)$$

The resulting $\eta_c K^*$ invariant mass spectrum is shown in Figure 6.15. To reduce the impact from the natural width of the η_c , the $\eta_c K^*$ invariant mass is corrected by subtracting the mass of the η_c candidate and adding the mass of the η_c meson according to the PDG [6]. As can be seen no significant enhancement is visible. And since no significant η_c peak is observable, the upper limit on the number of Z_{cs} mesons cannot be extracted by a fit to the $\eta_c K^*$ spectrum. Instead, by assuming that all observed reactions $e^+e^- \rightarrow \eta_c K^* K$ take place via an intermediate Z_{cs} the upper limit on the product of the production

cross section $\sigma_{\text{Born}}(e^+e^- \rightarrow Z_{cs}K)$ and the decay branching ratio $Z_{cs} \rightarrow \eta_c K^*$ can be calculated. The resulting value can then be compared with the corresponding value for the reaction $e^+e^- \rightarrow Z_{cs}^\pm K^\mp \rightarrow (D_s^\pm \bar{D}^{*0} + D_s^{*\pm} \bar{D}^0) K^\mp$ [27] by assuming isospin symmetry. This is done for the 4680 data sample and results in:

$$\begin{aligned} R &= \frac{\sigma_{\text{Born}}(e^+e^- \rightarrow Z_{cs}^\pm K^\mp) \cdot \text{Br}(Z_{cs}^\pm \rightarrow \eta_c K^{*\pm})}{\sigma_{\text{Born}}(e^+e^- \rightarrow Z_{cs}^\pm K^\mp) \cdot \text{Br}(Z_{cs}^\pm \rightarrow (D_s^\pm \bar{D}^{*0} + D_s^{*\pm} \bar{D}^0))} \\ &= \frac{\text{Br}(Z_{cs}^\pm \rightarrow \eta_c K^{*\pm})}{\text{Br}(Z_{cs}^\pm \rightarrow (D_s^\pm \bar{D}^{*0} + D_s^{*\pm} \bar{D}^0))} < \frac{0.5 \cdot 11.5 \text{ pb}}{4.4_{-1.6}^{+1.7} \text{ pb}} < 3.3, \end{aligned} \quad (6.52)$$

at a confidence level of 90%, which can be compared with the theoretical prediction from [84]²⁵:

$$\begin{aligned} R &= \frac{\Gamma(Z_{cs}^\pm \rightarrow \eta_c K^{*\pm})}{\Gamma(Z_{cs}^\pm \rightarrow (D_s^\pm \bar{D}^{*0} + D_s^{*\pm} \bar{D}^0))} \\ &= \frac{\text{Br}(Z_{cs}^\pm \rightarrow \eta_c K^{*\pm})}{\text{Br}(Z_{cs}^\pm \rightarrow (D_s^\pm \bar{D}^{*0} + D_s^{*\pm} \bar{D}^0))} = \frac{(10.8 \pm 6.2) \text{ MeV}}{(2.9 \pm 2.1) \text{ MeV}} = 3.7 \pm 3.5. \end{aligned} \quad (6.53)$$

As can be seen, the values are compatible, as the determined upper limit is at the center of the determined confidence interval for the theoretical value.

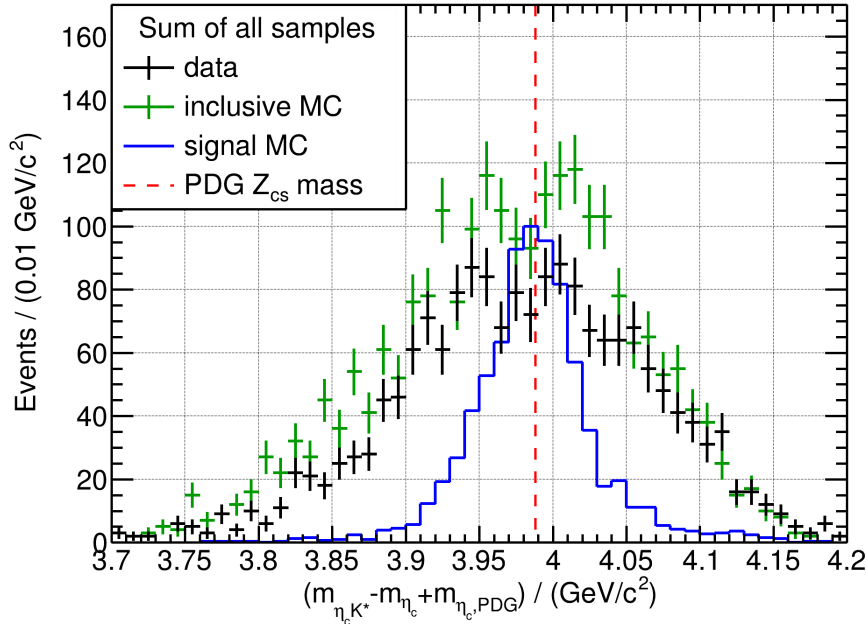


Figure 6.15.: Invariant mass spectrum of the $\eta_c K^*$ system summed over all final states and all center-of-mass energies. The data is presented in black, the inclusive MC in green and the signal MC in blue. The mass of the Z_{cs} according to the PDG [6] is indicated as a red dashed line.

²⁵For the calculation of the uncertainty of the theory prediction, it was assumed that all uncertainties are uncorrelated.

7. Conclusions and Outlook

In the context of this thesis, two different analyses were performed, both located in the field of hadron spectroscopy. The overall goal was to find candidates for exotic mesons. While in the $\psi(2S) \rightarrow \gamma\eta'\pi^+\pi^-$ analysis this was done using the decays of charmonia, in the $e^+e^- \rightarrow \eta_c K^* K$ analysis the direct production of an exotic meson in e^+e^- annihilation was investigated. The analyses used data samples collected with the BESIII experiment, including the world's largest data sample of $\psi(2S)$ decays, as well as large samples in the energy region between 4.6 GeV and 4.7 GeV.

For both analyses, the first step was the general event selection, which consists of a list of applied criteria used to reduce the large raw data samples, by removing events that are most likely not of interest for analyses being performed. These include the tracking, PID, and photon reconstruction algorithms developed and provided by the BESIII collaboration, as well as some initial selection criteria used as standard criteria in BESIII analyses. However, the number of background events in both analyses still greatly exceeded the number of signal events, and further selection criteria had to be developed. In both analyses, the background was investigated using the dedicated inclusive MC samples as well as by looking at the invariant mass spectra of all possible subsystems in the analyzed reactions. In the case of the $\psi(2S) \rightarrow \gamma\eta'\pi^+\pi^-$ analysis, the selection criteria were optimized to achieve the best possible significance of the signal over the background using a multidimensional figure-of-merit approach. This procedure was not applicable for the $e^+e^- \rightarrow \eta_c K^* K$ analysis due to the large number of different final states with only a small number of events each. Instead, the selection criteria were defined manually, taking into account the detector resolution, as well as, the natural width of the appearing resonances. A possible method to be explored in the future to replace the cut-driven event selection, is the use of artificial intelligence models that can be used to discriminate between signal and background [246]. In the context of this work, this approach was tested in the analysis of $\psi(2S) \rightarrow \gamma\eta'\pi^+\pi^-$ using an artificial neural network, presented in Appendix C. In the end, this method was not used for the full analysis because the interpretation of the applied event selection was difficult and it was unclear how to assign systematic uncertainties.

After applying the event selection criteria, it became clear that in the $\psi(2S) \rightarrow \gamma\eta'\pi^+\pi^-$ analysis still a large amount of non- η' background was present that could not be easily

accounted for in the subsequent analysis. Therefore, the sideband subtraction method was used to estimate this background, leaving the spectrum of interest, the invariant mass of the $\eta'\pi^+\pi^-$ system, with only a small number of background events. In the future, it should be investigated whether the sideband subtraction method could be replaced by a more sophisticated approach. One such approach is the Q -factor method [247], which assigns each event a weight corresponding to the probability of the event being a signal event. A major advantage of this method over the applied sideband subtraction method is that it does not produce histogram bins with negative weights.

Analysis of the resulting data samples after the entire event selection procedure for the $\psi(2S) \rightarrow \gamma\eta'\pi^+\pi^-$ analysis showed clear signals from the reactions $\chi_{c1,2}, \eta_c \rightarrow \eta'\pi^+\pi^-$ and the number of events was determined using least- χ^2 fits. After combining the information from the two different η' decays, the corresponding branching ratios were determined with unprecedented precision as

$$\text{Br}(\eta_c \rightarrow \eta'\pi^+\pi^-) = (1.67 \pm 0.14) \times 10^{-2}, \quad (7.1)$$

$$\text{Br}(\chi_{c1} \rightarrow \eta'\pi^+\pi^-) = (1.64 \pm 0.12) \times 10^{-3}, \quad (7.2)$$

$$\text{Br}(\chi_{c2} \rightarrow \eta'\pi^+\pi^-) = (2.95 \pm 0.29) \times 10^{-4}. \quad (7.3)$$

Although there are no theoretical predictions for these decay modes yet, these values are needed to complete our picture of the 1^3P_J and 1^1S_0 charmonium states, for which a large percentage of the decays are still unknown [6], and in the future predictions for these three-body decays may become feasible, with first predictions for two-body decays already possible [136–138]. Additionally, an upper limit for the CP violating decay $\chi_{c0} \rightarrow \eta'\pi^+\pi^-$ was obtained, which improves the existing upper limit by more than an order of magnitude:

$$\text{Br}(\chi_{c0} \rightarrow \eta'\pi^+\pi^-) < 1.46 \times 10^{-5}. \quad (7.4)$$

This observation is consistent with the so-called strong CP problem, i.e. the observation that all processes mediated by the strong interaction, seem to conserve the CP symmetry, even though the mathematical formulation of QCD allows for the inclusion of a CP violating term [40–42].

In addition to the already known charmonia decays, the hexaquark candidate $X(1835)$ was also observed for the first time in the production channel $\psi(2S) \rightarrow \gamma X(1835)$ and the product branching ratio was determined as

$$\text{Br}(\psi(2S) \rightarrow \gamma X(1835)) \cdot \text{Br}(X(1835) \rightarrow \eta'\pi^+\pi^-) = (2.89 \pm 0.64) \times 10^{-5}. \quad (7.5)$$

The first observation of this particle in the $\psi(2S)$ decay made it possible to compare the production branching ratios for $J/\psi \rightarrow \gamma X(1835)$ and $\psi(2S) \rightarrow \gamma X(1835)$, and the

resulting value is compatible with the corresponding value for the $X(p\bar{p})$. This result leads to the assumption, that these particles are indeed the same state. The observed different widths of the particle in the two decay channels can then be explained by a model which assumes that the particle is a baryonium, a bound state of a proton and antiproton [248–251].

The achieved signal purity in the χ_{cJ} region allowed it to perform a partial wave analysis, which was carried out for the decay of the χ_{c2} , since no scalar waves are allowed in this decay. Several models were tested and finally a solution including four f_2 resonances was found to be the best fit. While no significant contribution from the hybrid candidate $\pi_1(1600)^\pm$ was found, an upper limit on its product branching ratio was obtained:

$$\text{Br}(\chi_{c2} \rightarrow \pi_1(1600)^\pm \pi^\mp) \cdot \text{Br}(\pi_1(1600)^\pm \rightarrow \eta' \pi^\pm) < 3.26 \times 10^{-5}. \quad (7.6)$$

In the future, it would be useful to combine the two channels $\chi_{c1} \rightarrow \pi_1(1600)^\pm \pi^\mp$ and $\chi_{c2} \rightarrow \pi_1(1600)^\pm \pi^\mp$ in a combined partial wave analysis taking advantage of the shared decay branching ratio of the $\pi_1(1600)$. This could make it possible to extract the absolute branching ratio, which can then be compared with theoretical predictions for a hybrid meson [252, 253].

In the case of the $e^+e^- \rightarrow \eta_c K^* K$ analysis, the event selection showed no significant signal in any of the analyzed final states, so a sophisticated coupled fit was applied to combine information from all final states. With this fit it was possible to accurately describe all final states and to extract for the first time an upper limit for the cross section of the reaction $e^+e^- \rightarrow \eta_c K^* K$ in a range of ~ 10 pb to 40 pb, with the best upper limit being extracted for $\sqrt{s} = (4681.92 \pm 0.39)$ MeV with

$$\sigma_{\text{Born}}(e^+e^- \rightarrow \eta_c K^* K) < 11.5 \text{ pb}. \quad (7.7)$$

The applied procedure was validated on dedicated MC samples, which showed good agreement between the extracted and generated number of events.

After combining all final states and all center-of-mass energies, no significant signal for a contribution of the Z_{cs} was found. However, using the combined fit, it was possible to determine an upper limit for the ratio of the branching ratios of the Z_{cs} decay into $\eta_c K^*$ and the previously observed decay into $D_s^\pm \bar{D}^{*0} + D_s^{*\pm} \bar{D}^0$ [27], given by

$$R = \frac{\text{Br}(Z_{cs}^\pm \rightarrow \eta_c K^{*\pm})}{\text{Br}(Z_{cs}^\pm \rightarrow (D_s^\pm \bar{D}^{*0} + D_s^{*\pm} \bar{D}^0))} < 3.3. \quad (7.8)$$

This upper limit is in the middle of the theoretical prediction [84] for this ratio. In the future, to improve the sensitivity for this channel, additional η_c decay modes can be

included on the one hand, and on the other hand, it might be useful to systematically study all of the included channels to see if the upper limit could be improved by excluding from the fit some of the final states for which a large number of background events are expected. By improving the sensitivity, it may be possible to exclude some of the models that predict a large branching ratio of the Z_{cs} into $\eta_c K^*$ [92, 254–256]. Possible channels to add to the fit are e.g. $\eta_c \rightarrow K_S^0 K^\pm \pi^+ \pi^- \pi^\mp$ or $\eta_c \rightarrow 3(\pi^+ \pi^-)$. In addition, the BESIII experiment has now taken additional data samples between 4.7 GeV and 5.0 GeV, which can be added to the analysis. In this higher-mass region, an enhancement in the cross section for $e^+ e^- \rightarrow J/\psi K^+ K^-$ [237] was visible, which was described by a resonant state called $\psi(4710)$. This state could be a charmonium-like state or the previously unobserved $n^{2s+1} L_J = 5^3 S_1$ charmonium state. If such a state exists, it should increase the cross section for the production of the Z_{cs} [84], as it was observed for the Z_c in the reaction $\psi(4230) \rightarrow Z_c^\pm \pi^\mp \rightarrow J/\psi \pi^+ \pi^-$ [77], and thus support the observation of the decay $Z_{cs} \rightarrow \eta_c K^*$.

A. Analysis of the Decay

$$\psi(2S) \rightarrow \gamma\eta'\pi^+\pi^-$$

A.1. Integration of the Three-Body Phase Space

The three-body phase space $d\Phi_3(X; \eta', \pi^+, \pi^-)$ for the decay $X(1835) \rightarrow \eta'\pi^+\pi^-$ can be calculated recursively via [6]

$$d\Phi_3(X; \eta', \pi^+, \pi^-) = \int_{s_{\pi\pi, \min}}^{s_{\pi\pi, \max}} d\Phi_2(X; \eta', (\pi\pi)) d\Phi_2((\pi\pi); \pi^+, \pi^-) ds_{\pi\pi}. \quad (\text{A.1})$$

Here, $d\Phi_2(X; \eta', (\pi\pi))$ is the two-body phase space for the decay of the $X(1835)$ into the η' and an intermediate $\pi\pi$ system and $d\Phi_2((\pi\pi); \pi^+, \pi^-)$ is the phase space for the decay of the $\pi\pi$ system into the π^+ and π^- . The two-body phase space for a decay $a \rightarrow bc$ is determined by [6]

$$d\Phi_2(a; b, c) = \frac{1}{16\pi} \sqrt{\left(1 - \frac{(m_b + m_c)^2}{s_a}\right) \left(1 - \frac{(m_b - m_c)^2}{s_a}\right)}, \quad (\text{A.2})$$

with the masses of the particles m_b and m_c , as well as the squared invariant mass s_a of the particle system a . The integration over the squared invariant mass of the $(\pi\pi)$ system $s_{\pi\pi}$ in Equation (A.1) is performed from the minimum value

$$s_{\pi\pi, \min} = 4m_\pi^2 \quad (\text{A.3})$$

to the maximum value

$$s_{\pi\pi, \max} = (\sqrt{s_X} - m_{\eta'})^2, \quad (\text{A.4})$$

where s_X is the squared invariant mass of the $\eta'\pi^+\pi^-$ system. Inserting Equations (A.2) to (A.4) into Equation (A.1) results in

$$d\Phi_3(X; \eta', \pi^+, \pi^-) = \frac{1}{(16\pi)^2} \int_{4m_\pi^2}^{(\sqrt{s_X} - m_{\eta'})^2} \sqrt{1 - \frac{4m_\pi^2}{s_{\pi\pi}}} ds_{\pi\pi} \cdot \sqrt{\left(1 - \frac{(m_{\eta'} + 2m_\pi)^2}{s_X}\right) \left(1 - \frac{(m_{\eta'} - 2m_\pi)^2}{s_X}\right)}. \quad (\text{A.5})$$

The integration over $s_{\pi\pi}$ can be performed analytically resulting in

$$d\Phi_3(X; \eta', \pi^+, \pi^-) = \frac{1}{(16\pi)^2} \sqrt{\left(1 - \frac{(m_{\eta'} + 2m_\pi)^2}{s_X}\right) \left(1 - \frac{(m_{\eta'} + 2m_\pi)^2}{s_X}\right)} \left[(\sqrt{s_X} - m_{\eta'})^2 \sqrt{1 - \frac{4m_\pi^2}{(\sqrt{s_X} - m_{\eta'})^2}} - 4m_\pi^2 \tanh^{-1} \left(\sqrt{1 - \frac{4m_\pi^2}{(\sqrt{s_X} - m_{\eta'})^2}} \right) \right]. \quad (\text{A.6})$$

The phase space factor $\mathcal{P}(m)$ is now defined via

$$\mathcal{P}(m) = \frac{d\Phi_3(X; \eta', \pi^+, \pi^-)|_{s_X=m}}{d\Phi_3(X; \eta', \pi^+, \pi^-)|_{s_X=m_{X(1835)}}}, \quad (\text{A.7})$$

with the mass of the $X(1835)$ taken from the PDG $m_{X(1835)} = 1826.5^{+13.0}_{-3.4}$ MeV/ c^2 [6].

A.2. Blatt-Weisskopf Barrier Factors

The Blatt-Weisskopf barrier factors [223] $B_L(p/p_0)$ are phenomenologically introduced to damp the growth of the p^L term in the description of resonances [6]. They are given for $L < 3$ by

$$B_0(p/p_0) = 1, \quad (\text{A.8})$$

$$B_1(p/p_0) = \sqrt{\frac{1}{1 + (p/p_0)^2}}, \quad (\text{A.9})$$

$$B_2(p/p_0) = \sqrt{\frac{1}{9 + 3(p/p_0)^2 + (p/p_0)^4}}. \quad (\text{A.10})$$

The momentum scale is often chosen in the range 0.2 GeV/ c to 1 GeV/ c [6], however, it often only has a minimal effect of the visible line shape.

A.3. Systematic Uncertainties

In the following sections the systematic studies for all resonances except for the χ_{c1} are shown. The procedure for the determination is described in Section 5.6.

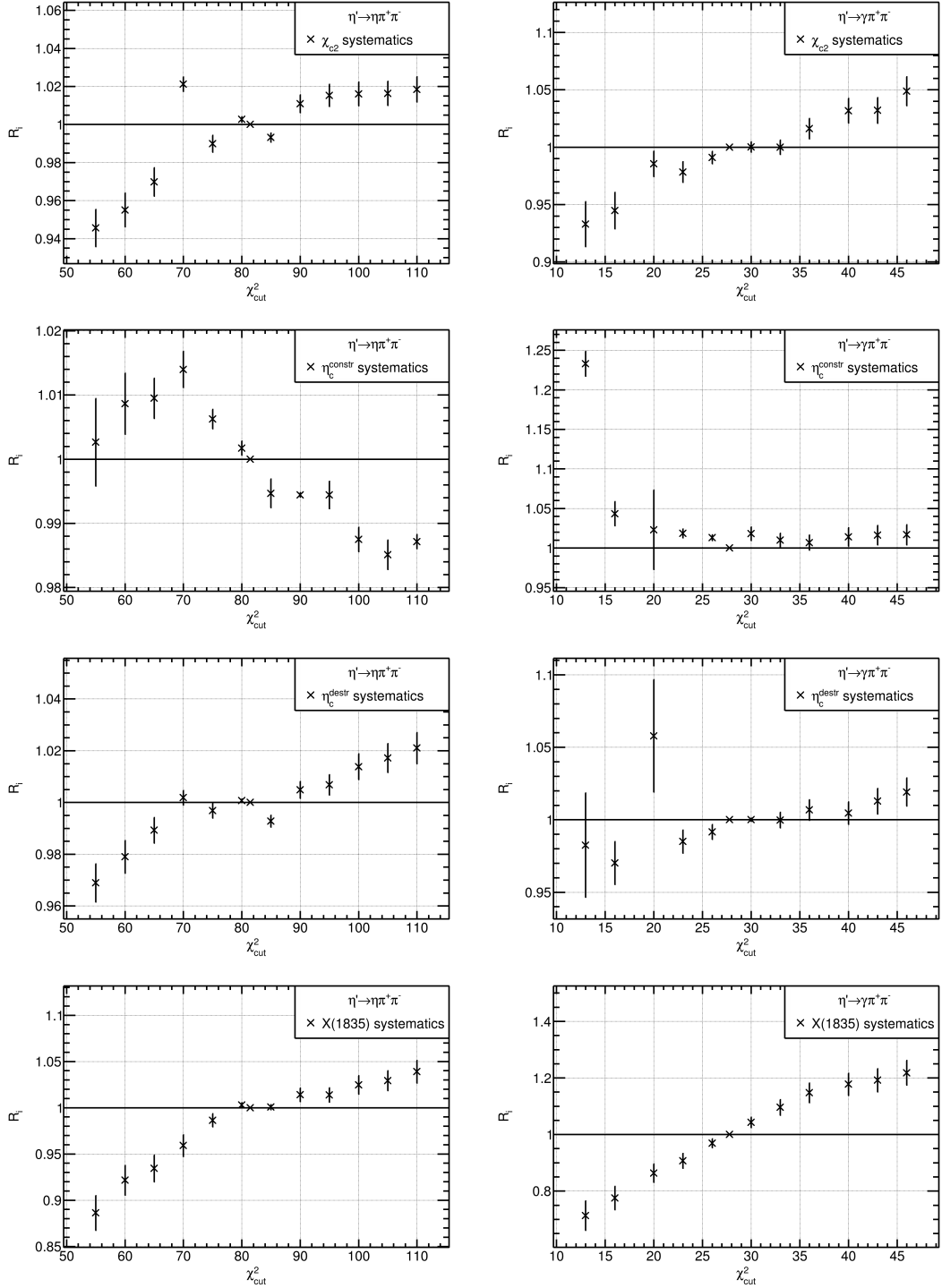
A.3.1. Kinematic Fit χ^2 Cut


Figure A.1.: Ratio of the variation and the nominal value for the branching ratio for the cut on the χ^2 of the kinematic fit, in the $\eta' \rightarrow \eta\pi^+\pi^-$ channel (left) and the $\eta' \rightarrow \gamma\pi^+\pi^-$ channel (right). The resonances from top to bottom are: χ_{c2} , η_c^{constr} , η_c^{destr} and $X(1835)$.

A.3.2. Minimum Photon Energy

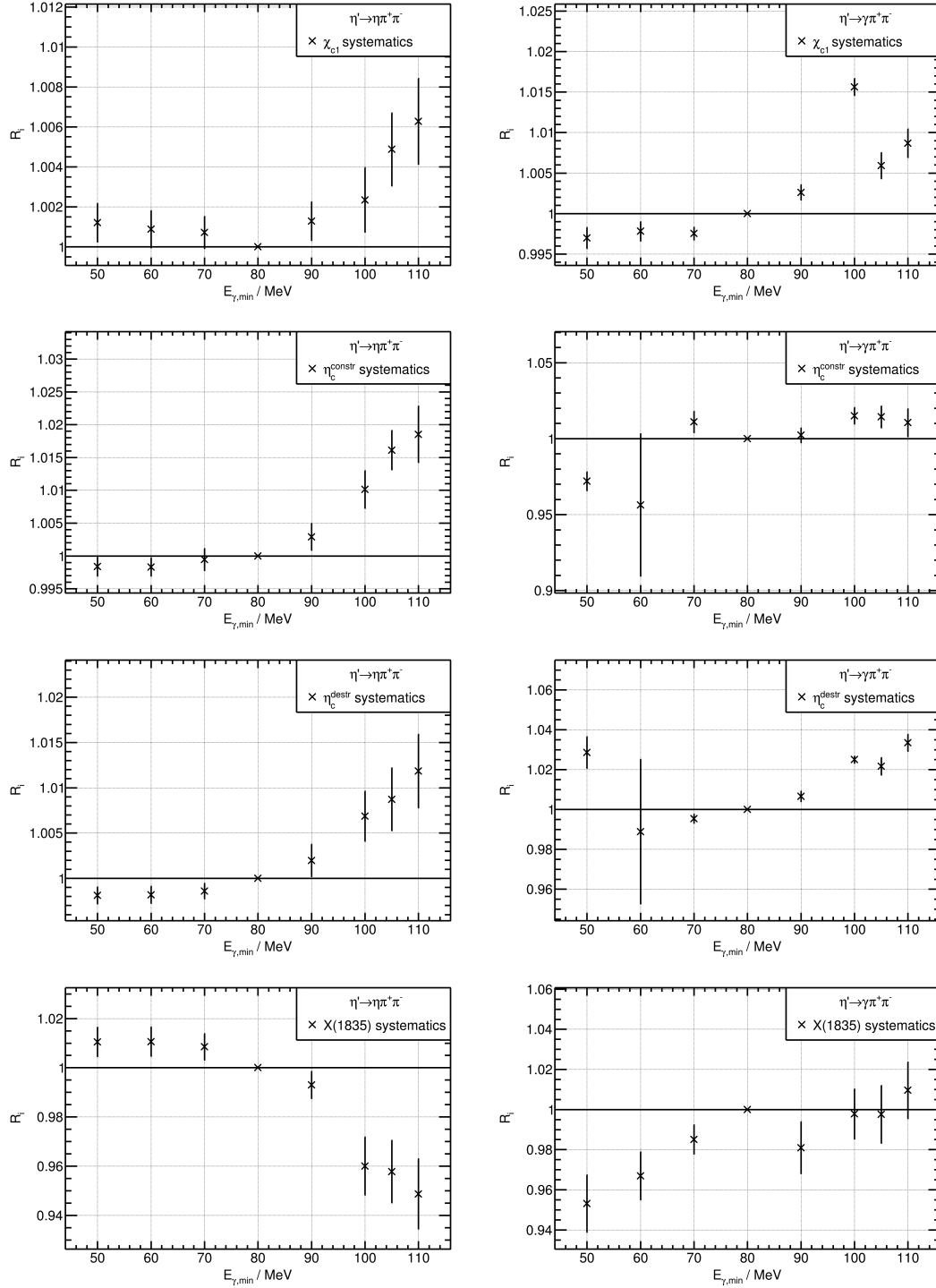


Figure A.2.: Ratio of the variation and the nominal value for the branching ratio for the minimum photon energy, in the $\eta' \rightarrow \eta\pi^+\pi^-$ channel (left) and the $\eta' \rightarrow \gamma\pi^+\pi^-$ channel (right). The resonances from top to bottom are: χ_{c1} , η_c^{constr} , η_c^{destr} and $X(1835)$.

A.3.3. J/ψ Veto in the $\pi^+\pi^-$ Recoil System

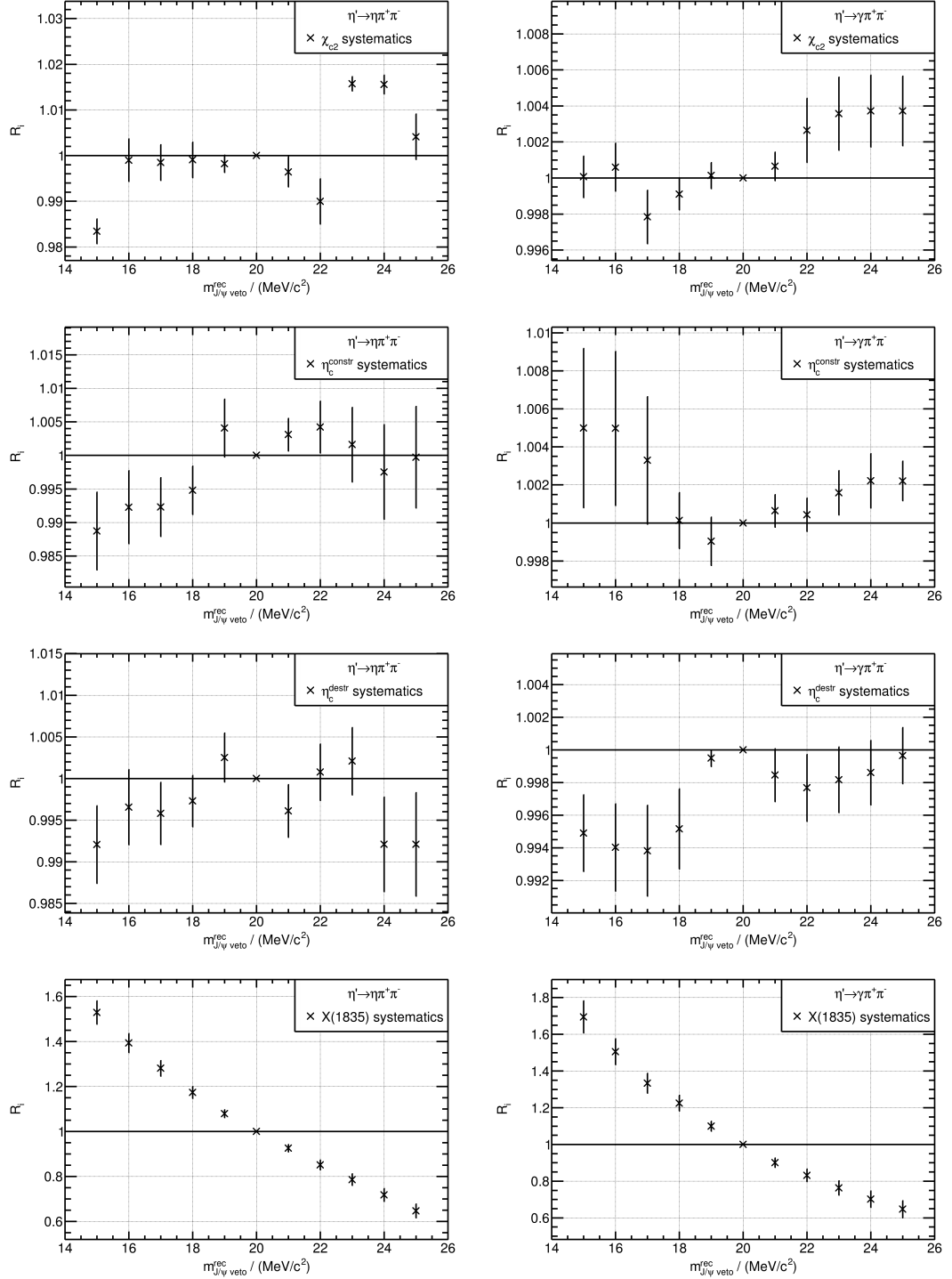


Figure A.3.: Ratio of the variation and the nominal value for the branching ratio for the J/ψ veto in the system recoiling against the $\pi^+\pi^-$ system, in the $\eta' \rightarrow \eta\pi^+\pi^-$ channel (left) and the $\eta' \rightarrow \gamma\pi^+\pi^-$ channel (right). The resonances from top to bottom are: χ_{c2} , η_c^{constr} , η_c^{destr} and $X(1835)$.

A.3.4. J/ψ Veto in the 4π System and ρ^0 Cut

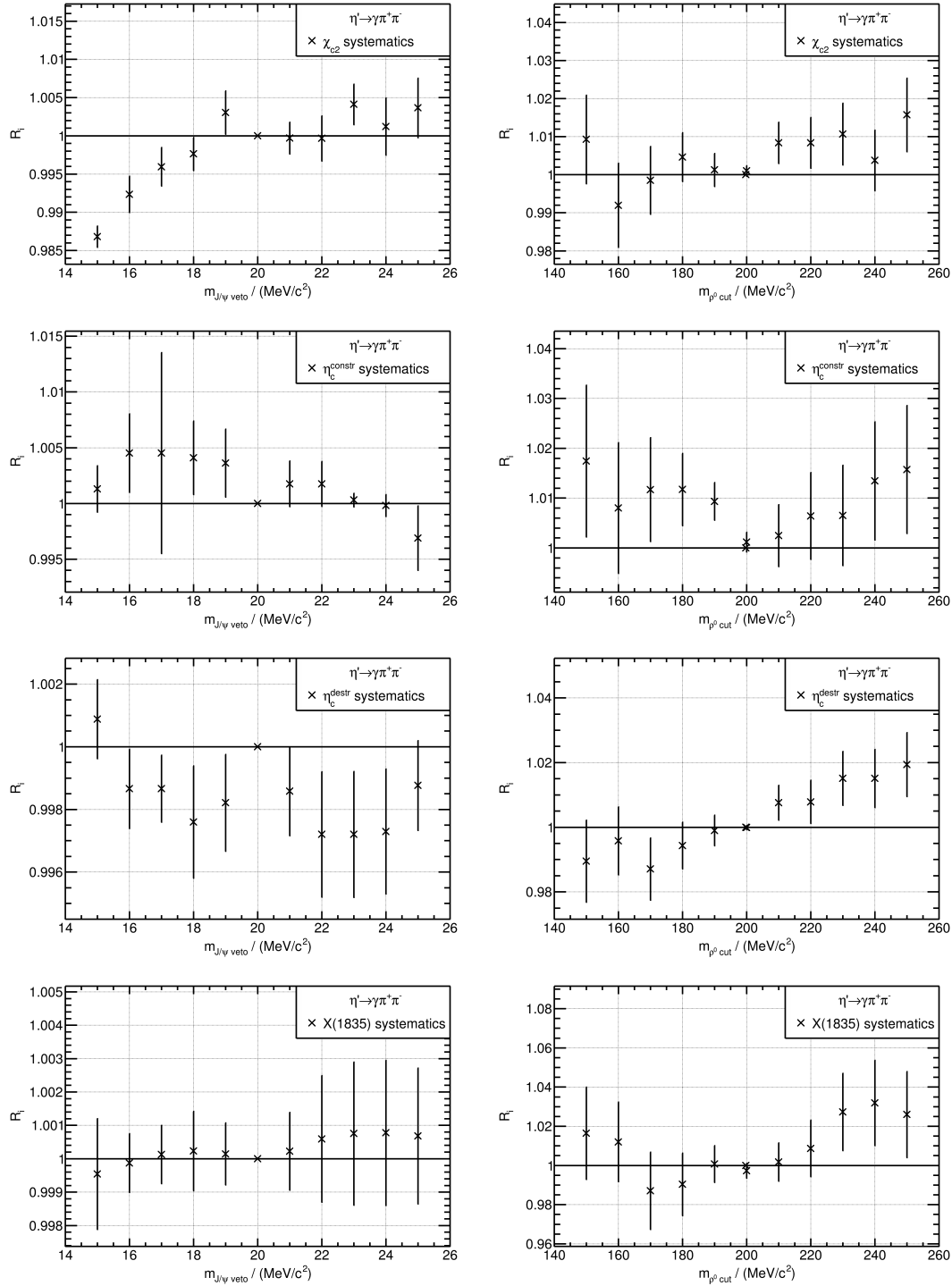


Figure A.4.: Ratio of the variation and the nominal value for the branching ratio for the J/ψ veto in the 4π system (left) and the cut on the ρ^0 in the $\pi^+\pi^-$ system coming from the decay $\eta' \rightarrow \gamma\pi^+\pi^-$ (right). The resonances from top to bottom are: χ_{c2} , η_c^{constr} , η_c^{destr} and $X(1835)$.

A.3.5. Sideband Subtraction

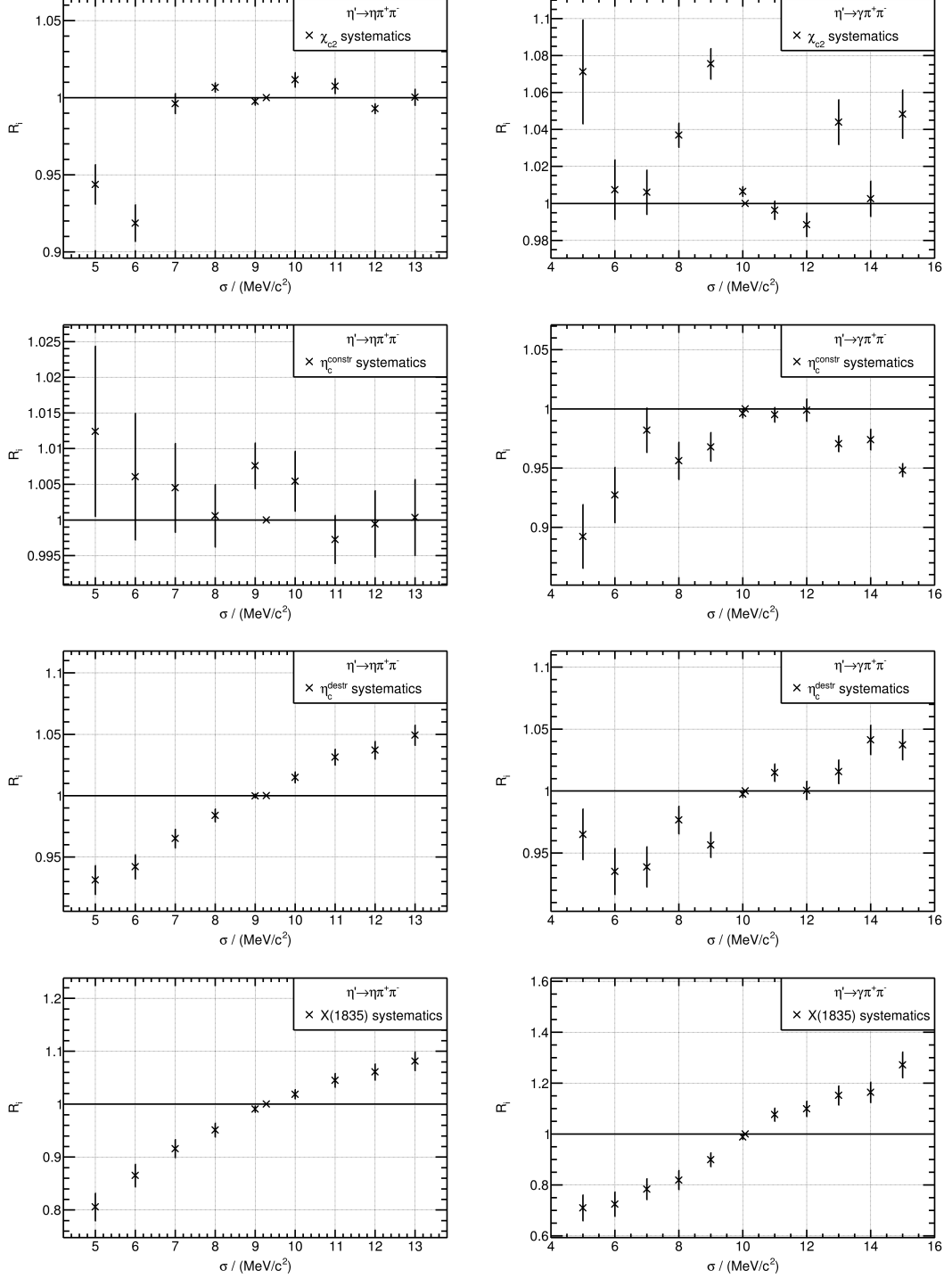


Figure A.5.: Ratio of the variation and the nominal value for the branching ratio for the width of the signal and sideband regions, in the $\eta' \rightarrow \eta\pi^+\pi^-$ channel (left) and the $\eta' \rightarrow \gamma\pi^+\pi^-$ channel (right). The resonances from top to bottom are: χ_{c2} , η_c^{constr} , η_c^{destr} and $X(1835)$.

A. Analysis of the Decay $\psi(2S) \rightarrow \gamma\eta'\pi^+\pi^-$

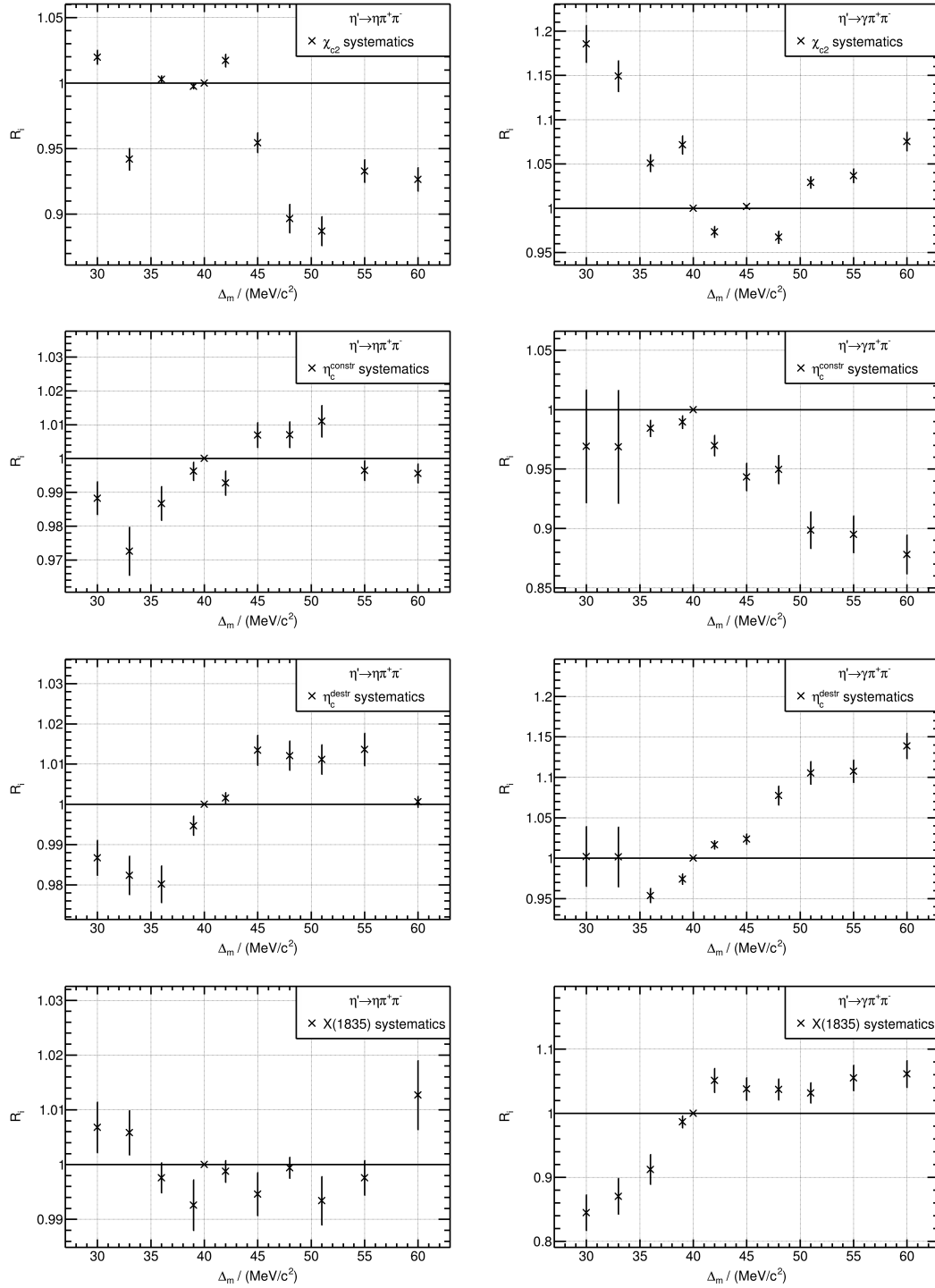


Figure A.6.: Ratio of the variation and the nominal value for the branching ratio for the distance between the signal and sideband regions, in the $\eta' \rightarrow \eta\pi^+\pi^-$ channel (left) and the $\eta' \rightarrow \gamma\pi^+\pi^-$ channel (right). The resonances from top to bottom are: χ_{c2} , η_c^{constr} , η_c^{destr} and $X(1835)$.

B. Analysis of the Reaction

$$e^+e^- \rightarrow \eta_c K^* K$$

B.1. Combined Fit to the η_c

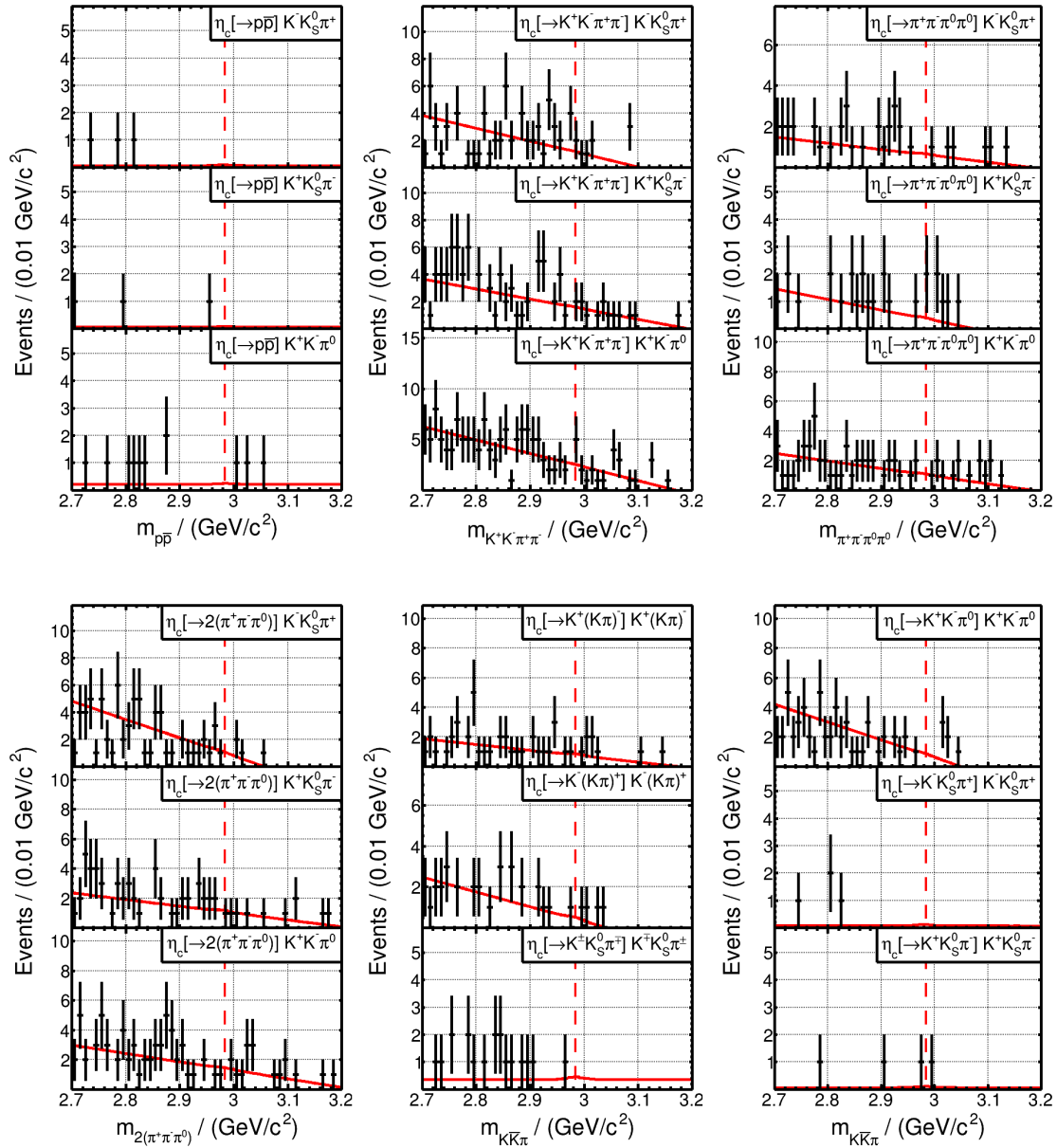


Figure B.1.: Combined fit to the 4600 data sample for the decays $\eta_c \rightarrow p\bar{p}$ (top left), $\eta_c \rightarrow K^+K^-\pi^+\pi^-$ (top middle), $\eta_c \rightarrow \pi^+\pi^-\pi^0\pi^0$ (top right), $\eta_c \rightarrow 2(\pi^+\pi^-\pi^0)$ (bottom left) and $\eta_c \rightarrow K\bar{K}\pi$ (bottom middle and right). The data is presented in black, the total fit as the red solid line and the mass of the η_c according to the PDG as the red dashed line.

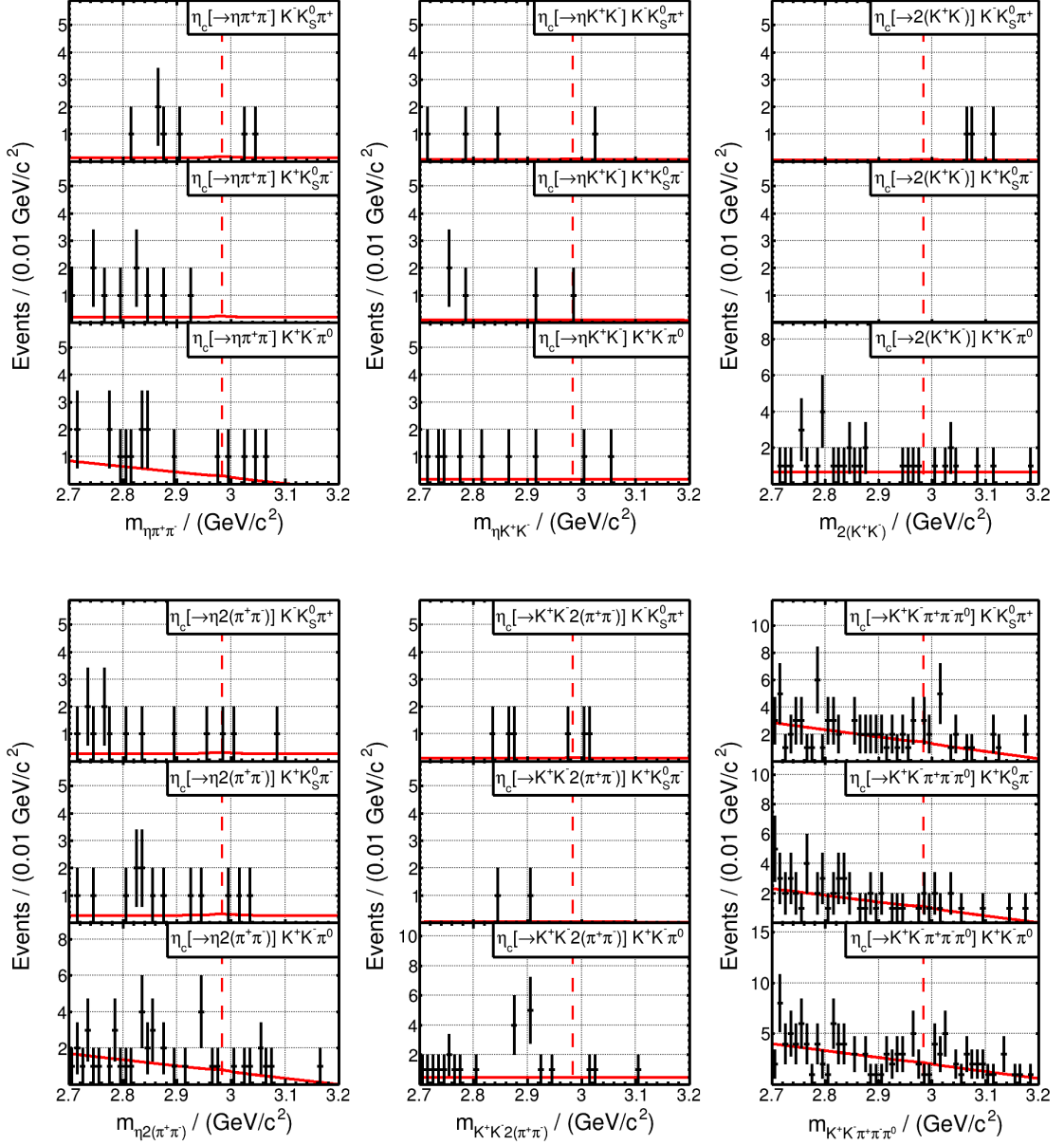


Figure B.2.: Combined fit to the 4600 data sample for the decays $\eta_c \rightarrow \eta\pi^+\pi^-$ (top left), $\eta_c \rightarrow \eta K^+K^-$ (top middle), $\eta_c \rightarrow 2(K^+K^-)$ (top right), $\eta_c \rightarrow \eta 2(\pi^+\pi^-)$ (bottom left), $\eta_c \rightarrow K^+K^- 2(\pi^+\pi^-)$ (bottom middle) and $\eta_c \rightarrow K^+K^-\pi^+\pi^-\pi^0$ (bottom right). The data is presented in black, the total fit as the red solid line and the mass of the η_c according to the PDG as the red dashed line.

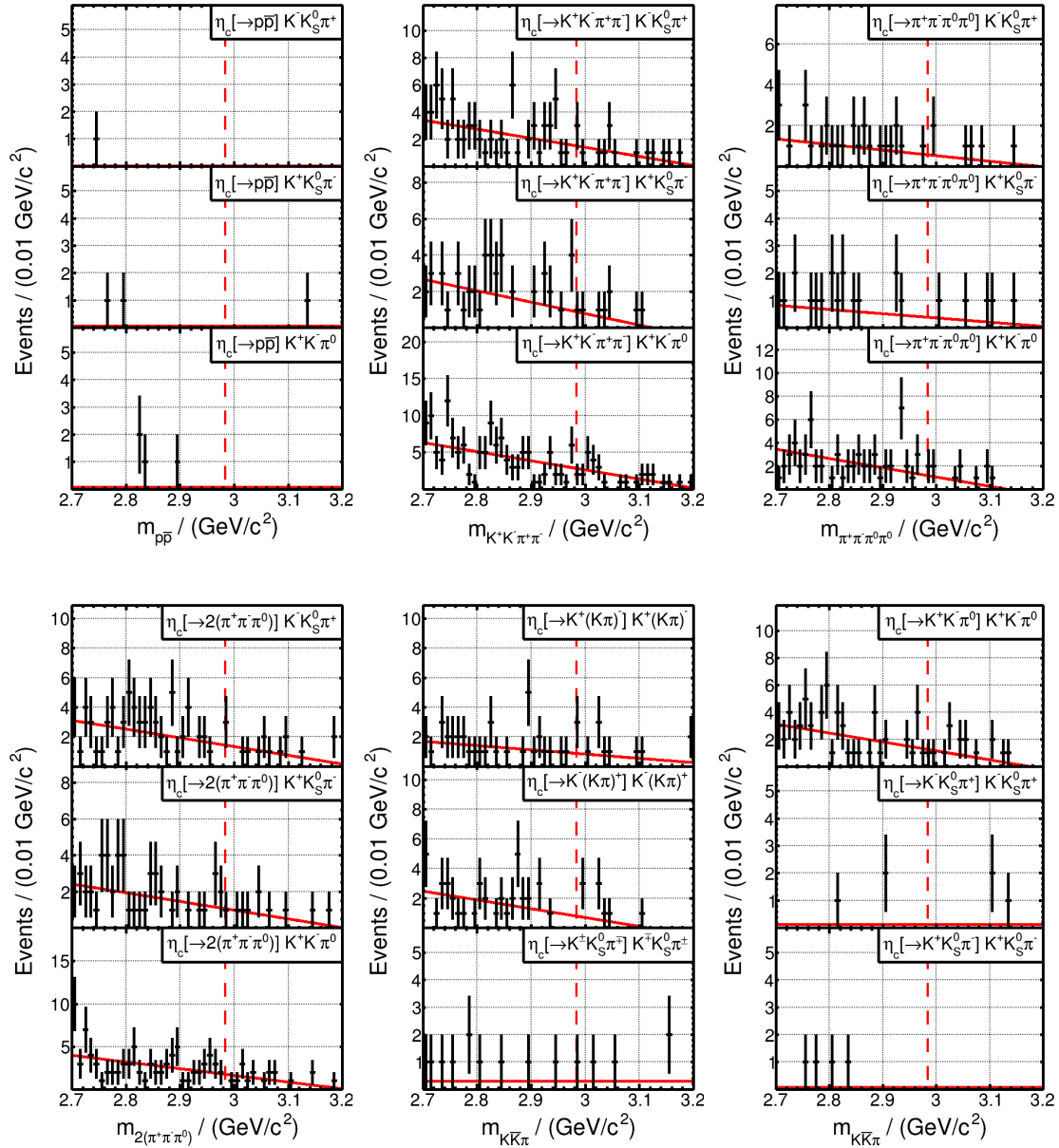


Figure B.3.: Combined fit to the 4620 data sample for the decays $\eta_c \rightarrow p\bar{p}$ (top left), $\eta_c \rightarrow K^+ K^- \pi^+ \pi^-$ (top middle), $\eta_c \rightarrow \pi^+ \pi^- \pi^0 \pi^0$ (top right), $\eta_c \rightarrow 2(\pi^+ \pi^- \pi^0)$ (bottom left) and $\eta_c \rightarrow K\bar{K}\pi$ (bottom middle and right). The data is presented in black, the total fit as the red solid line and the mass of the η_c according to the PDG as the red dashed line.

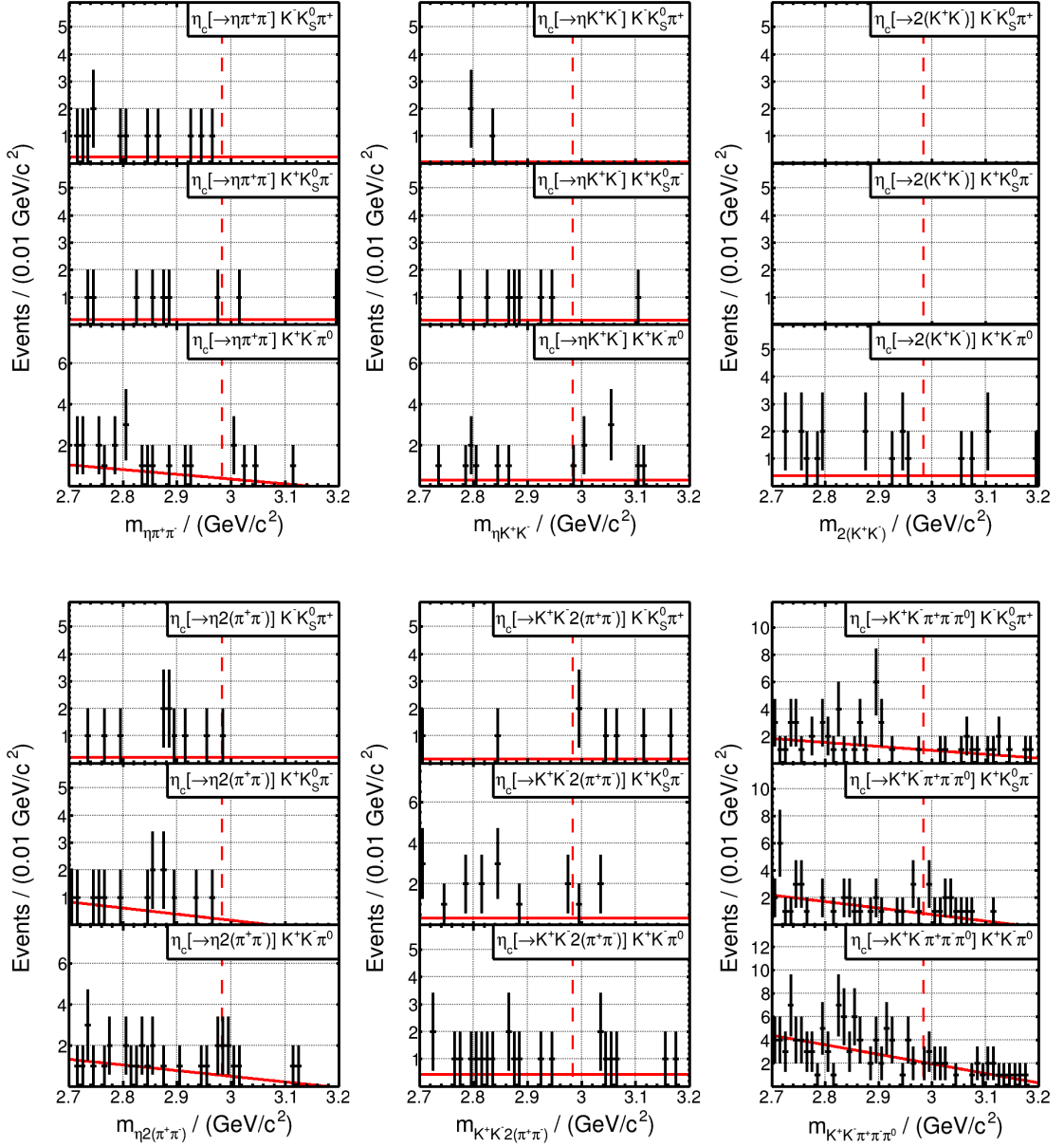


Figure B.4.: Combined fit to the 4620 data sample for the decays $\eta_c \rightarrow \eta\pi^+\pi^-$ (top left), $\eta_c \rightarrow \eta K^+K^-$ (top middle), $\eta_c \rightarrow 2(K^+K^-)$ (top right), $\eta_c \rightarrow \eta 2(\pi^+\pi^-)$ (bottom left), $\eta_c \rightarrow K^+K^- 2(\pi^+\pi^-)$ (bottom middle) and $\eta_c \rightarrow K^+K^-\pi^+\pi^-\pi^0$ (bottom right). The data is presented in black, the total fit as the red solid line and the mass of the η_c according to the PDG as the red dashed line.

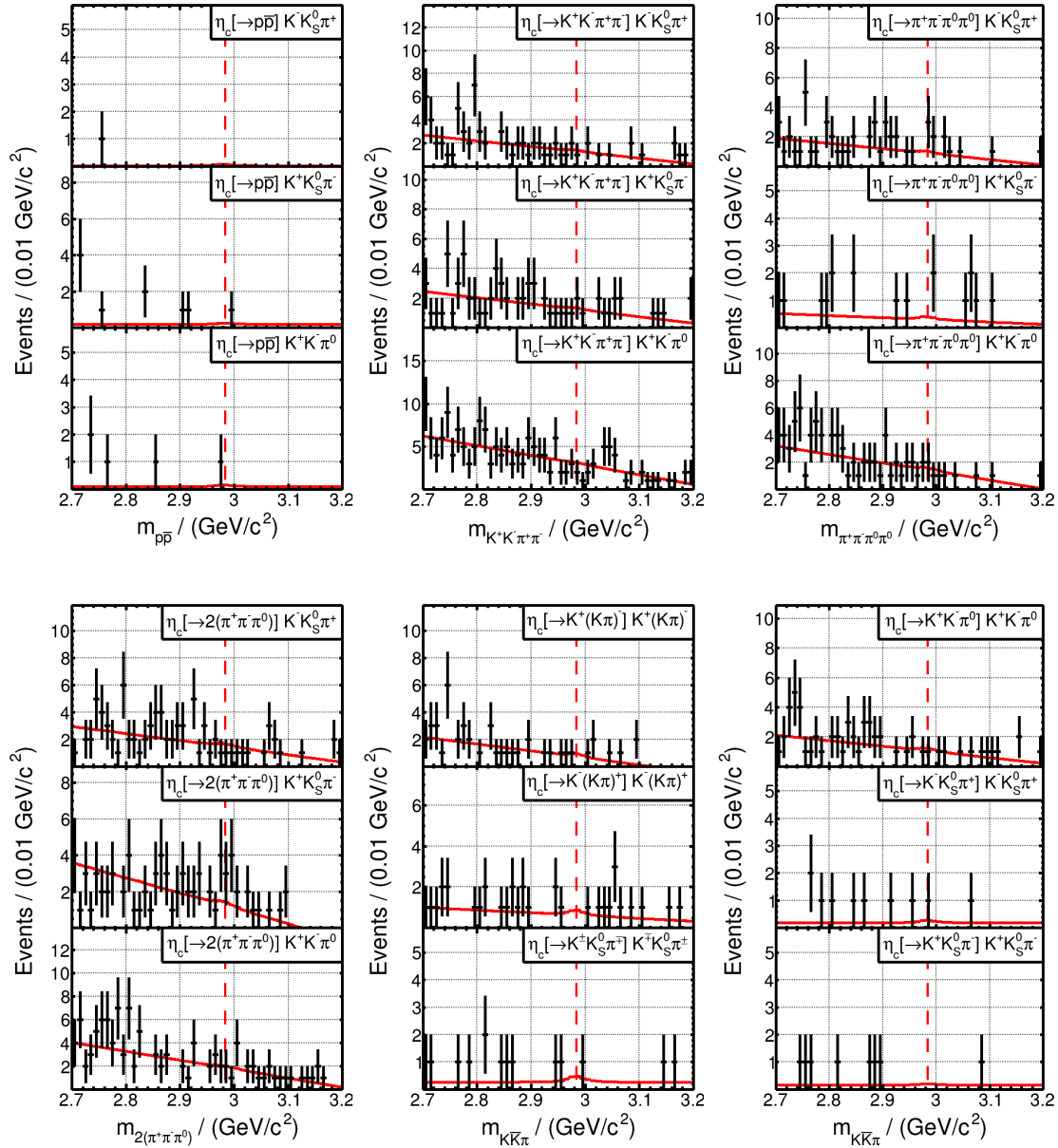


Figure B.5.: Combined fit to the 4640 data sample for the decays $\eta_c \rightarrow p\bar{p}$ (top left), $\eta_c \rightarrow K^+K^-\pi^+\pi^-$ (top middle), $\eta_c \rightarrow \pi^+\pi^-\pi^0\pi^0$ (top right), $\eta_c \rightarrow 2(\pi^+\pi^-\pi^0)$ (bottom left) and $\eta_c \rightarrow K\bar{K}\pi$ (bottom middle and right). The data is presented in black, the total fit as the red solid line and the mass of the η_c according to the PDG as the red dashed line.

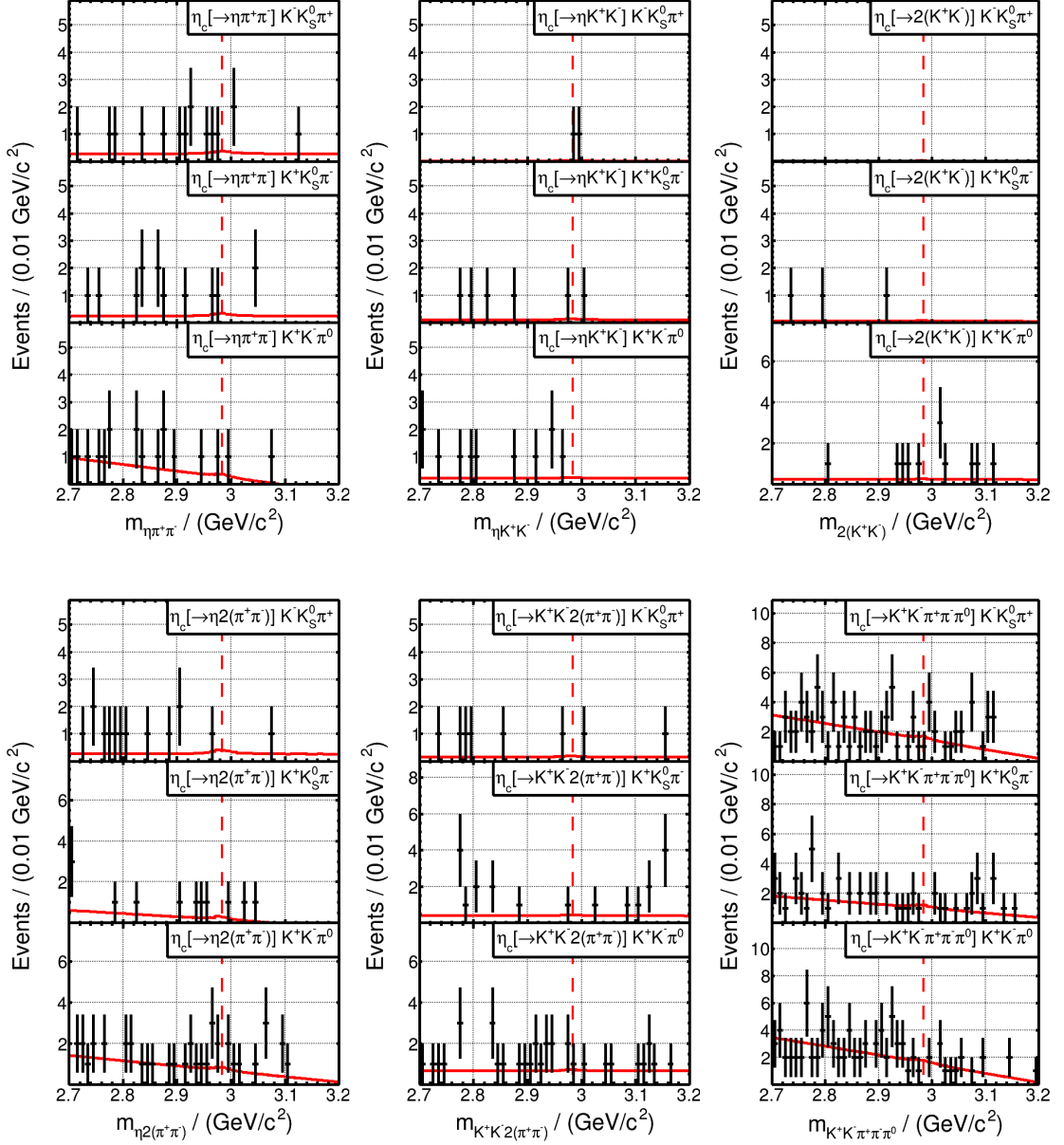


Figure B.6.: Combined fit to the 4640 data sample for the decays $\eta_c \rightarrow \eta \pi^+ \pi^-$ (top left), $\eta_c \rightarrow \eta K^+ K^-$ (top middle), $\eta_c \rightarrow 2(K^+ K^-)$ (top right), $\eta_c \rightarrow \eta 2(\pi^+ \pi^-)$ (bottom left), $\eta_c \rightarrow K^+ K^- 2(\pi^+ \pi^-)$ (bottom middle) and $\eta_c \rightarrow K^+ K^- \pi^+ \pi^- \pi^0$ (bottom right). The data is presented in black, the total fit as the red solid line and the mass of the η_c according to the PDG as the red dashed line.

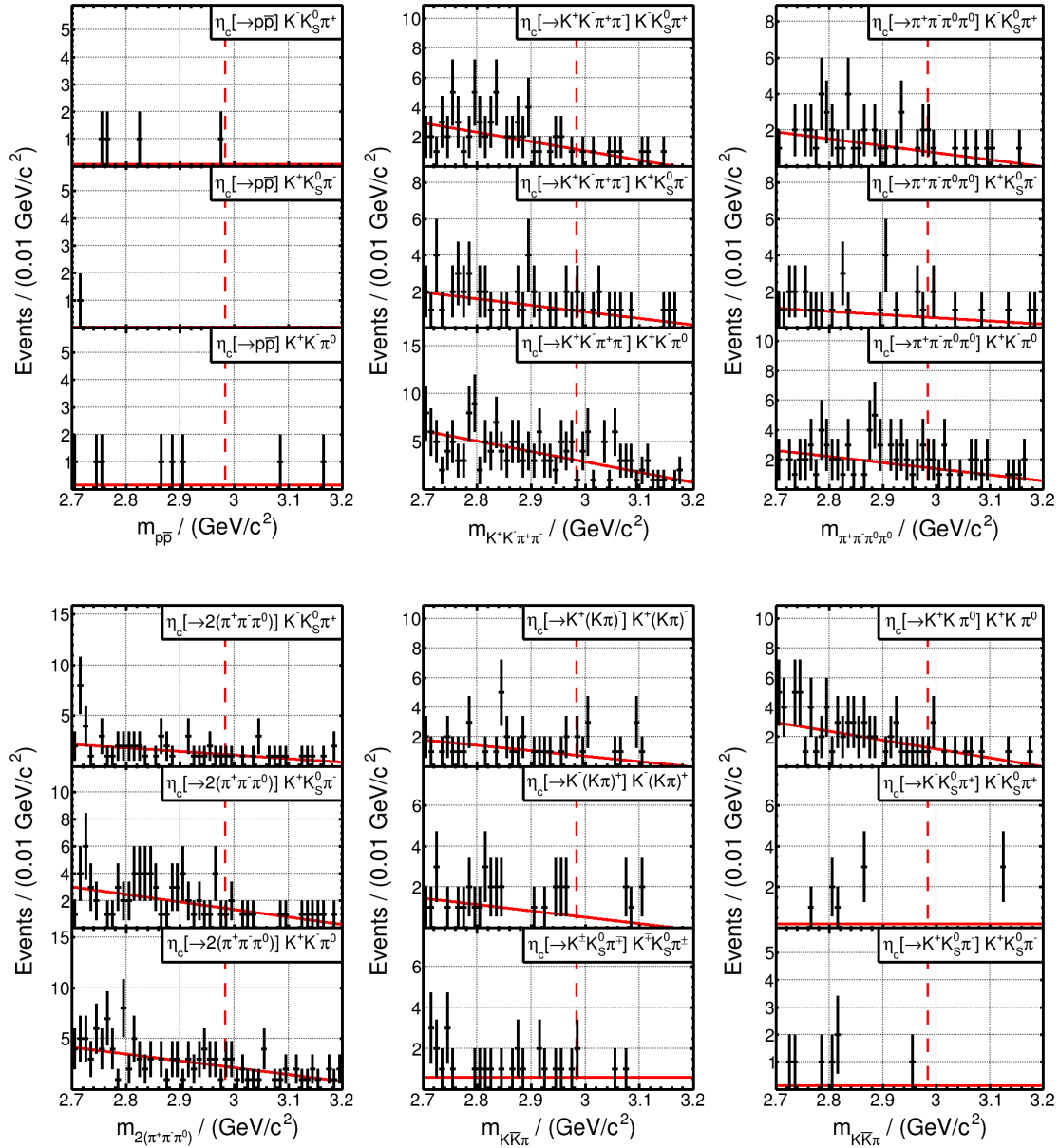


Figure B.7.: Combined fit to the 4660 data sample for the decays $\eta_c \rightarrow p\bar{p}$ (top left), $\eta_c \rightarrow K^+K^-\pi^+\pi^-$ (top middle), $\eta_c \rightarrow \pi^+\pi^-\pi^0\pi^0$ (top right), $\eta_c \rightarrow 2(\pi^+\pi^-\pi^0)$ (bottom left) and $\eta_c \rightarrow K\bar{K}\pi$ (bottom middle and right). The data is presented in black, the total fit as the red solid line and the mass of the η_c according to the PDG as the red dashed line.

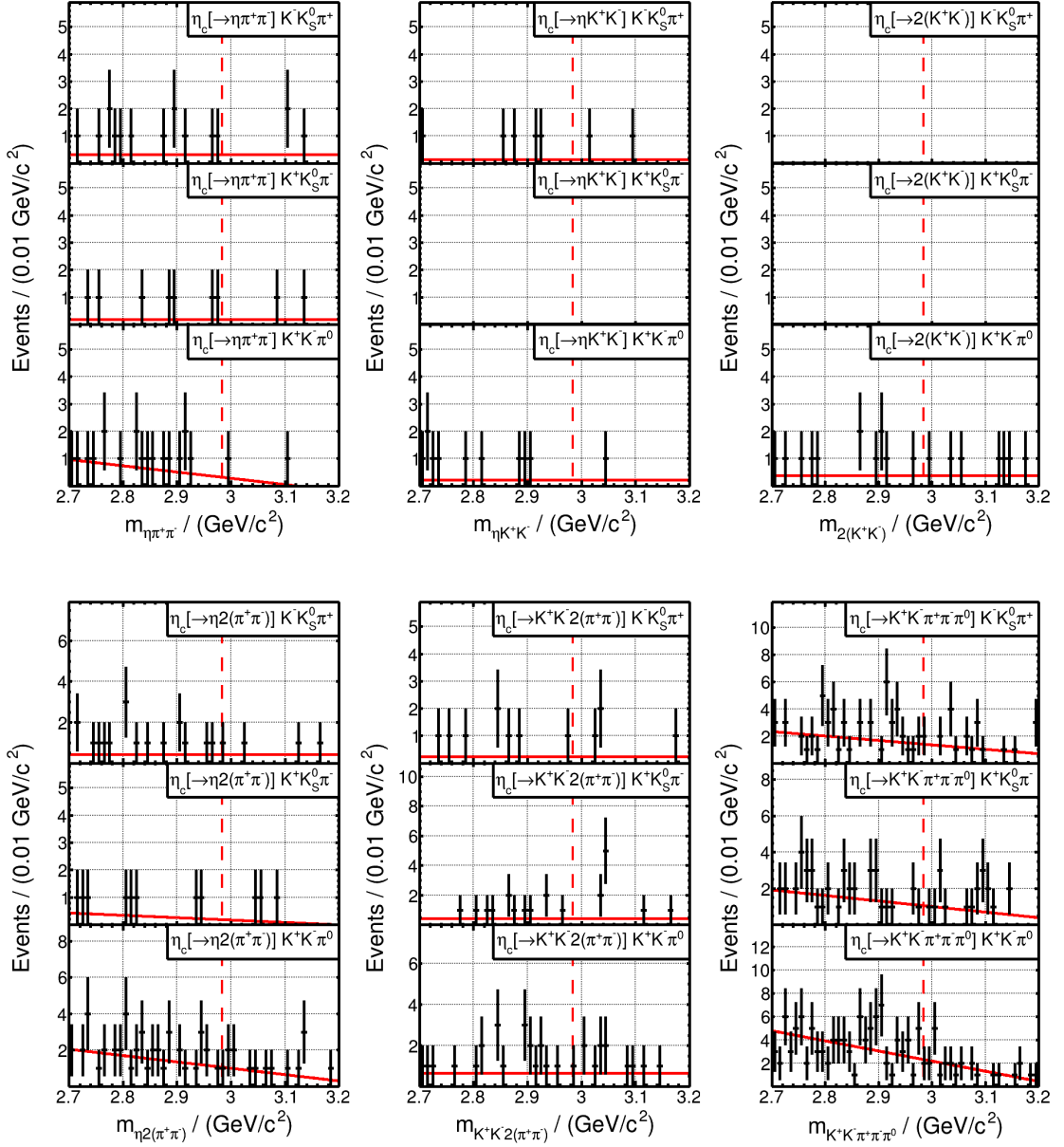


Figure B.8.: Combined fit to the 4660 data sample for the decays $\eta_c \rightarrow \eta\pi^+\pi^-$ (top left), $\eta_c \rightarrow \eta K^+K^-$ (top middle), $\eta_c \rightarrow 2(K^+K^-)$ (top right), $\eta_c \rightarrow \eta 2(\pi^+\pi^-)$ (bottom left), $\eta_c \rightarrow K^+K^- 2(\pi^+\pi^-)$ (bottom middle) and $\eta_c \rightarrow K^+K^-\pi^+\pi^-\pi^0$ (bottom right). The data is presented in black, the total fit as the red solid line and the mass of the η_c according to the PDG as the red dashed line.

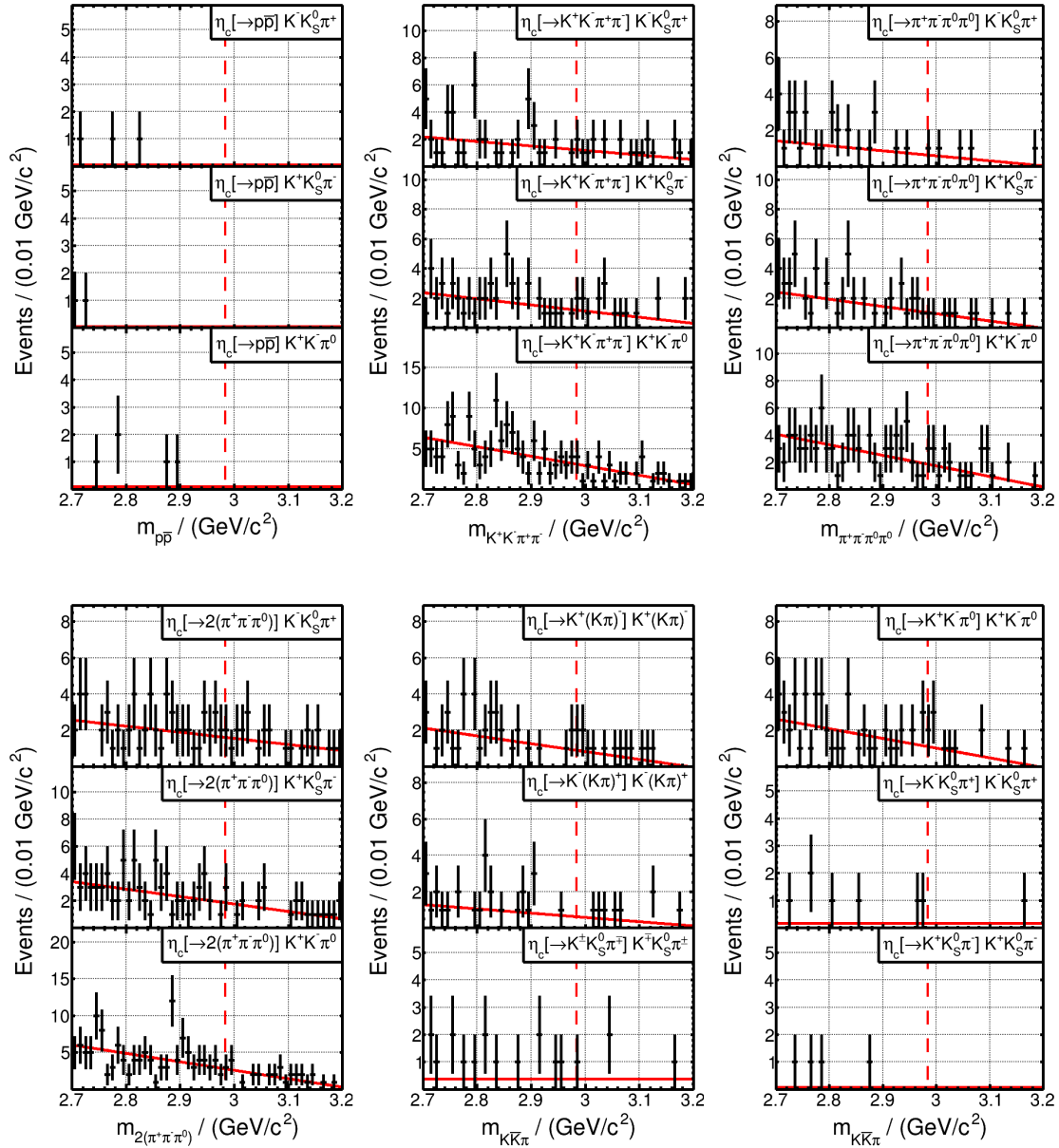


Figure B.9.: Combined fit to the 4700 data sample for the decays $\eta_c \rightarrow p\bar{p}$ (top left), $\eta_c \rightarrow K^+K^-\pi^+\pi^-$ (top middle), $\eta_c \rightarrow \pi^+\pi^-\pi^0\pi^0$ (top right), $\eta_c \rightarrow 2(\pi^+\pi^-\pi^0)$ (bottom left) and $\eta_c \rightarrow K\bar{K}\pi$ (bottom middle and right). The data is presented in black, the total fit as the red solid line and the mass of the η_c according to the PDG as the red dashed line.

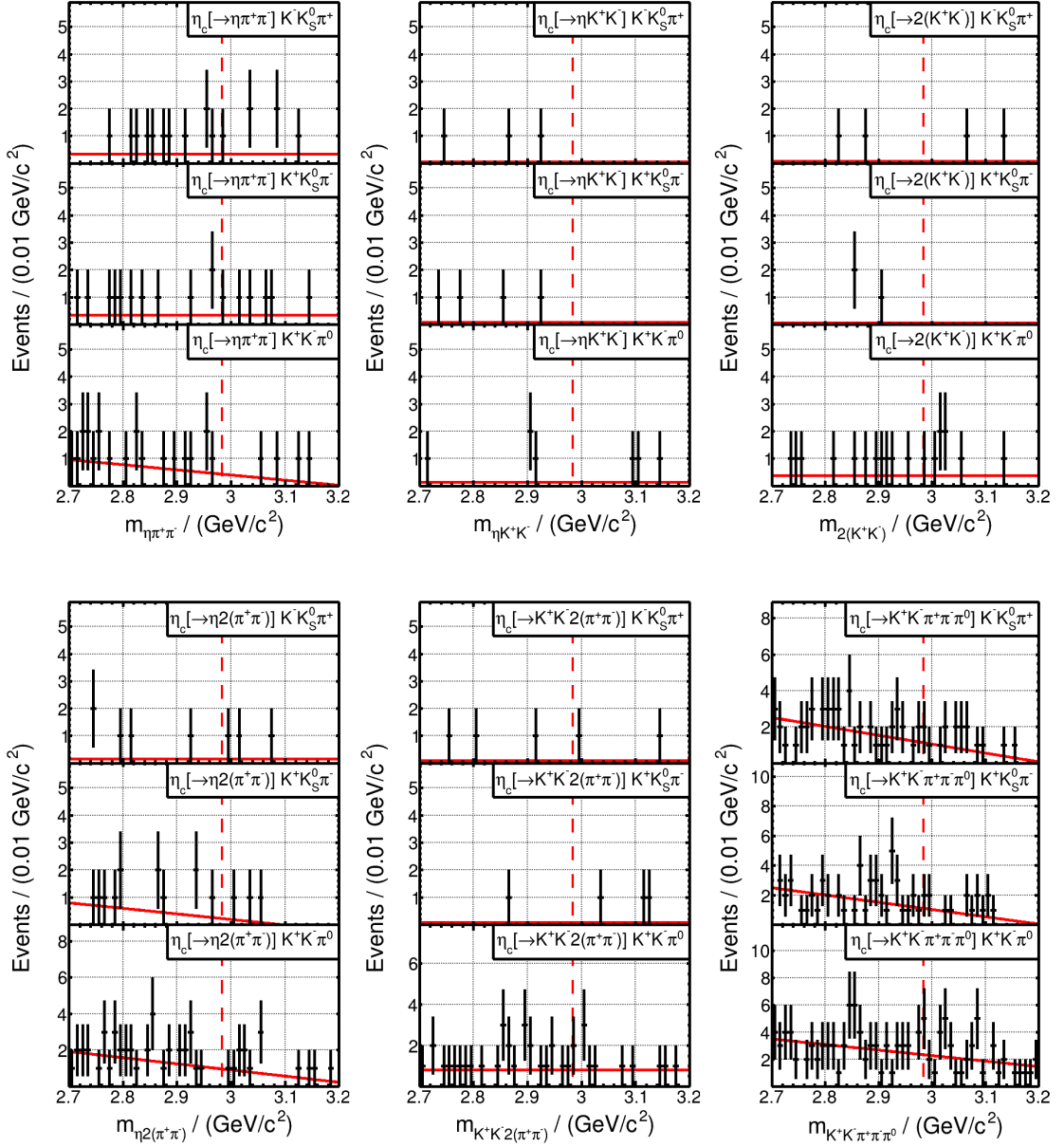


Figure B.10.: Combined fit to the 4700 data sample for the decays $\eta_c \rightarrow \eta \pi^+ \pi^-$ (top left), $\eta_c \rightarrow \eta K^+ K^-$ (top middle), $\eta_c \rightarrow 2(K^+ K^-)$ (top right), $\eta_c \rightarrow \eta 2(\pi^+ \pi^-)$ (bottom left), $\eta_c \rightarrow K^+ K^- 2(\pi^+ \pi^-)$ (bottom middle) and $\eta_c \rightarrow K^+ K^- \pi^+ \pi^- \pi^0$ (bottom right). The data is presented in black, the total fit as the red solid line and the mass of the η_c according to the PDG as the red dashed line.

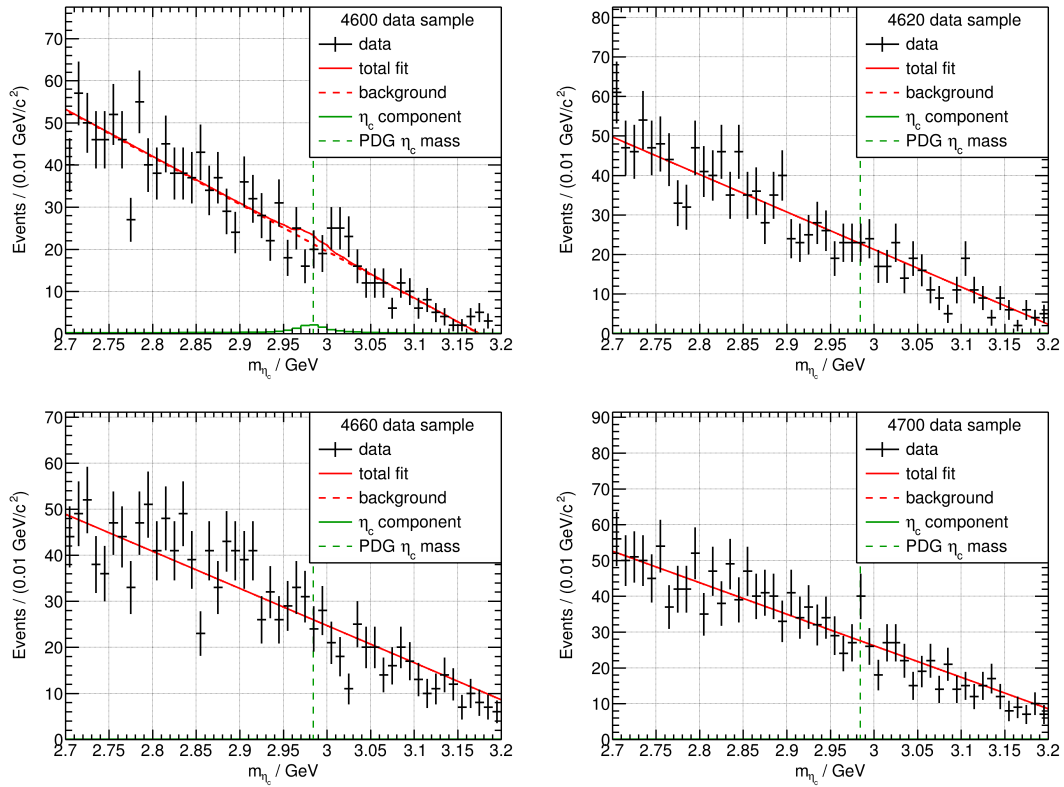


Figure B.11.: Invariant mass spectrum of η_c candidates summed over all final states for the 4600 data sample (top left), the 4620 data sample (top right), the 4660 data sample (bottom left) and the 4700 data sample (bottom right). The data is presented in black, the sum of all fitted functions for each final state as the red solid line, the sum of all background components as the dashed red line, the sum of all signal components as the solid green line and the mass of the η_c according to the PDG as the green dashed line.

B.2. Likelihood Profiles

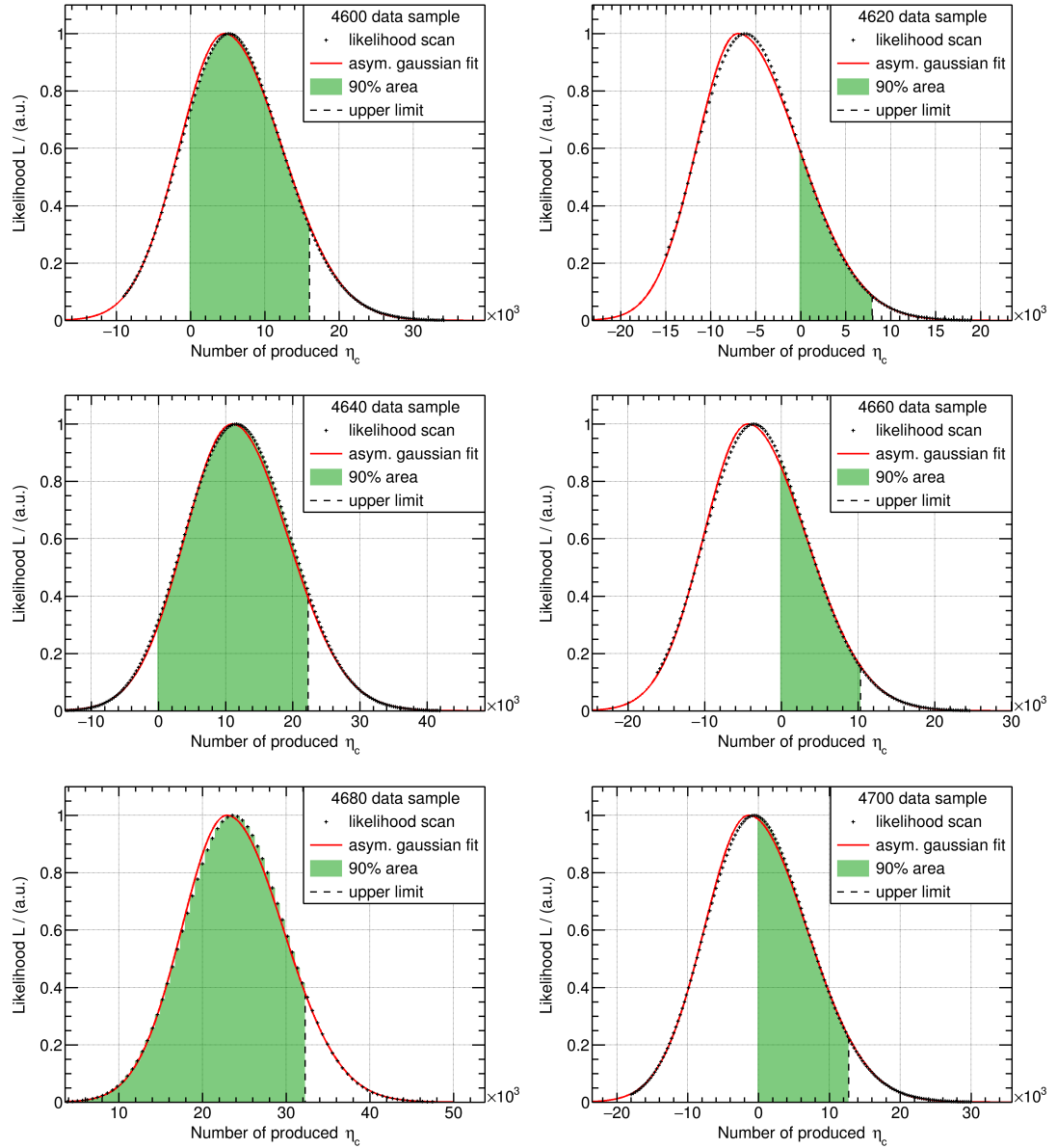


Figure B.12.: Likelihood profiles of the η_c fit for the 4600 data sample (top left), for the 4620 data sample (top right), for the 4640 data sample (middle left), for the 4660 data sample (middle right), for the 4680 data sample (bottom left) and for the 4700 data sample (bottom right). The scan values are shown as the black markers, the fit with an asymmetric Gaussian function is shown as the solid red line, the 90% area under the peak is shown in green and the resulting upper limit is marked with the black dashed line.

C. Machine Learning for Event Selection

As mentioned in Section 5.2.1 one way of optimizing the significance of the signal over the background is by a multidimensional cut optimization. In the context of this thesis also a different method was tested, which relies on an artificial neural network. In this case the neural network is realized as a multilayer perceptron [257–260] with an activation function of the hidden neurons given by a logistic function [261, 262]:

$$\mathcal{O}_{i,j}(x_{i,j}) = \frac{1}{1 + \exp(-x_{i,j})}. \quad (\text{C.1})$$

Here $\mathcal{O}_{i,j}(x)$ is the output of neuron i in layer j , where $x_{i,j}$ is calculated as a weighted sum over the outputs of the neurons of the prior layer:

$$x_{i,j} = \sum_{i=1}^{N_j} w_i \mathcal{O}_{i,j-1}(x_{i,j-1}), \quad (\text{C.2})$$

where N_j is the number of neurons in layer j . Different number of layers and neurons were tested and in the end a network with two hidden layers, the first with twelve neurons and the second with 3 neurons, was chosen. The resulting structure of the network can be seen in the left part of Figure C.1 and as the input for the network different kinematic variables are used. This was tested for the $\eta' \rightarrow \eta\pi^+\pi^-$ case and the variables used are the invariant mass of the photons from the $\eta \rightarrow \gamma\gamma$ decay, the invariant mass of the $\eta\pi^+\pi^-$ system, the χ^2 of the kinematic fit and the minimal distance of the invariant mass of any background $\gamma\gamma$ combination to the mass of the π^0 .

For the training of the network the inclusive MC is used, but with the background scaled such that the number of signal and background events is the same. This is needed since if the number of background events is much larger than the number of signal events, the network tends to classify every event as background [263]. The resulting sample is split in two samples of equal size and one of them is used for training and the other for validation. For the training the Broyden-Fletcher-Goldfarb-Shanno algorithm [264–267] is used with the training parameter set to $\tau = 3$. The training is done for a total of 50 epochs, to reduce the mean squared error between the training sample and the predictions of the network. As can be seen in the right part of Figure C.1 slight overfitting appears, as the loss of the training sample starts to deviate from the loss of the validation sample after five epochs. The result for the weights after the training can be seen in the left part of

Figure C.1 as the thickness of the lines and it turns out, that the invariant mass of the $\eta\pi^+\pi^-$ has the largest impact on the output.

After the training the neural network can be used on the training sample and the result is presented in Figure C.2. As can be seen the signal shows a clear peak at an output value of 0.9, while the background basically peaks at 0, which means that signal and background can be separated. However, for the final analysis the total inclusive MC sample has to be investigated, which is shown in Figure C.3. Here it can now be seen, that also the background shows a peak at high Output values, which can be explained by the fact, that not all background components can be classified as such with the input variables that were used. From these plots a cut value on the output of the neural network is now defined via a figure-of-merit, which is defined as for the conventional optimization in Equation (5.12). This results in an optimal cut value on the output of the network of 0.71. Comparing the resulting figure-of-merits from the conventional optimization with that of the neural network shows that the neural network performs slightly better with an improvement of the FOM of $\sim 10\%$.

However, in the end it was decided to not use the neural network for discriminating signal and background because of the interpretability of the procedure. While for the conventional method the applied selection criteria all have a physical interpretation, it is not entirely clear how the network assigns the weights. In addition, for the conventional method approved methods for determining systematic uncertainties coming from the event selection procedure are applicable. However, for the neural network this is less straight forward.

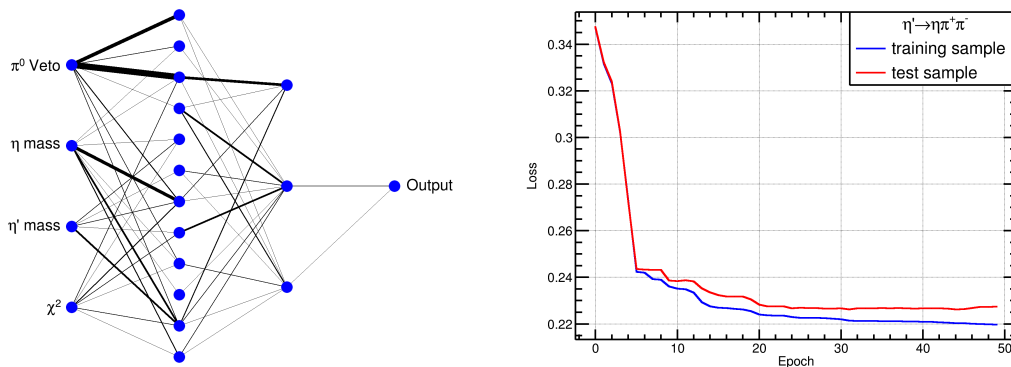


Figure C.1.: Left: Structure of the tested neural network. The neurons are shown as the blue markers and the thickness of the lines connecting them is proportional to the corresponding weight. Right: Learning curves of the training for the training sample in blue and for the validation sample in red.

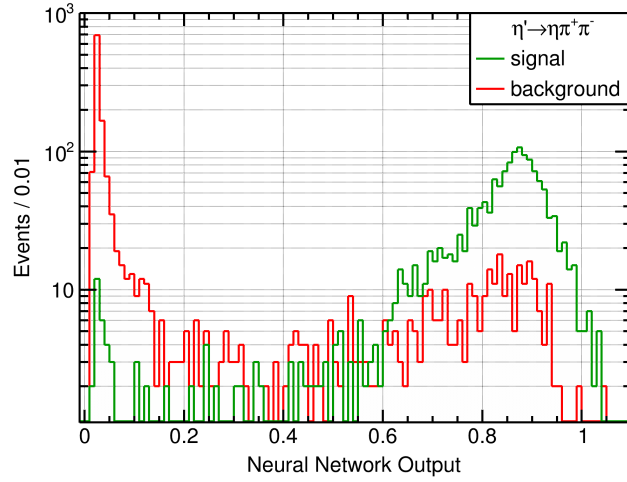


Figure C.2.: Result of the training of the neural network for the training sample. Plotted is the number of Events with a given Output of the network for the signal component (green) and the background component (red) of the training sample.

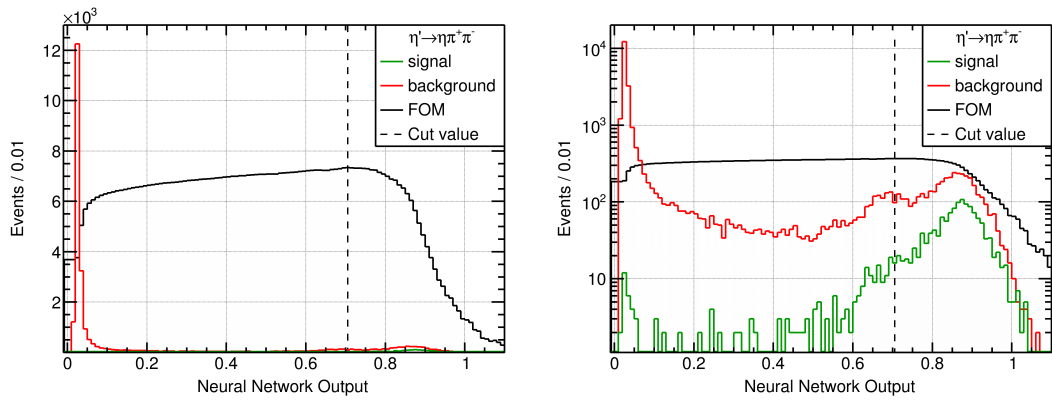


Figure C.3.: Result of the training of the neural network for the complete inclusive MC sample with a linear ordinate (left) and a logarithmic ordinate (right). Plotted is the number of Events with a given Output of the network for the signal component (green) and the background component (red) of the inclusive MC sample. In addition, the figure-of-merit with the resulting cut value is shown in black.

Bibliography

- [1] R. P. Feynman, *The value of science*, *Eng. Sci.* **19** (1955) 13–15.
- [2] J. H. Oort, *The structure of the cloud of comets surrounding the Solar System and a hypothesis concerning its origin*, *Bulletin of the Astronomical Institutes of the Netherlands* **11** (1950) 91–110.
- [3] S. Dunlop, T. Encrenaz, J. Bibring, M. Blanc, M. Barucci, F. Roques et al., *The Solar System*. Astronomy and Astrophysics Library. Springer Berlin Heidelberg, 2004.
- [4] R. Pohl et al., *The size of the proton*, *Nature* **466** (2010) 213–216.
- [5] M. D. Schwartz, *Quantum Field Theory and the Standard Model*. Cambridge University Press, 3, 2014.
- [6] PARTICLE DATA GROUP collaboration, S. Navas et al., *Review of particle physics*, *Phys. Rev. D* **110** (2024) 030001.
- [7] A. Einstein, *Die Grundlage der allgemeinen Relativitätstheorie*, *Annalen der Physik* **354** (1916) 769–822.
- [8] J. H. Oort, *The force exerted by the stellar system in the direction perpendicular to the galactic plane and some related problems*, *Bulletin of the Astronomical Institutes of the Netherlands* **6** (Aug., 1932) 249.
- [9] SUPER-KAMIOKANDE collaboration, Y. Fukuda et al., *Evidence for oscillation of atmospheric neutrinos*, *Phys. Rev. Lett.* **81** (1998) 1562–1567.
- [10] SUPER-KAMIOKANDE collaboration, S. Fukuda et al., *Solar 8B and hep neutrino measurements from 1258 days of Super-Kamiokande data*, *Phys. Rev. Lett.* **86** (2001) 5651–5655.
- [11] SNO collaboration, J. Farine, *Measurement of the rate of $\nu_e + d \rightarrow p + p + e^-$ interactions produced by 8B solar neutrinos at the Sudbury Neutrino Observatory*, *Phys. Atom. Nucl.* **65** (2002) 2147–2155.
- [12] R. Davis, D. S. Harmer and K. C. Hoffman, *Search for neutrinos from the sun*, *Phys. Rev. Lett.* **20** (May, 1968) 1205–1209.

- [13] B. T. Cleveland, T. Daily, R. Davis, Jr., J. R. Distel, K. Lande, C. K. Lee et al., *Measurement of the solar electron neutrino flux with the Homestake chlorine detector*, *Astrophys. J.* **496** (1998) 505–526.
- [14] K. Becker, M. Becker and J. H. Schwarz, *String theory and M-theory: A modern introduction*. Cambridge University Press, 2006, 10.1017/CBO9780511816086.
- [15] N. Lambert, *M-theory and maximally supersymmetric gauge theories*, *Annual Review of Nuclear and Particle Science* **62** (2012) 285–313.
- [16] L. D. Landau, A. A. Abrikosov and I. M. Khalatnikov, *The Removal of Infinities in Quantum Electrodynamics*, *Dokl. Akad. Nauk SSSR* **95** (1954) 607.
- [17] A. Deur, S. J. Brodsky and G. F. de Téramond, *The QCD running coupling*, *Progress in Particle and Nuclear Physics* **90** (2016) 1–74.
- [18] M. Gell-Mann, *A schematic model of baryons and mesons*, *Physics Letters* **8** (1964) 214–215.
- [19] G. Zweig, *An SU(3) model for strong interaction symmetry and its breaking*, *Developments in the Quark Theory of Hadrons* **1** (1980) 22–101.
- [20] BELLE collaboration, K. Abe et al., *Observation of a new narrow charmonium state in exclusive $B^\pm \rightarrow K^\pm \pi^+ \pi^- J/\psi$ decays*, in *21st International Symposium on Lepton and Photon Interactions at High Energies (LP 03)*, 8, 2003, [hep-ex/0308029](#).
- [21] BESIII collaboration, M. Ablikim et al., *Design and Construction of the BESIII Detector*, *Nucl. Instrum. Meth. A* **614** (2010) 345–399.
- [22] H. Geng, W. Liu, J. Qiu, J. Xing, C. Yu and Y. Zhang, *Lattice Design for BEPCII Upgrade*, in *International Particle Accelerator Conference (IPAC 12)*, pp. 3756–3758, 2021.
- [23] E852 collaboration, E. I. Ivanov et al., *Observation of exotic meson production in the reaction $\pi^- p \rightarrow \eta' \pi^- p$ at 18-GeV / c*, *Phys. Rev. Lett.* **86** (2001) 3977–3980, [[hep-ex/0101058](#)].
- [24] BES collaboration, M. Ablikim et al., *Observation of a resonance X(1835) in $J/\psi \rightarrow \gamma \pi^+ \pi^- \eta'$* , *Phys. Rev. Lett.* **95** (2005) 262001, [[hep-ex/0508025](#)].
- [25] BESIII collaboration, M. Ablikim et al., *Observation of an anomalous line shape of the $\eta' \pi^+ \pi^-$ mass spectrum near the $p\bar{p}$ mass threshold in $J/\psi \rightarrow \gamma \eta' \pi^+ \pi^-$* , *Phys. Rev. Lett.* **117** (2016) 042002, [[1603.09653](#)].

-
- [26] K. J. Peters, *A Primer on partial wave analysis*, *Int. J. Mod. Phys. A* **21** (2006) 5618–5624, [hep-ph/0412069].
- [27] BESIII collaboration, M. Ablikim et al., *Observation of a Near-Threshold Structure in the K^+ Recoil-Mass Spectra in $e^+e^- \rightarrow K^+(D_s^-D^{*0} + D_s^{*-}D^0)$* , *Phys. Rev. Lett.* **126** (2021) 102001, [2011.07855].
- [28] S. Lennartz, *Search for the open-strange charmonium-like structure Z_{cs} in the reaction $e^+e^- \rightarrow Z_{cs}(\rightarrow \eta_c K^*)K$ at BESIII*, master’s thesis, University of Münster, 2022.
- [29] M. K. Gaillard, P. D. Grannis and F. J. Sciulli, *The standard model of particle physics*, *Rev. Mod. Phys.* **71** (Mar, 1999) S96–S111.
- [30] R. P. Feynman, F. B. Morinigo and W. G. Wagner, *Feynman lectures on gravitation*, *European Journal of Physics* **24** (2003) 330.
- [31] E. Noether, *Invariante Variationsprobleme*, *Nachrichten von der Gesellschaft der Wissenschaften zu Göttingen, Mathematisch-Physikalische Klasse* **1918** (1918) 235–257.
- [32] P. W. Higgs, *Spontaneous symmetry breakdown without massless bosons*, *Phys. Rev.* **145** (May, 1966) 1156–1163.
- [33] F. Englert and R. Brout, *Broken symmetry and the mass of gauge vector mesons*, *Phys. Rev. Lett.* **13** (Aug, 1964) 321–323.
- [34] G. S. Guralnik, C. R. Hagen and T. W. B. Kibble, *Global conservation laws and massless particles*, *Phys. Rev. Lett.* **13** (Nov, 1964) 585–587.
- [35] S. Weinberg, *A model of leptons*, *Phys. Rev. Lett.* **19** (Nov, 1967) 1264–1266.
- [36] I. Neutelings, “Standard model.” https://tikz.net/sm_particles/. used under CC BY-SA 4.0, font changed and masses updated.
- [37] H. Fritzsch, M. Gell-Mann and H. Leutwyler, *Advantages of the color octet gluon picture*, *Physics Letters B* **47** (1973) 365–368.
- [38] C. N. Yang and R. L. Mills, *Conservation of isotopic spin and isotopic gauge invariance*, *Phys. Rev.* **96** (Oct, 1954) 191–195.
- [39] O. W. Greenberg, *Spin and unitary-spin independence in a paraquark model of baryons and mesons*, *Phys. Rev. Lett.* **13** (Nov, 1964) 598–602.
- [40] R. D. Peccei, *The Strong CP problem and axions*, *Lect. Notes Phys.* **741** (2008) 3–17, [hep-ph/0607268].

- [41] B. Graner, Y. Chen, E. G. Lindahl and B. R. Heckel, *Reduced limit on the permanent electric dipole moment of ^{199}Hg* , *Phys. Rev. Lett.* **116** (Apr, 2016) 161601.
- [42] C. A. Baker, D. D. Doyle, P. Geltenbort, K. Green, M. G. D. van der Grinten, P. G. Harris et al., *Improved experimental limit on the electric dipole moment of the neutron*, *Phys. Rev. Lett.* **97** (Sep, 2006) 131801.
- [43] D. J. Gross and F. Wilczek, *Ultraviolet behavior of non-abelian gauge theories*, *Phys. Rev. Lett.* **30** (Jun, 1973) 1343–1346.
- [44] H. D. Politzer, *Reliable perturbative results for strong interactions?*, *Phys. Rev. Lett.* **30** (Jun, 1973) 1346–1349.
- [45] J. Greensite, *An Introduction to the Confinement Problem*, vol. 821. Springer Berlin, 2011, 10.1007/978-3-642-14382-3.
- [46] B. Povh, K. Rith, C. Scholz, F. Zetsche and W. Rodejohann, *Particles and Nuclei. An Introduction to the Physical Concepts*. Graduate Texts in Physics. Springer Berlin, Heidelberg, 2015, 10.1007/978-3-662-46321-5.
- [47] M. Gell-Mann, *The Eightfold Way: A Theory of strong interaction symmetry*, . doi: 10.2172/4008239.
- [48] Y. Ne'eman, *Derivation of strong interactions from a gauge invariance*, *Nuclear Physics* **26** (1961) 222–229.
- [49] T. Ohata, K. Takeuchi and K. Tsumura, *Baryon number nonconservation as pececi-quinn mechanism*, *Phys. Rev. D* **104** (Aug, 2021) 035026.
- [50] G. 't Hooft, *Symmetry breaking through Bell-Jackiw anomalies*, *Phys. Rev. Lett.* **37** (Jul, 1976) 8–11.
- [51] E. W. Kolb and S. Wolfram, *Baryon Number Generation in the Early Universe*, *Nucl. Phys. B* **172** (1980) 224. [Erratum: *Nucl.Phys.B* 195, 542 (1982)].
- [52] A. Young, *On quantitative substitutional analysis*, *Proceedings of the London Mathematical Society* **s1-33** (1900) 97–145.
- [53] V. E. Barnes et al., *Observation of a Hyperon with Strangeness Minus Three*, *Phys. Rev. Lett.* **12** (1964) 204–206.
- [54] A. Bramon, R. Escribano and M. D. Scadron, *Mixing of $\eta - \eta'$ mesons in J/ψ decays into a vector and a pseudoscalar meson*, *Phys. Lett. B* **403** (1997) 339–343, [[hep-ph/9703313](#)].

-
- [55] KLOE collaboration, A. Aloisio et al., *Measurement of $\Gamma(\phi \rightarrow \eta'\gamma)/\Gamma(\phi \rightarrow \eta\gamma)$ and the pseudoscalar mixing angle*, *Phys. Lett. B* **541** (2002) 45–51, [[hep-ex/0206010](#)].
- [56] F. Ambrosino et al., *A Global fit to determine the pseudoscalar mixing angle and the gluonium content of the η' meson*, *JHEP* **07** (2009) 105, [[0906.3819](#)].
- [57] CRYSTAL BARREL collaboration, C. Amsler et al., *The Pseudoscalar mixing angle Θ_{ps} from η and η' production in $\bar{p}p$ annihilation at rest*, *Phys. Lett. B* **294** (1992) 451–456.
- [58] C. Amsler, *Proton - anti-proton annihilation and meson spectroscopy with the crystal barrel*, *Rev. Mod. Phys.* **70** (1998) 1293–1340, [[hep-ex/9708025](#)].
- [59] J. H. Christenson, J. W. Cronin, V. L. Fitch and R. Turlay, *Evidence for the 2π Decay of the K_2^0 Meson*, *Phys. Rev. Lett.* **13** (Jul, 1964) 138–140.
- [60] KTeV COLLABORATION collaboration, A. Alavi-Harati, I. F. Albuquerque, T. Alexopoulos, M. Arenton, K. Arisaka, S. Averitte et al., *Observation of Direct CP Violation in $K_{S,L} \rightarrow \pi\pi$ Decays*, *Phys. Rev. Lett.* **83** (Jul, 1999) 22–27.
- [61] V. Fanti, A. Lai, D. Marras, L. Musa, A. Bevan, T. Gershon et al., *A new measurement of direct CP violation in two pion decays of the neutral kaon*, *Physics Letters B* **465** (1999) 335–348.
- [62] LHCb collaboration, R. Aaij et al., *Observation of CP Violation in Charm Decays*, *Phys. Rev. Lett.* **122** (2019) 211803, [[1903.08726](#)].
- [63] BABAR collaboration, B. Aubert et al., *Observation of CP violation in the B^0 meson system*, *Phys. Rev. Lett.* **87** (2001) 091801, [[hep-ex/0107013](#)].
- [64] BELLE collaboration, K. Abe et al., *Observation of large CP violation in the neutral B meson system*, *Phys. Rev. Lett.* **87** (2001) 091802, [[hep-ex/0107061](#)].
- [65] LHCb collaboration, R. Aaij et al., *First observation of CP violation in the decays of B_s^0 mesons*, *Phys. Rev. Lett.* **110** (2013) 221601, [[1304.6173](#)].
- [66] T2K collaboration, K. Abe et al., *Constraint on the matter–antimatter symmetry-violating phase in neutrino oscillations*, *Nature* **580** (2020) 339–344, [[1910.03887](#)]. [Erratum: *Nature* 583, E16 (2020)].
- [67] M. D. Scadron, R. Delbourgo and G. Rupp, *Constituent quark masses and the electroweak standard model*, *J. Phys. G* **32** (2006) 735–745, [[hep-ph/0603196](#)].
- [68] T. Barnes, S. Godfrey and E. S. Swanson, *Higher charmonia*, *Phys. Rev. D* **72** (Sep, 2005) 054026.

- [69] E. Eichten, K. Gottfried, T. Kinoshita, K. D. Lane and T. M. Yan, *Charmonium: Comparison with experiment*, *Phys. Rev. D* **21** (Jan, 1980) 203–233.
- [70] C. Amsler, *The Quark Structure of Hadrons: An Introduction to the Phenomenology and Spectroscopy*. Springer, 01, 2018, 10.1007/978-3-319-98527-5.
- [71] S. Godfrey and N. Isgur, *Mesons in a relativized quark model with chromodynamics*, *Phys. Rev. D* **32** (Jul, 1985) 189–231.
- [72] PARTICLE DATA GROUP collaboration, R. L. Workman et al., *Review of Particle Physics*, *PTEP* **2022** (2022) 083C01.
- [73] B. Wang, L. Meng and S.-L. Zhu, *Molecular tetraquarks and pentaquarks in chiral effective field theory*, *Nucl. Part. Phys. Proc.* **324-329** (2023) 45–48, [2210.08227].
- [74] H. Sazdjian, *The interplay between compact and molecular structures in tetraquarks*, *Symmetry* **14** (2022) 515.
- [75] J. Y. Panteleeva, I. A. Perevalova, M. V. Polyakov and P. Schweitzer, *Tetraquarks with hidden charm and strangeness as ϕ - $\psi(2S)$ hadrocharmonium*, *Phys. Rev. C* **99** (Apr, 2019) 045206.
- [76] X. Li and M. B. Voloshin, *$Y(4260)$ and $Y(4360)$ as mixed hadrocharmonium*, *Modern Physics Letters A* **29** (2014) 1450060.
- [77] BESIII collaboration, M. Ablikim et al., *Observation of a Charged Charmoniumlike Structure in $e^+e^- \rightarrow \pi^+\pi^-J/\psi$ at $\sqrt{s} = 4.26$ GeV*, *Phys. Rev. Lett.* **110** (2013) 252001, [1303.5949].
- [78] BELLE collaboration, Z. Q. Liu et al., *Study of $e^+e^- \rightarrow \pi^+\pi^-J/\psi$ and Observation of a Charged Charmoniumlike State at Belle*, *Phys. Rev. Lett.* **110** (2013) 252002, [1304.0121]. [Erratum: *Phys. Rev. Lett.* **111** (2013) 019901].
- [79] BESIII collaboration, M. Ablikim et al., *Observation of $Z_c(3900)^0$ in $e^+e^- \rightarrow \pi^0\pi^0J/\psi$* , *Phys. Rev. Lett.* **115** (2015) 112003, [1506.06018].
- [80] T. Xiao, S. Dobbs, A. Tomaradze and K. K. Seth, *Observation of the Charged Hadron $Z_c^\pm(3900)$ and Evidence for the Neutral $Z_c^0(3900)$ in $e^+e^- \rightarrow \pi\pi J/\psi$ at $\sqrt{s} = 4170$ MeV*, *Phys. Lett. B* **727** (2013) 366–370, [1304.3036].
- [81] BESIII collaboration, M. Ablikim et al., *Observation of a charged $(D\bar{D}^*)^\pm$ mass peak in $e^+e^- \rightarrow \pi D\bar{D}^*$ at $\sqrt{s} = 4.26$ GeV*, *Phys. Rev. Lett.* **112** (2014) 022001, [1310.1163].

-
- [82] BESIII collaboration, M. Ablikim et al., *Observation of a Neutral Structure near the $D\bar{D}^*$ Mass Threshold in $e^+e^- \rightarrow (D\bar{D}^*)^0\pi^0$ at $\sqrt{s} = 4.226$ and 4.257 GeV*, *Phys. Rev. Lett.* **115** (2015) 222002, [1509.05620].
- [83] D.-Y. Chen and X. Liu, *Predicted charged charmoniumlike structures in the hidden-charm dipion decay of higher charmonia*, *Phys. Rev. D* **84** (Aug, 2011) 034032.
- [84] D.-Y. Chen, X. Liu and T. Matsuki, *Predictions of charged charmoniumlike structures with hidden-charm and open-strange channels*, *Phys. Rev. Lett.* **110** (Jun, 2013) 232001.
- [85] E. van Beveren, X. Liu, R. Coimbra and G. Rupp, *Possible $\psi(5S)$, $\psi(4D)$, $\psi(6S)$ and $\psi(5D)$ signals in $\Lambda_c\bar{\Lambda}_c$* , *EPL* **85** (2009) 61002, [0809.1151].
- [86] BELLE collaboration, G. Pakhlova et al., *Observation of a Near-Threshold Enhancement in the $e^+e^- \rightarrow \Lambda_c^+\Lambda_c^-$ Cross Section Using Initial-State Radiation*, *Phys. Rev. Lett.* **101** (2008) 172001, [0807.4458].
- [87] Y.-s. Oh, T. Song and S. H. Lee, *J/ψ absorption by π and ρ mesons in meson exchange model with anomalous parity interactions*, *Phys. Rev. C* **63** (2001) 034901, [nucl-th/0010064].
- [88] R. Casalbuoni, A. Deandrea, N. Di Bartolomeo, R. Gatto, F. Feruglio and G. Nardulli, *Phenomenology of heavy meson chiral lagrangians*, *Physics Reports* **281** (1997) 145–238.
- [89] P. Colangelo, F. De Fazio and T. Pham, *$B^- \rightarrow K^- \chi_{c0}$ decay from charmed meson rescattering*, *Physics Letters B* **542** (2002) 71–79.
- [90] P. Colangelo, F. De Fazio and T. N. Pham, *Nonfactorizable contributions in B decays to charmonium: The Case of $B^- \rightarrow K^- h_c$* , *Phys. Rev. D* **69** (2004) 054023, [hep-ph/0310084].
- [91] LHCb collaboration, R. Aaij et al., *Observation of New Resonances Decaying to $J/\psi K^+$ and $J/\psi \phi$* , *Phys. Rev. Lett.* **127** (2021) 082001, [2103.01803].
- [92] J. M. Dias, X. Liu and M. Nielsen, *Prediction for the decay width of a charged state near the $D_s\bar{D}^*/D_s^*\bar{D}$ threshold*, *Phys. Rev. D* **88** (Nov, 2013) 096014.
- [93] M. Shifman, A. Vainshtein and V. Zakharov, *QCD and resonance physics. theoretical foundations*, *Nuclear Physics B* **147** (1979) 385–447.
- [94] L. Reinders, H. Rubinstein and S. Yazaki, *Hadron properties from QCD sum rules*, *Physics Reports* **127** (1985) 1–97.

- [95] BESIII collaboration, M. Ablikim et al., *Evidence for a Neutral Near-Threshold Structure in the K_S^0 recoil-mass spectra in $e^+e^- \rightarrow K_S^0 D_s^+ D^{*-}$ and $e^+e^- \rightarrow K_S^0 D_s^{*+} D^-$* , *Phys. Rev. Lett.* **129** (2022) 112003, [2204.13703].
- [96] M. Bashkanov et al., *Double-Pionic Fusion of Nuclear Systems and the ABC Effect: Approaching a Puzzle by Exclusive and Kinematically Complete Measurements*, *Phys. Rev. Lett.* **102** (2009) 052301, [0806.4942].
- [97] WASA-AT-COSY collaboration, P. Adlarson et al., *ABC Effect in Basic Double-Pionic Fusion — Observation of a new resonance?*, *Phys. Rev. Lett.* **106** (2011) 242302, [1104.0123].
- [98] WASA-AT-COSY collaboration, P. Adlarson et al., *Isospin Decomposition of the Basic Double-Pionic Fusion in the Region of the ABC Effect*, *Phys. Lett. B* **721** (2013) 229–236, [1212.2881].
- [99] WASA-AT-COSY collaboration, P. Adlarson et al., *Evidence for a New Resonance from Polarized Neutron-Proton Scattering*, *Phys. Rev. Lett.* **112** (2014) 202301, [1402.6844].
- [100] BESIII collaboration, M. Ablikim et al., *Observation of a structure at $1.84 \text{ GeV}/c^2$ in the $3(\pi^+\pi^-)$ mass spectrum in $J/\psi \rightarrow \gamma 3(\pi^+\pi^-)$ decays*, *Phys. Rev. D* **88** (2013) 091502, [1305.5333].
- [101] BESIII collaboration, M. Ablikim et al., *Observation and Spin-Parity Determination of the $X(1835)$ in $J/\psi \rightarrow \gamma K_S^0 K_S^0 \eta$* , *Phys. Rev. Lett.* **115** (2015) 091803, [1506.04807].
- [102] BESIII collaboration, M. Ablikim et al., *Study of $\eta(1475)$ and $X(1835)$ in radiative J/ψ decays to $\gamma\phi$* , *Phys. Rev. D* **97** (2018) 051101, [1801.02127].
- [103] BES collaboration, J. Z. Bai et al., *Observation of a near threshold enhancement in the $p\bar{p}$ mass spectrum from radiative $J/\psi \rightarrow \gamma p\bar{p}$ decays*, *Phys. Rev. Lett.* **91** (2003) 022001, [hep-ex/0303006].
- [104] CLEO collaboration, J. P. Alexander et al., *Study of $\psi(2S)$ Decays to $\gamma p\bar{p}$, $\pi^0 p\bar{p}$ and $\eta p\bar{p}$ and Search for $p\bar{p}$ Threshold Enhancements*, *Phys. Rev. D* **82** (2010) 092002, [1007.2886].
- [105] BESIII collaboration, M. Ablikim et al., *Spin-Parity Analysis of $p\bar{p}$ Mass Threshold Structure in J/ψ and ψ' Radiative Decays*, *Phys. Rev. Lett.* **108** (2012) 112003, [1112.0942].

-
- [106] A. Sibirtsev, J. Haidenbauer, S. Krewald, U.-G. Meissner and A. W. Thomas, *Near threshold enhancement of the $p\bar{p}$ mass spectrum in J/ψ decay*, *Phys. Rev. D* **71** (2005) 054010, [[hep-ph/0411386](#)].
- [107] G. Y. Chen, H. R. Dong and J. P. Ma, *Near Threshold Enhancement of $p\bar{p}$ System and $p\bar{p}$ Elastic Scattering*, *Phys. Lett. B* **692** (2010) 136–142, [[1004.5174](#)].
- [108] B. S. Zou and H. C. Chiang, *One pion exchange final state interaction and the $p\bar{p}$ near threshold enhancement in $J/\psi \rightarrow \gamma p\bar{p}$ decays*, *Phys. Rev. D* **69** (2004) 034004, [[hep-ph/0309273](#)].
- [109] N. Isgur, R. Kokoski and J. Paton, *Gluonic excitations of mesons: Why they are missing and where to find them*, *Phys. Rev. Lett.* **54** (Mar, 1985) 869–872.
- [110] F. E. Close and P. R. Page, *The Production and decay of hybrid mesons by flux tube breaking*, *Nucl. Phys. B* **443** (1995) 233–254, [[hep-ph/9411301](#)].
- [111] P. Lacock, C. Michael, P. Boyle and P. Rowland, *Hybrid mesons from quenched QCD*, *Physics Letters B* **401** (1997) 308–312.
- [112] MILC collaboration, C. W. Bernard et al., *Exotic mesons in quenched lattice QCD*, *Phys. Rev. D* **56** (1997) 7039–7051, [[hep-lat/9707008](#)].
- [113] COMPASS collaboration, M. Aghasyan et al., *Light isovector resonances in $\pi^- p \rightarrow \pi^- \pi^- \pi^+ p$ at 190 GeV/c*, *Phys. Rev. D* **98** (2018) 092003, [[1802.05913](#)].
- [114] COMPASS collaboration, M. G. Alexeev et al., *Exotic meson $\pi_1(1600)$ with $J^{PC} = 1^{-+}$ and its decay into $\rho(770)\pi$* , *Phys. Rev. D* **105** (2022) 012005, [[2108.01744](#)].
- [115] COMPASS collaboration, C. Adolph et al., *Odd and even partial waves of $\eta\pi^-$ and $\eta'\pi^-$ in $\pi^- p \rightarrow \eta^{(\prime)}\pi^- p$ at 191 GeV/c*, *Phys. Lett. B* **740** (2015) 303–311, [[1408.4286](#)]. [Erratum: *Phys.Lett.B* 811, 135913 (2020)].
- [116] E852 collaboration, J. Kuhn et al., *Exotic meson production in the $f_1(1285)\pi^-$ system observed in the reaction $\pi^- p \rightarrow \eta\pi^+\pi^-\pi^- p$ at 18 GeV/c*, *Phys. Lett. B* **595** (2004) 109–117, [[hep-ex/0401004](#)].
- [117] E852 collaboration, M. Lu et al., *Exotic meson decay to $\omega\pi^0\pi^-$* , *Phys. Rev. Lett.* **94** (2005) 032002, [[hep-ex/0405044](#)].
- [118] CRYSTAL BARREL collaboration, Albrecht, M., Amsler, C., Dünneweber, W., Faessler, M. A., Heinsius, F. H., Koch, H. et al., *Coupled channel analysis of $\bar{p}p \rightarrow \pi^0\pi^0\eta, \pi^0\eta\eta$ and $K^+K^-\pi^0$ at 900 MeV/c and of $\pi\pi$ -scattering data*, *Eur. Phys. J. C* **80** (2020) 453.

- [119] B. Kopf, M. Albrecht, H. Koch, M. Küßner, J. Pychy, X. Qin et al., *Investigation of the lightest hybrid meson candidate with a coupled-channel analysis of $\bar{p}p^-$, $\pi^- p^-$ and $\pi\pi$ -Data*, *Eur. Phys. J. C* **81** (2021) 1056, [2008.11566].
- [120] BESIII collaboration, M. Ablikim et al., *Observation of an Isoscalar Resonance with Exotic $J^{PC} = 1^{-+}$ Quantum Numbers in $J/\psi \rightarrow \gamma\eta\eta'$* , *Phys. Rev. Lett.* **129** (2022) 192002, [2202.00621]. [Erratum: *Phys. Rev. Lett.* 130, 159901 (2023)].
- [121] HADRON SPECTRUM collaboration, J. J. Dudek, R. G. Edwards, P. Guo and C. E. Thomas, *Toward the excited isoscalar meson spectrum from lattice QCD*, *Phys. Rev. D* **88** (2013) 094505, [1309.2608].
- [122] CLEO collaboration, G. S. Adams et al., *Amplitude analyses of the decays $\chi_{c1} \rightarrow \eta\pi^+\pi^-$ and $\chi_{c1} \rightarrow \eta'\pi^+\pi^-$* , *Phys. Rev. D* **84** (2011) 112009, [1109.5843].
- [123] E. Braaten, *Introduction to the NRQCD factorization approach to heavy quarkonium*, in *3rd International Workshop on Particle Physics Phenomenology*, 11, 1996, hep-ph/9702225.
- [124] S. Kim, P. Petreczky and A. Rothkopf, *Lattice NRQCD study of S- and P-wave bottomonium states in a thermal medium with $N_f = 2 + 1$ light flavors*, *Phys. Rev. D* **91** (2015) 054511, [1409.3630].
- [125] F. Schwabl, *Advanced Quantum Mechanics*. Springer Berlin, Heidelberg, 2008, <https://doi.org/10.1007/978-3-540-85062-5>.
- [126] G. T. Bodwin, E. Braaten and G. P. Lepage, *Rigorous QCD analysis of inclusive annihilation and production of heavy quarkonium*, *Phys. Rev. D* **51** (1995) 1125–1171, [hep-ph/9407339]. [Erratum: *Phys.Rev.D* 55, 5853 (1997)].
- [127] R. G. Newton, *Optical theorem and beyond*, *American Journal of Physics* **44** (1976) 639–642.
- [128] E. Braaten and Y.-Q. Chen, *Dimensional regularization in quarkonium calculations*, *Phys. Rev. D* **55** (Mar, 1997) 2693–2707.
- [129] G. T. Bodwin, D. K. Sinclair and S. Kim, *Lattice calculation of quarkonium decay matrix elements*, *Int. J. Mod. Phys. A* **12** (1997) 4019–4028, [hep-ph/9609371].
- [130] H.-W. Huang and K.-T. Chao, *QCD predictions for annihilation decays of P wave quarkonia to next-to-leading order in α_s* , *Phys. Rev. D* **54** (1996) 6850–6854, [hep-ph/9606220]. [Erratum: *Phys.Rev.D* 56, 1821 (1997)].
- [131] L. D. Landau, *On the angular momentum of a system of two photons*, *Dokl. Akad. Nauk SSSR* **60** (1948) 207–209.

-
- [132] C. N. Yang, *Selection rules for the dematerialization of a particle into two photons*, *Phys. Rev.* **77** (Jan, 1950) 242–245.
- [133] J. P. Ma, J. X. Wang and S. Zhao, *Breakdown of QCD Factorization for P-Wave Quarkonium Production at Low Transverse Momentum*, *Phys. Lett. B* **737** (2014) 103–108, [1405.3373].
- [134] W. Beenakker, R. Kleiss and G. Lustermaans, *No Landau-Yang in QCD*, 1508.07115.
- [135] G. T. Bodwin, E. Braaten and G. P. Lepage, *Rigorous qcd predictions for decays of p-wave quarkonia*, *Phys. Rev. D* **46** (Sep, 1992) R1914–R1918.
- [136] S. M. H. Wong, *Color octet contribution in exclusive P wave charmonium decay*, *Nucl. Phys. B Proc. Suppl.* **93** (2001) 220–225, [hep-ph/0009016].
- [137] W.-L. Sang, R. Rashidin, U.-R. Kim and J. Lee, *Relativistic Corrections to the Exclusive Decays of C-even Bottomonia into S-wave Charmonium Pairs*, *Phys. Rev. D* **84** (2011) 074026, [1108.4104].
- [138] L.-B. Chen and C.-F. Qiao, *P-wave Quarkonium Decays to Meson Pair*, *JHEP* **11** (2012) 168, [1204.0215].
- [139] S.-X. Fang and S.-Y. Chen, *The Beijing Electron Positron Collider*, *Part. Accel.* **26** (1990) 51–61.
- [140] M.-H. Ye and Z.-P. Zheng, *BEPC, the Beijing Electron Positron Collider*, *Int. J. Mod. Phys. A* **2** (1987) 1707–1725.
- [141] C. Yu et al., *BEPCII Performance and Beam Dynamics Studies on Luminosity*, in *7th International Particle Accelerator Conference*, p. TUYA01, 2016.
- [142] BESIII collaboration, M. Ablikim et al., *Search for $\Delta S = 2$ nonleptonic hyperon decays $\Omega^- \rightarrow \Sigma^0 \pi^-$ and $\Omega^- \rightarrow n K^-$* , *JHEP* **05** (2024) 141, [2403.13437].
- [143] BESIII collaboration, M. Ablikim et al., *Future Physics Programme of BESIII*, *Chin. Phys. C* **44** (2020) 040001, [1912.05983].
- [144] C. Zhang, L. Ma, G. Pei and J. Wang, *Construction and Commissioning of BEPCII*, in *Particle Accelerator Conference (PAC 09)*, p. MO3RAI03, 2010.
- [145] Q. Qin et al., *Design and Optimization of the BEPCII Synchrotron Radiation Mode*, in *Particle Accelerator Conference (PAC 09)*, p. TU5RFP019, 2010.
- [146] H. Geng, J. Xing, C. Yu and Y. Zhang, *An Alternative Design for BEPCII Upgrade*, in *International Particle Accelerator Conference (IPAC 13)*, p. WEOXGD3, 2022.

- [147] M. Küßner, *Coupled channel partial wave analysis of two-photon reactions at BESIII*, doctoralthesis, Ruhr-Universität Bochum, Universitätsbibliothek, 2022. 10.13154/294-8590.
- [148] X. Li, Y. Sun, C. Lî, Z. Liu, Y. Heng, M. Shao et al., *Study of MRPC technology for BESIII endcap-TOF upgrade*, *Radiat. Detect. Technol. Methods* **1** (2017) 13.
- [149] BES collaboration, J. Z. Bai et al., *The BES detector*, *Nucl. Instrum. Meth. A* **344** (1994) 319–334.
- [150] J. Bai, H. Bao et al., *The BES upgrade*, *Nucl. Instrum. Meth. A* **458** (2001) 627–637.
- [151] D. M. Asner et al., *Physics at BES-III*, *Int. J. Mod. Phys. A* **24** (2009) S1–794.
- [152] Q. Gang, L. Jun-Guang, H. Kang-Lin, B. Jian-Ming, C. Guo-Fu, D. Zi-Yan et al., *Particle identification using artificial neural networks at BESIII*, *Chinese Physics C* **32** (2008) 1.
- [153] P. Cao et al., *Design and construction of the new BESIII endcap Time-of-Flight system with MRPC Technology*, *Nucl. Instrum. Meth. A* **953** (2020) 163053.
- [154] X. Li et al., *Study of MRPC technology for BESIII endcap-TOF upgrade*, *Radiat. Detect. Technol. Methods* **1** (2017) 13.
- [155] M. Xiang et al., *Determination of event start time at BESIII*, *Chinese Physics C* **32** (10, 2010) 744.
- [156] BES collaboration, F. A. Harris, *BEPCII and BESIII*, *Int. J. Mod. Phys. A* **24** (2009) 377–384.
- [157] BESIII collaboration, M. Ablikim et al., *Oscillating features in the electromagnetic structure of the neutron*, *Nature Phys.* **17** (2021) 1200–1204, [2103.12486].
- [158] BESIII collaboration, M. Ablikim et al., *Measurement of the Cross Section for $e^+e^- \rightarrow \text{Hadrons}$ at Energies from 2.2324 to 3.6710 GeV*, *Phys. Rev. Lett.* **128** (2022) 062004, [2112.11728].
- [159] BESIII collaboration, M. Ablikim et al., *Determination of the number of $\psi(3686)$ events taken at BESIII*, *Chin. Phys. C* **48** (2024) 093001.
- [160] BESIII collaboration, M. Ablikim, *Measurement of the integrated luminosities of the data taken by BESIII at $\sqrt{s} = 3.650$ and 3.773 GeV*, *Chin. Phys. C* **37** (2013) 123001, [1307.2022].

-
- [161] Z. Jian-Yong et al., *Upgrade of Beam Energy Measurement System at BEPC-II*, *Chin. Phys. C* **40** (2016) 076001, [1510.08167].
- [162] BESIII collaboration, M. Ablikim et al., *First Observation of the Direct Production of the χ_{c1} in e^+e^- Annihilation*, *Phys. Rev. Lett.* **129** (2022) 122001, [2203.13782].
- [163] BESIII collaboration, M. Ablikim et al., *Measurement of the center-of-mass energies at BESIII via the di-muon process*, *Chin. Phys. C* **40** (2016) 063001, [1510.08654].
- [164] BESIII collaboration, M. Ablikim et al., *Luminosities and energies of e^+e^- collision data taken between 4.61 GeV and 4.95 GeV at BESIII*, *Chin. Phys. C* **46** (2022) 113003, [2205.04809].
- [165] BESIII collaboration, M. Ablikim et al., *Measurement of integrated luminosities at BESIII for data samples at center-of-mass energies between 4.0 and 4.6 GeV*, *Chin. Phys. C* **46** (2022) 113002, [2203.03133].
- [166] G. Barrand et al., *GAUDI - A software architecture and framework for building HEP data processing applications*, *Comput. Phys. Commun.* **140** (2001) 45–55.
- [167] R. Brun and F. Rademakers, *ROOT: An object oriented data analysis framework*, *Nucl. Instrum. Meth. A* **389** (1997) 81–86.
- [168] Z.-Y. Deng, G.-F. Cao, C.-D. Fu, M. he, H.-M. Liu, Y. Mao et al., *Object-oriented BESIII detector simulation system*, *Chinese Physics C* **30** (2006) 371–377.
- [169] GEANT4 collaboration, S. Agostinelli et al., *GEANT4—a simulation toolkit*, *Nucl. Instrum. Meth. A* **506** (2003) 250–303.
- [170] R.-G. Ping, *Event generators at BESIII*, *Chin. Phys. C* **32** (2008) 599.
- [171] N. Metropolis, A. W. Rosenbluth, M. N. Rosenbluth, A. H. Teller and E. Teller, *Equation of state calculations by fast computing machines*, *J. Chem. Phys.* **21** (1953) 1087–1092.
- [172] G. S. Fishman, *Monte Carlo*. Springer New York, NY, 1996, <https://doi.org/10.1007/978-1-4757-2553-7>.
- [173] S. Jadach, B. F. L. Ward and Z. Was, *The Precision Monte Carlo event generator KK for two-fermion final states in e^+e^- collisions*, *Comput. Phys. Commun.* **130** (2000) 260–325, [hep-ph/9912214].
- [174] D. J. Lange, *The EvtGen particle decay simulation package*, *Nucl. Instrum. Meth. A* **462** (2001) 152–155.

- [175] E. Barberio and Z. Was, *PHOTOS: A Universal Monte Carlo for QED radiative corrections. Version 2.0*, *Comput. Phys. Commun.* **79** (1994) 291–308.
- [176] P. Rong-Gang and P. Cai-Ying, *Monte Carlo Generators for Tau-Charm-Physics at BESIII*, 2006. http://bes.ihep.ac.cn/bes3/phy_book/book/phy/generators_ping.pdf.
- [177] BESIII collaboration, M. Ablikim et al., *Precision Study of $\eta' \rightarrow \gamma\pi^+\pi^-$ Decay Dynamics*, *Phys. Rev. Lett.* **120** (2018) 242003, [1712.01525].
- [178] J. Wess and B. Zumino, *Consequences of anomalous Ward identities*, *Phys. Lett. B* **37** (1971) 95–97.
- [179] E. Witten, *Global Aspects of Current Algebra*, *Nucl. Phys. B* **223** (1983) 422–432.
- [180] J. C. Chen, G. S. Huang, X. R. Qi, D. H. Zhang and Y. S. Zhu, *Event generator for J/ψ and $\psi(2S)$ decay*, *Phys. Rev. D* **62** (2000) 034003.
- [181] R.-L. Yang, R.-G. Ping and H. Chen, *Tuning and Validation of the Lundcharm Model with J/ψ Decays*, *Chin. Phys. Lett.* **31** (2014) 061301.
- [182] B. Andersson, G. Gustafson and T. Sjostrand, *A Three-Dimensional Model for Quark and Gluon Jets*, *Z. Phys. C* **6** (1980) 235.
- [183] T. Sjostrand, *The Lund Monte Carlo for Jet Fragmentation*, *Comput. Phys. Commun.* **27** (1982) 243.
- [184] Z. Yao, Z. Xue-Yao, L. Wei-Dong, M. Ze-Pu, M. Qiu-Mei, M. Xiang et al., *Pattern-Matching Track Reconstruction for the BESIII Main Drift Chamber*, *Chinese Physics C* **31** (2007) 570–575.
- [185] L. Qiu-Guang, Z. Shi-Lei, L. Wei-Guo, M. Ze-Pu, B. Jian-Ming, C. Guo-Fu et al., *Track reconstruction using the TSF method for the BESIII main drift chamber*, *Chinese Physics C* **32** (2008) 565.
- [186] Y. Zhang, J. Zhang, Y. Yuan and H. Liu, *Track Reconstruction Using the Hough Transform at BESIII*, in *Proceedings of The 39th International Conference on High Energy Physics — PoS(ICHEP2018)*, vol. 340, p. 888, 2019.
- [187] J.-K. Wang et al., *BESIII track fitting algorithm*, *Chin. Phys. C* **33** (2009) 870–879.
- [188] H. Bethe, *Zur Theorie des Durchgangs schneller Korpuskularstrahlen durch Materie*, *Annalen der Physik* **397** (1930) 325–400.
- [189] F. Bloch, *Zur Bremsung rasch bewegter Teilchen beim Durchgang durch Materie*, *Annalen der Physik* **408** (1933) 285–320.

-
- [190] G. Molière, *Theorie der Streuung schneller geladener Teilchen II Mehrfach- und Vielfachstreuung*, *Zeitschrift für Naturforschung A* **3** (1948) 78–97.
- [191] E. Ramsden, *Hall-Effect Sensors*. Newnes, 2006, <https://doi.org/10.1016/B978-0-7506-7934-3.50018>.
- [192] R. E. Kalman, *A New Approach to Linear Filtering and Prediction Problems*, *Journal of Basic Engineering* **82** (1960) 35–45.
- [193] X.-X. Cao et al., *Studies of dE/dx measurements with the BESIII*, *Chin. Phys. C* **34** (2010) 1852–1859.
- [194] L. List, *Statistical Methods for Data Analysis*. Springer Cham, 2023, 10.1007/978-3-031-19934-9.
- [195] M. He, *Simulation and reconstruction of the BESIII EMC*, *J. Phys. Conf. Ser.* **293** (2011) 012025.
- [196] Z. Wang, “Design of the Reconstruction Software for BESIII Electromagnetic Calorimeter.” unpublished internal document.
- [197] B. Brabson, R. Crittenden, A. Dzierba, T. Foxford, J. Gunter, R. Lindenbusch et al., *A study of two prototype lead glass electromagnetic calorimeters*, *Nuclear Instruments and Methods in Physics Research Section A: Accelerators, Spectrometers, Detectors and Associated Equipment* **332** (1993) 419–443.
- [198] M. Xu et al., *Primary vertex reconstruction based on the Kalman filter technique at BESIII*, *Chin. Phys. C* **34** (2010) 92–98.
- [199] O. Forster, *Analysis 2: Differentialrechnung im \mathbb{R}^n , gewöhnliche Differentialgleichungen*. Vieweg+Teubner Verlag Wiesbaden, 2011, <https://doi.org/10.1007/978-3-8348-8103-8>.
- [200] CLEO collaboration, S. B. Athar et al., χ_{cJ} Decays to $h^+h^-h^0$, *Phys. Rev. D* **75** (2007) 032002, [[hep-ex/0611032](https://arxiv.org/abs/hep-ex/0611032)].
- [201] P. Vischia, *Pseudosignificances as figures of merit: a systematic study and exploration of Bayesian solutions*, *PoS Confinement2018* (2019) 249.
- [202] F. James and M. Roos, *Minuit: A System for Function Minimization and Analysis of the Parameter Errors and Correlations*, *Comput. Phys. Commun.* **10** (1975) 343–367.
- [203] L. Faddeev, A. J. Niemi and U. Wiedner, *Glueballs, closed flux tubes and eta(1440)*, *Phys. Rev. D* **70** (2004) 114033, [[hep-ph/0308240](https://arxiv.org/abs/hep-ph/0308240)].

- [204] C. Amsler et al., *Production and decay of $\eta'(958)$ and $\eta(1440)$ in $\bar{p}p$ annihilation at rest*, *Eur. Phys. J. C* **33** (2004) 23–30.
- [205] J. H. Friedman, *Data Analysis Techniques for High-Energy Particle Physics*, in *3rd CERN School of Computing*, p. 271, 10, 1974.
- [206] A. Gelman, J. Carlin, H. Stern and D. Rubin, *Bayesian Data Analysis*. Texts in statistical science series. Chapman & Hall/CRC, 2004.
- [207] E. Eichten, S. Godfrey, H. Mahlke and J. L. Rosner, *Quarkonia and their transitions*, *Rev. Mod. Phys.* **80** (2008) 1161–1193, [[hep-ph/0701208](#)].
- [208] CLEO collaboration, R. E. Mitchell et al., *J/ψ and $\psi(2S)$ Radiative Decays to η_c* , *Phys. Rev. Lett.* **102** (2009) 011801, [[0805.0252](#)]. [Erratum: *Phys.Rev.Lett.* 106, 159903 (2011)].
- [209] BESIII collaboration, M. Ablikim et al., *Measurements of the mass and width of the η_c using $\psi' \rightarrow \gamma\eta_c$* , *Phys. Rev. Lett.* **108** (2012) 222002, [[1111.0398](#)].
- [210] K. Zhu, X. H. Mo, C. Z. Yuan and P. Wang, *A mathematical review on the multiple-solution problem*, *Int. J. Mod. Phys. A* **26** (2011) 4511–4520, [[1108.2760](#)].
- [211] BESIII collaboration, M. Ablikim et al., *Measurement of $\eta' \rightarrow \pi^+\pi^-e^+e^-$ and $\eta' \rightarrow \pi^+\pi^-\mu^+\mu^-$* , *Phys. Rev. D* **87** (2013) 092011, [[1303.7360](#)].
- [212] W.-L. Yuan, X.-C. Ai, X.-B. Ji, S.-J. Chen, Y. Zhang, L.-H. Wu et al., *Study of tracking efficiency and its systematic uncertainty from $J/\psi \rightarrow p\bar{p}\pi^+\pi^-$ at BESIII*, *Chin. Phys. C* **40** (2016) 026201, [[1507.03453](#)].
- [213] BESIII collaboration, M. Ablikim et al., *Cross section measurement of $e^+e^- \rightarrow f_1(1285)\pi^+\pi^-$ at center-of-mass energies between 3.808 and 4.951 GeV*, 2501.14206.
- [214] BESIII collaboration, M. Ablikim et al., *Study of χ_{cJ} radiative decays into a vector meson*, *Phys. Rev. D* **83** (2011) 112005, [[1103.5564](#)].
- [215] R. Barlow, *Systematic errors: Facts and fictions*, in *Conference on Advanced Statistical Techniques in Particle Physics*, pp. 134–144, 7, 2002, [hep-ex/0207026](#).
- [216] O. Behnke, K. Kröniger, T. Schörner-Sadenius and G. Schott, eds., *Data analysis in high energy physics: A practical guide to statistical methods*. Wiley-VCH, Weinheim, Germany, 2013.
- [217] BESIII collaboration, M. Ablikim et al., *Cross section measurements of $e^+e^- \rightarrow p\bar{p}\pi^0$ at center-of-mass energies between 4.008 and 4.600 GeV*, *Phys. Lett. B* **771** (2017) 45–51, [[1701.04198](#)].

-
- [218] K.-T. Chao, Z.-G. He, D. Li and C. Meng, *Search for $C = +$ charmonium states in $e^+e^- \rightarrow \gamma + X$ at BEPCII/BESIII*, 1310.8597.
- [219] D. Herndon, P. Soding and R. J. Cashmore, *A Generalized Isobar Model Formalism*, *Phys. Rev. D* **11** (1975) 3165.
- [220] J. D. Richman, *An Experimenter's Guide to the Helicity Formalism*, . report CALT-68-1148.
- [221] E. P. Wigner, *Gruppentheorie und ihre Anwendung auf die Quantenmechanik der Atomspektren*, vol. 85. Vieweg+Teubner Verlag Wiesbaden, 01, 1931, 10.1007/978-3-663-02555-9.
- [222] BESIII collaboration, M. Ablikim et al., *Observation of $\eta_c \rightarrow \omega\omega$ in $J/\psi \rightarrow \gamma\omega\omega$* , *Phys. Rev. D* **100** (2019) 052012, [1905.10318].
- [223] J. M. Blatt and V. F. Weisskopf, *Theoretical nuclear physics*. Springer, New York, 1952, 10.1007/978-1-4612-9959-2.
- [224] M. Shepherd, J. Stevens, R. Mitchell, M. Albrecht, B. Grube, A. Austregesilo et al., *AmpTools: Version 0.15.3*, 2024. 10.5281/zenodo.10961168.
- [225] W. Rudin, *Principles of Mathematical Analysis*. International series in pure and applied mathematics. McGraw-Hill, 1976.
- [226] H. Lebesgue, *Intégrale, Longueur, Aire, Annali di Matematica Pura ed Applicata* **7** (1902) 231.
- [227] BESIII collaboration, M. Ablikim et al., “Observation of exotic state $\pi_1(1600)$ in $\psi(2S) \rightarrow \gamma\chi_{c1}$, $\chi_{c1} \rightarrow \eta'\pi^+\pi^-$.” internal note, to be published.
- [228] M. Schmelling, *Averaging correlated data*, *Phys. Scripta* **51** (1995) 676–679.
- [229] G. D’Agostini, *On the use of the covariance matrix to fit correlated data*, *Nucl. Instrum. Meth. A* **346** (1994) 306–311.
- [230] MARK-III collaboration, R. M. Baltrusaitis et al., *Hadronic Decays of the η_c (2980)*, *Phys. Rev. D* **33** (1986) 629.
- [231] BELLE collaboration, Q. N. Xu et al., *Measurement of $\eta_c(1S)$, $\eta_c(2S)$ and non-resonant $\eta'\pi^+pi^-$ production via two-photon collisions*, *Phys. Rev. D* **98** (2018) 072001, [1805.03044].
- [232] BABAR collaboration, J. P. Lees et al., *Light meson spectroscopy from Dalitz plot analyses of η_c decays to $\eta'K^+K^-$, $\eta'\pi^+\pi^-$, and $\eta\pi^+\pi^-$ produced in two-photon interactions*, *Phys. Rev. D* **104** (2021) 072002, [2106.05157].

- [233] S. M. Flatte, *Coupled - Channel Analysis of the pi eta and K anti-K Systems Near K anti-K Threshold*, *Phys. Lett. B* **63** (1976) 224–227.
- [234] N. Cabibbo, *Unitary Symmetry and Leptonic Decays*, *Phys. Rev. Lett.* **10** (1963) 531–533.
- [235] M. Kobayashi and T. Maskawa, *CP Violation in the Renormalizable Theory of Weak Interaction*, *Prog. Theor. Phys.* **49** (1973) 652–657.
- [236] BESIII collaboration, M. Ablikim et al., *Measurements of $e^+e^- \rightarrow \eta_c \pi^+ \pi^- \pi^0$, $\eta_c \pi^+ \pi^-$ and $\eta_c \pi^0 \gamma$ at \sqrt{s} from 4.18 to 4.60 GeV, and search for a Z_c state close to the $D\bar{D}$ threshold decaying to $\eta_c \pi$ at $\sqrt{s} = 4.23$ GeV*, *Phys. Rev. D* **103** (2021) 032006, [2010.14415].
- [237] BESIII collaboration, M. Ablikim et al., *Observation of a Vector Charmoniumlike State at 4.7 GeV/c² and Search for Z_{cs} in $e^+e^- \rightarrow K^+K^-J/\psi$* , *Phys. Rev. Lett.* **131** (2023) 211902, [2308.15362].
- [238] BESIII collaboration, M. Ablikim et al., *Precise Measurement of Born Cross Sections for $e^+e^- \rightarrow D\bar{D}$ at $\sqrt{s}=3.80\text{--}4.95$ GeV*, *Phys. Rev. Lett.* **133** (2024) 081901, [2402.03829].
- [239] BESIII collaboration, M. Ablikim et al., *Evidence of a resonant structure in the $e^+e^- \rightarrow \pi^+D^0D^{*-}$ cross section between 4.05 and 4.60 GeV*, *Phys. Rev. Lett.* **122** (2019) 102002, [1808.02847].
- [240] BESIII collaboration, M. Ablikim et al., *Observation of Three Charmoniumlike States with $J^{PC} = 1^{--}$ in $e^+e^- \rightarrow D^{*0}D^{*-}\pi^+$* , *Phys. Rev. Lett.* **130** (2023) 121901, [2301.07321].
- [241] BESIII collaboration, M. Ablikim et al., *Cross section measurements of the $e^+e^- \rightarrow D^{*+}D^{*-}$ and $e^+e^- \rightarrow D^{*+}D^-$ processes at center-of-mass energies from 4.085 to 4.600 GeV*, *JHEP* **05** (2022) 155, [2112.06477].
- [242] BESIII collaboration, M. Ablikim et al., *Precise Measurement of the $e^+e^- \rightarrow D_s^+D_s^-$ Cross Section at Center-of-Mass Energies from Threshold to 4.95 GeV*, *Phys. Rev. Lett.* **133** (2024) 261902, [2403.14998].
- [243] BESIII collaboration, M. Ablikim et al., *Precise Measurement of the $e^+e^- \rightarrow D_s^{*+}D_s^{*-}$ Cross Sections at Center-of-Mass Energies from Threshold to 4.95 GeV*, *Phys. Rev. Lett.* **131** (2023) 151903, [2305.10789].
- [244] F. Jegerlehner, *Electroweak effective couplings for future precision experiments*, *Nuovo Cim. C* **034S1** (2011) 31–40, [1107.4683].

-
- [245] BESIII collaboration, M. Ablikim et al., *Study of the resonance structures in the process $e^+e^+ \rightarrow \pi^+\pi^- J/\psi$* , *Phys. Rev. D* **106** (2022) 072001, [2206.08554].
- [246] HEP ML Community, “A Living Review of Machine Learning for Particle Physics.” <https://iml-wg.github.io/HEPML-LivingReview/>.
- [247] M. Williams, M. Bellis and C. A. Meyer, *Multivariate side-band subtraction using probabilistic event weights*, *JINST* **4** (2009) P10003, [0809.2548].
- [248] S.-L. Zhu and C.-S. Gao, *$X(1835)$: A Possible baryonium?*, *Commun. Theor. Phys.* **46** (2006) 291, [hep-ph/0507050].
- [249] J. P. Dedonder, B. Loiseau, B. El-Bennich and S. Wycech, *On the structure of the $X(1835)$ baryonium*, *Phys. Rev. C* **80** (2009) 045207, [0904.2163].
- [250] G.-J. Ding and M.-L. Yan, *Productions of $X(1835)$ as baryonium with sizable gluon content*, *Eur. Phys. J. A* **28** (2006) 351–360, [hep-ph/0511186].
- [251] Z.-G. Wang and S.-L. Wan, *$X(1835)$ as a baryonium state with QCD sum rules*, *J. Phys. G* **34** (2007) 505–511, [hep-ph/0601105].
- [252] V. Shastry, C. S. Fischer and F. Giacosa, *The phenomenology of the exotic hybrid nonet with $\pi 1(1600)$ and $\eta 1(1855)$* , *Phys. Lett. B* **834** (2022) 137478, [2203.04327].
- [253] C. A. Meyer and E. S. Swanson, *Hybrid Mesons*, *Prog. Part. Nucl. Phys.* **82** (2015) 21–58, [1502.07276].
- [254] Q.-N. Wang, W. Chen and H.-X. Chen, *Exotic molecular states and tetraquark states with $J^P = 0^+, 1^+, 2^+$* , *Chin. Phys. C* **45** (2021) 093102, [2011.10495].
- [255] Z.-G. Wang, *Decay widths of $Z_{cs}(3985/4000)$ based on rigorous quark-hadron duality*, *Chin. Phys. C* **46** (2022) 103106, [2205.03203].
- [256] B.-D. Wan and C.-F. Qiao, *About the exotic structure of Z_{cs}* , *Nucl. Phys. B* **968** (2021) 115450, [2011.08747].
- [257] F. Rosenblatt, *The perceptron: a probabilistic model for information storage and organization in the brain.*, *Psychological review* **65 6** (1958) 386–408.
- [258] C. Bishop, *Neural Networks For Pattern Recognition*, vol. 227. Clarendon Press/OUP, 01, 2005, 10.1093/oso/9780198538493.001.0001.
- [259] H. He and E. Garcia, *Learning from imbalanced data*, *Knowledge and Data Engineering, IEEE Transactions on* **21** (10, 2009) 1263 – 1284.
- [260] I. Goodfellow, Y. Bengio and A. Courville, *Deep Learning*. MIT Press, 2016.

- [261] J. Garnier and A. Quetelet, *Correspondance mathématique et physique*. M.Hayez, imprimeur, 1838.
- [262] L. Bain, *Applied regression analysis*, *Technometrics* **9** (04, 2012) 182–183.
- [263] H. He and E. A. Garcia, *Learning from imbalanced data*, *IEEE Transactions on Knowledge and Data Engineering* **21** (2009) 1263–1284.
- [264] C. G. Broyden, *The Convergence of a Class of Double-rank Minimization Algorithms 1. General Considerations*, *Ima J. Appl. Math.* **6** (1970) 76–90.
- [265] R. Fletcher, *A new approach to variable metric algorithms*, *Comput. J.* **13** (1970) 317–322.
- [266] D. Goldfarb, *A family of variable-metric methods derived by variational means*, *Mathematics of Computation* **24** (1970) 23–26.
- [267] D. F. Shanno, *Conditioning of quasi-newton methods for function minimization*, *Mathematics of Computation* **24** (1970) 647–656.

List of Figures

2.1.	The particle content of the SM	7
2.2.	Ground state baryon octet and decuplet	11
2.3.	Overview of the conventional meson nonets built from the three lightest quarks	13
2.4.	Nonets of the pseudoscalar mesons and vector mesons	15
2.5.	The charmonium(-like) spectrum.	19
2.6.	Diagrams showing the ISChE mechanism.	21
3.1.	Overview of the IHEP campus around the BEPCII complex.	33
3.2.	Schematic drawing of the BESIII detector.	34
3.3.	Energy loss for different particle species in the MDC	36
3.4.	Calculated mass squared for particles in the TOF	37
3.5.	Center-of-mass energies and luminosities of the BESIII data samples.	39
3.6.	Schematic representation of the simulated process $e^+e^- \rightarrow c\bar{c} \rightarrow X$	42
4.1.	Schematic illustration of the helix parametrization.	47
5.1.	Invariant mass spectrum of η' candidates.	57
5.2.	Invariant mass spectrum of η candidates and two-dimensional distribution of $m_{\gamma\gamma}$ against $m_{\eta\pi^+\pi^-}$	58
5.3.	Composition of the inclusive MC for η' candidates compared with data for $\eta' \rightarrow \eta\pi^+\pi^-$	59
5.4.	Composition of the inclusive MC for η' candidates compared with data for $\eta' \rightarrow \gamma\pi^+\pi^-$	59
5.5.	Composition of the inclusive MC for the $\eta'\pi^+\pi^-$ system compared with data for $\eta' \rightarrow \eta\pi^+\pi^-$	60
5.6.	Composition of the inclusive MC for the $\eta'\pi^+\pi^-$ system compared with data for $\eta' \rightarrow \gamma\pi^+\pi^-$	60
5.7.	The $\chi^2_{+1\gamma}$ plotted against χ^2 for both channels.	65
5.8.	The $\chi^2_{-1\gamma}$ plotted against χ^2 for both channels.	65
5.9.	χ^2 distributions.	66
5.10.	Invariant mass spectrum of each combination of two photons.	67
5.11.	Invariant mass of the system recoiling against the $\pi^+\pi^-$ system.	68

5.12. Invariant mass of the 4π system.	69
5.13. Invariant mass of the $\pi^+\pi^-$ system resulting from the $\eta' \rightarrow \gamma\pi^+\pi^-$ decay.	70
5.14. Invariant mass of the $\eta\pi^+\pi^-$ system, with the definition of the signal and sideband regions.	72
5.15. Invariant mass of the $\gamma\pi^+\pi^-$ system, with the definition of the signal and sideband regions.	72
5.16. Invariant mass of the $\eta'\pi^+\pi^-$ system.	74
5.17. Invariant mass of the $\eta'\pi^+\pi^-$ system, with the fit to the χ_{cJ} for the $\eta' \rightarrow \eta\pi^+\pi^-$ channel.	78
5.18. Invariant mass of the $\eta'\pi^+\pi^-$ system, with the fit to the χ_{cJ} for the $\eta' \rightarrow \gamma\pi^+\pi^-$ channel.	79
5.19. Likelihood scans for the χ_{c0}	80
5.20. Invariant mass of the $\eta'\pi^+\pi^-$ system, with a Breit-Wigner fit to the η_c for the $\eta' \rightarrow \eta\pi^+\pi^-$ channel.	82
5.21. Invariant mass of the $\eta'\pi^+\pi^-$ system with a fit to the η_c including interference with the background.	84
5.22. Invariant mass of the $\eta'\pi^+\pi^-$ system, with a Breit-Wigner fit to the $X(1835)$	86
5.23. Invariant mass of the $\eta'\pi^+\pi^-$ system, with a Breit-Wigner fit to the $X(1835)$ considering the phase space.	88
5.24. Systematic uncertainties for the χ^2 -cut.	92
5.25. Systematic uncertainties for the minimum photon energy.	92
5.26. Systematic uncertainties for the J/ψ veto in the $\pi^+\pi^-$ recoil system.	93
5.27. Systematic uncertainties for the J/ψ veto in the 4π system and the ρ^0 cut in the $\pi^+\pi^-$ system.	93
5.28. Systematic uncertainties for the choice of the signal and sideband regions.	95
5.29. PWA results for the projections on the invariant masses.	103
5.30. PWA results for the projections on the azimuthal angles.	104
5.31. PWA results for the projections on the polar angles.	105
5.32. Likelihood scan for the $\pi_1(1600)$	106
5.33. Comparison of the PWA results of $\chi_{c1} \rightarrow \eta'\pi^+\pi^-$ and $\chi_{c2} \rightarrow \eta'\pi^+\pi^-$	107
6.1. Invariant mass spectra of signal resonances.	116
6.2. Invariant mass spectra of K^* candidates.	117
6.3. Figure of merit for the cut on the χ^2 of the kinematic fit.	117
6.4. Invariant mass spectra of appearing background resonances.	118
6.5. Invariant mass spectra of systems with appearing $D_{(s)}^{(*)}$ background resonances.	120
6.6. Invariant mass spectra of η_c candidates.	121
6.7. Input-output check.	125
6.8. Input-output check (cont.).	126

6.9. Results of the 1200 input-output checks.	127
6.10. Combined fit to the 4680 data sample.	129
6.11. Combined fit to the 4680 data sample (cont.).	130
6.12. η_c spectrum for the summed final states for the 4640 and 4680 data sample.	131
6.13. Likelihood profile for the 4680 data sample.	131
6.14. Feynman diagrams for $e^+e^- \rightarrow \gamma^* \rightarrow X$	132
6.15. Invariant mass spectrum of the $\eta_c K^*$ system.	133
A.1. Systematic uncertainties for the χ^2 -cut.	141
A.2. Systematic uncertainties for the minimum photon energy.	142
A.3. Systematic uncertainties for the J/ψ veto in the $\pi^+\pi^-$ recoil system. . . .	143
A.4. Systematic uncertainties for the J/ψ veto in the 4π system and the cut on the ρ^0	144
A.5. Systematic uncertainties for width of the signal and sideband regions. . .	145
A.6. Systematic uncertainties for distance between the signal and sideband regions.	146
B.1. Combined fit to the 4600 data sample.	148
B.2. Combined fit to the 4600 data sample (cont.).	149
B.3. Combined fit to the 4620 data sample.	150
B.4. Combined fit to the 4620 data sample (cont.).	151
B.5. Combined fit to the 4640 data sample.	152
B.6. Combined fit to the 4640 data sample (cont.).	153
B.7. Combined fit to the 4660 data sample.	154
B.8. Combined fit to the 4660 data sample (cont.).	155
B.9. Combined fit to the 4700 data sample.	156
B.10. Combined fit to the 4700 data sample (cont.).	157
B.11. η_c spectrum for the summed final states.	158
B.12. Likelihood profile for all data samples.	159
C.1. Structure and learning curves of the neural network.	162
C.2. Result of the training of the neural network for the training sample. . . .	163
C.3. Result of the training of the neural network for the inclusive MC sample.	163

List of Tables

2.1. Quantum numbers of the quarks.	10
3.1. Operational parameters of BEPC, BEPCII and BEPCII-U.	32
3.2. Parameters of the BESIII detector compared with its predecessor BESII.	35
3.3. Resonance data samples used in this thesis.	41
3.4. Scan data samples used in this thesis.	41
3.5. XYZ data samples used in this thesis.	41
3.6. Decay chain and models used in the BesEvtGen generator.	43
5.1. Signal reactions for the $\eta' \rightarrow \eta\pi^+\pi^-$ channel.	62
5.2. Background reactions for the $\eta' \rightarrow \eta\pi^+\pi^-$ channel.	62
5.3. Signal reactions for the $\eta' \rightarrow \gamma\pi^+\pi^-$ channel.	63
5.4. Background reactions for the $\eta' \rightarrow \gamma\pi^+\pi^-$ channel.	63
5.5. Parameters of the fits to the invariant mass of the η' candidate.	74
5.6. Determined efficiencies for all resonances.	76
5.7. Parameters of the fits to the invariant mass of the χ_{c1} and χ_{c2} candidates in the $\eta' \rightarrow \eta\pi^+\pi^-$ channel.	78
5.8. Parameters of the fits to the invariant mass of the χ_{c1} and χ_{c2} candidates in the $\eta' \rightarrow \gamma\pi^+\pi^-$ channel.	79
5.9. Determined branching ratios for the decays $\chi_{cJ} \rightarrow \eta'\pi^+\pi^-$	81
5.10. Fit to the η_c in the using a relativistic Breit-Wigner function with the CLEO pre-factor.	83
5.11. Parameters of the fit to the η_c candidates.	85
5.12. Determined branching ratios for the decay $\eta_c \rightarrow \eta'\pi^+\pi^-$	85
5.13. Parameters of the fits to the $X(1835)$ candidates.	88
5.14. Determined branching ratios for the decay $X(1835) \rightarrow \eta'\pi^+\pi^-$	88
5.15. External systematic uncertainties.	89
5.16. Systematic uncertainties coming from the event selection.	91
5.17. Resonances considered in the PWA.	102
5.18. Combined branching ratios.	110
6.1. Considered decays of the η_c	113

6.2. List of values needed for the calculation of the observed cross section and Born cross section.	132
---	-----

Acknowledgments

Am Ende dieser Arbeit möchte ich natürlich noch einigen Menschen Danke sagen, ohne die diese Arbeit nicht zustande gekommen wäre.

Alfons: Zuerst danke ich dir natürlich für die Möglichkeit meine Doktorarbeit mit dir als Doktorvater zu schreiben. Was vor fast 10 Jahren mit der Bachelorarbeit anfang hat nun mit der Doktorarbeit ihren Höhepunkt gefunden und wird auch noch weiter gehen. Danke für alle Unterstützung während der Doktorarbeit und das immer positive Feedback und die gute ansteckende Stimmung, vorallem als es am Ende etwas schleppend voran ging.

Anton und Karol: Vielen Dank für die Bereitschaft als zweiter und dritter Prüfer zur Verfügung zu stehen.

Dr. Evil Nyls: Auch unsere gemeinsame Zeit fing mit meiner Bachelorarbeit an und deine Betreuung während der Bachelorarbeit war einfach klasse. Danke das du auch jetzt, wo du nicht mehr hier in Münster bist, jederzeit für Fragen zur Verfügung stehst.

Josh: Auch wenn es bei mir am Ende deutlich länger gedauert hat, war unsere gemeinsame Doktorzeit eine schöne Zeit, die ich nicht vergessen werde.

CF37 und Andre: Danke für die tolle Zeit. Achja und: *Marcel? Maaaaarcel? Wo bist duuuuuuuuu?*

Anja: Danke für all die Diskussion über Partialwellen, den FSFilter, ROOT, Es wurde nie langweilig. Danke natürlich auch für das Korrekturlesen meiner Arbeit. Ich bin mir sicher, dass du in nicht allzu ferner Zukunft ebenfalls deine Arbeit erfolgreich abschließen wirst.

Antonio und Lois: Ohne euch beide wäre die Doktorzeit sicherlich nur halb so interessant gewesen. Bei Photoshop-Aktionen, Lebensgroßen Pappaufstellern, unserem gemeinsamen Minecraft-Server, ... war immer was zu lachen. Danke das ich euch meine Freunde nennen darf. Und Danke Antonio für das Korrekturlesen meiner Arbeit.

Die AG Khoukaz: Danke für die super Atmosphäre, für den Spaß bei unseren gemeinsamen Unternehmungen, den Mensagängen, DPG Tagungen, ... und Kuchen. Jede Menge Kuchen. Danke natürlich auch an die Bachelor und Master Studierenden, die ich betreut habe, es hat mir viel Spaß gemacht. Besonderer Dank geht hierbei an Sascha, für die große Hilfe bei der Z_{cs} Analyse.

Matthias und Matthias: Gemeinsam angefangen im Bachelor und auch wenn ihr euch dann anderen Zielen gewidmet habt so sind wir doch gute Freunde geblieben und unsere Gloomhaven- (und jetzt Frosthaven-) Runden waren ein fester Bestandteil seit viele Jahren

und werden es auch hoffentlich noch weiterhin bleiben.

Malte: Seit über 15 Jahren sind wir gemeinsam unterwegs, ob auf Zeltlagern, über Silvester im Schnee (Go Tigers!), oder jetzt seit kurzem auch hier an der Uni. Du warst jederzeit mein Vorbild als Wissenschaftler und niemand hat es mehr verdient jetzt eine Professur zu erhalten als du.

Meine Familie: Es wurde mir ja quasi schon in die Wiege gelegt einmal Physik zu studieren, Danke, dass ihr mich auf meinem Weg immer unterstützt habe und das ich immer einen Platz zu Hause hatte.

Frederik Weidner

Lebenslauf

Persönliche Daten

Name Frederik Weidner
Geburtsdatum 22.01.1994
Geburtsort Münster
Nationalität Deutsch

Bildungsweg

seit 04/2020 **Promotionsstudium (Dr. rer. nat.), Physik, Universität Münster**
unter Betreuung von Prof. Dr. A. Khoukaz

02/2019 – 08/2024 **Assoziiertes Mitglied im Graduiertenkolleg „2149 Starke und Schwache Wechselwirkung - von Hadronen zur Dunklen Materie“, Universität Münster**

10/2016 – 09/2018 **Masterstudium (M. Sc.), Physik, Universität Münster**
Abschlussarbeit: *Search for exotic states in $e^+e^- \rightarrow p\bar{p}\omega$ at center-of-mass energies above 4 GeV at BESIII*

10/2013 – 09/2016 **Bachelorstudium (B. Sc.), Physik, Universität Münster**
Abschlussarbeit: *Untersuchung der Reaktion $p + d \rightarrow {}^3\text{He} + \pi^+ + \pi^-$ unter besonderer Berücksichtigung des ABC-Effektes*

06/2013 **Allgemeine Hochschulreife**

09/2004 – 06/2013 **Immanuel Kant Gymnasium, Münster**

09/1999 – 08/2004 **Ludgerusschule Hiltrup, Münster**

Berufstätigkeit

seit 03/2020 **Wissenschaftlicher Mitarbeiter, Universität Münster, Institut für Kernphysik**

10/2018 – 02/2020 **Studentische Hilfskraft, Universität Münster, Institut für Kernphysik**

07/2016 – 02/2020 **Technische Betreuung von Fotobox-Systemen, PhotoBuzz Münster**